

IMPROVED OPTICAL FIBER PROBES FOR SCANNING NEAR FIELD
OPTICAL MICROSCOPY

BY

BRYAN R. WHEATON

A THESIS
SUBMITTED TO THE FACULTY OF

ALFRED UNIVERSITY

IN PARTIAL FULFILLMENT OF THE REQUIREMENTS
FOR THE DEGREE OF

DOCTOR OF PHILOSOPHY

IN
GLASS SCIENCE

ALFRED, NEW YORK

DECEMBER, 2004

Alfred University theses are copyright protected and may be used for education or personal research only. Reproduction or distribution in part or whole is prohibited without written permission from the author.

IMPROVED OPTICAL FIBER PROBES FOR SCANNING NEAR FIELD
OPTICAL MICROSCOPY

BY

BRIAN R. WHEATON

A.A.S. ALFRED STATE COLLEGE (1983)

B.S. ALFRED UNIVERSITY (2003)

SIGNATURE OF AUTHOR _____ (Signature on file) _____

APPROVED BY _____ (Signature on file) _____
ALEXIS CLARE, ADVISOR

_____ (Signature on file) _____
THOMAS P. SEWARD III, ADVISORY COMMITTEE

_____ (Signature on file) _____
WILLIAM C. LaCOURSE, ADVISORY COMMITTEE

_____ (Signature on file) _____
MATTHEW HALL, ADVISORY COMMITTEE

_____ (Signature on file) _____
DOREEN EDWARDS, CHAIR, ORAL THESIS DEFENSE

ACCEPTED BY _____ (Signature on file) _____
ALASTAIR CORMACK, DEAN,
SCHOOL OF ENGINEERING

ACKNOWLEDGEMENTS

I would like to thank everyone that helped to make my journey to receiving a Ph.D. possible. My formal education has taken place over the course of nearly four decades, and has been made possible through the insight and help of many. My mother, a terrific person, provided a basis of trust, honesty, hard work and integrity that has helped me become the person I am today. My elementary and high school faculty all played a role, especially key were; Mrs. Yarnell, my 6th grade teacher who had a new approach to learning and started to make education enjoyable for myself; Mr. Nosky, my junior high English teacher who taught me so much about what I was capable of; Mr. Baier, my high school science teacher who gave me a start in the science field; Mr. Cleaves, Mr. Smith and Mr. Henderson who taught me so much through sports, including the ability to win and lose with dignity, and the rewards that come from consistent effort and team work.

Thanks to my managers, colleagues, direct reports and mentors at Corning Incorporated, all of whom played a role in my development as a Corning employee, as well as professionally. Bill Schuler and Karen Morrissey believed enough in my abilities to set in motion educational leaves that allowed me to complete both my B.S. and Ph.D. degrees, and I feel very fortunate to have worked for both of them. Colleagues and mentors like Ed Bush, Doug Beall, Linda Pinckney, Greg Merkel and Marty Murtagh, just to name a few, made coming to work fun, exciting and rewarding. Erika Stapleton and Lisa Noni were able to continue to provide necessary characterization and development needs in diffraction and AFM, allowing me to dedicate the necessary time to my studies at Alfred. Thanks to Corning Incorporated for providing the opportunity to achieve my Ph.D., through a very generous education leave program.

I would like to thank the faculty at Alfred University with special thanks to Dr. Shelby and Dr. Hall (the professor, former colleague and friend) for many helpful and insightful discussions. I would also like to thank Dr. LaCourse and Dr. Seward for taking the time to read and correct my thesis. Thanks to all my fellow students, office mates and study partners: Michelle, Sutham, Matt, Doug(s), Fabienne, Aladdin, Jurgen, Dan, Chris, Liz, etc..

I will always be indebted to my thesis advisor, Dr. Clare, who provided guidance to my project, insight and direction when asked, and room to find my own way when it was necessary. Dr. Clare leads by example, and is truly committed to her students and the University, which is very lucky to have such a dedicated faculty member.

I am saving this last section of acknowledgements for the people who mean the most to me, my family. Thanks to Luann, my wife of 20 years, who has not only put up with me and partnered with me for all of those 20 years, but has provided extra support and encouragement throughout the last four years while I pursued my Ph.D.. Thanks to Drew and Kelin who I feel fortunate to be the father of, as I have watched them grow and mature from newborns to the fine young men that they are today. I could not be more proud of the family I have, and the time we spend together is the highlight of everyday.

I would like to dedicate this thesis to Luann, Drew and Kelin as well as my late mother, Inez, who I am sure is very proud of my accomplishments.

Table of Contents

Table of Contents	iv
List of Tables	vii
List of Figures	viii
Abstract	xv
1.0 INTRODUCTION	1
1.1 History of Scanning Probe Microscopy	2
1.2 Advantages of AFM	3
1.3 Limitations of AFM	3
1.4 Use of AFM in the Study of Glasses.....	4
1.4.1 Examples of General AFM Studies of Glasses	5
1.4.2 Study of Optical Fibers	9
1.4.3 High Resolution Study of Glass Surfaces.....	9
1.4.4 Chemical Force Microscopy and Glasses	11
1.5 References	12
2.0 EXPERIMENTAL PROCEDURE	14
2.1 Atomic Force Microscopy	15
2.2 References	21
3.0 UNDERSTANDING THE NEAR-FIELD SCANNING OPTICAL MICROSCOPY FIBER OPTIC TIP FORMATION PROCESS	22
3.1 Abstract	23
3.2 Introduction	23
3.2.1 Near-Field Scanning Optical Microscopy Overview	23
3.2.2 Modes of NSOM Operation.....	27
3.2.3 Applications of NSOM	30
3.2.4 Methods for Producing NSOM Tips	31
3.2.4.1 Fiber Pulling	33
3.2.4.2 Fiber Etching	34
3.2.4.3 Micro-Machined NSOM Tips	36
3.2.4.4 Apertureless NSOM Tips	37
3.3 Experimental Procedures.....	39
3.3.1 Safety Precautions	39
3.3.2 Preparation of Etch Solutions.....	40
3.3.3 Fiber Etching Procedures	42
3.3.4 Characterization of Etched Fiber End Faces.....	44
3.3.4.1 Optical Microscopy/Scanning Electron Microscopy	44
3.3.4.2 Atomic Force Microscopy.....	44

3.4 Results and Discussion	44
3.4.1 Initial Study of SMF28 and HI Optical Fibers.....	44
3.4.2 More Detailed Evaluation of the SMF28 Fiber Etching Process	60
3.5 Conclusions	77
3.6 References	78
4.0 EVALUATION OF PHASE SEPARATION IN GLASSES WITH ATOMIC FORCE MICROSCOPY	82
4.1 Abstract	83
4.2 Introduction	83
4.2.1 Phase Separation in Glasses	83
4.2.2 Characterization of Phase Separated Glasses.....	87
4.3 Experimental Procedures.....	88
4.3.1 Glass Melting and Sample Preparation.....	88
4.3.2 Atomic Force Microscopy	91
4.4 Results and Discussion	94
4.4.1 Alkali Borosilicate Results.....	94
4.4.2 Sodium Silicate Results	98
4.5 Conclusions	118
4.6 References	119
5.0 THIN FILM COPPER OXIDE LAYERS GROWN IN-SITU ON ALKALI BOROSILICATE GLASSES	122
5.1 Abstract	123
5.2 Introduction	123
5.2.1 Structure of Alkali Borosilicate Glasses	123
5.2.2 Copper in Glasses	124
5.2.3 Copper Oxide Films on Glasses	124
5.3 Experimental Procedures.....	125
5.3.1 Sample Preparation.....	125
5.3.2 UV-Vis Spectroscopy	128
5.3.3 Scanning Electron Microscopy	128
5.3.4 Differential Scanning Calorimetry	129
5.3.5 Thermo-gravimetric Analysis	129
5.3.6 X-ray Diffraction	130
5.3.7 Atomic Force Microscopy	130
5.3.8 XPS	133
5.4 Results and Discussion	134
5.4.1 Initial Characterization of Glass Lab Sample	134
5.4.2 Characterization of Glass Batch CU090403	140
5.4.3 Characterization of Sodium Borosilicate Glasses	150
5.4.3.1 Effect of Copper Level on Copper Oxide Film Formation	150
5.4.3.2 Heat Treatment Studies of Composition CU102903	157
5.4.3.3 Effect of Heat Treatment Atmosphere on Film Formation	174
5.4.3.4 Mechanism for Copper Oxide Film Formation	178
5.4.3.5 Effect of Alkali on Copper Oxide Film Formation.....	185

5.5 Conclusions	191
5.6 References	193
6.0 THESIS CONCLUSIONS	196
6.1 Understanding the Near-Field Scanning Optical Microscopy Fiber Optic Tip Formation Process.....	197
6.2 Evaluation of Phase Separation in Glasses with Atomic Force Microscopy	198
6.3 Thin Film Copper Oxide Layers Grown In-Situ on Alkali Borosilicate Glasses.....	198
Appendix A. Monolithic Lens Formed Through Etching at End of Optical Fiber	200
Appendix B. Trigonometric Analysis of Optical Fiber Radial Etch Rate.....	204

List of Tables

Table 3.1	Chemistry of Fiber Etch Solutions	41
Table 3.2	Summary of AFM Measurements	52
Table 3.3	Summary of AFM Results for SMF28 Fiber Etch Study	62
Table 3.4	Etch Rates Calculated from AFM Data	71
Table 4.1	Composition of Corning 7070 Glass	90
Table 4.2	Average Surface Roughness and Grain Size Results form 650°C Heat Treatment Study for Glass Composition 12.5Na ₂ O*87.5 SiO ₂	106
Table 4.3	Percent Area Due to High Silica Phase for 12.5Na ₂ O*87.5 SiO ₂ Heat Treated at 650°C	110
Table 4.4	Percent Interfacial Area for Various Heat Treatment Times at 650°C for Glass Composition 12.5Na ₂ O*87.5 SiO ₂	116
Table 5.1	Composition of Glass Batches Studied.....	127
Table 5.2	Composition of S1 Ceramic Crucible	128
Table 5.3	Bulk Composition of Glass Lab Specimen by XRF	140
Table 5.4	Summary of DSC Results for Copper Sodium Borosilicate Glasses	153
Table 5.5	Summary of AFM Results for Glass Composition CU102903	168
Table 5.6	Average Composition of Bulk Glasses	180
Table 5.7	XPS determined glass compositions in atomic %	190

List of Figures

Figure 1.1	AFM surface roughness analysis of silica glass after two polishing steps	6
Figure 1.2	Example of the characterization of surface features with AFM.	7
Figure 1.3	Polished sample of glass showing presence of very fine surface particles that resulted from the cleaning process.	7
Figure 1.4	AFM results of an as formed fusion drawn glass surface compared to the same surface after a wet chemical etch treatment.....	8
Figure 2.1	Interatomic force vs. distance curve for AFM interactions.	16
Figure 2.2	Schematic of TappingMode® AFM operation.	17
Figure 2.3	Schematic of EFM image collection in LiftMode™	19
Figure 2.4	Geometry used to prepare high quality fracture cross sections for evaluation of phase separation as well as film/glass interface for thickness determination via AFM.....	20
Figure 3.1	Sketch of different types of NSOM image generation.....	28
Figure 3.2	Schematic of a typical fiber tip NSOM set-up operated in illumination mode.	29
Figure 3.3	Mode propagation in a tapered metal-coated optical fiber at a wavelength of 488 nm.....	32
Figure 3.4	Diagram illustrating the techniques used to fabricate fiber optic NSOM probe tips.	38
Figure 3.5	Schematic of etch set-up.	43
Figure 3.6	Schematic of light rays guided by total internal reflection in a step index single mode optical fiber. The ratio of the diameter of the core to the cladding has been exaggerated for schematic purposes.	48
Figure 3.7	SEM and AFM image of an etched optical fiber illustrating the relationship between the core and cladding for a single mode fiber.	49

Figure 3.8	Three dimensional AFM views along with section views of the SMF28 and HI germanium silicate fibers etched in un-buffered HF	50
Figure 3.9	Results of AFM analysis for fibers etch in 1:1:2 etch solution for 10 minutes. a) 3D of SMF28, b) 3D view of HI, c) 2D section view of SMF2 and d) 2D section view of HI.....	51
Figure 3.10	Variation of core height with etch time.	53
Figure 3.11	Evolution of cone angle as a function of etch time.	56
Figure 3.12	AFM section profile of SMF28 fiber etched for 40 minutes in a 1:1:3 etch solution. Variations in height across the core region are the result of compositional variations resulting from the fiber process.....	56
Figure 3.13	AFM side views with projected full cone for a) SMF28 after 40 minute etch in 1:1:2, b) SMF28 after 40 minute etch in 1:1:6, c) HI after 40 minute etch in 1:1:2 and d) HI after 7.5 minute etch in 1:1:6.	57
Figure 3.14	Example of calculation of full cone angle from the AFM side view images.....	58
Figure 3.15	Relationship between clad/core differential etch rate and tip cone angle.....	59
Figure 3.16	Plot of the core height as a function of the value of X in the etch solution for etch times of 10 minutes.....	61
Figure 3.17	AFM profiles showing the evolution of the tip structure of an SMF28 fiber etched in a 1:1:4 solution.....	64
Figure 3.18	AFM profiles showing the evolution of the tip structure of an SMF28 fiber etched in a 1:1:2 solution.....	65
Figure 3.19	Plot of cone angle as a function of etch time for SMF28 fiber in various etch solutions.....	66
Figure 3.20	Final cone angle as a function of etch concentration.....	67
Figure 3.21	Tip height as a function of etch time and etch concentration.....	72
Figure 3.22	Schematic of the relationship between the height and width of an evolving cone ant the etch rates of the core and cladding.....	72
Figure 3.23	AFM section analysis for SMF28 fiber etched for 20 minutes and 60 minutes in 1:1:5 etch solution.	73
Figure 3.24	Plot of core radial etch rate and differential etch rate as a function	

of the value of X in the etch solution.....	74
Figure 3.25 Plot of the ratio of core etch rate to differential etch rate for SMF28 fiber.	75
Figure 3.26 Plot of the relationship between core radial etch rate, differential etch rate and cone angle for SMF28 fiber etched in buffered HF solutions.....	76
Figure 4.1 Free energy versus composition curve for a glass in the immiscibility region.	84
Figure 4.2 Metastable immiscibility diagram for the sodium silicate system with typical microstructures expected from the various regions of the system.	86
Figure 4.3 Geometry used to prepare high quality fracture surfaces of bulk glasses for AFM analysis.	91
Figure 4.4 Schematic of TappingMode [®] AFM operation.	93
Figure 4.5 AFM images of Corning 7070 glass after heat treatment to 700°C.	95
Figure 4.6 Predicted vs. observed growth of phase separation for nucleation and growth type mechanism in Corning 7070 glass.	96
Figure 4.7 Time dependence of the droplet radius for samples of Corning 7070 heat treated at 700°C.....	97
Figure 4.8 Immiscibility diagram for sodium silicate glass along with AFM images displaying the morphology of 12.5%Na ₂ O*87.5%SiO ₂ glass heat treated for 15 minutes at temperatures of 637, 720, 778 and 791°C.	101
Figure 4.9 Sodium silicate glass heat treated at 778°C for 15 minutes showing secondary phase separation within the high sodium matrix phase.	102
Figure 4.10 AFM topographical images displaying the evolution of phase separation in 12.5%Na ₂ O*87.5%SiO ₂ glass heat treated for various times at 650°C.	103
Figure 4.11 Predicted versus observed growth of phase separation for the spinodal-type mechanism.	104
Figure 4.12 Average surface roughness (Ra) as a function of heat treatment	

Time at 650°C for glass composition 12.5Na ₂ O*87.5SiO ₂ ,	107
Figure 4.13 Average surface roughness (Ra), <i>during chemical segregation stage of spinodal decomposition</i> , as a function of square root of heat treatment time at 650°C for glass of composition 12.5Na ₂ O*87.5SiO ₂ ,	107
Figure 4.14 AFM Grain Size analysis for glass of composition 12.5Na ₂ O*87.5SiO ₂ heat treated at 650°C for 1020 minutes.....	111
Figure 4.15 Average area of inhomogeneity as a function of heat treatment time at 650°C for glass of composition 12.5Na ₂ O*87.5SiO ₂ ,	112
Figure 4.16 Average area of inhomogeneity, during ripening stage of spinodal decomposition, as a function of heat treatment time at 650°C for glass of composition 12.5Na ₂ O*87.5SiO ₂ ,	112
Figure 4.17 Results of bearing analysis for a 1020 minute heat treatment at 650°C for glass of composition 12.5Na ₂ O*87.5SiO ₂ ,	113
Figure 4.18 Image analysis routine of Flugel showing the reduction of the interfacial area between silica rich and sodium rich phases for an isothermal heat treatment at 650°C.....	115
Figure 4.19 Trend in interfacial area, as determined by the routine of Flugel, as a function of cube root of heat treatment time at 650°C for glass of composition 12.5Na ₂ O*87.5SiO ₂ ,	116
Figure 4.20 Three dimensional AFM image of 12.5Na ₂ O*87.5SiO ₂ heat treated at 650°C for 1020 minutes.	117
Figure 5.1 Schematic of EFM image collection in LiftMode TM	132
Figure 5.2 Geometry used to prepare high quality fracture cross sections of the film/glass interface for thickness determination via AFM.....	133
Figure 5.3 SEM image of “over-the-edge” fracture surface of Glass Lab specimen.....	136
Figure 5.4 EDX analysis of bulk glass and film surface (10kV).	137
Figure 5.5 Surface XRD trace of Glass Lab specimen thin film.....	138
Figure 5.6 Results of AFM analysis of thin film formed on Glass Lab Specimen.	139
Figure 5.7 Surface XRD results of glass CU090403 after heat treatment at	

600°C for 10 hours.....	144
Figure 5.8 Spectral reflectance results of glass CU090403 as melted and after heat treatment at 600°C for 10 hours.....	144
Figure 5.9 SEM and AFM results of the as melted surface of glass CU090403.	145
Figure 5.10 AFM section analysis and 3-D view of the as formed surface of glass CU090403.....	146
Figure 5.11 SEM results of glass CU090403 heat treated 10 hours at 600°C.....	147
Figure 5.12 AFM results of glass CU090403 heat treated at 600°C for 10 hour.....	148
Figure 5.13 SEM images of glass micro-spheres formed from glass CU090304.....	149
Figure 5.14 Surface XRD results of glass composition CU093003 after heat treatment at 500°C for 24 hours.	153
Figure 5.15 Variation in glass transition temperature as a function of copper oxide concentration in the glass.	154
Figure 5.16 Results of DSC analysis of copper sodium borosilicate glasses with 10 and 15 weight percent CuO.	155
Figure 5.17 Results of XRD analysis of 15% CuO composition after DSC analysis to 600°C.	156
Figure 5.18 AFM top view, 3D view and section analysis of the as melted surface of glass composition CU102903.	159
Figure 5.19 AFM top view, 3D view and section analysis of the film surface of glass composition CU102903 after heat treatment at 400°C/24 hours.....	160
Figure 5.20 AFM top view (top) with phase (bottom) for higher resolution look at the film surface of glass composition CU102903 after heat treatment at 400°C/24 hours.....	161
Figure 5.21 AFM top view, 3D view and section analysis of the film surface of glass composition CU102903 heat treated at 500°C/2 hours.....	162
Figure 5.22 AFM top view, 3D view and section analysis of the film surface of glass composition CU102903 after heat treatment at 500°C/24 hours.	163

Figure 5.23 AFM top view with phase for higher resolution look at the film surface of glass composition CU102903 after heat treatment at 500°C/24 hours.....	164
Figure 5.24 EFM results on the film surface of glass composition CU102903, after heat treatment at 500°C/24 hours.	165
Figure 5.25 Plot of surface roughness as a function of heat treatment time, and heat treatment temperature for glass composition CU102903.....	168
Figure 5.26 AFM section analysis for glass composition CU102903 heat treated at 510°C for various times.....	169
Figure 5.27 AFM section analysis for glass composition CU102903 heat treated at 490°C for various times.	170
Figure 5.28 AFM section analysis, with equivalent z-scales, for the 66 hour heat treatment at 490°C and the 71 hour heat treatment at 510°C.....	171
Figure 5.29 Film thickness, as determined by AFM, for glass composition CU102903 heat treated at 490°C and 510°C.....	171
Figure 5.30 Cross section AFM images of glass/film/air interfaces for glass composition CU102903 heat treated at 490 and 510°C.	172
Figure 5.31 Results of TGA analysis for a 3 hour isothermal hold at 500°C of glass powder from composition CU102903.	173
Figure 5.32 Weight gain as a function of the square root of treatment time for an isothermal hold at 500°C for glass powder from composition CU102903.	173
Figure 5.33 Pressure-temperature phase stability diagram for the Cu-Cu ₂ O-CuO system.....	174
Figure 5.34 Surface XRD result of copper oxide film formed under vacuum.	176
Figure 5.35 Surface XRD result of copper film formed under hydrogen atmosphere.	176
Figure 5.36 AFM images of metallic copper film grown under hydrogen atmosphere.	177
Figure 5.37 Sputter depth profile of a section of as-polished glass of composition CU102903.	182

Figure 5.38	Sputter depth profile of a polished and heat treated section of glass composition CU102903.....	182
Figure 5.39	High resolution XPS Cu 2p spectra from the heat treated specimen, comparing chemical state at the film surface with that at the beginning of Region 2.....	183
Figure 5.40	High resolution XPS Cu 2p spectra from the as-polished specimen, comparing chemical state at the surface with that of the bulk.	183
Figure 5.41	High resolution Cu 2p spectra from the heat treated sample showing changes across the CuO-glass interface (Region 2).	184
Figure 5.42	AFM images of the as poured surface of glass composition CU042104 (lithium containing glass).....	187
Figure 5.43	AFM images of the surface of glass composition CU042004 (potassium containing glass) after a 24 hour heat treatment at 515°C for 24 hours.....	188
Figure 5.44	AFM of as polished surface of glass composition CU041904 (lithium containing) showing the presence of phase separation.....	189
Figure 5.45	Representative high resolution Cu 2p spectra comparing copper chemical state between glasses prepared with various alkali. The CuO layer from sample CU102903 is shown for comparison.	190
Figure A1	3D AFM images of optical fiber etched in 1:1:1.9 etch solution for a) 1 minute and b) 5 minutes.....	202
Figure A2	Section AFM images of optical fiber etched in 1:1:1.9 etch solution for: a) 1 min and b) 5 minutes.	203

Abstract

The motivation behind this work stems from a combination of my interest in atomic force microscopy (AFM) and the need to apply AFM to several areas of glass research. AFM was used as the main characterization tool in the study of near-field scanning optical microscopy (NSOM) tip formation, evaluation of phase separation in glasses and copper oxide semiconductor film formation.

The use of atomic force microscopy (AFM) to evaluate the evolving tip structure of an optical fiber probe for NSOM was studied. This study demonstrates the feasibility of predicting the final tip cone angle, without taking the etching process to completion. Cone angles reported in this study ranged from 58 to 152 degrees, depending on the fiber type and etch conditions. The ability to vary the probe cone angle, and utilize AFM to evaluate the cone angle that results from a set of etch conditions, are valuable additions to the development of NSOM fiber tips.

The chemical and spatial variation of phase separated morphologies in glasses can range from a few angstroms to microns, often requiring very high magnification for detection. Historically phase separated glasses have been characterized by transmission electron microscopy (TEM), a time consuming and costly technique. Atomic force microscopy (AFM) provides an inexpensive alternative to TEM and has proven to be a powerful tool in the evaluation of type, degree and scale of phase separation in glasses down to the nanometer level.

AFM was used to show that the thickness and uniformity of the CuO films grown in-situ on the surface of copper containing alkali borosilicate glasses increased with time and temperature, however an upper time limit was reached in which no further thickness increases were realized. Tenorite, cuprite and copper metal films were produced depending on the heat treatment environment. XPS was utilized to confirm that copper oxide film formation during heat treatments of glasses near T_g results from the oxidation of copper ions, in the near surface region of the glass, from the 1^+ to the 2^+ state.

Chapter 1

Introduction:

Atomic Force Microscopy in the Study of Glasses

1.1 History of Scanning Probe Microscopy

Scanning probe microscopy (SPM) got its start with the invention of the scanning tunneling microscope (STM) in 1982 by Binning and Rohrer of IBM, Zurich.¹ The impact the invention of SPM would have on characterization at the nanoscale was evident and led to the awarding of the Nobel Prize in Physics to Binning and Rohrer in 1986. Due to development of personal computers in the early 1980's, STM rapidly advanced from a complex, ultrahigh vacuum, specialty instrument to a low cost commercially available non-vacuum microscope, and closely related techniques began to emerge by the mid 1980's. The main drawback to the STM was that a conducting surface was required.

The atomic force microscope (AFM) was developed in 1986 when scientists realized that the forces that a very sharp tip exerted on the sample surface could be used to map surface topography on a nanoscale.² AFM, based on these local force interactions between a sharp probe tip and the sample surface, allowed for imaging of non-conducting materials by SPM for the first time. The first commercial AFMs were not available until the late 1980's, making SPM a relatively new analytical technique.

A plethora of new SPM techniques have emerged within the last 15 years that have extended the level of understanding of materials on the nanoscale. Current capabilities of SPM include:

- scanning tunneling microscopy (STM)
- contact mode atomic force microscopy (AFM)
- intermittent-contact or tapping mode AFM
- non-contact mode AFM
- chemical force microscopy (CFM)
- magnetic force microscopy (MFM)
- lateral force microscopy (frictional properties) (LFM)
- force modulation (elastic properties) FMAFM
- electrostatic force (surface charge distribution)

- phase imaging
- electrical force microscopy (EFM)
- scanning capacitance microscopy (SCM)
- thermal imaging

The main feature that all SPMs have in common is that measurements are performed with a sharp probe maintained in the near field, that is, scanning over the sample surface while maintaining a very close spacing to the surface. The development of the SPM has allowed scientists and engineers to see structure and detail with unsurpassed resolution in three dimensions without the need for rigorous sample preparation. For a complete description of the various AFM modes and the many uses of AFM, see the recent article by Jandt.³

1.2 Advantages of AFM

The AFM is quite simple to operate, allows for air, fluid or vacuum imaging, and if sample preparation is necessary the time commitment and necessary equipment is usually minimal. Sub-nanometer resolution in three dimensions is the main advantage of AFM over other microscopy techniques. The resolution of AFM is better than 1 nm in x and y, and can exceed 1 Å in z. In addition to the outstanding resolution AFM analysis is often non-destructive, quantitative and analysis time is in the range of a few minutes.

1.3 Limitations of AFM

SPM, as with any characterization tool, has drawbacks in addition to the advantages of the technique. Artifacts due to the measuring system, the finite tip shape and the surface topography have led to erroneous interpretation of results. It is important to understand the different artifacts that may result from SPM imaging, and realize when they are present. Good reviews of possible image artifacts to consider, how to avoid them, and how to manage them are provided elsewhere.⁴ Due to a finite tip shape of the

AFM cantilever combined with long range interactions, individual atoms can not be imaged on glasses in air. Atomic resolution of glasses requires ultra-high vacuum which greatly increases the cost of otherwise rather inexpensive characterization equipment.

In addition to artifacts, there is a limited field of view associated with SPM. Typical piezo-electric scanners have x and y ranges of 50 -200 microns, and z ranges less than 10 microns. Due to the small scan range, and the fact that image size is usually in the micron to nanometer range, sample surface homogeneity must be understood, and the question always has to be asked; “is this image representative of the overall sample surface?”

Excellent vibration and acoustic isolation from the environment is necessary to avoid mechanical, electrical or acoustical noise. Isolation becomes more critical the higher the resolution required and the smoother the surface being evaluated. Charging of glass surfaces can cause problems with adequate contact between the tip and the sample, and lead to poor results.

1.4 Use of AFM in the Study of Glasses

Since the introduction of STM in 1982, SPM has been successfully applied to observe the surface of ceramic materials, metals, semiconductors, polymers and bio-molecules. AFM is also used extensively in the study of glasses because a conducting surface is not required as with SEM. In addition, some of the more difficult sample preparation routines that can have negative effects on brittle glasses are not required for AFM analysis. AFM provides information on glass structure and surface defects as well as changes in surface topology due to treatments such as polishing, cleaning, corrodng, weathering, aging and annealing and is considered both a routine analytical tool as well as a research grade instrument. This section will look at the application of SPM to the study of glasses where resolutions from several microns to atomic levels have been reported.

1.4.1 Examples of General AFM Studies of Glasses

AFM has become a common tool for evaluation of the quality of glass surfaces. Measurement of surface roughness and detection of surface defects are among the more general uses of AFM in the study of glass surfaces. Surface roughness analysis is routinely completed on glass samples and provides information on how process steps or use effect the quality of the sample surface. Figure 1.1 displays an example of AFM surface roughness for silica glass polished under two separate conditions. Clearly the bottom image shows a very well polished surface compared to the top, even though the top surface had a fairly low average roughness value of around 0.4 nm. In addition to overall surface roughness, quantitative information about surface defects can be obtained from routine AFM analysis. Figure 1.2 displays an AFM section analysis across a clearly visible scratch in a polished glass surface. The deepest scratch on the surface was only 3 nm deep, however the excellent z resolution of AFM made imaging and quantification of the scratch rather straightforward.

AFM provides a tool capable of evaluating surface contamination on glasses that may result from process steps. Figure 1.3 is a topographical AFM image of a polished glass surface that was left with an elevated contact angle after a process washing step. The AFM was able to resolve surface contamination on the order of 10 nm that was not able to be imaged by other techniques. AFM is also a powerful tool to evaluate changes to the surface of glasses due to exposure to corrosive environments. Frischat states that AFM can be used to examine surface defects, and changes in overall surface topology caused by treatments such as cleaning, aging, polishing or corroding.⁵ Figure 1.4 shows an as-formed alkali-free borosilicate glass surface with an average roughness around 0.2 nm and the same glass after a brief exposure to dilute HF acid. The acid exposed surface has about a 4 fold increase in surface roughness, and the section lines in Figure 1.4 provide a visual look at the changes.

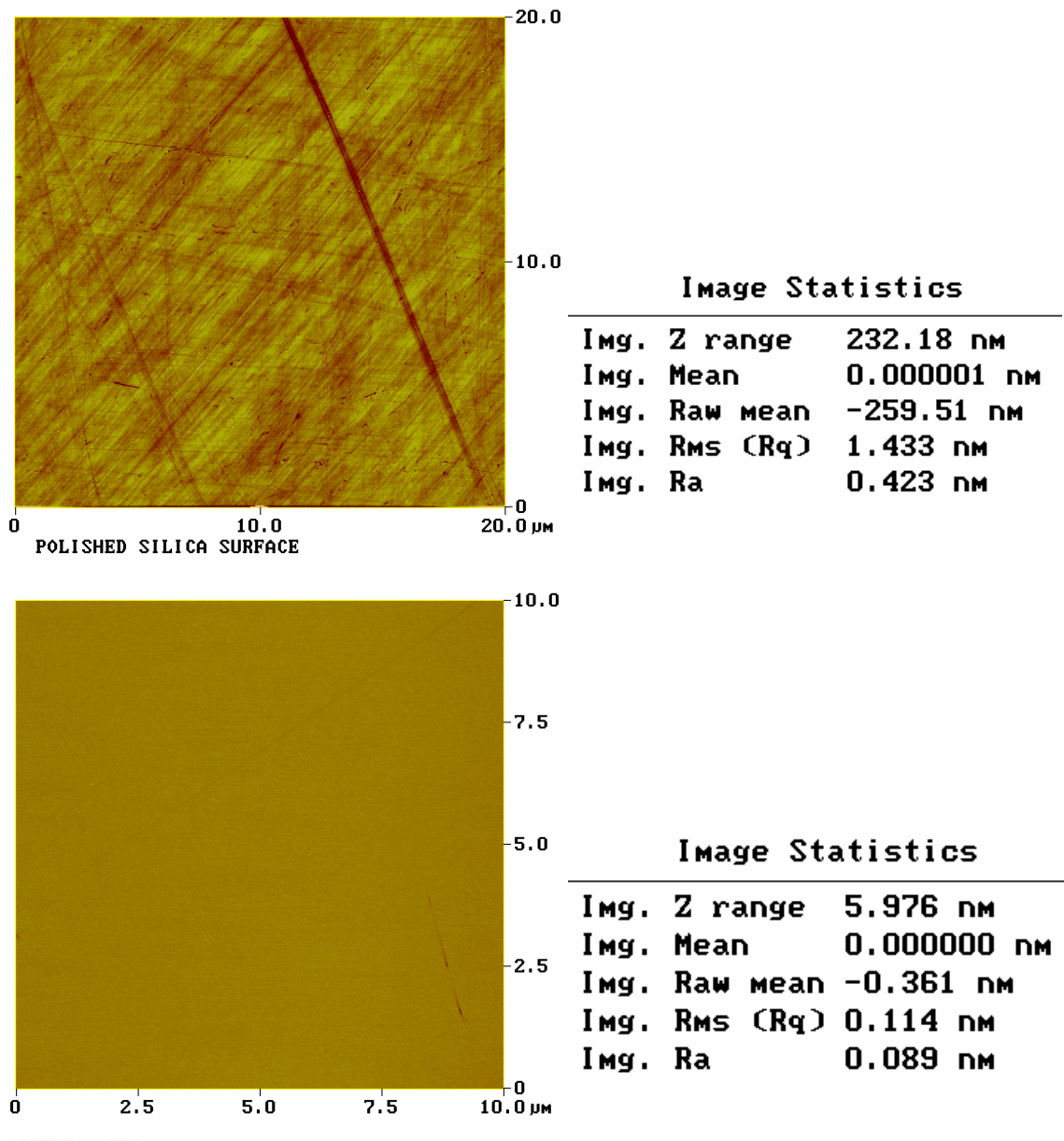


Figure 1.1. AFM surface roughness analysis of silica glass after two polishing steps.

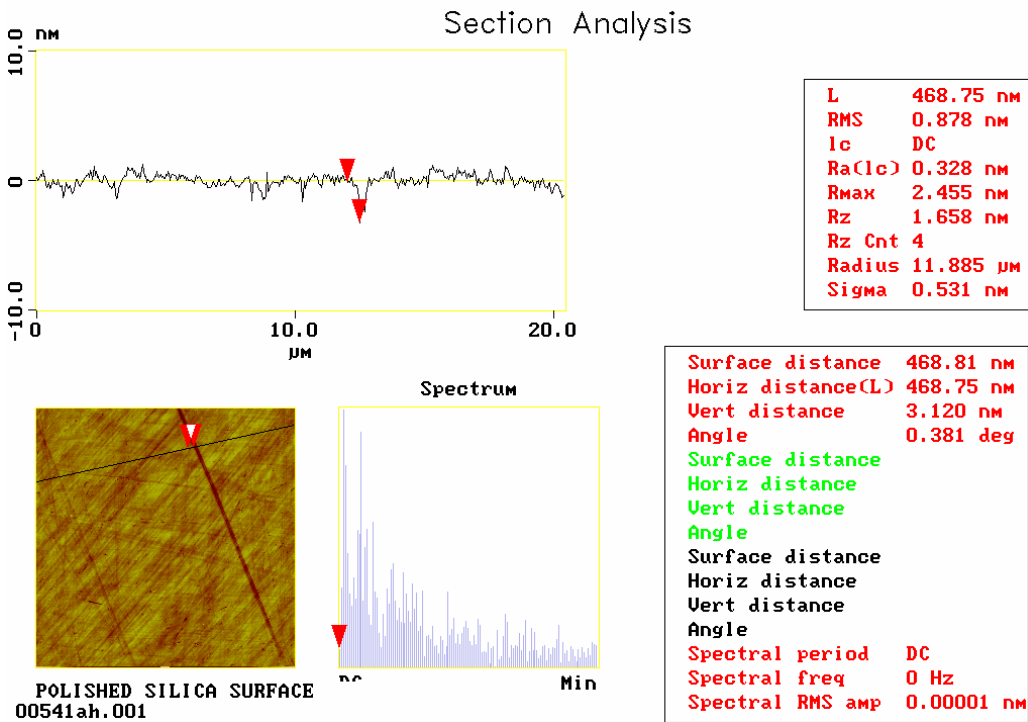


Figure 1.2. Example of the characterization of surface features with AFM.

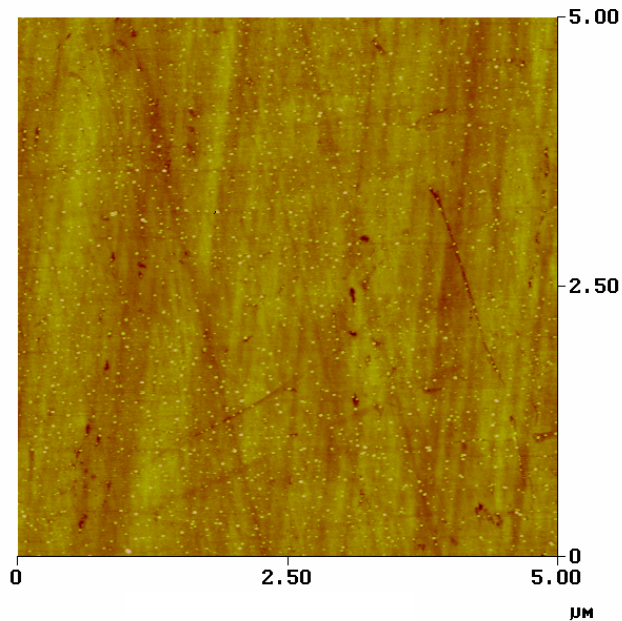


Figure 1.3. Polished sample of glass showing presence of very fine surface particles that resulted from the cleaning process.

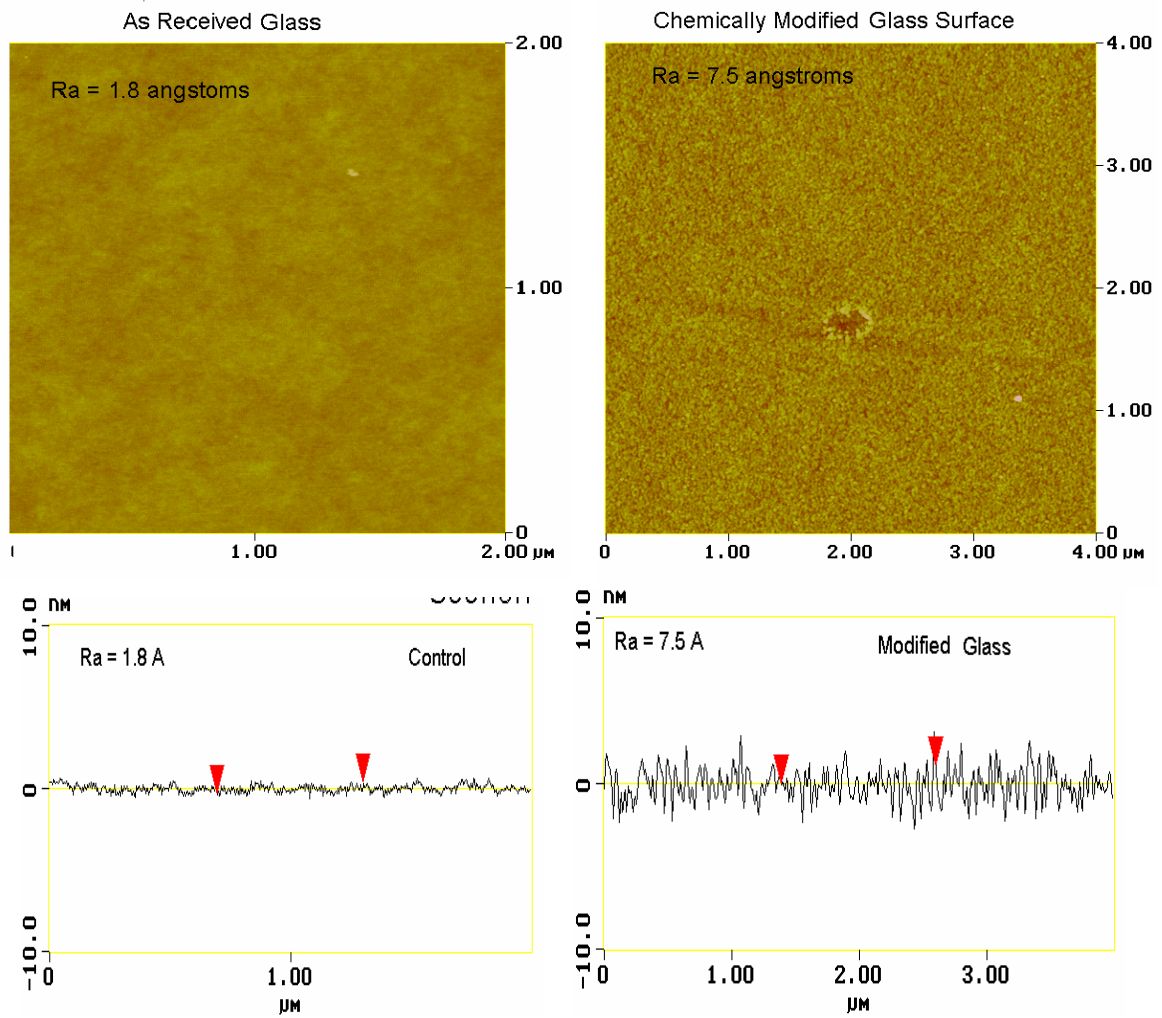


Figure 1.4. AFM results of an as formed fusion drawn glass surface compared to the same surface after a wet chemical etch treatment.

1.4.2 Study of Optical Fibers

AFM has been used to study dopant profiles of optical fibers, which can be important to the transmission properties and functionality of the thin glass wires. The geometry, structure and chemistry of the optical fiber determine properties such as refractive index, waveguide dispersion, polarized mode dispersion, and mode-coupling. The surface topography of cleaved and etched optical fibers is related to the chemical composition profile and therefore the refractive index of the fiber. The structures of the core, cladding, and interfaces can be studied with presently unsurpassed spatial resolution. Optical fibers can be evaluated by AFM in air with no conductive coating, and analysis time is typically less than 15 minutes, including sample preparation.

AFM was first used to study cleaved and etched optical fibers by Zhong and Inniss of Bell Laboratories, whose work was published in 1994.⁶ Zhong and Inniss correlated etch profiles of germanium doped silica optical fibers to refractive index, thereby allowing a direct estimate of refractive index changes based on topographical changes of the etched fiber end face. The variation in etch rate was used as a fingerprint to determine the effect of dopant chemistry and preform fabrication conditions on the fiber structure. Structural distortions of the lightguiding structures were measured directly with AFM providing very high spatial resolution. Also, by establishing a correlation between the refractive index change and the etching topography three dimensional refractive index profiles were generated from the AFM data. Tsai and Chung of the National Chung Cheng University of Taiwan followed the work of Zhong and Inniss with two papers on studying the structure of optical fiber with AFM.^{7,8}

1.4.3 High Resolution Study of Glass Surfaces

AFM provides a powerful tool to evaluate the surface of as-formed as well as fractured glass surfaces. The first reported study of AFM in glass research was presented in 1991 by Arribart et al.⁹ The work studied the air and tin sides of float glass, polishing grooves and defects and tin oxide coating on glass with resolutions as good as 1 nm.

Since this first paper hundreds of publications have been reported using some form of SPM in glass research.

Gupta et al. reported on the use of AFM to study melt-formed and fracture surfaces of silica and E-glass.¹⁰ This groups' conclusions stated that the nanoscale roughness of a melt-formed glass surface was controlled by surface tension of the melt at the glass transition temperature and the nanoscale roughness observed in the mirror region of a fractured glass is due to intrinsic inhomogeneities in the structure of the glass. Surface roughness of melt-formed surfaces were shown to have root mean square (RMS) roughness values less than 2 Å, while the smoothest mirror region of the fracture surfaces had RMS roughness values of 4-8 Å. The fracture surfaces were assumed to follow the weak regions of the inhomogeneous glass structure, similar to a trans-granular brittle fracture in a polycrystalline ceramic.

Ichikawa applied high resolution STM and AFM to the study of semi-conducting Ge₂₀Te₈₀ glasses and observed structural evolution during annealing.^{11,12} Local ordering was reported on limited portions of the surface, however interpretation of the images was limited and 'humps' in the STM images may have been due to electron density from bonds between atoms instead of atom positions themselves. The combination of STM and AFM revealed short range order (0.5nm), medium range order (2-3 nm) and supra-medium range order (15-20nm).

The first report of direct determination of glass structure by AFM imaging was reported by Raberg and Wandelt for barium silicate glasses in 1997.¹³ Hexagonal rings that consisted of six SiO₄ tetrahedra separated by 0.26nm, the length of a siloxane bridge, were visible on the AFM images.

Frischat et al. provided atomic resolution of fracture surfaces of silica, silicate, borosilicate and heavy metal fluoride glasses with the AFM under ultra-high vacuum conditions.^{5,14,15} The preparation of fracture surfaces in vacuum prevents the reaction of water vapor with the highly reactive fresh fracture surface, which allows the direct imaging of the surface without the interfering water layer. The very high (atomic) resolution non-contact AFM results from these studies, along with detailed image analysis, yielded features that were interpreted as inter-atomic distances, grouping of atoms, network holes, distribution of atomic distances, percolation paths and topological

connectivities of the glass structure. The atomically resolved images displayed a fully interconnected random network arrangement for silica, a modified random network with percolation paths for silicate glasses, a structure with higher connectivity and short percolation paths for borosilicate glass and a highly interconnected structure for the heavy metal fluoride glasses, with some chain and ring-like geometries. The work of Frischat and colleagues is currently considered state of the art for atomic resolution of glasses, however considerable interpretation of the images is necessary.

1.4.4 Chemical Force Microscopy and Glasses

The ability to chemically modify the AFM tip and utilize the tip as a chemical probe to evaluate various chemical species on the surface of a glass is currently a major thrust in the area of AFM research. Tips can be modified with functional groups such as -COOH and -CH₃ to provide contrast in the AFM image due to hydrophobicity variation on the sample surface. AFM tips can also be functionalized with a species that is of interest to study, such as proteins or DNA. Glass micro-spheres of known composition can be attached to AFM cantilevers to evaluate the interaction of the glass with substrates and coatings under various conditions, such as pH. Greater adhesion between a functionalized tip and the sample leads to higher pull-off forces and more cantilever deflection. Using proteins as surface probes, Korwin-Edson determined that CFM was the most promising surface characterization technique for evaluation of binding forces between proteins and glass surfaces.¹⁶

1.5 References

1. G. Binning, H. Rohrer, C. Gerber, and E. Weibel, "Surface Studies by Scanning Tunneling Microscopy," *Phys. Rev. Lett.*, **49** [1] 57-61 (1982).
2. G. Binning and C.F. Quate, "Atomic Force Microscopy," *Phys. Rev. Lett.*, **6** [9] 930-3 (1986).
3. K.D. Jandt, "Atomic Force Microscopy of Biomaterials Surfaces and Interfaces," *Surf. Sci.*, **491** [3] 303-32 (2001).
4. R. Howland and L. Benatar, *A Practical Guide to Scanning Probe Microscopy*; pp. 65-70. Park Scientific Instruments, Sunnyvale, CA, 1996.
5. E. Radlein and G.H. Frischat, "Atomic Force Microscopy as a Tool to Correlate Nanostructure to Properties of Glasses," *J. Non-cryst. Solids*, **222** [11] 89-92 (1997).
6. Q. Zong and D. Inniss, "Characterization of the Lightguiding Structure of Optical Fibers by Atomic Force Microscopy," *J. Lightwave Technol.*, **12** [9] 1517-23 (1994).
7. D. Tsai and Y. Chung, "Study of Optical Fibre Structures by Atomic Force Microscopy," *Opt. Quant. Electron.*, **28** 1563-70 [10] (1996).
8. D. Tsai and Y. Chung, "Study of Optical Fiber Structures Using Atomic Force Microscopy and Scanning Near-Field Optical Microscopy," *SPIE*, **2695**, 204-10, (1996).
9. H. Arribart and D. Abriou, "Ten Years of Atomic Force Microscopy in Glass research," *Ceram.-Silik.*, **44** [4] 121-8 (2000).
10. P.K. Gupta, D. Inniss, C.R. Kurkjian, and J. Zhong, "Nanoscale Roughness of Oxide Glass Surfaces," *J. Non-cryst. Solids*, **262** [1-3] 200-6 (2000).
11. K. Ichikawa, "The Effect of Annealing on the Structure of Ge₂₀Te₈₀ glass: Atomic -Scale Imaging Using a Scanning Tunneling Microscope," *J. Non-cryst. Solids*, **150** [1-3] 435-9 (1992).
12. K. Ichikawa, "The Nanoscopic Structure of Annealed Ge₂₀Te₈₀ Glass: Quasi-Atomic-Scale Imaging Using Atomic Force Microscopy," *J. Phys.: Condens. Matter*, **7** [10] L135-39 (1995).

13. W. Raberg and K. Wandelt, "Atomically Resolved AFM Investigations of the Amorphous Bariumsilicate Surface," *Appl. Phys. A: Solids Surf.*, **66**, [Supp. 1] S1143-6 (1998).
14. J.F. Poggemann, G. Heide, and G.H. Frischat, "Direct View of the Structure of Different Glass Fracture Surfaces by Atomic Force Microscopy," *J. Non-cryst. Solids*, **326-327** [1-3] 15-20 (2003).
15. G.H. Frischat, J.F. Poggemann, and G. Heide, "Nanostructure and Atomic Structure of Glass Seen by Atomic Force Microscopy," *J. Non-cryst. Solids*, **345-346**, 197-202 (2004).
16. M.L. Korwin-Edson, "Silica Surface Characterization as a Function of Formation and Surface Treatment Using Traditional Methods and Proteins as Surface Probes"; Ph.D. Thesis. Alfred University, Alfred, NY, 2004.

Chapter 2

Experimental Procedures – Atomic Force Microscopy

2.1 Atomic Force Microscopy

Each chapter of this thesis has its own section on experimental procedures. However, atomic force microscopy (AFM) is used extensively throughout the thesis, requiring a more detailed explanation of the technique than the individual chapter procedure sections provide.

The common feature of a scanning probe microscope (SPM) is that a solid probe with a sharp tip is physically scanned over the surface of the sample, with a separation between the tip and the sample maintained in the near-field through a feedback loop. The tip, which has a radius of curvature often less than 10 nm, is located at the free end of a cantilever that is 100 to 200 microns in length. Forces between the tip and the sample surface alter the movement of the cantilever causing it to bend or change its oscillation amplitude. A detector measures the cantilever movements as the tip is scanned over the sample surface with the use of a piezoelectric tube scanner. The measured cantilever motion allows the generation of a digital map of surface topography.

AFM images can be generated from several interaction forces between the tip and the sample, with the most common force associated with AFM being the interatomic force or van der Waals force. The van der Waals interaction forces will be controlled by the tip to sample distance as shown in the interatomic force vs. distance curve depicted in Figure 2.1. In contact mode imaging the cantilever is maintained in the van der Waals repulsive region and results in the largest interactive forces between the tip and the sample. The tip is in constant physical contact with the sample during contact mode imaging often resulting in damage to the sample surface.

The AFM cantilever is vibrated near the sample surface for non-contact imaging, with the spacing between the tip and the surface on the order of hundreds of angstroms. The lightest interaction forces between the tip and the sample are realized with non-contact imaging, however the resolution and image quality is often poor compared to other AFM imaging modes.

Intermittent-contact or tapping mode imaging bridges the gap between contact and non-contact AFM imaging providing the highest resolution with very low forces between the tip and the sample. Tapping mode imaging also uses a vibrating cantilever

similar to non-contact mode, except the cantilever is brought close enough to the sample surface that at the bottom of its oscillation it just makes contact with the surface and therefore barely “taps” the sample. The cantilever’s oscillation amplitude is affected by surface topography providing a feedback mechanism by which tapping mode AFM images are collected.

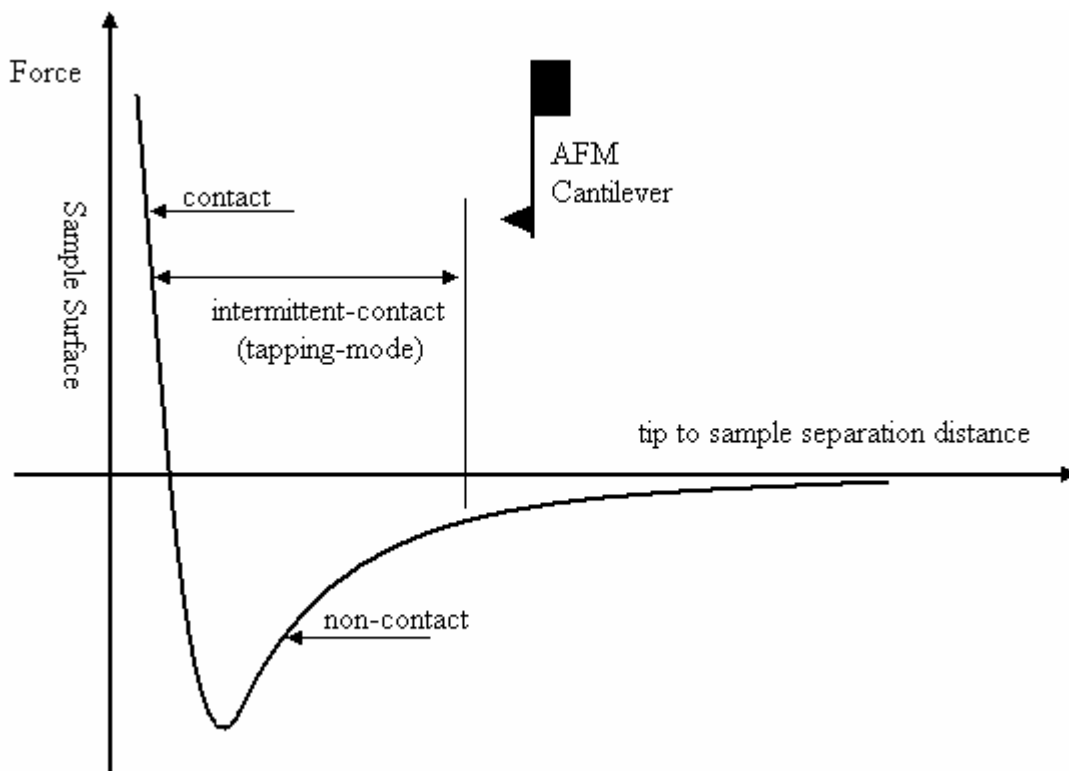


Figure 2.1. Interatomic force vs. distance curve for AFM interactions.

In the research reported here, a Digital Instruments Dimension 3100 Scanning Probe Microscope with a Nanoscope IIIA controller was used in TappingMode® to produce three-dimensional topographical images, phase and electrical force images. Pyramidal etched silicon probes with a half cone angle of 18° and an approximate radius of curvature of 10nm were used for all measurements. Figure 2.2 displays a simple schematic of all the key components of a typical AFM system operating in TappingMode®.

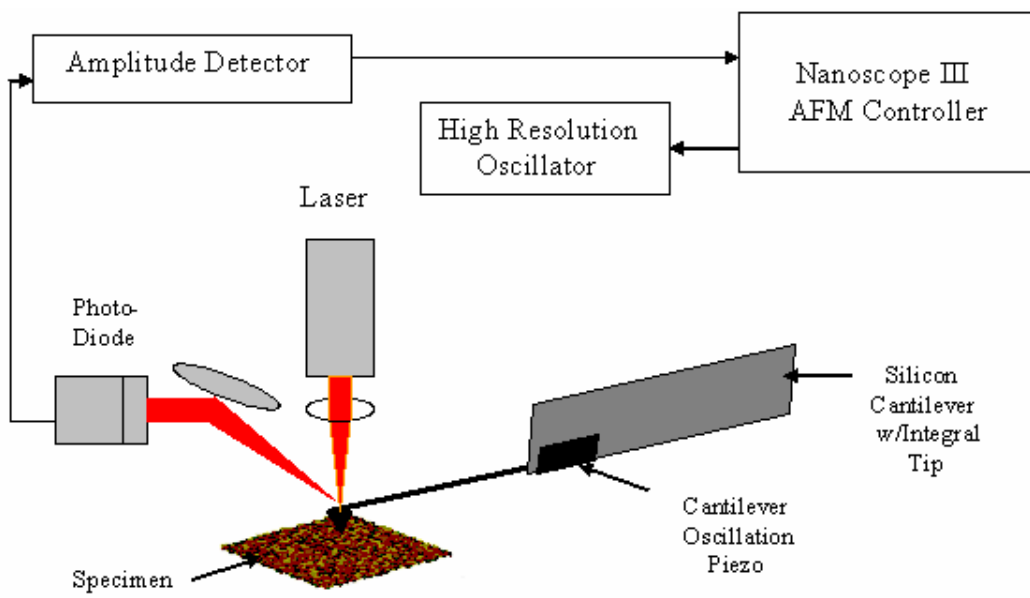


Figure 2.2. Schematic of TappingMode® AFM operation.

A more detailed description of AFM image collection during tapping mode operation will be provided here. Tapping mode images are generated by scanning a very sharp probe tip, on the end of an integrated cantilever that is oscillated at or near its resonance frequency, in a raster pattern over the sample surface while lightly “tapping” on the surface. The motion of the tip above the sample is controlled by a piezoelectric tube scanner, and the tip-sample interaction is monitored by reflecting a laser off the top of the cantilever into a split photodiode detector. An electronic feedback circuit, between the photo-detector and the z-piezo, maintains the tip oscillation at a constant set-point amplitude during scanning by moving the scanner vertically at every x,y data point. The three dimensional digital image is produced by mapping the motion of the z-piezo required to maintain a constant oscillation amplitude at each lateral data point.

The tip-sample interaction is affected by van der Waals forces between the tip and the sample surface, air damping, cantilever elastic response, sample elasticity, a capillary force from adsorption of a monolayer of water on the sample surface, etc.^{1,2} Once the tip is in intermittent contact with the sample surface, adjustments to a series of parameters

that control the feedback loop and scanning conditions are adjusted until the best possible image quality is realized.

Phase images are generated simultaneously with the topographical images by monitoring the phase delay between the detected value and the drive signal of the oscillating cantilever with the use of the Phase Extender Module. Phase Imaging is a powerful extension of TappingMode® AFM that provides nanometer scale resolution about surface structure and properties that may not be revealed by simple topography.³ Phase images provide image contrast based on a differential interaction between the tip and the sample surface. Phase images have limited sensitivity to surface topography but provide contrast based on adhesion, hardness, friction, viscoelasticity, and composition as well as other properties.

The AFM silicon cantilever is excited into resonance oscillation with a piezoelectric driver and the oscillation amplitude is used as the feedback signal to measure surface topography of the sample. The phase lag of the cantilever oscillation relative to the drive signal is monitored by the Phase Extender Module to provide the simultaneous phase image. The topography and phase image are viewed and collected simultaneously in real time. Phase imaging can often highlight edges and is not affected by large-scale height differences providing good grain boundary contrast even when a rough surface is being imaged.

The AFM was also used to carry out electrical force microscopy (EFM) measurements of thin copper oxide films on glass. EFM is a special AFM technique that characterizes sample surfaces based on electrical properties. A conductive AFM tip interacts with the sample through long-range Coulomb forces, which affect the oscillation amplitude and phase of the AFM cantilever. EFM images are collected in LiftMode™ which is a two-pass technique that separates topographical information from the electrical response. For each separate scan line, the topographical data is recorded in normal tapping mode as described above. A second pass of the known topography is made with the tip lifted a given height above the sample surface, usually in the 10-100 nm range. The tip to sample separation is constant during the second pass and only the longer range electrical forces affect the oscillation of the cantilever. Figure 2.3 is a simple schematic of

AFM operated in LiftModeTM where the dark regions near the surface are regions of the sample that symbolize the source of contrast in the EFM image.

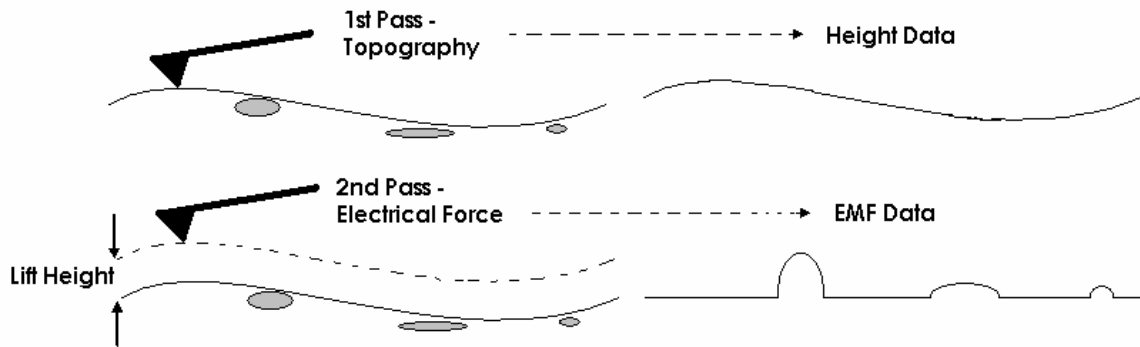


Figure 2.3. Schematic of EFM image collection in LiftModeTM.

To determine the thickness of the films by AFM, a special sample preparation technique was utilized. A low speed, precision saw was used to create a small, thin region of specimen that contained the glass/film interface. Just prior to AFM analysis the specimens were fractured under slight tension, producing a cross section that could be evaluated out to the very edge of the film. Figure 2.4 displays a schematic of the specimen preparation for AFM analysis of fractured specimens for evaluation of phase separation and film thickness. The fractured surfaces were etched in a suitable solution to provide topographical relief for phase separation evaluation. For film thickness evaluation, the fracture pattern provides topography of the film region, allowing for straight forward determination of the glass/film interface.

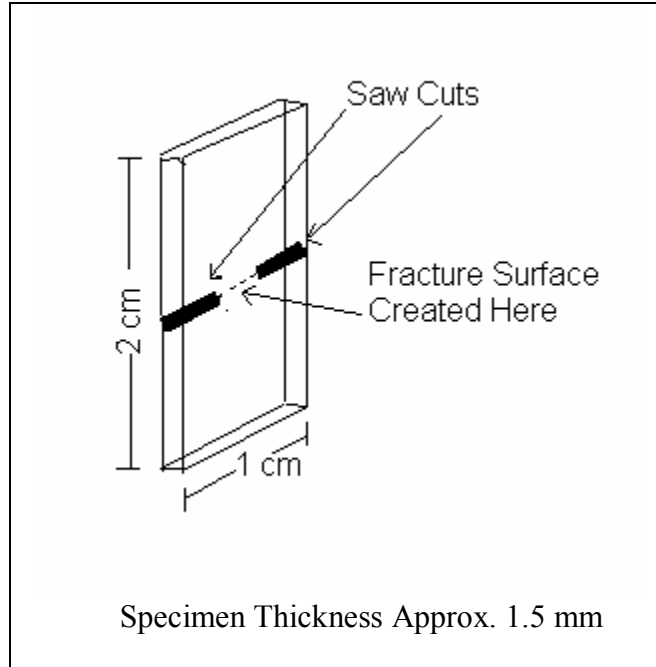


Figure 2.4. Geometry used to prepare high quality fracture cross sections for evaluation of phase separation as well as film/glass interface for thickness determination via AFM.

2.2 References

1. R. Jones, H.M. Pollock, J.A.S. Cleaver, and C.S. Hodges, "Adhesion Forces Between Glass and Silicon Surfaces in Air Studied by AFM: Effects of Relative Humidity, Particle Size, Roughness and Surface Treatment," *Langmuir*, **18** [21] 8045-55 (2002).
2. L. Zitzler, S. Herminghaus, and F. Mugele, "Capillary Forces in Tapping Mode Atomic Force Microscopy," *Phys. Rev. B: Condens. Matter Mater. Phys.*, **66** [15] 1554361-8 (2002).
3. K.L. Babcock and C.B. Prater, "Phase Imaging: Beyond Topography, Application Note," Veeco Instruments, Santa Barbara, CA., 1995.

Chapter 3

Understanding the Near-Field Scanning Optical Microscopy Fiber Optic Tip Formation Process

3.1 Abstract

The current state of near-field scanning optical microscopy (NSOM) is limited by the ability to produce high quality fiber optic probes with adequate optical throughput and sufficient damage thresholds. The use of atomic force microscopy (AFM) to evaluate the evolving tip structure of an optical fiber probe for NSOM was studied. The cone angle was dependent on the concentration of GeO₂ in the fiber core as well as the concentration of the etch solution. Two single mode optical fibers were studied, with etch concentrations of 1 part water:1 part 50% HF:X parts 40% NH₄F, with X varying from 1 to 6. This study demonstrates the feasibility of predicting the final tip cone angle, without taking the etching process to completion. The final cone angle can be predicted by the differential etch rate between the core and the cladding, as well as measuring the angle directly with the use of the AFM. Cone angles reported in this study range from 58 to 152 degrees, depending on the fiber type and etch conditions. The ability to vary the probe cone angle, and utilize AFM to evaluate the cone angle that results from a set of etch conditions are valuable additions to the development of NSOM fiber tips.

3.2 Introduction

3.2.1 Near-Field Scanning Optical Microscopy Overview

Modern science relies strongly on spectroscopic and microscopic techniques for material characterization. Optical microscopy has long been an important and powerful characterization tool in the area of scientific research, as it provides a considerable amount of information about structure and dynamics as a result of the interaction of light with matter. The combination of spectroscopy and microscopy is especially useful in material characterization when spectral features can be spatially resolved. Resolution of an optical system is determined by how close two objects can reside and still be distinguished as two separate objects.

The diffraction limit in conventional optical microscopy arises from the size of the spot to which a light beam can be focused with normal lens elements. Ernst Abbe¹, in

1873, determined that the diffraction limit sets the maximum achievable lateral resolution of objects in a light microscope to:

$$d = 0.61 (\lambda_0 / n \sin \theta) \quad (1)$$

where, d is the distance between two resolvable objects, λ_0 is the vacuum wavelength of the incident radiation, n is the refractive index of the medium the light travels in and θ is the light convergence angle for the focusing element. The denominator in Equation 1, $n \sin \theta$, is also referred to as the numerical aperture (NA) of the objective. Numerical apertures of 1.3-1.4 are possible with high quality objective lenses and working in mediums of water or oil (immersion lenses), simplifying the right side of Equation 1 to $\lambda/2$. Diffraction therefore limits the resolution of an ordinary optical system to the characteristics of the light source and the photo-detector along with the optical elements in between. For conventional optical microscopy with a visible light source, resolution is diffraction limited to 200-300nm. However, in an apparatus-limited measurement the resolution is improved considerably when a sub-wavelength structure is utilized, enabling microscopic electromagnetic interactions to couple with the incident and outgoing light waves. Near field optics and photonics are classified as apparatus-limited measurements, and interactions occurring on a sub-wavelength scale are relevant to the optical properties of interest.

Near-Field imaging occurs when light is transmitted through an optical probe with a sub-wavelength aperture that is positioned a short distance from the sample surface. The near-field is defined as the region that is less than one wavelength of the incident light above the sample surface. Within this short distance above the sample surface, the evanescent light is not diffraction limited resulting in nanometer scale spatial resolution. The near-field phenomenon allows for non-diffraction limited optical microscopy and spectroscopy with resolutions that are not possible with conventional optical imaging techniques.

Near-Field Scanning Optical Microscopy (NSOM) is a relatively new analytical technique capable of providing optical information of materials with a resolution better than 50 nanometers. The chief use of NSOM is to generate high lateral resolution images

of optical transmission, fluorescence emission, and birefringence from transparent samples. A sharp optical probe tip with nanometer dimensions generates optical information, in the near-field, by sending, collecting, or diffracting light at the sample surface. Laser light coupled into a single mode optical fiber passes through a sub-wavelength aperture at the end of the fiber. Transmitted light or laser induced fluorescence emission is collected by an objective and imaged onto a detector. An image is formed by raster scanning the sample and recording the collected light intensity as a function of scan position.

The idea of near-field optical microscopy is not a new one, as the theory first appeared in a 1928 paper by Edward H. Synge.² Given a certain excitation wavelength and an aperture of sub-wavelength dimension, the optical near-field was defined by Synge as the region of space less than one wavelength from the light source within which diffraction does not occur. Synge proposed the use of a scanned aperture to construct a microscope whose resolution was a function of only the size of the light source and the distance from the sample providing resolution far beyond the diffraction limit. When the aperture becomes considerably smaller than the wavelength of light, the transmitted electric field is localized close to the opening and the intensity decreases exponentially, (evanescent waves) away from the opening.³ Synge's ideas were ahead of the technology available at the time and experimental demonstrations of his idea had to wait for technology able to fabricate a sub-wavelength size probe tip, and control the tip with high precision, as well as computer power capable of digital image processing.

The first experimental demonstration of near-field scanning microscopy was carried out nearly half a century after the initial near-field paper by Synge. Ash and Nichols⁴ used 3 cm wavelength microwaves to achieve $\lambda/60$ resolution in the first experimental demonstration of NSOM in 1972. The first modern NSOM experiments using visible light were credited to the simultaneous work of several groups in the mid 1980's. D.W. Pohl,⁵ et al. in 1984 recorded a sub-wavelength resolution optical image by moving an extremely narrow aperture along a test object equipped with fine-line structures. Detail, 25 nm in size, was recognized using 488-nm radiation. The result indicated a resolving power of at least $\lambda/20$ which was compared with the values of $\lambda/2$ obtainable in conventional optical microscopy. Also in 1984 Lewis et al.,⁶ describe a scanning optical

microscope based on near-field imaging with 300Å diameter aperture capable of resolution as small as one-tenth the wavelength of incident light. Lewis et al.,⁶ also demonstrated the use of a near-field microscope in 1984 capable of sub-micron resolution.

Although the technique is finding many applications in the area of glass and photonics research, the overall success of the technique is limited by problems associated with producing high quality, reproducible, and robust optical fiber probe tips, and continues to be largely a technique in progress today. Betzig and Trautman⁷ introduced the first aperture probe in 1992 which allowed for sub-diffraction fluorescence imaging and further stimulated interests in material and biological sciences.

The quality and properties of the tip is one of the most important aspects of a scanning probe microscopy technique. The geometry of the tip end and the interactions of the tip and the sample determines the instrument's overall performance and ultimately limits the resolution. Near field scanning optical microscopy (NSOM), even more so than other scanning probe techniques, requires very well characterized optical probes for light emission and collection. Optical information with resolution as good as 10 nanometers has been achieved with NSOM, however consistency and quality of the optical fiber probes have limited the overall success of the technique. The ideal NSOM fiber probe is characterized by high transmission of light through an aperture with a diameter of tens of nanometers. Desirable properties of NSOM probes are high brightness, a well defined circular aperture, no loss of light through the sides of the tapered region, and a high damage threshold.

The transmission coefficient of an aperture fiber probe at a given wavelength is defined as the ratio of the light power emitted by the aperture to the power of the light coupled into the taper region. Transmission coefficients as high as 10^{-4} have been reported, however typical transmission coefficients of glass fiber probes are in the range of 10^{-5} to 10^{-6} .⁸ This means that only one photon in approximately one million is available for measurement. A second problem with the current state of optical fiber NSOM probes is poor damage thresholds. The optical fiber probes are coated with metal to absorb stray light at the tapered fiber end, where light is no longer isolated to the fiber core by total internal reflection. The metal/glass interface is a weak link in the integrity of the fiber, and spalling of the metal occurs at a certain power level, known as the

damage threshold. More light demanding applications, such as NSOM Raman and NSOM laser ablation, require much higher transmission coefficients and higher damage thresholds for brighter sample illumination.⁸

The following sections will briefly review the modes of NSOM operation, describe some promising applications and results of the technique, and review the current state of NSOM probes.

3.2.2 *Modes of NSOM Operation*

There are several possible modes of NSOM operation that result in optical resolution in the range of 10's of nanometers. The various modes provide flexibility in the intensity of the light incident on the sample, the microscope geometry and the sample type (thick, thin, opaque, transparent, etc). Figure 3.1 is a schematic of various modes of NSOM sample illumination and collection.

For illumination mode NSOM, light is coupled into the waveguide from an external source, such as a laser, and guided through the tip of the probe. The probe must be designed so that the radiation only passes through the small aperture in the end of the probe. The light scattered from the sample, usually scanned beneath the probe tip, is collected in the far field through an objective used in either reflection or transmission.³ Illumination by the tip is one of the easier modes to interpret and provides relatively strong signal.

The sample is illuminated with a macroscopic light source from the top or bottom in collection mode imaging and the probe is used to collect the evanescent field from the sample surface. The NSOM probe can also be used for both illumination of the sample surface and collection of the reflected signal referred to as illumination/collection mode imaging. The illumination/collection mode has the drawback of elevated background due to the light which is reflected back up the fiber without interacting with the sample surface, and requires additional filtering to remove the background.

The optical image is formed digitally by assigning the measured optical intensity to the corresponding x/y scanning position. Sensitive feedback control is required to maintain a constant tip to sample distance in the near-field and provide optimal resolution.

must remain constant, and in the near-field during the scanning process, requiring sensitive feedback control for optimal resolution. A topographical image is also formed from the feedback conditions that maintain a constant separation between the tip and the sample surface. The topographical image is critical for interpretation of the optical image to avoid misinterpretation resulting from topographically induced optical features. Figure 3.2 is a schematic of a NSOM operating in transmission, normal force mode with all the components required for operation.

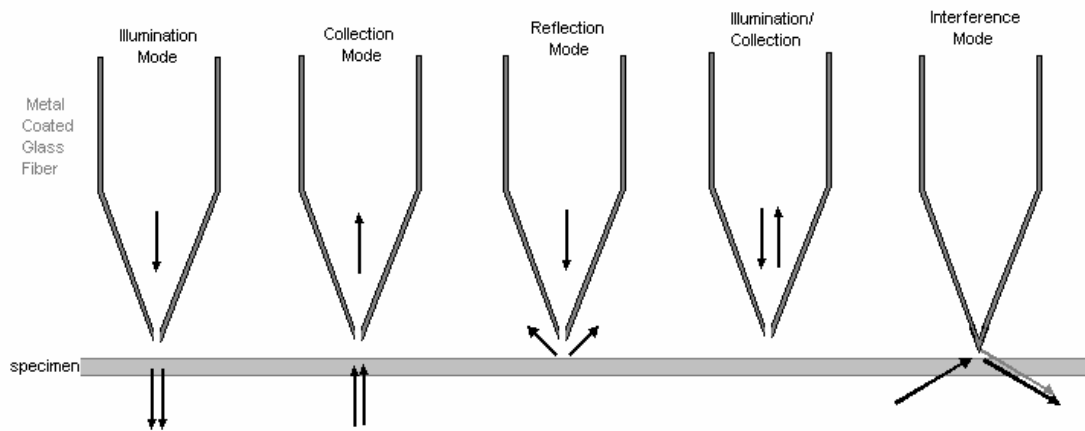


Figure 3.1. Sketch of different types of NSOM image generation.

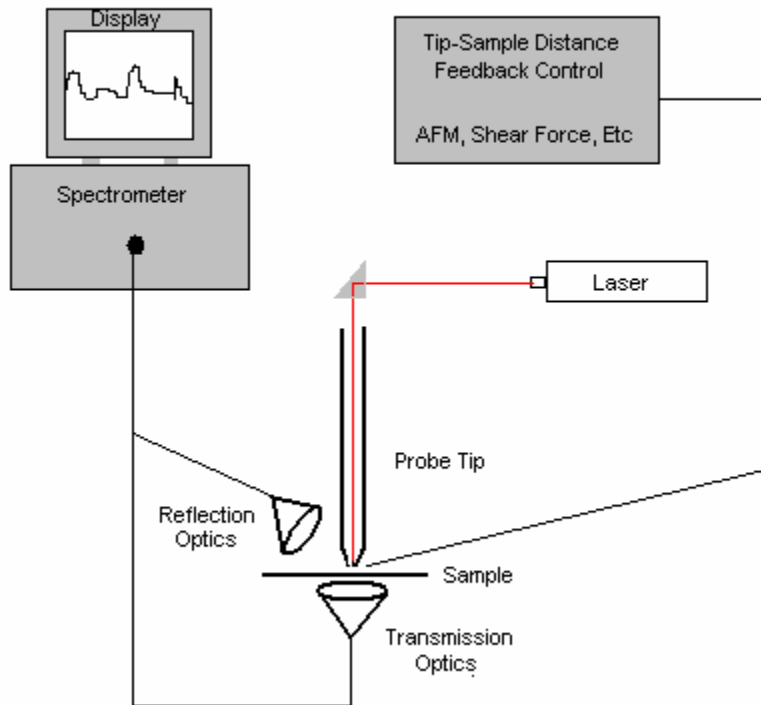


Figure 3.2. Schematic of a typical fiber tip NSOM set-up operated in illumination mode. Laser light is coupled into a sub-wavelength aperture, that illuminates a sample placed in the near field of the tip. The scattered light from the sample is collected in the far field through objectives placed in either transmission or reflection.

3.2.3 Applications of NSOM

Gaining a better understanding of materials at the molecular and even atomic levels is a requirement for many areas of material research. NSOM has been successfully applied in many studies to gain information about physical and chemical properties of materials at the nanometric level. However, unlike the more mature AFM technology NSOM is still very new and a large percentage of the work published in this field is related to understanding and modifying the technique itself. However NSOM has evolved to a point where very unique and useful measurements can be made on a wide variety of materials.

Changes in light intensity are usually used to create contrast in a NSOM image, although it is possible to use changes in the polarization of the light as a contrast mechanism or even the dependence of the light intensity from the wavelength used to illuminate the sample. There are several properties of a sample that can give contrast in the NSOM image. The following list provides many of the NSOM contrast mechanisms discussed in the literature:

- Changes in the index of refraction^{9,10}
- Changes in the transparency
- Changes in the polarization⁹
- Changes in reflectivity
- Stress at certain points of the sample that cause changes in the optical properties
- Magnetic properties which cause changes in the optical properties
- Fluorescence³
- Topographical variation in the surface
- Raman shift^{3,11-13}
- Thermal imaging¹⁴
- Laser ablation combined with mass spectrometry^{3,15}

Several comprehensive reviews exist that discuss applications of NSOM to various fields of research. Hsu¹⁶ reviews applications of NSOM in the study of electronic and

photonic materials and devices. De Serio et al.³ review areas of NSOM research utilizing fluorescence, Raman scattering and laser ablation combined with mass spectrometry. DeAro,⁹ et al. discusses applications of NSOM to the study of various nanostructured materials. This review covers engineered semiconductor nanostructures such as quantum wells, quantum wires, and quantum dots as well as domain formation in polymers, molecular crystals, Langmuir-Blodgett films and layered organic self-assemblies.

Robert Dunn, a pioneer in NSOM studies, reviews the use of NSOM for single molecule detection, thin film analysis and biological applications.¹⁷ Spectral characterization of single molecules eliminates the averaging encountered in bulk spectroscopy opening possibilities for observing fundamental molecular level processes that may be hidden in the bulk analysis. The ability to observe the fluorescence from a single protein combined with the ability of NSOM to image in fluid, offers opportunities for dynamic, *in vitro* biological studies.

3.2.4 Methods for Producing NSOM Tips

The sub-wavelength dimensioned light source is one of the most important components of a near-field microscope. The formation of probe tips is a crucial step in any form of scanning probe microscopy (SPM), but is a larger hurdle for NSOM than more mature forms of SPM like atomic force microscopy, where knowledge of glass science is not necessary. The geometry and optical characteristics of the NSOM fiber optic tip have a direct impact on image quality and ultimately instrument resolution.

The mode structure and importance of the taper region in a metallic waveguide at optical frequencies was calculated by Novotny and Hafner.¹⁸ The results of the work of Novotny and Hafner can be interpreted such that in a tapered waveguide, where the core diameter decreases gradually, one mode of propagation after another runs into cutoff until only one mode remains, designated the HE₁₁ mode. Cutoff is defined as the diameter of the core at which the wave vector becomes imaginary and the mode field decays exponentially. The transmission coefficient of the light is determined by the power still propagating in the HE₁₁ mode compared to the power contained in the cutoff modes,

which is largely dependent on the geometry of the optical fiber tip taper. The schematic in Figure 3.3 illustrates mode propagation in a tapered metal-coated fiber at a wavelength of 488nm. Below an inner probe tip diameter of 160nm even the HE₁₁ mode runs out of room for 488nm light. The wave vector becomes imaginary at the cutoff and the mode field decays exponentially. Due to the exponential decay of the mode field, the power actually reaching the aperture, and available for NSOM imaging depends heavily on the distance between the HE₁₁ cutoff diameter and the aperture plane. Larger cone angles will therefore result in a shorter distance between the HE₁₁ cutoff diameter and the aperture plane resulting in improved transmission coefficients for optical fiber probes.

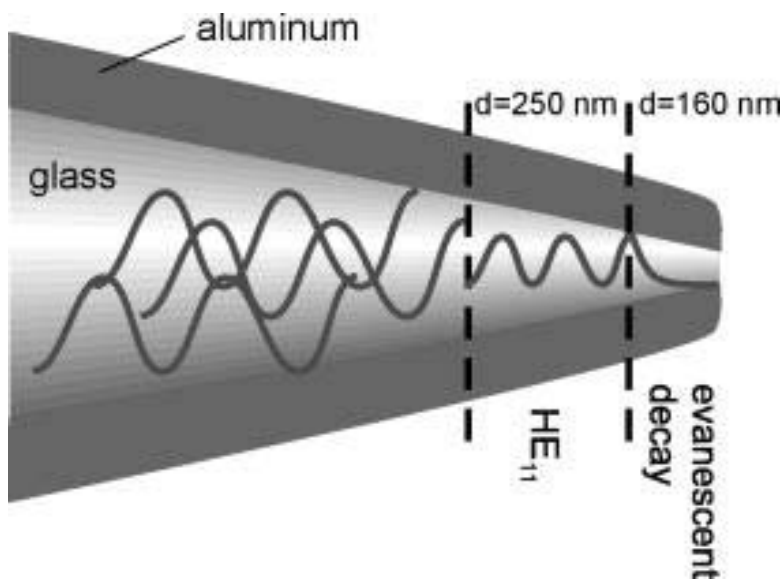


Figure 3.3. Mode propagation in a tapered metal-coated optical fiber at a wavelength of 488 nm¹⁹. Cutoff diameters taken from the work of Novotny and Hafner.¹⁸ Reprinted with permission from Bert Hecht, Beate Sick, Urs P. Wild, Volker Deckert, Renato Zenobi, Olivier J. F. Martin, and Dieter W. Pohl, Journal of Chemical Physics, 112, 7761 (2000). Copyright 2000, American Institute of Physics.

As described above the desirable properties of NSOM probes are high brightness, a well defined circular aperture, no loss of light through the sides of the tapered region, and a high damage threshold. Applied tip fabrication processes are currently capable of

producing NSOM tips that vary dramatically in geometry, surface characteristics and optical properties. NSOM probes have been reported to be fabricated from many materials including cleaved crystals, AFM cantilever tips, fabricated semiconductor structures, glass pipettes, metal strands, and most often tapered optical fibers. Two methods are routinely employed for creating the necessary NSOM optical fiber probe architecture. Single mode optical fibers can be heated and pulled into a fine tip,^{20,21} or the fibers can be etched to produce a cone at the fiber end.^{20,22} Both processes require metal sputter coating of the tapered fiber probes. Figure 3.4 is a schematic of the various techniques used to develop NSOM tips from optical fibers. This section will review the types of NSOM tips available as well as summarize the fabrication processes involved with each type.

3.2.4.1 Fiber Pulling

The fiber pulling method has been the most popular formation process for NSOM tip fabrication. The method of fiber pulling utilizes a CO₂ laser to heat a small area of a fiber under tension. The fiber is heated and pulled until it elongates and breaks leaving a long fiber tip. The fiber pulling method is rapid when compared to tip etching, and control over heating and pulling parameters results in excellent reproducibility. Commercial micropipette pullers are available that allow for variation in pulling parameters, such as temperature and speed resulting in reproducible NSOM fiber probes. The heating and pulling method produces long tips with well defined apertures and very smooth sidewalls. The smooth sidewall surfaces allow for good metallization with Al grain size on the order of a few nanometers.²³

The drawback to the fiber pulling technique is that the tapers are very long, and cone angles are very small, leading to mechanical instability and poor collection efficiency. In the taper region of the NSOM fiber tip the diameter of the fiber becomes so small that, for a given wavelength, the modes can no longer propagate by total internal reflection and the wave becomes evanescent resulting in an exponential decay of the transmitted intensity. Transmission through fiber tips produced with the pulling process

are very low, in the range of 10^{-5} to 10^{-6} .²⁴ Compared to chemical etching, the fiber pulling technique is considerably more capital intensive, requiring a CO₂ laser and pipette pulling apparatus.

3.2.4.2 Fiber Etching

Fiber etching provides a simple and less expensive alternative to fiber pulling in the fabrication of fiber optic probe tips for NSOM applications. There are several variations to the chemical etching methodology for producing NSOM probe tips with the majority of methods incorporating hydrofluoric acid (HF) or a buffered HF solution. Chemical etching has the advantage of producing very short tapers, and therefore larger cone angles and higher transmission coefficients. The ability to vary the cone angle with fiber etching is an advantage over the fiber pulling technique. The cone angle of the resulting NSOM fiber tip will depend on the type of fiber, type of solvent, type of etch solution and concentration as well as the etch solution temperature. Transmission coefficients are often orders of magnitude higher for fibers produced by chemical etching than by fiber pulling, as a result of the larger cone angles that can be achieved by etching versus pulling optical fibers. Additionally, the taper is much shorter with the etching techniques when compared to fiber pulling resulting in better preservation of polarization properties of the source. The main disadvantage of chemically etched tips is poor fiber surface quality that influences the metallization process in a negative manner. Irregularities in the cone surface can result in areas of poor metal adhesion and result in a lower damage threshold due to thermal degradation of the metal coating. Another significant disadvantage of the etching techniques are the very hazardous chemicals, such as HF, that are required for the etching process.

D.R. Turner²⁵ patented a technique in 1984 to fabricate NSOM tips by etching the glass fibers with hydrofluoric acid. The taper is formed by the acid meniscus at the liquid-liquid-glass interface which declines with time. By changing the HF concentration, temperature, and the type of organic overlayer the glass taper angle can be controlled to some extent. Sayah et al.²³ used a meniscus etching technique originally patented by Turner to achieve optical transmissions as high as 10^{-3} , and cone angles that varied from

18 to 33 degrees. Singlemode optical fibers were etched in aqueous HF covered by a layer of immiscible solvent. The solvent has several roles, as it provides protection to the environment against toxic HF vapors, protects the fiber after etching and serves to form a meniscus along the fiber tip during etching. The surface properties of the protective layer effect the shape and contact angle of the meniscus formed, and therefore varying the protective layer affects the cone angle of the fiber tip produced. A conical tip forms at the interface between the solvent and the HF solution due to the decrease of the meniscus height related to a decrease of the tip diameter.

Suh and Zenobi⁸ describe a tube etching technique, also referred to as selective etching that results in NSOM fiber probes with smoother surfaces, although the ability to vary the cone angle is diminished considerably. The optical fiber's protective polymer coating is left on during etching, allowing the entire etching process to take place inside the hollow cylinder formed by the fiber's protective coating. Tube etching was shown to be reproducible, allows for some variation of the cone angle, and has the main advantage of providing smoother sidewalls for aluminum coating. The smooth tapers are a result of a reduction in the sensitivity to vibrations during etching. The tube etching process was reported to be self-limiting, meaning that no further tip deterioration occurs if etching continues after tip formation is complete. The tips were reported to have much higher damage thresholds allowing higher input power resulting in brighter transmission for NSOM Raman and NSOM laser ablation techniques.

Puygranier et al.^{26,27} evaluated the properties of NSOM fiber tips produced from a HF solution buffered with ammonium fluoride (NH₄F). Without the presence of the ammonium fluoride buffer the etch rate of the fiber core would exceed the etch rate of the fiber cladding resulting in a negative tip structure when etching takes place in the bulk of the etch solution. The cleaved fiber tip may be formed in the bulk of the etch solution or, as described above, at the meniscus region where the fiber enters the etch solution. Tip height and cone angle were found to depend strongly on etchant composition and temperature for cleaved fiber tips etched in the bulk of the etch solution. In contrast the authors found that tip formation in the meniscus region was nearly independent of etchant composition and temperature. Puygranier and Dawson^{26,27} explained the tip formation

process with the use of a simple model in which only the fiber core diameter along with the etch rates of the core and cladding were considered to be pertinent parameters.

It is worth noting that research has also been carried out utilizing a combination of pulling and etching to produce hybrid NSOM probes. Essaidi et al.,²⁸ as well as Courjon et al.,¹⁰ describe a two-step fabrication process that resulted in improved performance fiber optic probes for NSOM applications. A parabolic taper ending with a thin filament was initially produced with the use of a CO₂ laser. A subsequent rapid etch with buffered HF was used to remove the thin taper and increase the final cone angle to as large as 80 degrees. With this technique the authors state that nanoprobes were developed with apex sizes as small as 10 nanometers, and improved transmission coefficients.

3.2.4.3 Micro-Machined NSOM Tips

Micro-machined NSOM tips are often referred to as the next generation of NSOM tip, and currently used by some NSOM manufacturers as an alternative to fiber tips. A combination of micro-machining and photolithography leads to the fabrication of silicon and silicon nitride cantilevers, similar to AFM cantilever with an aperture through the tip. Micro-machined tips have the advantage of being processed in a batch process, leading to more consistent and robust tips. The micro-machined tips also provide an easy way to combine the optical information from NSOM with topographical and other contrast mechanisms available with AFM, as the tip geometry is nearly identical to AFM cantilevers. The aperture is often formed by coating the silicon cantilever with an opaque aluminum film, then creating a nanometer sized opening through the tip apex by milling with a focused ion beam (FIB)^{29,30}. Light is then coupled into the tip by focusing a laser beam into the probe cavity from the top, resulting in the sub 100 nanometer spot at the tip apex. Although micro-machining requires very large capital investment compared to the other techniques for fabricating NSOM probes, it has the advantage of excellent reproducibility and parallel processing allowing for hundreds of tips to be produced from a single substrate. FIB milling of the end of a completely metallized optical fiber tip, in a direction normal to the tip axis, has been reported to significantly reduce topographical artifacts due to multiple protrusions at the end of the probe tip.³¹

3.2.4.4 Apertureless NSOM Tips

Aperatureless NSOM probes have shown promise for improving spatial resolution of NSOM techniques requiring higher intensity, while overcoming some of the limitations imposed by fiber optic tips. Low light throughput and finite thickness of the metal coating limit the resolving power of optical fiber NSOM probes due to low light transmission. Novotny³² introduced the scheme of apertureless NSOM in 1998, and has been a pioneer in the development of the technique since. The technique makes use of a strongly enhanced electric field that results from a sharply pointed metal tip that is illuminated with laser radiation. The tip is held nanometers above the sample surface and highly localized interactions between the enhanced field and the tip are achieved. Resolution as good as 20 nm has been demonstrated using the apertureless NSOM technique, and is limited only by the radius of curvature of the metal probe tip.^{7,33-36} In addition to enhanced resolution, apertureless NSOM has the advantage of being able to work over a large wavelength range, from visible to infrared illumination with only slight modifications.¹⁴

Near-Field Raman¹¹ and fluorescence³⁴ spectroscopy with spatial resolutions of 10 to 20nm was demonstrated with the use of apertureless NSOM. Combining NSOM with techniques such as fluorescence and Raman spectroscopy provides promising characterization tools for identifying the molecular composition of complex materials, while at the same time providing spatial resolution at the nanometer level. Raman scattering probes the unique vibrational spectrum of the sample and allows for determination of its chemical composition and molecular structure directly. Raman spectroscopy typically suffers from very low intensity, as only about one in 10^6 photons is Raman active. However with the technique of surface-enhanced Raman scattering induced by the nanometer sized metal tip, the problem of a low scattering cross-section can be overcome to provide Raman information at the single molecule level by providing enhancement factors of up to 10^{15} .³⁷

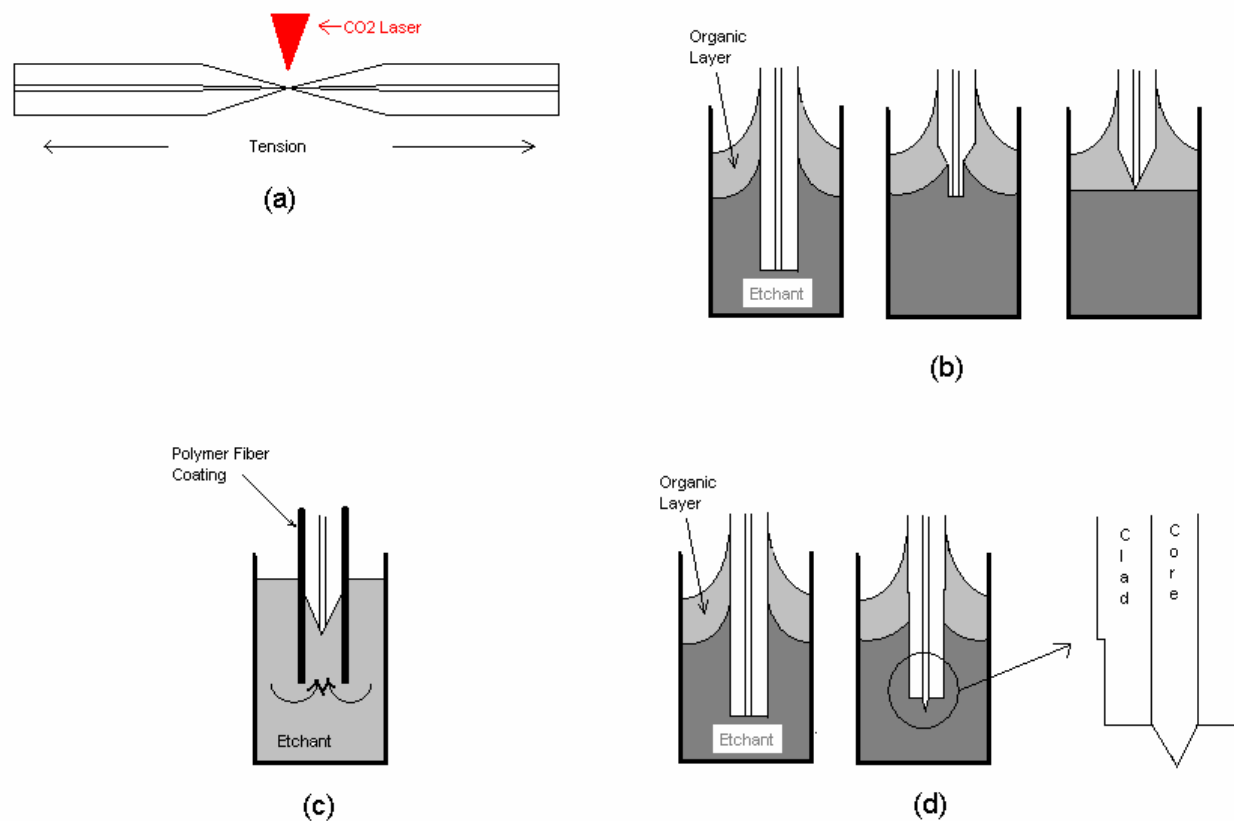


Figure 3.4. Diagram illustrating the techniques used to fabricate fiber optic NSOM probe tips; a) fiber pulling, b) meniscus etching, c) tube etching and d) bulk etching.

3.3 Experimental Procedures

3.3.1 Safety Precautions



The etch procedures described in this section require the use of hydrofluoric acid (HF) and ammonium fluoride (NH_4F), and special caution is necessary. Prevention of exposure to or injury from contact with these chemicals must be a primary goal of any laboratory procedure that uses them. Everyone who handles HF must be aware of its properties, dangers, and safety precautions. The health and contact rating for HF is “extreme (4)”, while that for NH_4F is “severe (3).” Proper training in HF safety, including the personal protective equipment necessary for its use, appropriate treatment for accidental exposure and knowledge of the Material Safety Data Sheet (MSDS) is required prior to use. Necessary lab protective equipment for the use of both chemicals includes goggles, face shield, lab coat, along with the proper gloves and protective apron. Due to the extreme nature of HF it is necessary to double glove before handling. Due to the dangers involved with inhalation of HF fumes all work must be carried out inside a fume hood, with special attention to cleanliness and with the utmost respect for the chemicals used. All HF solutions must be stored in polypropylene bottles due to the corrosive nature of HF when in contact with glass.

Exposure to hydrofluoric acid produces harmful health effects that may not be immediately apparent. The fluoride ion readily penetrates the skin causing destruction of deep tissue layers and bone. Symptoms are usually not immediate and can be delayed eight hours or longer. Even moderate exposures to concentrated HF may progress to fatality if left untreated.

3.3.2 Preparation of Etch Solutions

During the course of this work, several etch solutions were used to produce structures at the end of cleaved optical fibers. Buffered HF etch solutions used in this study were similar to those used in work previously reported by Puygranier and Dawson.^{26,27} The buffered etch solutions consisted of water, 50 volume percent HF acid and 40 weight percent NH₄F in a volume ratio of 1:1:X, with X varying from 1 to 6. Starting chemicals consisted of Nanopure® filtered water, 50% Fisher Scientific ACS certified HF acid and Fisher Scientific ACS certified crystalline ammonium fluoride. The 40 weight percent solution of NH₄F was prepared by dissolving 100 grams of crystalline ammonium fluoride (specific gravity = 1.01 g/cm³) into 150 ml of filtered water.

The pH of each etch solution was determined with the use of an Orion Research digital pH meter cell. A summary of the recipe for the etch solutions prepared, along with the final volume percent of HF and NH₄F, and the measured pH value is listed in Table 3.1. The total volume of etch solutions with ratios between 1:1:1.5 and 1:1:1.9 was slightly larger as more accurate measurement of each etch component was necessary.

Table 3.1 - Chemistry of Fiber Etch Solutions

Etch Solution ID	ml Water	ml 50% HF	ml 40% NH ₄ F	Final Concentration		
				% HF	% NH ₄ F	Measured pH
1. Buffered 1:1:1.0	20	20	20	16.7	13.4	3.35
2. Buffered 1:1:1.5	28.6	28.6	42.8	14.3	17.1	
3. Buffered 1:1:1.6	27.8	27.8	44.4	13.9	17.8	
4. Buffered 1:1:1.7	27.0	27.0	46.0	13.5	18.4	
5. Buffered 1:1:1.8	26.3	26.3	47.4	13.2	19.0	
6. Buffered 1:1:1.9	25.6	25.6	48.7	12.8	19.5	
7. Buffered 1:1:2.0	15	15	30	12.5	20.0	4.70
8. Buffered 1:1:3.0	12	12	36	10.0	24.0	5.29
9. Buffered 1:1:4.0	10	10	40	8.3	26.7	5.62
10. Buffered 1:1:5.0	8.6	8.6	42.8	7.2	28.5	5.75
11. Buffered 1:1:6.0	7.5	7.5	45	6.3	30.0	5.88

3.3.3 Fiber Etching Procedures

Two step index germanium doped silica single mode optical fibers with vastly different core diameters and dopant profiles were studied. Corning SMF-28 with a GeO₂ concentration in the core region of approximately 8 weight percent was compared to a high index, small diameter core fiber with a GeO₂ concentration of approximately 20 weight percent. The Corning high index, small diameter fiber will be referred to as HI fiber for the remainder of this paper. Two methods of fiber preparation were used depending on whether tube etching or bulk etching was carried out. For bulk etching the polymer coating of the fibers was mechanically stripped using fiber stripping tools. Lengths of the stripped optical fibers were cleaned with ethanol and cleaved (both ends) into 3 inch samples utilizing a standard York FK11 fiber cleaver. The cleaved fibers have ends that are smooth and nearly perpendicular to the fiber length. For tube etching the fiber coating was also mechanically removed, however cleaving was carried out within 1 mm of the un-striped fiber region.

One end of the cleaved fibers was fastened to a holder utilizing double stick tape, allowing the other end to be lowered vertically into the desired etch solution. Caution was taken to assure the fibers were suspended vertically in the etch solution, unless otherwise noted, as gravity was shown to play a role in the etch process. The etch solutions were covered with a thin layer of iso-octane. The organic liquid played several roles in the etching process, including:

- forms a thin protective layer to avoid damage to the fiber above the etch solution
- protects the environment from toxic HF vapors
- limits the evaporation of the etch solution helping to reduce variations in the etch concentration over the duration of the etch process.

All etches were carried out inside a fume hood, and a large beaker was used to cover the etching system to avoid disturbance to the etching system due to air flow currents. Three

fibers of each type were etched in the static solutions at room temperature for times ranging from 1 minute to hours. Figure 3.5 is a schematic of the set-up used for the etching process.

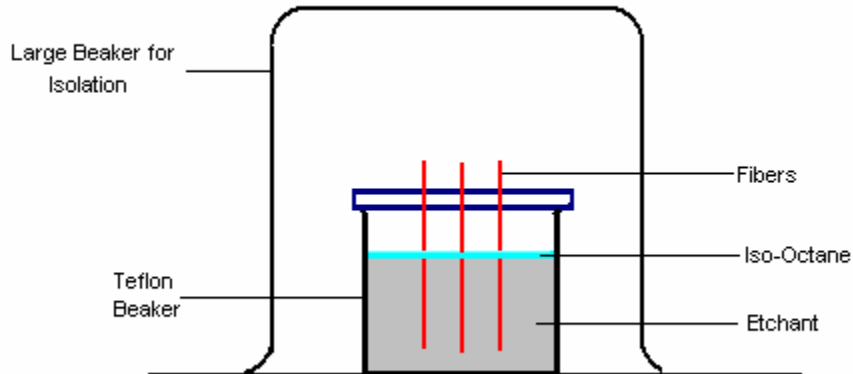


Figure 3.5. Schematic of etch set-up.

The majority of the fiber samples initially etched were difficult to characterize due to deposits that formed on the fiber end faces during to the etch process. The following post-etch rinsing procedure was developed and resulted in fiber end faces that were clear of any deposits or contamination that would interfere with the quality of the microscopy images:

- quick rinse in ethanol to remove any residual organic material from the fiber coating or iso-octane layer
- 1 minute static rinse in saturated boric acid to complex and dissolve any crystalline fluoride deposits that formed on the fiber end
- rinse in DI water
- rinse in ethanol
- dried with clean compressed air

3.3.4 Characterization of Etched Fiber End Faces

3.3.4.1 Optical Microscopy/Scanning Electron Microscopy

Optical microscopy images were collected with the use of a Nikon Optiphot-2-Pol equipped with a Sony CCD camera and video printer. Scanning electron microscopy (SEM) images were collected on an Amray 1845FE field emission instrument, with the use of the secondary detector.

3.3.4.2 Atomic Force Microscopy

The high spatial resolution of atomic force microscopy (AFM) makes it an ideal tool to evaluate the fiber end structure after short etch times, and help predict the final tip geometry. AFM results provide quantitative information about the evolving NSOM tip structure including tip height, cone angle, plateau width and the differential etch rate between the core and the cladding. The difference in the etch rate between the core and cladding will be related to the cone angle of the final tip, an important variable in the NSOM tip process and one that can not be controlled by the fiber pulling process.

A Digital Instruments Dimension 3100 SPM with a Nanoscope IIIA controller was operated in TappingMode® to produce three-dimensional profiles of the etched fiber ends. Pyramidal shaped etched silicon probes (TESP) with a half cone angle of approximately 18 degrees were used for all AFM measurements. The cleaved and etched fiber ends were placed in a special holder designed to hold the fiber vertically under the AFM tip.

3.4 Results and Discussion

3.4.1 Initial study of SMF28 and HI Optical Fibers

Development of an etch technique that is reproducible and allows for variation of the resulting cone angle is the focus of this work. Puygranier and Dawson²⁶ state that the

tip height and cone angle of the etched fiber depends strongly on the fiber geometry and etch concentrations. They showed that the important physical parameters of the fiber were the core diameter and the differential etch rate between the core and the cladding. The method used by Puygranier and Dawson to determine the etch rates of the core and cladding was tedious and improvement to the technique is the driving force behind the current study.

Two single mode optical fibers, Corning SMF-28 and a higher index HI fiber were initially compared to evaluate the effect of core diameter and GeO_2 concentrations on the fiber etching process. The GeO_2 dopant is introduced to the core region of the fiber to increase the refractive index and provide total internal reflection. An optical fiber is a conduit for light made of two concentric glass cylinders. A central cylinder, called the core, has a refractive index denoted n_1 , and the outer cylinder, called the cladding, has a slightly lower index denoted n_2 ($n_1 > n_2$). Light waves traveling in the core of the fiber are totally reflected at the core/clad interface if the angle of incidence is greater than some critical angle, θ_c that is related to the refractive index of the core and cladding through the following relation:

$$\theta_c = \sin^{-1} (n_2 / n_1) \quad (2)$$

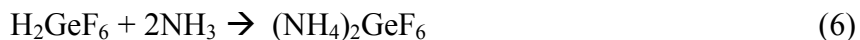
Figure 3.6 is a schematic of light being guided through the core of a single mode optical fiber by total internal reflection. Figure 3.7 displays SEM and AFM images of the cross section of an optical waveguide fiber showing the core and cladding regions. The AFM image in Figure 3.7 is at a much higher magnification than the SEM image and only a small portion of the cladding region is included.

The chemical reactions of SiO_2 and GeO_2 with HF acid are:^{38,39}



The difference in the solubility of the fluorosilicic (H_2SiF_6) and hexafluorgermanic (H_2GeF_6) acids leads to a differential etch rate between the fiber core and fiber clad. The solubility of the GeO_2 containing core exceeds that of the pure SiO_2 cladding resulting in a fiber end with a depressed core region (concave tip). Figure 3.8 displays three dimensional AFM views along with section views of the SMF28 and HI germanium silicate fibers etched in un-buffered HF resulting in a depressed core region. Concave fiber tip structures, like that shown in Figure 3.8 are not useful for NSOM applications. However by etching optical fiber ends in a dilute, un-buffered HF solution a plethora of qualitative and quantitative information can be gained about the optical fiber structures.

Addition of a buffer, NH_4F , to the HF solution results in additional steps in the etching process involving NH_3 ionized from the solution:



The solubility of $(NH_4)_2SiF_6$ exceeds that of $(NH_4)_2GeF_6$ resulting in the etch rate of the SiO_2 cladding exceeding that of the GeO_2 doped core forming a convex tip as the core rises out of the cladding during the etch process. Figure 3.9 displays three dimensional AFM views along with section views for SMF28 and HI optical fibers etched for 10 minutes in the 1:1:2 etch solution (volume ratio of water:50 percent HF acid:40 weight percent NH_4F). The tip cone angle that results from etching the optical fibers in a buffered HF solution will be a function of the etch composition and etch temperature as well as the fiber composition (GeO_2 loading), diameter and index profile. It should be noted that the vertical scales in Figures 3.8 and 3.9 are not equal, and that the vertical scale is expanded considerably in comparison to the horizontal scale in most AFM images.

The section lines in Figure 3.9 are a 2-d representation of the line drawn through the center of the core region. Three sets of cursors strategically placed on the section line provide information on the core geometry that has evolved from the etching process.

- The red cursors are placed at the outside edges of the top of the core and the horizontal distance between the two cursors determines the rate that the tip is forming (differential etch rate).
- The green cursors are placed on the cladding surface and the core surface. The vertical distance between the green cursors provides the height difference between the core and the cladding. This height difference is directly proportional to the differential etch rate between the core and the cladding.
- The black cursors are placed at the top and the bottom of the core sidewall, and the angle between the two cursors is the complimentary angle to the half cone angle that would result from projecting these sidewalls into a full cone.

Once the cladding is etched down and the core is exposed on the sides (previously the core/clad interface) the core will not only be etched from the top down, but also be radially inward along the sidewalls resulting in a cone. The more rapidly the cladding is etched away from the core and the lower the solubility of the core, the sharper the cone angle that results. Therefore the differential etch rate is inversely proportional to the final cone angle. The evolution of the tip height is the sole result of the difference in the etch rate of the core (d_{co}) and cladding (d_{cl}). Noting that the etch rate of the cladding exceeds the etch rate of the core, so that the evolving tip structure will have a time dependent height given by:

$$H_{tip} = (d_{cl} - d_{co}) t \quad (7)$$

where H_{tip} is the tip height that results after a given etch time, t .

The initial etch study evaluated both fiber types in the lightly buffered 1:1:2 and the heavily buffered 1:1:6 etch solutions for times between one and 40 minutes. Table 3.2 is a summary of the AFM measurements that resulted from these initial etches. Figure 3.10 is a plot of the AFM measured core height as a function of etch time between one and 20 minutes for the two fibers and two etch solutions. From Equation 7, the slope of the lines in Figure 3.10 (H_{tip}/t), is the differential etch rate between the core and the cladding, ($d_{cl} - d_{co}$). The higher the slope of the lines in Figure 3.10, the higher the solubility of the cladding with respect to the core. As discussed earlier the higher the

differential etch rate between the cladding and the core, the smaller the cone angle that should result from the complete etch process.

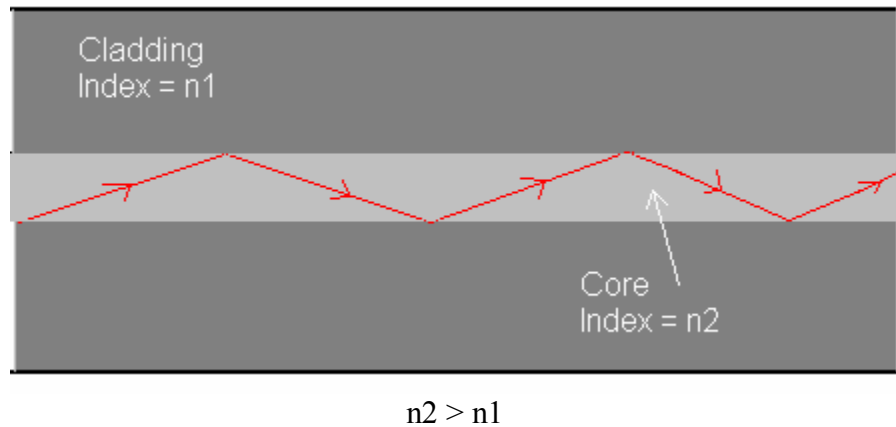


Figure 3.6. Schematic of light rays guided by total internal reflection in a step index single mode optical fiber. The ratio of the diameter of the core to the cladding has been exaggerated for schematic purposes.

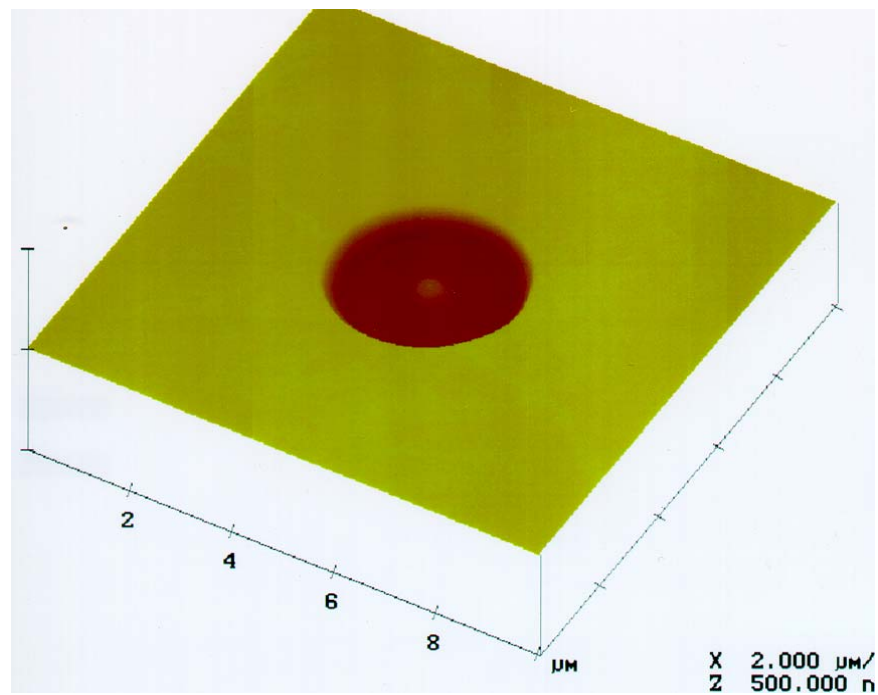
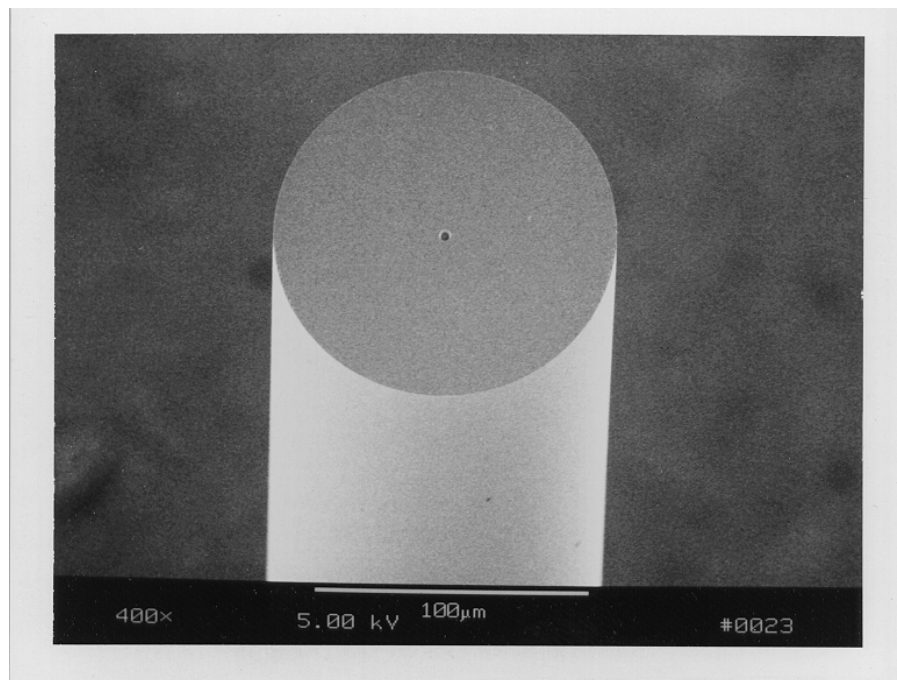


Figure 3.7. SEM and AFM image of an etched optical fiber illustrating the relationship between the core and cladding for a single mode fiber. The AFM image shows only a portion of the cladding region.

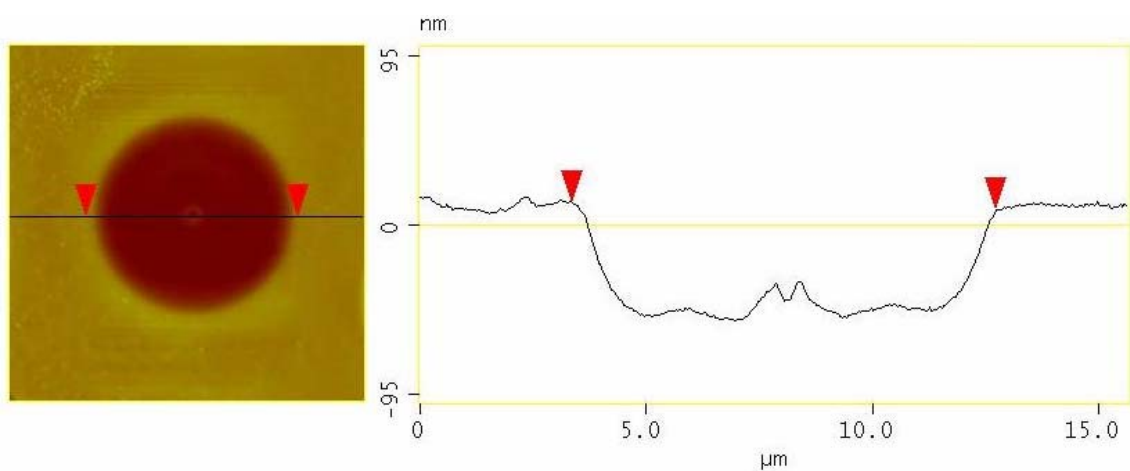
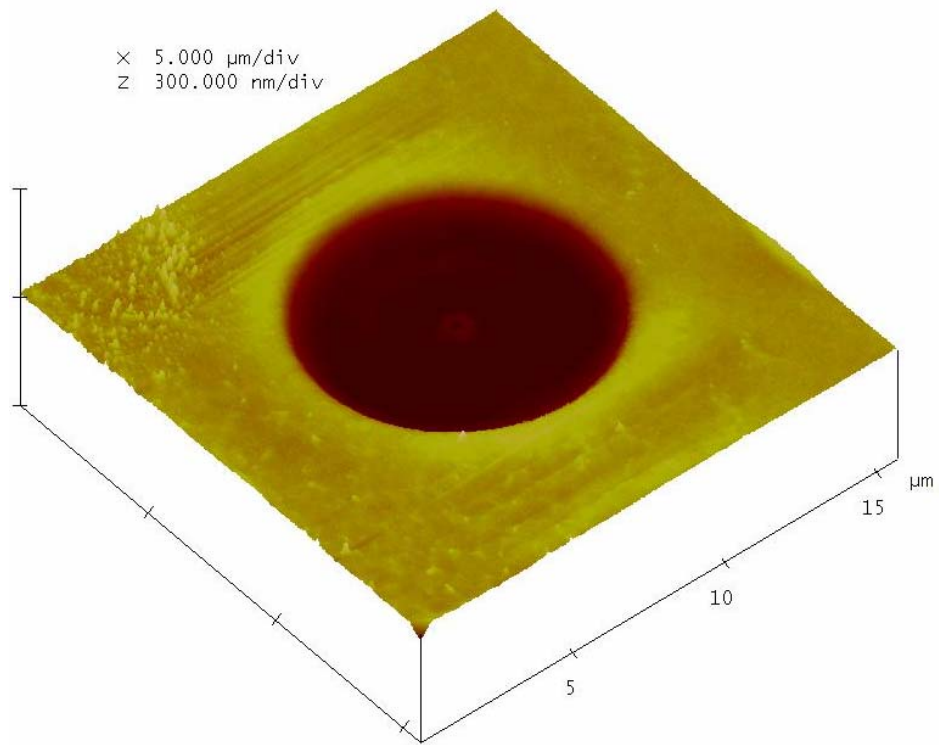


Figure 3.8. Three dimensional AFM views along with section views of the SMF28 and HI germanium silicate fibers etched in un-buffered HF.

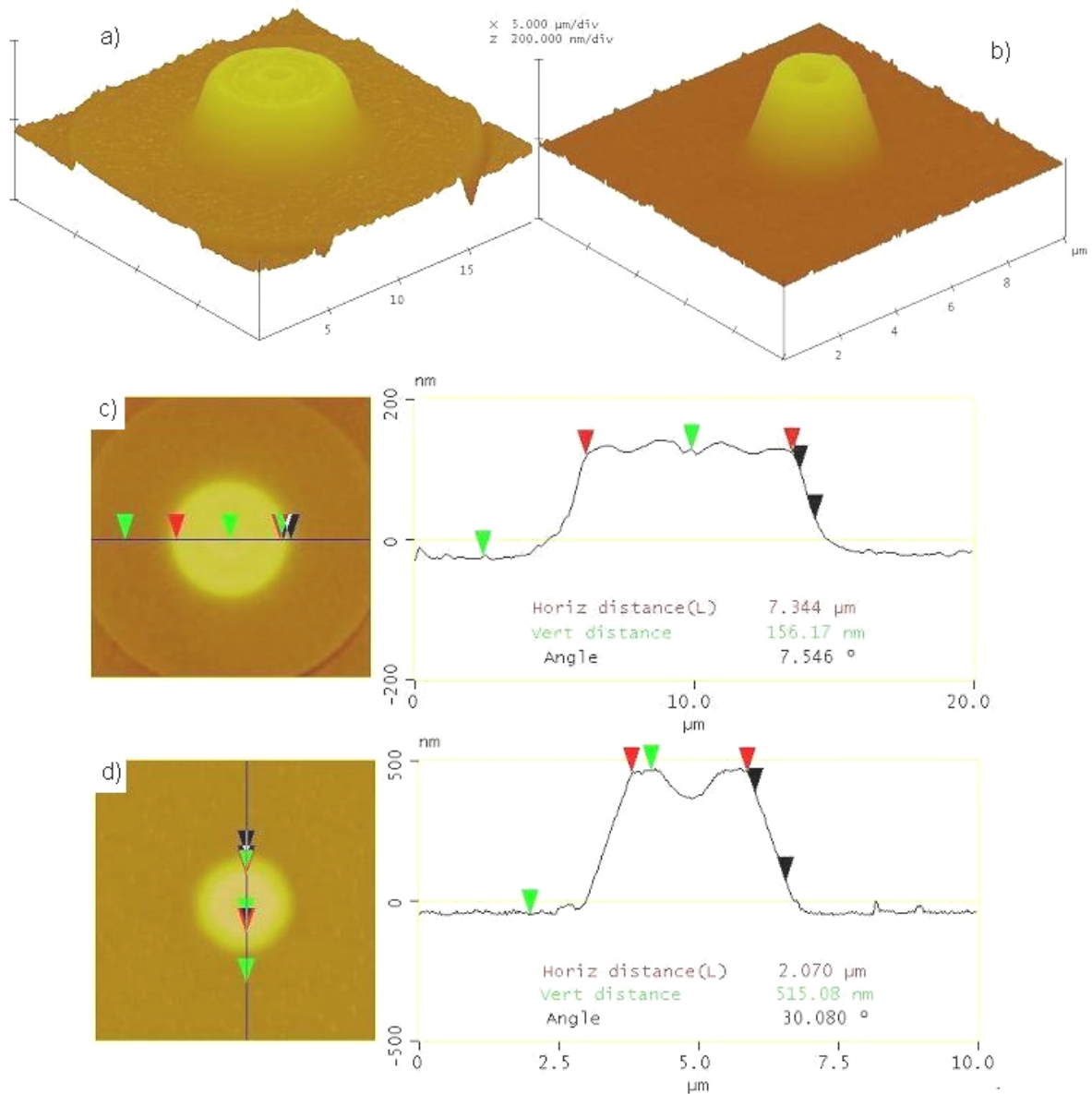


Figure 3.9. Results of AFM analysis for fibers etched in 1:1:2 etch solution for 10 minutes. a) 3D of SMF28, b) 3D view of HI, c) 2D section view of SMF28 and d) 2D section view of HI.

Table 3.2 Summary of AFM Measurements

SMF28 Fiber in 1:1:2 Etch Solution

Etch Time (minutes)	Measured Sidewall Angle (deg)	Projected Tip Cone Angle (deg)	Core Height (nm)	Core Top Width (um)
1	0.6	179	16.8	8.02
2	1.6	177	26.5	7.89
5	4.5	171	76.7	7.42
10	6.4	167	155	7.34
15	10.5	159	234	6.99
20	13.1	154	284	6.88
30	14.3	152	565	5.39
40	14	152	716	4.3

SMF28 Fiber in 1:1:6 Etch Solution

Etch Time (minutes)	Measured Sidewall Angle (deg)	Projected Tip Cone Angle (deg)	Core Height (nm)	Core Top Width (um)
1	0.8	178	11.8	8
2	2	176	42.4	7.5
5	6.6	167	116	7.5
10	14	152	249	7.3
15	20	140	412	7.3
20	25	130	540	7.2
30	27	126	757	6.6
40	29	122	1018	6

HI Fiber in 1:1:2 Etch Solution

Etch Time (minutes)	Measured Sidewall Angle (deg)	Projected Tip Cone Angle (deg)	Core Height (nm)	Core Top Width (um)
1	9.5	161	50.4	3.3
2	24	132	101	3.1
5	30	120	245	2.7
10	29	122	366	2.2
15	30	120	534	1.6
20	32	116	671	1.1
30	32	116	881	
40	32	116	909	

HI Fiber in 1:1:6 Etch Solution

Etch Time (minutes)	Measured Sidewall Angle (deg)	Projected Tip Cone Angle (deg)	Core Height (nm)	Core Top Width (um)
2	14	152	124	3.1
7.5	60	60	538	3.1
10	61	58	759	3.3

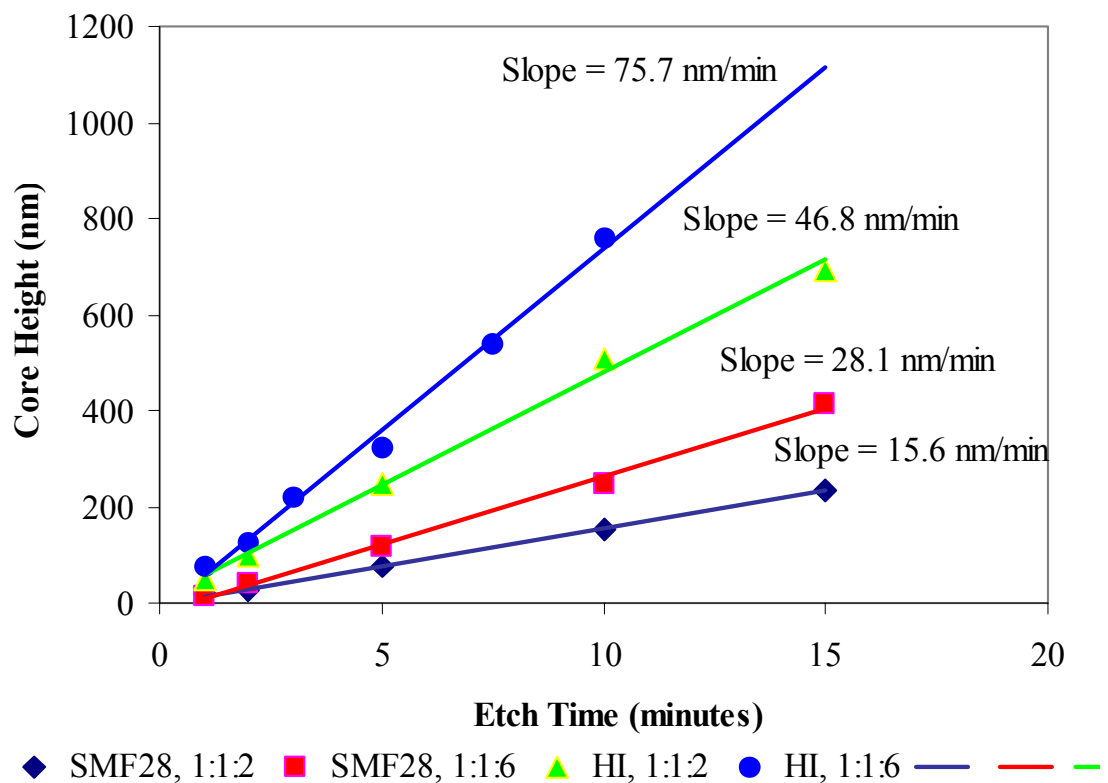


Figure 3.10 Variation of core height with etch time.

Figure 3.11 is a plot of the cone angle, estimated from the AFM measurements, as a function of the etch time for each condition. Each curve in figure 3.11 appears to have two slopes, one for short etch times and one for longer etch times and the final cone angle is achieved by 40 minute etch times for all conditions.. The transition between the two lines is a function of composition and etch solution. It is believed the two slopes are due to the fact that the interface between the core and the cladding is not perfectly sharp, even in the step index fibers. This interface is engineered to be a clean transition during the lay-down of the soot in the vapor deposition process. However the abrupt change in GeO_2 concentration at the core/clad interface provides a large driving force for diffusion of the GeO_2 from the core into the pure SiO_2 cladding. This composition gradient along with the thermal energy that results from the elevated temperatures during consolidation, overcladding and fiber draw makes the possibility of GeO_2 diffusion quite likely. The diffusion results in a short distance where a GeO_2 gradient exists at the core/clad interface. Figure 3.12 is an AFM section view of a SMF28 fiber etched for 40 minutes in a 1:1:3 etch solution showing that the top of the core region is not of uniform height due to chemical variations through the core region. The edges of the core show a gradual increase in height from outside in due to diffusion of GeO_2 at the core/clad interface. Additionally the center of the core is enriched in SiO_2 as a result of the fiber soot lay-down process which initially deposits a high silica region on the bait rod before the heavy GeO_2 doping begins. The lateral etching of the core is initially controlled by the lower GeO_2 levels, and until the region of the gradient is removed, the cone angle is continually changing.

Figure 3.13 displays side on views from the AFM data for SMF28 fiber etched in 1:1:2 and 1:1:6 etch solution for 40 minutes and HI fiber etched in 1:1:2 for 40 minutes and 1:1:6 for 7.5 minutes. The partial tip structures have been projected to full cones to show an estimate of the final tip structure. All images in figure 3.13 have the same vertical scale of $1\mu/\text{division}$, however due to the smaller core the horizontal scale is expanded for the HI fibers. The cone is nearly completely formed for the HI fiber etched in the 1:1:2 solution for 40 minutes, while the other conditions are at various stages of completion. Equation 8 provides the relationship between the angle measured by AFM (α) and the final cone angle (θ). The angle measured by AFM is the compliment to the

half cone angle that results from extending to a full cone as demonstrated in Figure 3.14 by manually extending the sidewalls in Figure 3.13c to a full cone and calculating the angles based on distances in the image.

$$\theta = 2(90 - \alpha) \quad (8)$$

The result of the calculation in Figure 3.14 provides confirmation that the angle measured by AFM is the acute angle between the tip sidewall and the horizontal.

Figure 3.15 is a plot of the resulting cone angle of the etched fiber tip as a function of the clad/core differential etch rate ($d_{cl} - d_{co}$). The differential etch rates were determined from the slopes of the best fit linear lines from Figure 3.10. The general trend that smaller cone angles result from a larger differential etch rate is observed. Figure 3.15 also shows that the core diameter plays a role in the cone angles achieved, as is evident by the offset that results from the different fiber types. Larger cone angles are desired for NSOM applications due to the shorter distance the evanescent wave has to travel before exiting the fiber tip. For this reason a more detailed study of the SMF28 fiber, which has the ability to produce a wider range of larger cone angles, was carried out, and the results are summarized in the next section.

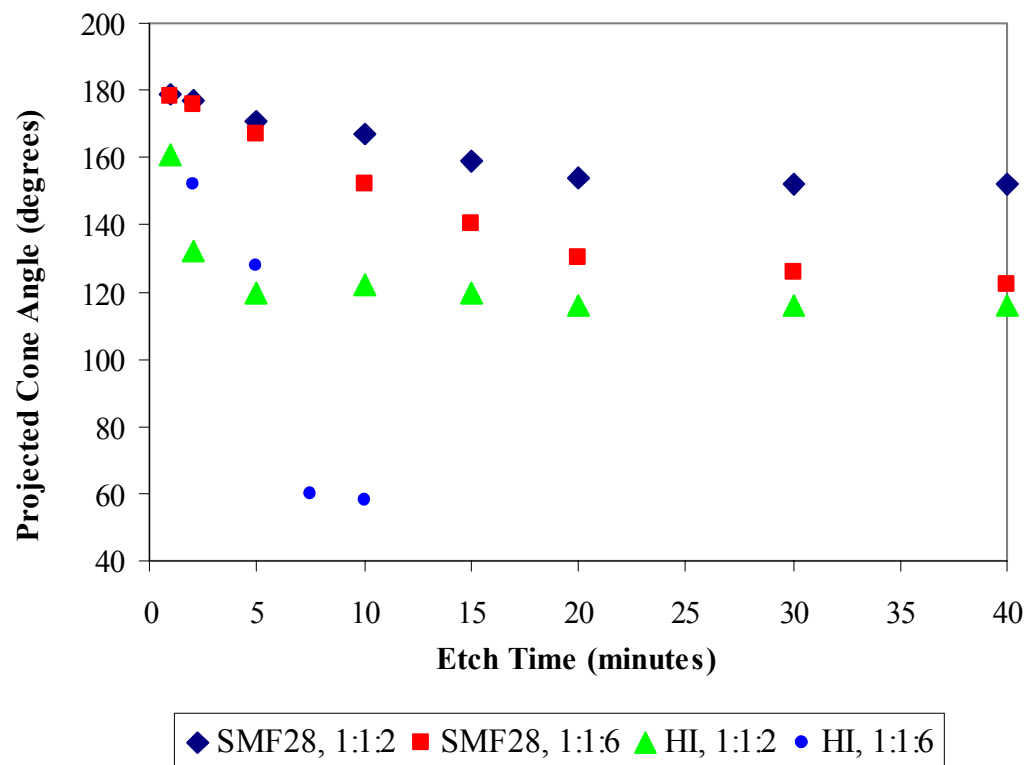


Figure 3.11. Evolution of cone angle as a function of etch time.

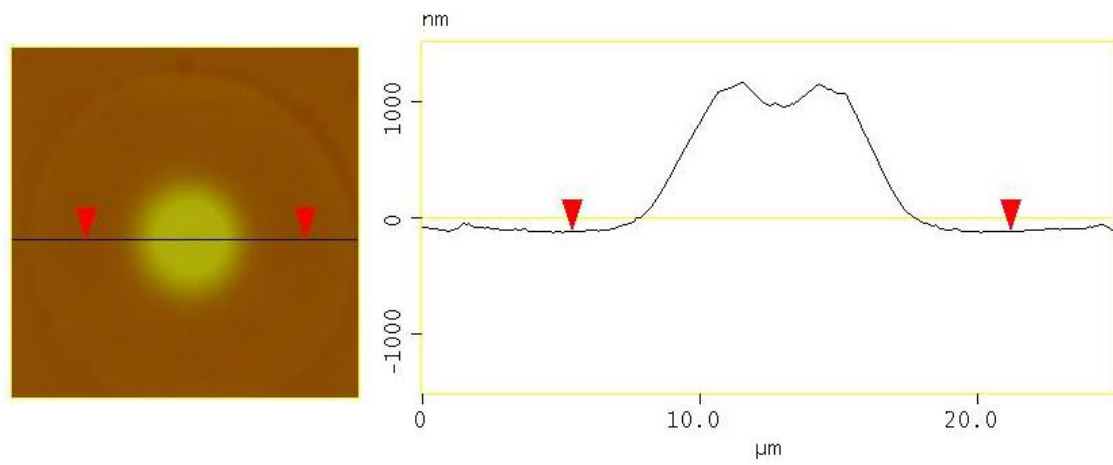


Figure 3.12. AFM section profile of SMF28 fiber etched for 40 minutes in a 1:1:3 etch solution. Variations in height across the core region are the result of compositional variations resulting from the fiber process.

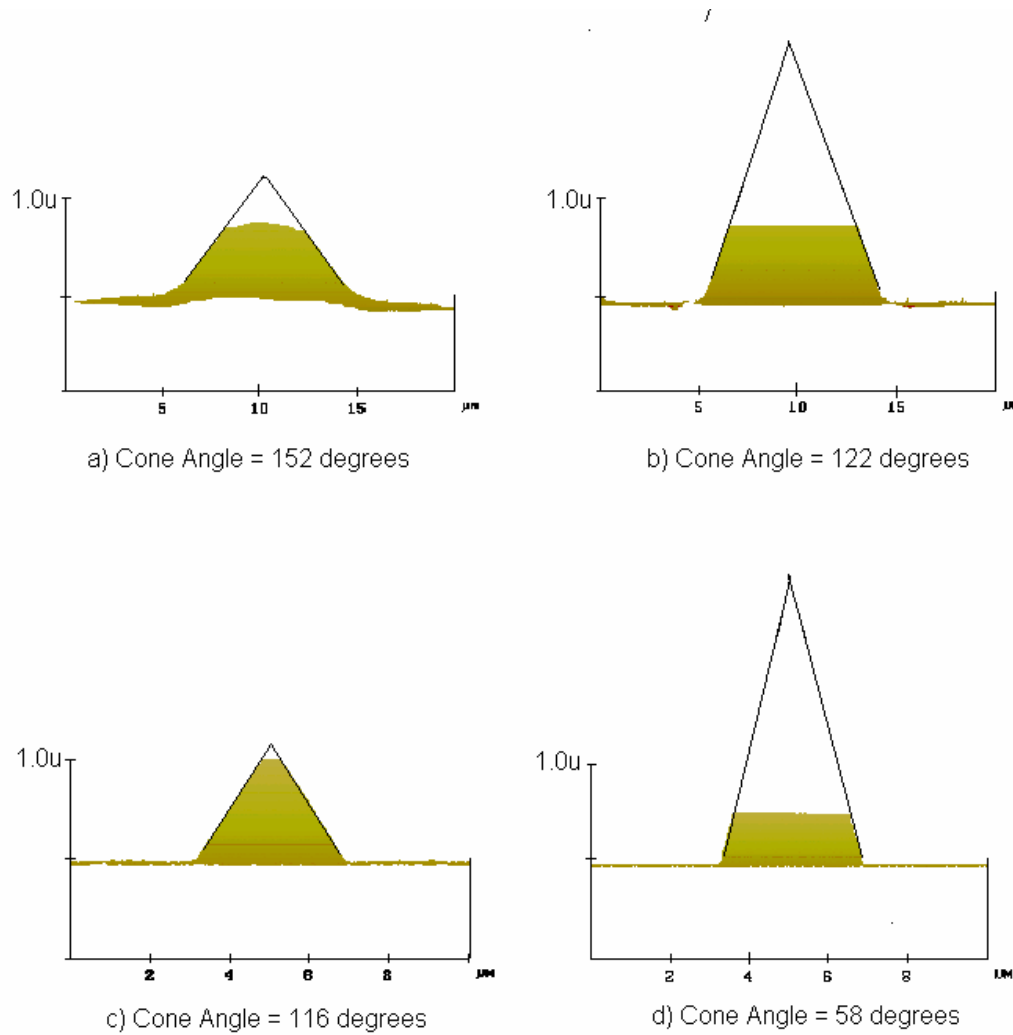
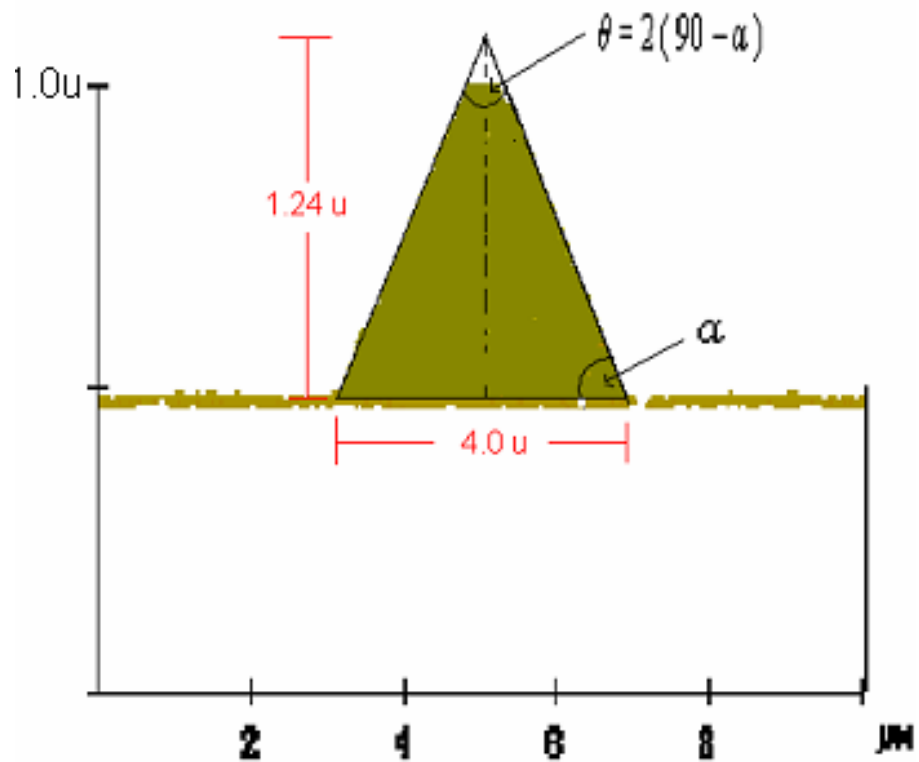


Figure 3.13. AFM side views with projected full cone for a) SMF28 after 40 minute etch in 1:1:2, b) SMF28 after 40 minute etch in 1:1:6, c) HI after 40 minute etch in 1:1:2 and d) HI after 7.5 minute etch in 1:1:6.



Calculation

$$\alpha = \tan^{-1} (1.24 / 2.0) = 31.8 \text{ degrees}$$

α measured from AFM = 32 degrees

$$\theta = 2 (90 - \alpha) = 2 (90 - 31.8) = 116 \text{ degrees}$$

θ measured from AFM = 116 degrees

Figure 3.14. Example of calculation of full cone angle from the AFM side view images.

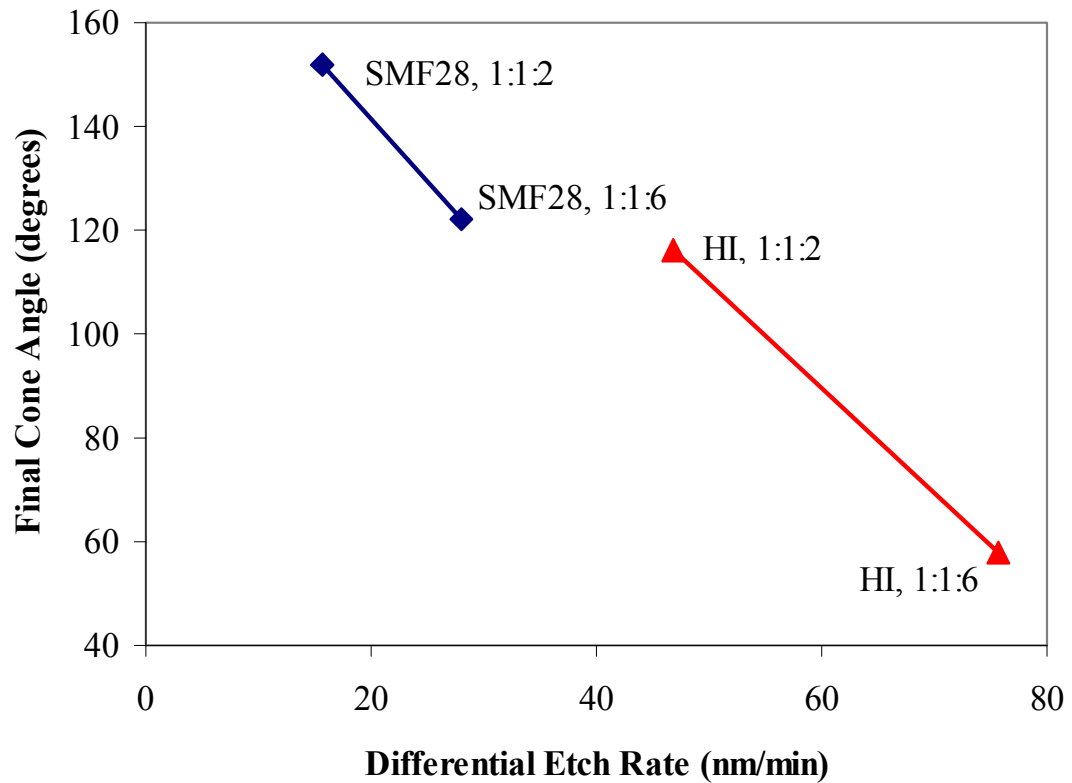


Figure 3.15. Relationship between clad/core differential etch rate and tip cone angle.

3.4.2 More Detailed Evaluation of the SMF28 Fiber Etching Process

Cleaved SMF28 fibers were etched for times between 10 minutes and 2 hours in etch solutions of compositions 1:1:X (1 part H₂O:1 part 50% HF:X parts NH₄F). The value of X in the etch solutions varied from 1.5 to 6.0. To determine the minimum buffer concentration required to form a positive tip structure (the core is elevated with respect to the cladding), cleaved sections of SMF28 fiber were etched for 10 minutes in solutions ranging in composition from 1:1:1.5 to 1:1:2.0. The tip height for each etch condition was determined by AFM analysis and the results are included in Figure 3.16. Negative results for tip height in Figure 3.16 indicate that the core etch rate exceeded the cladding etch rate resulting in a concave tip structure. The cross-over point of the best fit line in Figure 3.16 has an X value of 1.63. This is the concentration that would result in no tip structure, as the etch rate of the core is exactly that of the cladding. This information was used to determine a lowest practical value of X for this detailed study. The information was also used to develop curved tip structures for possible monolithic lenses at the end of optical fibers. Further work in the development of monolithic lenses is included in Appendix A.

The differential etch rate between the core and cladding is very small for etch solutions below 2.0. The small differential etch rates would result in very long etch times to form a complete tip structure, and are not practical due to the increased roughness that will result from the extended etch times. To provide an idea of the reproducibility of the etch process and the AFM analysis, three SMF28 fibers were etched and characterized for each condition. Initially, whole number values for X from 2 to 6 were evaluated for etch times of 20, 40, 60, 90 and 120 minutes. Single analysis for X values of 1.8 and 2.5 were completed to provide additional data for rapidly changing slopes in several plots. Table 3.3 is a summary of the AFM results for this series.

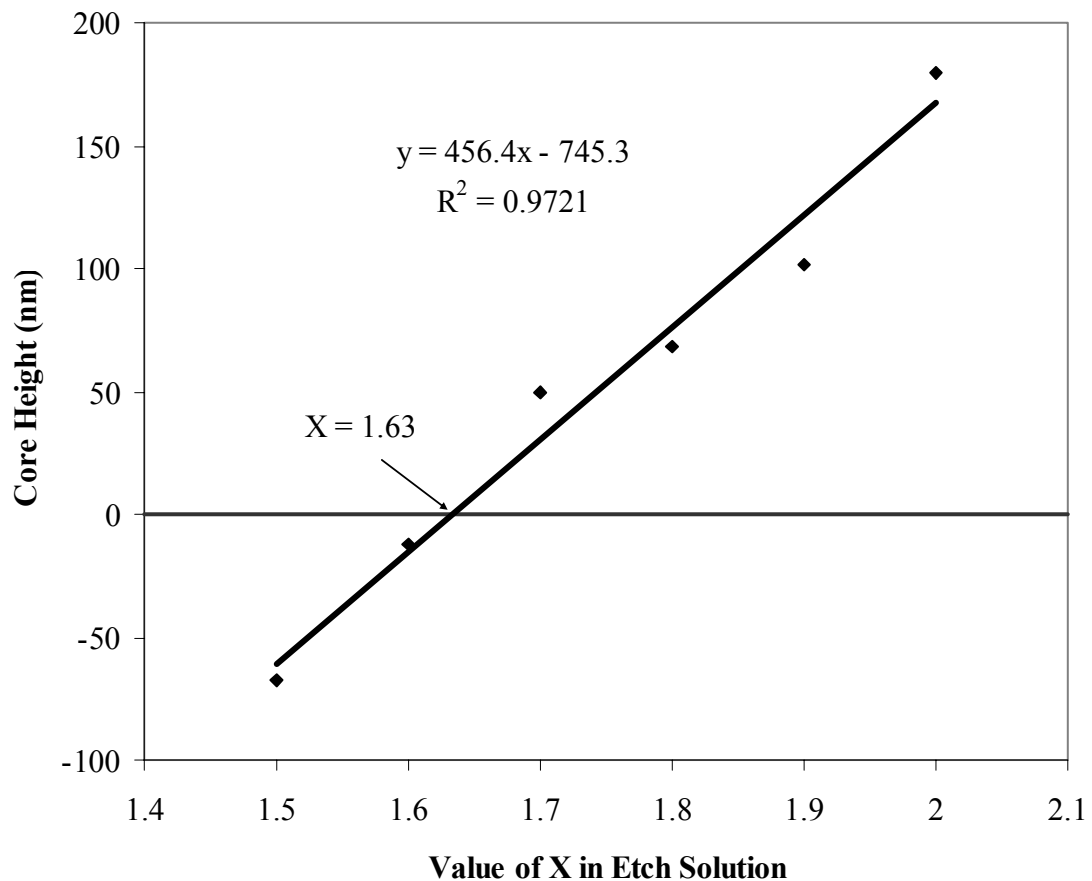


Figure 3.16. Plot of the core height as a function of the value of X in the etch solution for etch times of 10 minutes.

Table 3.3 Summary of AFM Results for SMF28 Fiber Etch Study

X	Etch Time (min)	α (degrees)	θ (degrees)	Plateau Width (nm)	Tip Height (nm)
1.8	20	10.6	158.8	7300	219
1.8	40	11.3	157.4	5300	636
1.8	60	11.4	157.2	3900	690
1.8	90	10.9	158.2	1500	732
1.8	120	11.5	157.0	0	922
2.0	20	13.9	152.2	6.6	379
2.0	40	16.0	148.0	5.0	729
2.0	60	16.2	147.5	2.5	1053
2.0	90	15.9	148.1	0.0	1260
2.0	120	16.0	147.9	0.0	1335
2.5	20	20.2	139.6	6.5	584
2.5	40	22.3	135.4	3.8	1164
2.5	60	22.9	134.2	2.15	1490
2.5	90	23.9	132.2	0	1971
2.5	120	23.4	133.2	0	1960
3.0	20	22.4	135.1	6.5	661
3.0	40	25.7	128.7	4.7	1224
3.0	60	26.5	127.0	2.4	1607
3.0	90	26.3	127.3	0.0	2138
3.0	120	26.0	127.9	0.0	2200
4.0	20	25.5	129.1	6.9	649
4.0	40	29.4	121.2	5.4	1250
4.0	60	30.3	119.5	3.2	1694
4.0	90	30.3	119.5	1.1	2394
4.0	120	29.5	121.0	0.0	2545
5.0	20	27.5	125.1	7.2	584
5.0	40	32.6	114.9	5.8	1173
5.0	60	34.4	111.9	4.3	1699
5.0	90	33.0	114.4	2.0	2201
5.0	120	33.7	112.7	1.6	2498
6.0	20	28.4	123.2	7.3	529
6.0	40	33.6	112.7	6.1	1112
6.0	60	34.1	111.9	5.0	1440
6.0	90	33.3	113.3	2.7	2064
6.0	120	33.5	113.1	2.3	2303

Figure 3.17 displays three dimensional AFM views with a 90 degree tilt (viewing etched fibers perpendicular to the length of the fiber) showing the evolution of the SMF28 fiber tip structure etched in a 1:1:4 solution for times between 20 and 120 minutes. Figure 3.18 is an Excel plot of the two dimensional section lines drawn through the center of each tip structures shown in Figure 3.17. Figures 3.17 and 3.18 show that as the tip structure evolves there is very little change in the sidewall angle. This result provides an opportunity to estimate the final tip cone angle even after very short etch times, and without the time-consuming process of taking the etching process to completion.

Figure 3.19 is a plot of the cone angle, estimated from AFM analysis, as a function of etch time for SMF28 fiber. In addition to the data collected for this expanded study of SMF28 fiber, the preliminary data for short etch times in 1:1:2 and 1:1:6 solutions is included to show the overall trend. The cone angles of the evolving tip structures initially decreases, for a given etch concentration, up to etch times of about 40 minutes. The error bars in Figure 3.19, which are two times the standard deviation, show that within the 95% confidence range all etch solutions have reached their final cone angle by 40 minutes, and the 1:1:5 and 1:1:6 etch solutions result in nearly identical etch profiles.

Figure 3.20 is a plot of the final cone angle as a function of the ratio of NH₄F in the etch solution (the X value in the 1:1:X designation). The line fit to the data in Figure 3.20 shows an exponential relationship between the evolving cone angle and the concentration of NH₄F in the etch solution. The majority of the variation in final cone angle occurred between the 1:1:2 and 1:1:5 etch solutions, which allows for formation of tips with cone angles between 157 and 112 degrees. This large variation in cone angle allows for good control over the trade off between the longer, sharper tips that result when a smaller cone angle is present and higher transmission coefficients that are possible with larger cone angles due to the cutoff location for the propagation mode being closer to the aperture.



Figure 3.17. AFM profiles showing the evolution of the tip structure of an SMF28 fiber etched in a 1:1:4 solution. The height of the tip structures range from 500 nm for the 20 minute etch to 2500 nm for the 120 minute etch.

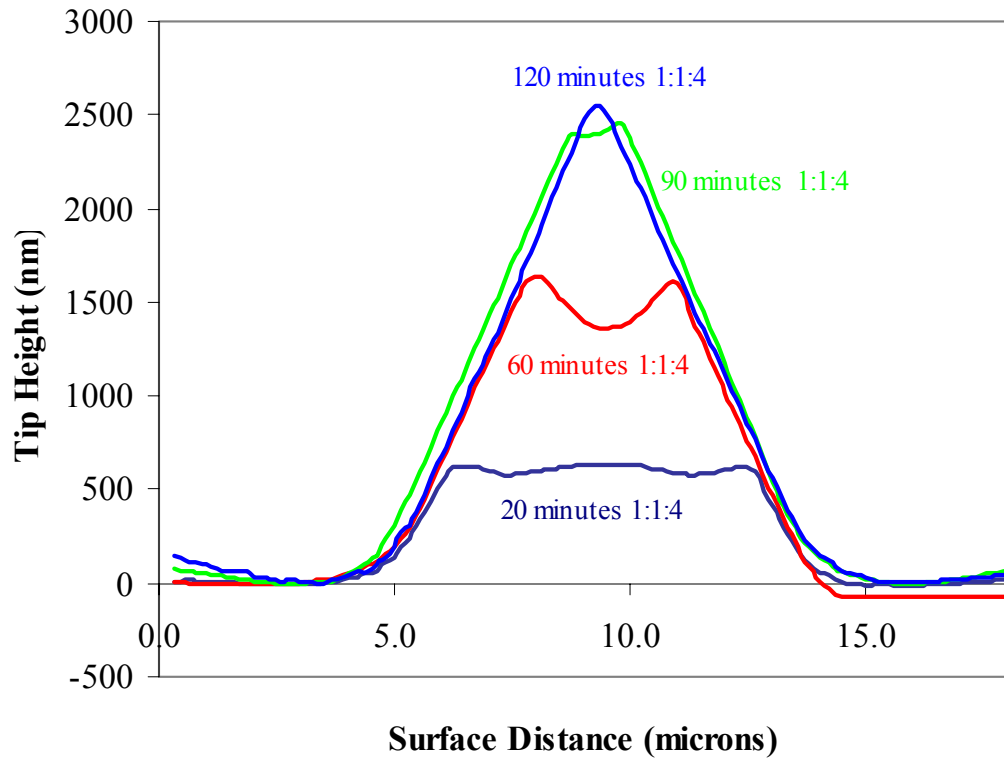


Figure 3.18. AFM profiles showing the evolution of the tip structure of an SMF28 fiber etched in a 1:1:2 solution.

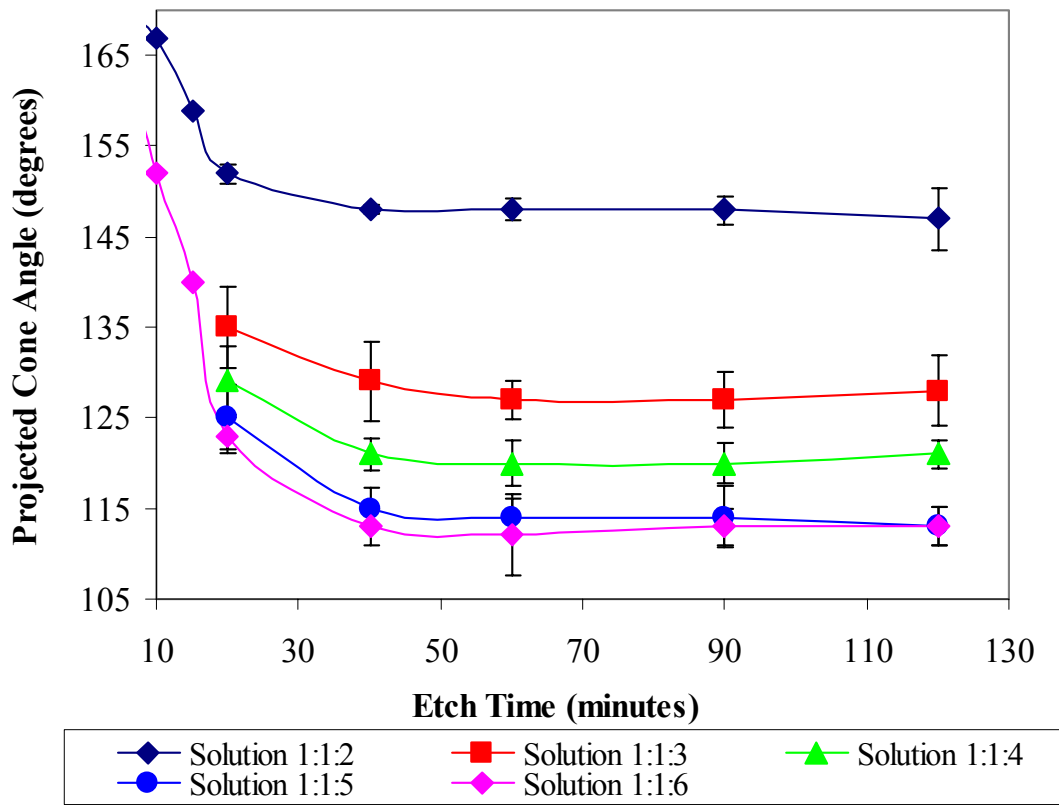


Figure 3.19. Plot of cone angle as a function of etch time for SMF28 fiber in various etch solutions. Error bars represent ± 2 standard deviations, or 95% confidence interval.

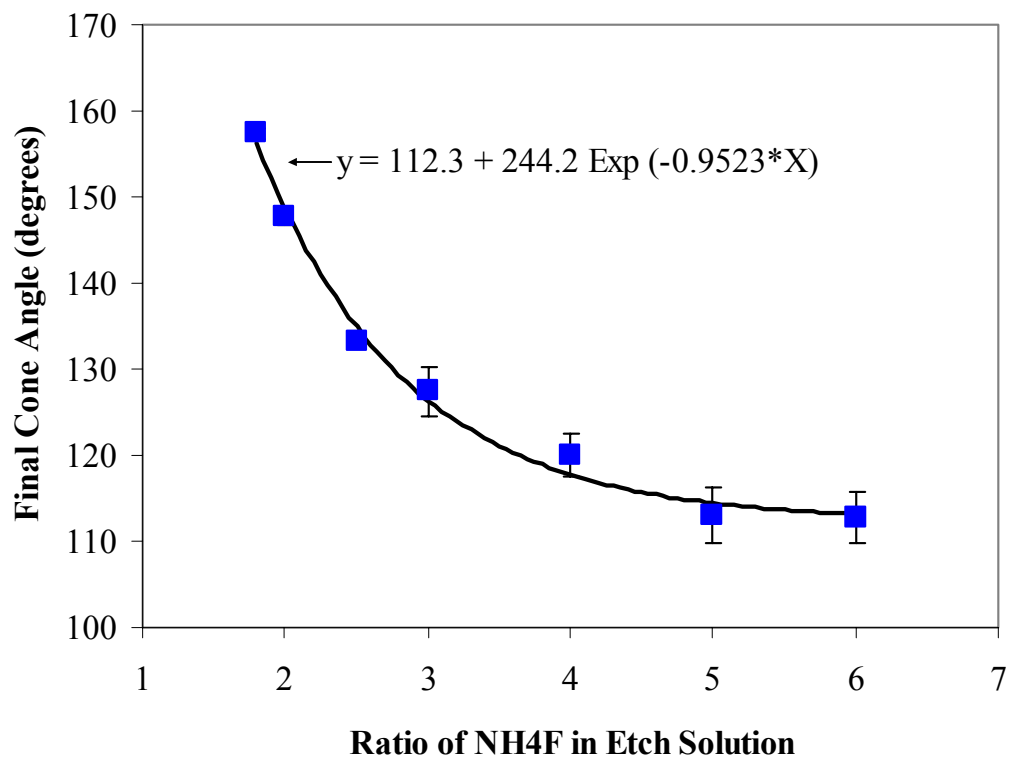


Figure 3.20. Final cone angle as a function of etch concentration.

Figure 3.21 is a graphical representation of the height of the evolving tip structure as a function of etch time as well as the value of X in the etch solution. Based on the differential etch rate between the core and the cladding, the tip height will continue to grow until a full cone is realized. Although the tip height continues to grow, Figure 3.19 showed that changes in cone angle only occurred up to 40 minute etch times. These results indicate that the differential etch rate of the core and cladding may be changing during the short etch times, but reach a steady state prior to the 40 minute etch time. The changes in the radial etch rate of the core, due to the variation in the chemical profile at the core/clad interface is assumed to be the driving force behind the initial changes in the differential etch rate. This chemical variation and its effect on the radial etch rate of the core was discussed in the preliminary section above. It should be noted that the tip structures plotted in Figure 3.21 are at various stages of completion when comparing tip heights for specific etch times. For example, the 1:1:5 and 1:1:6 etch solutions will result in the tallest tip structure when a full cone is realized, however at the 120 minute etch time the tip structure is not as close to completion as the 1:1:4 resulting in a shorter tip height.

The relationship between cone angle, core radial etch rate and the differential etch rate was predicted by Puygranier and Dawson²⁶ in a simple model derived from basic geometry. Figure 3.22 is a schematic of an evolving tip structure with the height and width distances described as functions of the various etch rates. Equation 7 stated the relationship between the evolving tip height, H_{tip} , and the differential etch rate, $(d_{cl} - d_{co})$. The distance the core is etched back once exposed will be a function of the core etch rate, d_{co} , and the etch time. From Figure 3.22 the development of a cone-tip structure with a cone angle, θ , is given by:

$$\tan\left(\frac{\theta}{2}\right) = \frac{(d_{co})t}{(d_{cl} - d_{co})t} = \frac{d_{co}}{d_{cl} - d_{co}}. \quad (9)$$

Rearranging Equation 9, and solving for θ , results in Equation 10 which provides a relationship between the cone angle and the ratio of clad and core etch rates.

$$\theta = 2 * \tan^{-1} \left(\frac{1}{\frac{d_{cl}}{d_{co}} - 1} \right) \quad (10)$$

Determining the cladding etch rate, d_{cl} , directly from the current AFM measurements is not possible, however the core etch rate and the differential etch rate can easily be determined directly from the AFM measurements. An indirect calculation of the cladding etch rate is possible by adding the core etch rate to the differential etch rate, however use of Equation 9 only requires the core radial etch rate and the differential etch rate.

The model described by Puygranier and Dawson²⁶ assumes a radial etch normal to the cone surface, and does not account for etching of the core region in both the radial and axial directions. Dr. Thomas Seward pointed out that the core etch rate should be a combination of a radial component, $d_{co} \cos\left(\frac{\theta}{2}\right)$, and an axial component $d_{co} \sin\left(\frac{\theta}{2}\right)$. If you assume that the steady state shape of the etched tip is a cone of angle θ , then during etching the volume rate of exposure of the new core is $\pi r^2 d_{cl}$, where r is the core radius. The volume rate of etching away the conic core is $\pi r^2 \cosec\left(\frac{\theta}{2}\right) d_{co}$. Equating these rates in steady state gives:

$$d_{cl}/d_{co} = \cosec\left(\frac{\theta}{2}\right) \quad (11)$$

and therefore:

$$\left(\frac{\theta}{2}\right) = \cosec^{-1}(d_{cl}/d_{co}) \quad (12)$$

The complete analysis, as described by Dr. Seward is included in Appendix B. For comparison to the model described by Puygranier and Dawson²⁶, Equation 9 was used for further analysis and graphs.

The differential etch height was calculated from the height of the evolving tip structure after a 20 minute etch time, and is simply the tip height determined from section analysis divided by the etch time (20 minutes), and is reported in units of nm/min. Determination of the core radial etch rate required longer etch times, due to the variation in chemistry at the core/clad interface and the fact that radial etching of the core only begins once the sidewall of the core is exposed. The 60 minute etch time was used to calculate the core radial etch rate, as the tip plateau was exposed for the majority of the 60 minutes, resulting in the most consistent results. Longer etch times were not used as the tip structure had evolved to a complete cone for some of the etch solutions. The original core radius of the SMF28 fiber is five microns. To determine the core radial etch rate, one half the plateau width of the evolving tip structure after 60 minutes of etch time was subtracted from the original five micron radius, and the result was divided by 60 minutes, resulting in units of nm/min. Figure 3.23 displays section analysis for etch times of 20 minutes and 60 minutes for SMF28 fiber etched in 1:1:2 etch solution, with example calculations for the core and differential etch rates. Table 3.4 is a summary of the results of the calculations of core radial etch rate and differential etch rate from AFM data.

Table 3.4 – Etch Rates Calculated from AFM Data

X	Cone Angle	Core Etch Rate (60')	Diff Etch Rate (20')	Core/Diff Etch Rate
1.8	157.4	50.8	11	4.62
2.0	147.8	62.5	19	3.29
2.5	133.2	65.4	28.5	2.29
3.0	127.4	63.3	33.1	1.91
4.0	120	56.7	33.8	1.68
5.0	113	46.8	30.2	1.55
6.0	112.8	41	26.8	1.53

Figure 3.24 is a plot of the core radial etch rate and the differential etch rate as a function of the value of X in the etch solution. Although both curves in Figure 3.24 display the same general overall trend in the etch rate, initially increasing then decreasing, the ratio of core to differential etch rate is continually decreasing in an exponential fashion. Figure 3.25 is a plot of the ratio of core etch rate to differential etch rate as a function of the value of X in the etch solution.

The cone angle as a function of the ratio of the core to differential etch rate is plotted in Figure 3.26 for the experimental data as well as the trend predicted by Equation 8. The error bars on the experimental data in Figure 3.26 represent (+/-) two times the standard deviation of the measured cone angles. An excellent correlation between the experimental data and the model of Equation 8 is realized.

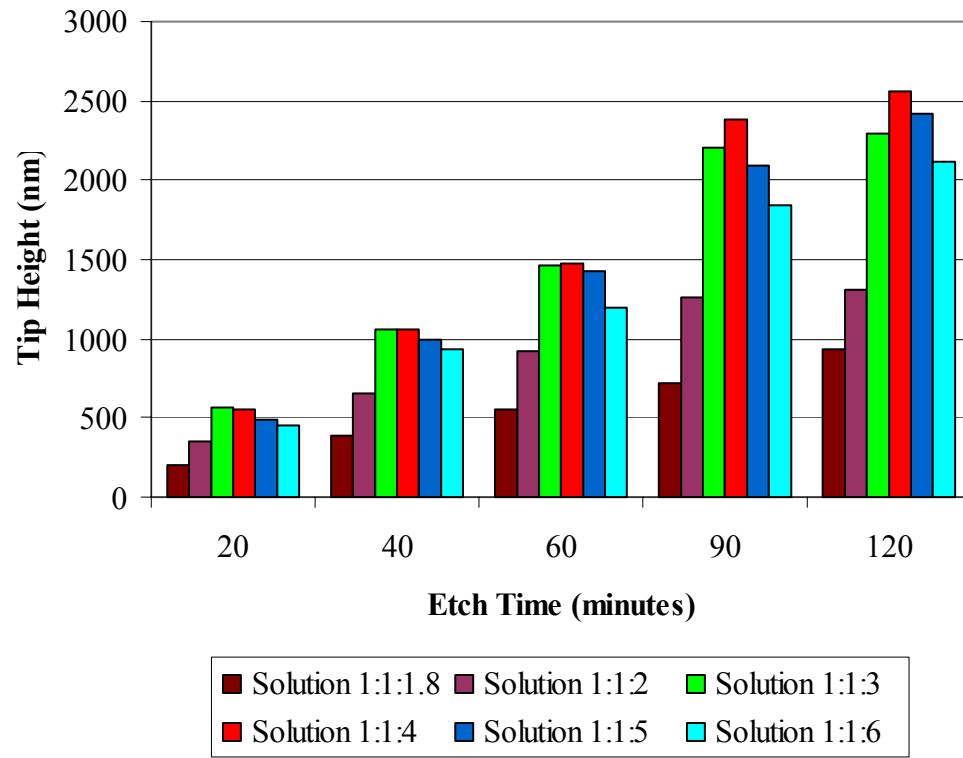


Figure 3.21. Tip height as a function of etch time and etch concentration.

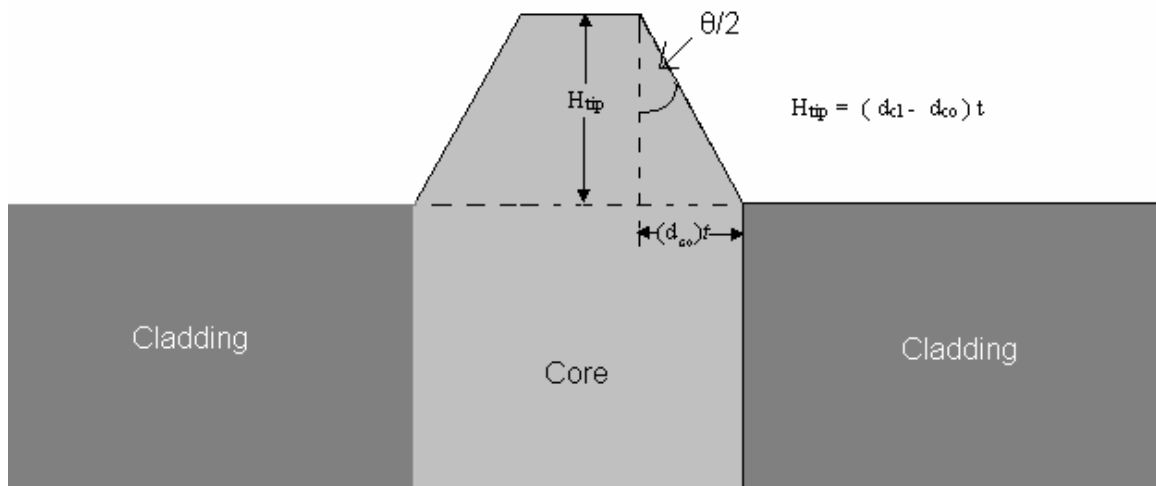
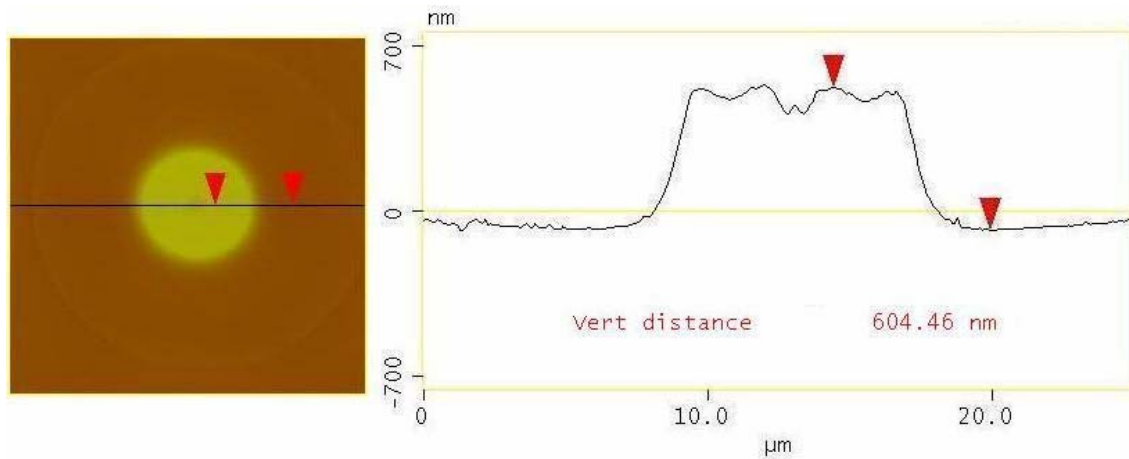


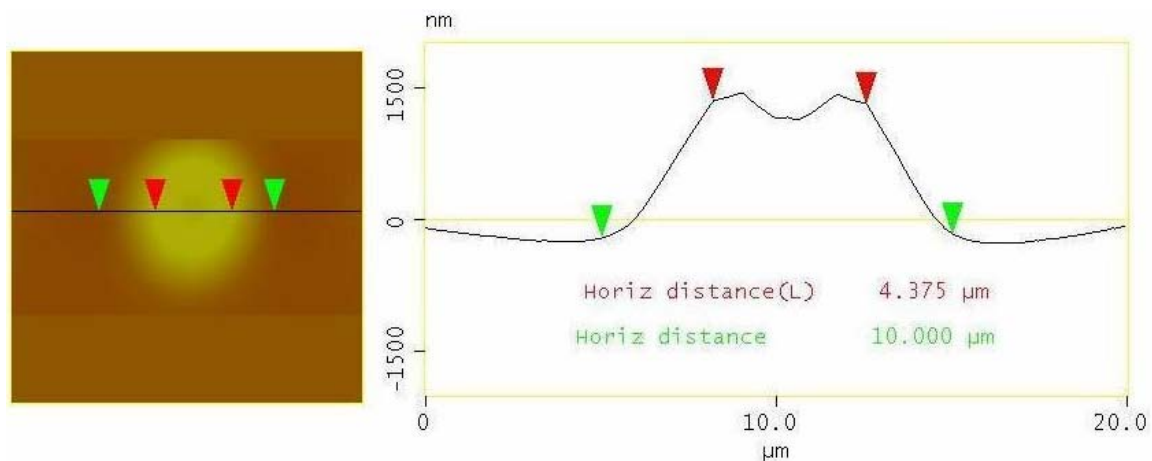
Figure 3.22. Schematic of the relationship between the height and width of an evolving cone and the etch rates of the core and cladding.



Calculation of differential etch rate:

Core height after 20 minute etch time = 604.5 nm

Differential etch rate = $604.5 \text{ nm} / 20 \text{ minutes} = 30.2 \text{ nm/min}$



Calculation of core radial etch rate:

Initial Core Radius = 5000 nm

Core radius at plateau top after 60 minute etch = 2187.5 nm

Distance core has etched radially in 60 minutes = $5000 - 2187.5 = 2812.5 \text{ nm}$

Core radial etch rate = $2812.5 \text{ nm} / 60 \text{ minutes} = 46.9 \text{ nm/min}$

Figure 3.23. AFM section analysis for SMF28 fiber etched for 20 minutes and 60 minutes in 1:1:5 etch solution. Example calculation of the core and differential etch rates are included below the images.

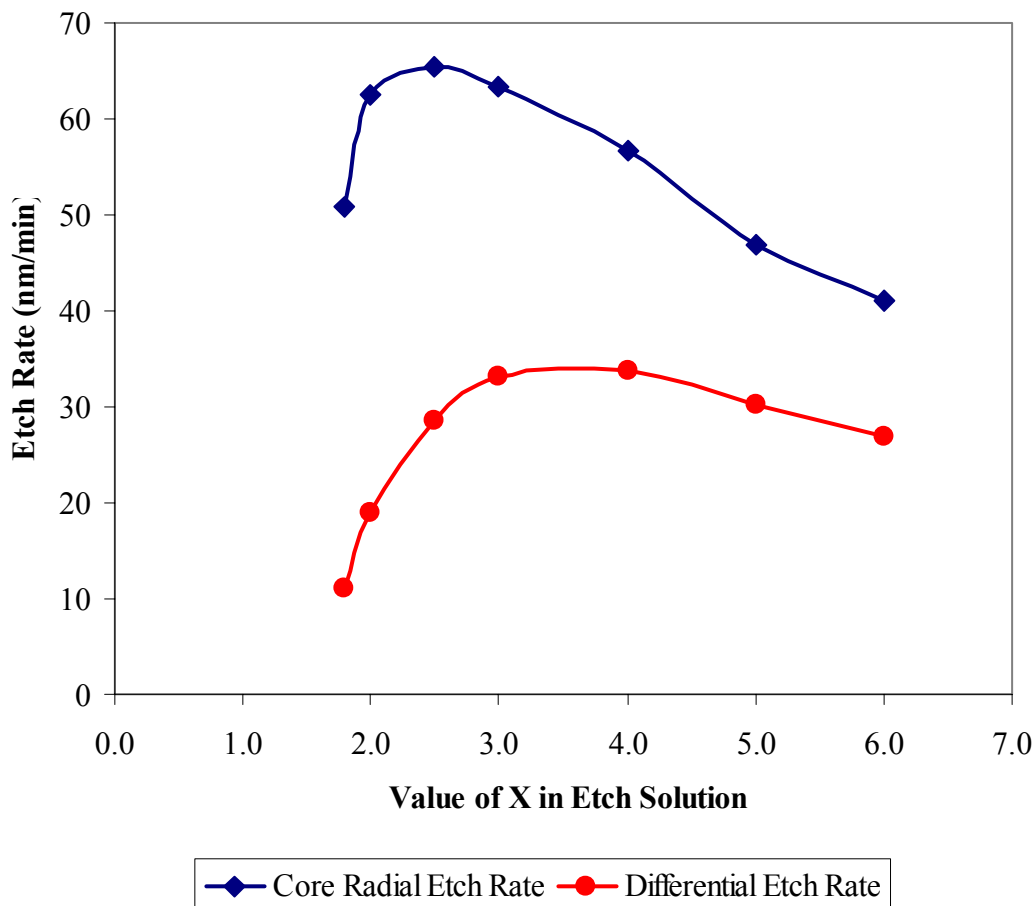


Figure 3.24. Plot of core radial etch rate and differential etch rate as a function of the value of X in the etch solution.

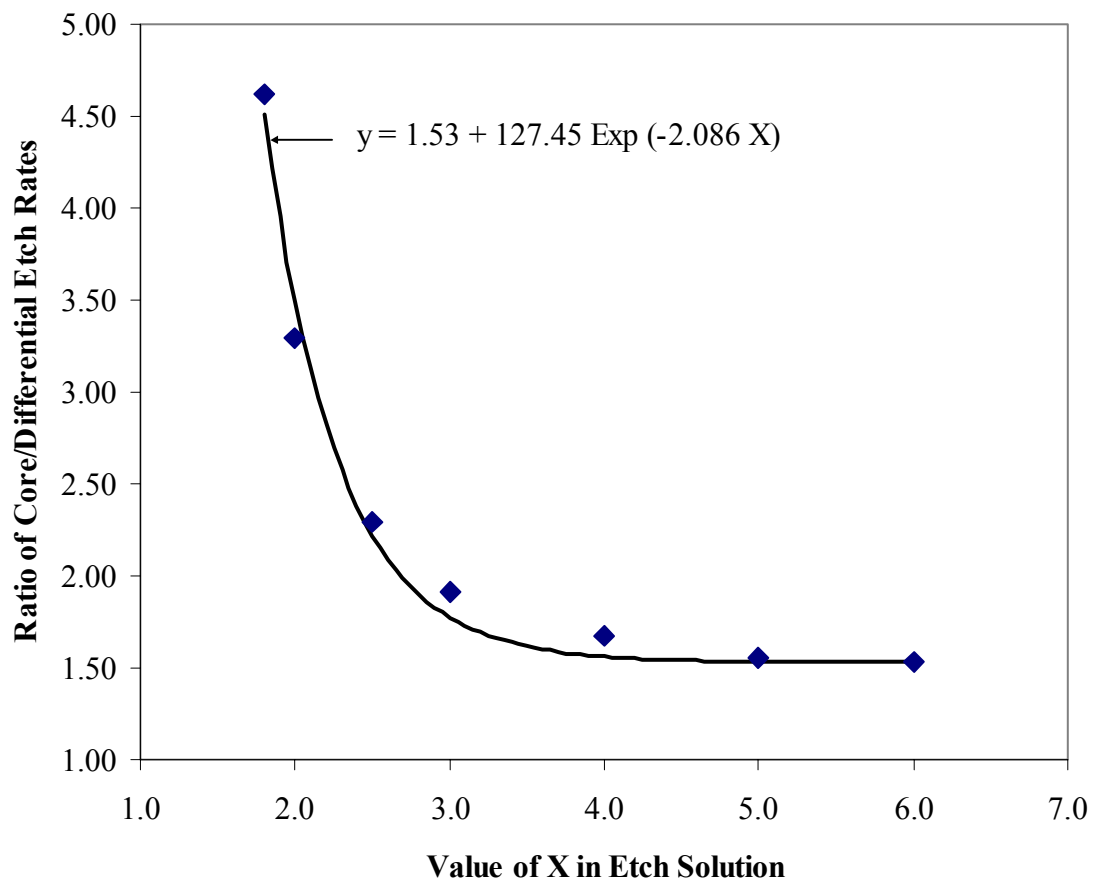


Figure 3.25. Plot of the ratio of core etch rate to differential etch rate for SMF28 fiber.

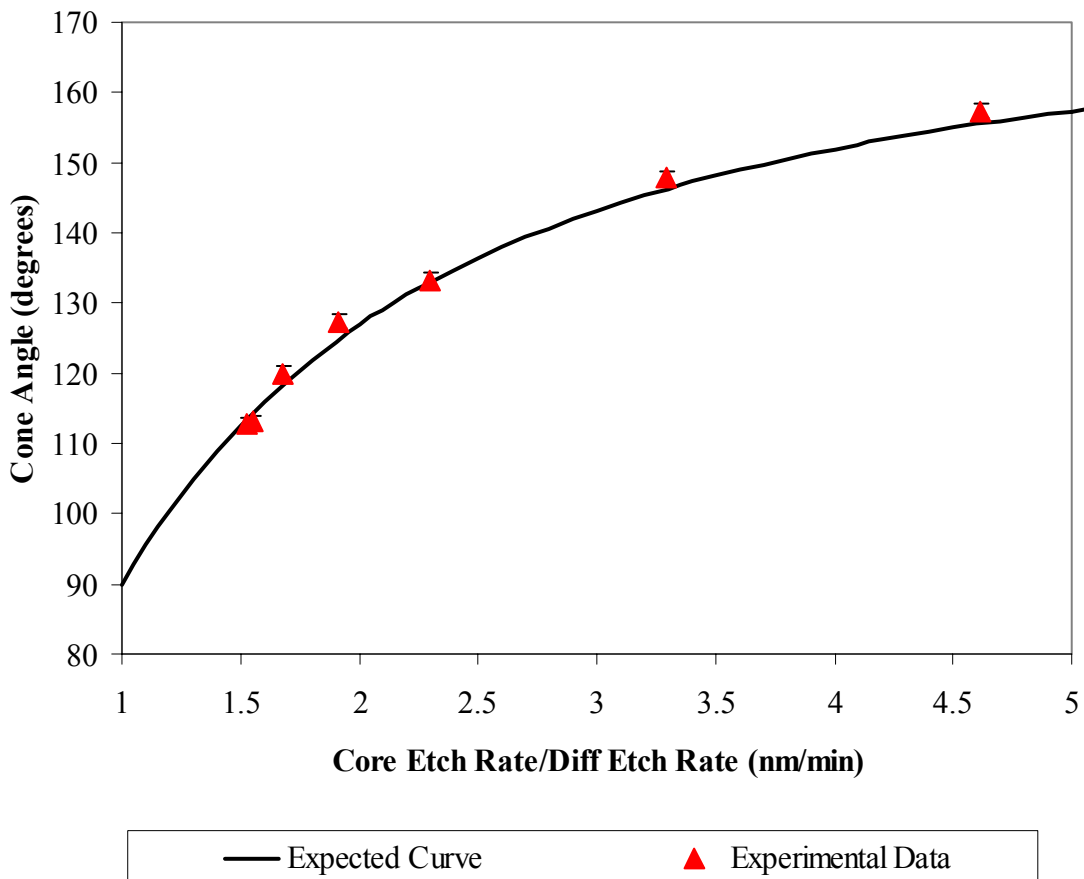


Figure 3.26. Plot of the relationship between core radial etch rate, differential etch rate and cone angle for SMF28 fiber etched in buffered HF solutions.

3.5 Conclusions

The cone angle is an important variable in producing NSOM tips and the ability to vary the cone angle is a major advantage of the fiber etching method over producing NSOM tips by fiber pulling. This study demonstrates the feasibility of predicting the cone angle after short etch times, without taking the etching process to completion, which may take several hours. It has been demonstrated that AFM is a powerful characterization tool for visualizing the evolution of the tip that results from etching single mode optical fibers. The data gathered for short etch times showed that the cone angle changed initially, but then leveled off with further etching.

The relationship between cone angle and the ratio of core etch rate to differential etch rate was demonstrated through a simple model and shown to correlate extremely well with experimental data. The larger the differential etch rate between the core and the cladding, and therefore the smaller the ratio of core etch rate to differential etch rate, the smaller the cone angle that evolves. Cone angles reported in this study ranged from 157 degrees for an SMF28 fiber in a 1:1:1.8 solution to 58 degrees for a HI fiber in a 1:1:6 solution. Additionally it was shown that the cone angle possible for the SMF28 fiber varied from 157 to 113 degrees providing excellent opportunity to modify the NSOM tip for specific applications. Larger cone angles result in shorter tips and improve the transmission coefficient as the propagation mode runs into cut-off and begins an exponential decay closer to the aperture. However if sharper tips are needed, and intensity can be sacrificed the smaller cone angles result in longer, sharper tips and may provide better resolution for some applications.

3.6 References

1. E. Abbe, "Beiträge zur Theorie des Mikroskops und der Mikroskopischen Wahrnehmung," *Arch. Mikrosk. Anat.*, **9** [1] 413-68 (1873).
2. E. Synge, "A Suggested Method for Extending the Microscopic Resolution into the Ultramicroscopic Region," *Philos. Mag.*, **6** [1] 356-62 (1928).
3. M. De Serio, R. Zenobi, and V. Deckert, "Looking at the Nanoscale: Scanning Near-Field Optical Microscopy," *TrAC Trends Anal. Chem.*, **22** [2] 70-7 (2003).
4. E.A. Ash and G. Nichols, "Super-Resolution Aperture Microscopy Using 3 cm Radiation," *Nature*, **237** [5357] 510-15 (1972).
5. D.W. Pohl, W. Denk, and M. Lanz, "Optical Stethoscopy: Image Recording with Resolution Wavelength/20," *Appl. Phys. Lett.*, **44** [7] 651-3 (1984).
6. A. Lewis, M. Isaacson, A. Harootunian, and A. Muray, "Development of a 500 Å Spatial Resolution Light Microscope : I. Light is Efficiently Transmitted Through [Lambda]/16 Diameter Apertures," *Ultramicroscopy*, **13** [3] 227-31 (1984).
7. E. Betzig and J.K. Trautman, "Near-Field Optics: Microscopy, Spectroscopy and Surface Modification Beyond the Diffraction Limit," *Science*, **257** [5067] 189-95 (1992).
8. Y.D. Suh and R. Zenobi, "Improved Probes for Scanning Near-Field Optical Microscopy," *Adv. Mater.*, **12** [15] 1139-42 (2000).
9. J.A. DeAro, K.D. Weston, and S.K. Buratto, "Near-Field Scanning Optical Microscopy of Nanostructures," *Phase Transitions.*, **68** [1] 27-57 (1999).
10. D. Courjon, C. Bainier, and M. Spajer, "Imaging of Submicron Index Variations by Scanning Optical Tunneling," *J. Vac. Sci. Technol., B*, **10** [6] 2436-9 (1992).
11. A. Hartschuh, N. Anderson, and L. Novotny, "Near-Field Raman Spectroscopy Using a Sharp Metal Tip," *J. Microsc.*, **210** [3] 234-40 (2003).
12. C.A. Michaels, S.J. Stranick, L.J. Richter, and R.R. Cavanagh, "Scanning Near-Field Infrared Microscopy and Spectroscopy with a Broadband Laser Source," *J. Appl. Phys.*, **88** [8] 4832-9 (2000).
13. R. Stockle, Y.D. Suh, V. Deckert, and R. Zenobi, "Nanoscale Chemical Analysis by Tip-Enhanced Raman Spectroscopy," *Chem. Phys. Lett.*, **318** [1-3] 131-6 (2000).

14. F. Formanek, Y. De Wilde, L. Aigouy, W.K. Kowk, L. Paulius, and Y. Chen, "Nanometer-Scale Probing of Optical and Thermal Near-Fields with and Apertureless NSOM," *Superlattices Microstruct.* **35** [3-6] 315-23 (2004).
15. D. Zeisel, S. Nettesheim, B. Dutoit, and R. Zenobi, "Pulsed Laser Induced Desorption and Optical Imaging on a Nanometer Scale with Scanning Near-Field Microscopy Using Chemically Etched Fiber Tips," *Appl. Phys. Lett.*, **68** [18] 2491-2 (1996).
16. J.W.P. Hsu, "Near-Field Scanning Optical Microscopy Studies of Electronic and Photonic Materials and Devices," *Mater. Sci. Eng., R*, **33** [1] 1-50 (2001).
17. R.C. Dunn, "Near-Field Scanning Optical Microscopy," *Chem. Rev.*, **99** [10] 2891-927 (1999).
18. L. Novotny and C. Hafner, "Light Propagation in Cylindrical Waveguide with a Complex, Metallic, Dielectric Function," *Phys. Rev. E: Stat. Phys. Plasmas, Fluids, Relat. Interdiscip. Top.*, **50** [5] 4094-109 (1994).
19. B. Hecht, B. Sick, U.P. Wild, V. Deckert, R. Zenobi, M. Olivier, and D. Pohl, "Special Topic: Near-Field Microscopy and Spectroscopy," *J. Chem. Phys.*, **112** [18] 7761-74 (2000).
20. X. Lui, J. Wang, and D. Li, "Simple Device and Reproducible Approach for Producing High Efficiency Optical Fiber Tips for a Scanning Near-Field Optical Microscope," *Rev. Sci. Instrum.*, **69** [9] 3439-40 (1998).
21. R.L. Williamson and M.J. Miles, "Melt-Drawn Scanning Near-Field Optical Microscopy Probe Profiles," *J. Appl. Phys.*, **80** [9] 4804-12 (1996).
22. M. Ohtsu, "Progress of High-Resolution Photon Scanning Tunneling Microscopy Due to Nanometric Fiber Probe," *J. Lightwave Technol.*, **13** [7] 1200-21 (1995).
23. A. Sayah, C. Philipona, P. Lambelet, M. Pfeffer, and F. Marquis-Weible, "Fiber Tips for Scanning Near-Field Optical Microscopy Fabricated by Normal and Reverse Etching," *Ultramicroscopy*, **71** [1-4] 59-63 (1998).
24. M. Ohtsu and H. Hori, *Near-Field Nano-Optics: From Basic Principles to Nano-Fabrication and Nano-Photonics*; p. 386. Academic/Plenum Publishers, New York, 1999.
25. D.R. Turner, AT&T Bell Laboratories, "Etch Procedures for Optical Fibers," U.S. Pat. 4,469,554 (1983).
26. B.A.F. Puygranier and P. Dawson, "Chemical Etching of Optical Fibre Tips - Experiment and Model," *Ultramicroscopy*, **85** [4] 235-48 (2000).

27. B.A.F. Puygranier, S. Montgomery, J. Ashe, R.J. Turner, and P. Dawson, "Imaging Tip Formation in Single-Mode Optical Fibres," *Ultramicroscopy*, **86** [3-4] 223-39 (2001).
28. N. Essaidi, Y. Chen, V. Kottler, E. Cambril, C. Mayeux, N. Ronarch, and C. Vieu, "Fabrication and Characterization of Optical-Fiber Nanoprobes for Scanning Near-Field Optical Microscopy," *Appl. Opt.*, **37** [4] 609-15 (1998).
29. C. Lehrer, L. Frey, S. Petersen, T. Sulzbach, O. Ohlsson, T. Dziomba, H.U. Danzebrink, and H. Ryssel, "Fabrication of Silicon Aperture Probes for Scanning Near-Field Optical Microscopy by Focused Ion Beam Nano Machining," *Microelectron. Eng.*, **57-58** [1] 721-8 (2001).
30. J.A. Veerrman, A.M. Otter, L. Kuipers, and N.F. van Hulst, "High Definition Aperture Probes for Near-Field Optical Microscopy Fabricated by Focused Ion Beam Milling," *Appl. Phys. Lett.*, **72** [24] 3115-7 (1998).
31. B. Hecht, H. Bielefeldt, Y. Inouye, D. Pohl, and L. Novotny, "Facts and Artifacts in Near-Field Optical Microscopy," *J. Appl. Phys.*, **81** [6] 2492-8 (1997).
32. L. Novotny, E.J. Sanchez, and X. Sunney Xie, "Near-Field Optical Imaging Using Metal Tips Illuminated by Higher-Order Hermite-Gaussian Beams," *Ultramicroscopy*, **71** [1-4] 21-9 (1998).
33. L. Novotny, E.J. Sanchez, and X.S. Xie, "Near-Field Optical Spectroscopy Based on the Field Enhancement at Laser Illuminated Metal Tips," *Opt. Photonics News*, **10** [12] 24 (1999).
34. E.J. Sanchez, L. Novotny, and X.S. Xie, "Near-Field Fluorescence Microscopy Based on Two-Photon Excitation with Metal Tips," *Phys. Rev. Lett.*, **82** [20] 4014-7 (1999).
35. A. Hartschuh, B. M.R., A. Bouhelier, and L. Novotny, "Tip-Enhanced Optical Spectroscopy," *Philos. Trans. R. Soc. London, Ser. A*, **262** [1-2] 807-19 (2004).
36. A. Bouhelier, L. Beversluis, and L. Novotny, "Applications of Field Enhanced Near-Field Optical Microscopy," *Ultramicroscopy*, **100** [3-4] 413-9 (2004).
37. S. Nie and S.R. Emory, "Probing Single Molecule and Single Nanoparticles by Surface-Enhanced Raman Scattering," *Science*, **275** [5303] 1102-5 (1997).
38. D. Burns, A. Townshend, and A. Catchpole, *Inorganic Reaction Chemistry: Systematic Chemical Separation*; p. 33. Ellis Horwood, Chichester, UK, 1980.

39. E. Rochow, *Comprehensive Inorganic Chemistry*, Vol. 1; p. 26. Pergamon, Oxford, UK, 1973.

Chapter 4

Evaluation of Phase Separation in Glasses with Atomic Force Microscopy

4.1 Abstract

Glass forming melts frequently exhibit liquid-liquid immiscibility resulting in phase separation. The chemical and spatial variation of phase separated morphologies in glasses can range from a few angstroms to microns, often requiring very high magnification for detection. Many properties of phase separated glasses are influenced by the compositions and connectivity of the phases present, leading to interesting property trends. The presence of phase separation in glasses and the ability to engineer the form and scale of the glass microstructure allows the potential for tailoring properties of glasses for specific applications.

Historically, phase separated glasses have been characterized by transmission electron microscopy (TEM). This technique is very time consuming and costly, requiring specialized equipment and training. Atomic force microscopy (AFM) provides an inexpensive alternative to TEM and has proven to be a powerful tool in the characterization of phase separation in glasses. AFM provides rapid and accurate evaluation of the type, degree and scale of phase separation in glasses down to the nanometer level. This paper will present sample preparation techniques and results for evaluation of phase separation in alkali borosilicate and sodium silicate glass systems.

4.2 Introduction

4.2.1 *Phase Separation in Glasses*

Liquid-liquid immiscibility is very common in glass melts, in fact so common that Shelby¹ states that far more binary glassfoming melts exhibit liquid-liquid immiscibility than exhibit homogeneous liquid behavior. Phase separation in glasses influences a variety of properties and has been a subject of debate over the last half century. Mazurin² references Shvetsov (1932) as publishing the first account of metastable immiscibility as a cause for chemical inhomogeneity in glasses. A number of review articles dealing with phase separation in glasses have been published, including frequently referenced publications by Mazurin,^{2,3} Tomozawa,^{4,5} Uhlmann⁶ and James.⁷

Models for phase separation, based on thermodynamics and the free energy of mixing arguments, are described in detail by several authors.^{1,2,7,8} Immiscibility in glasses is controlled by the free energy of mixing, where below a critical temperature, T_c , the competition between the enthalpy of mixing and the entropy of mixing results in a free energy versus composition curve similar to Figure 4.1. Above T_c the entropy term will always dominate and free energy of mixing will always be lower for the homogeneous melt. The free energy curve displayed in Figure 4.1, for temperatures below T_c , shows that the free energy is lower if the melt separates into two phases with compositions A and B than if it remains a homogeneous melt with the free energy described by the curve.

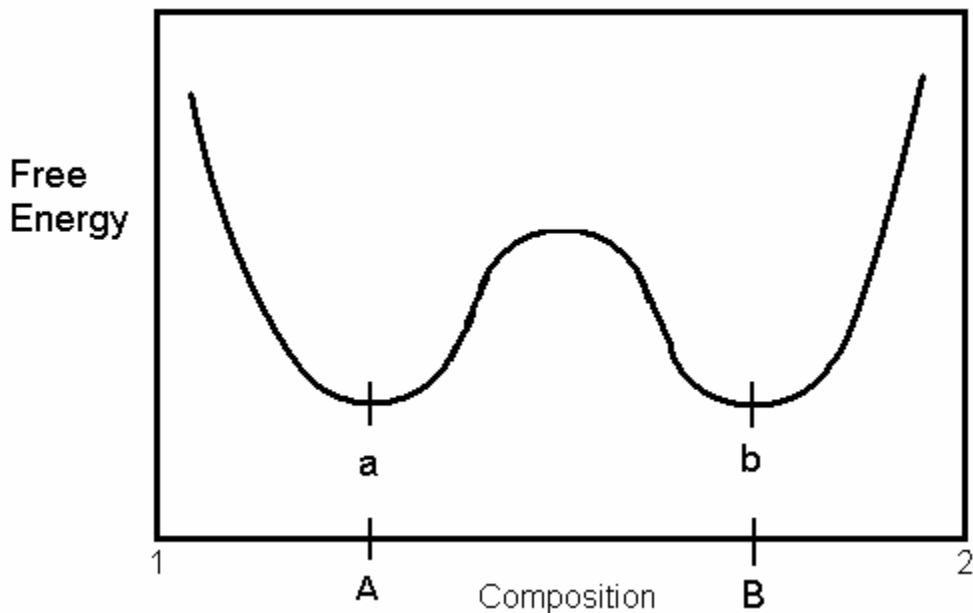


Figure 4.1. Free energy versus composition curve for a glass in the immiscibility region.

While the thermodynamic models predict when phase separation will occur, there are two distinct mechanisms by which phase separation can evolve. The two mechanisms, referred to as nucleation and growth and spinodal decomposition, lead to very different microstructures and properties. The curvature of the free energy of mixing at the bulk composition of the melt will indicate the mechanism by which phase separation occurs.

Figure 4.2 displays an idealized immiscibility diagram for the binary sodium silicate system, and the typical microstructures that will evolve, if allowed by kinetics, when heat treated within the various regions of the phase diagram.

Within the nucleation and growth region of the phase diagram a large change in composition must occur to cause a decrease in the free energy of the system, and the formation of a nuclei. This region is referred to as the metastable region as the system is unstable to small fluctuations in composition, but can be stable to larger changes in composition. Once nucleated, the new phase will grow in size through diffusion and regions may coalesce depending on their proximity. During the growth stage the chemical composition of the nucleated phase is invariant with respect to time at isothermal temperature. Phase separation resulting from nucleation and growth is characterized by distinctly separated spherical droplets of the nucleated phase in a continuous matrix of a second phase, as shown in Figure 4.2. The spheres will have a composition of the phase which differs the greatest from the bulk composition. The spherical phase will nucleate randomly and have poor connectivity.

Phase separation in the spinodal region begins as small fluctuations in composition that given time grow in compositional differences resulting in two continuous interpenetrating phases. Because these changes occur spontaneously, and no energy barrier to separation is present, the region is considered unstable with respect to immiscibility. The system will lower its free energy by continually changing the composition of the two phases until the equilibrium compositions are reached. Once the equilibrium compositions are realized the free energy is at its lowest state. The spatial variations of the structure remain fairly constant until the equilibrium compositions are achieved, after which the phase separated regions will grow in size through diffusion, thereby reducing the interfacial energy of the system. Both phases formed in the spinodal region will show a high degree of connectivity.

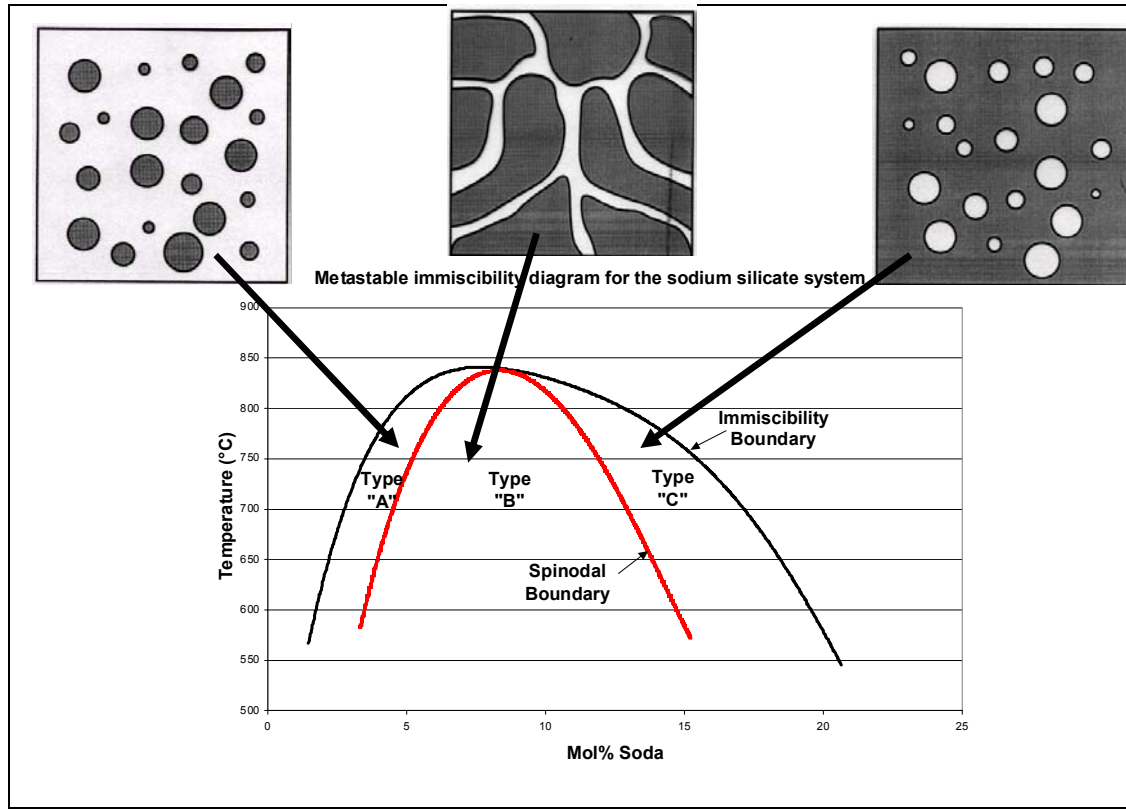


Figure 4.2. Metastable immiscibility diagram for the sodium silicate system with typical microstructures expected from the various regions of the system. Dark phase in drawings is sodium rich and light phase is silica rich. Immiscibility and spinodal boundaries were reproduced from data of Shelby.¹

4.2.2 Characterization of Phase Separation in Glasses

The traditional characterization techniques most often used to study fine scale phase separation in glasses are transmission electron microscopy (TEM) and small angle x-ray scattering (SAXS). Replica TEM is an indirect method that is capable of determining size, shape and distribution of phases through surface topography of a phase separated glass.⁹ Direct TEM can detect phase separation on a finer scale than replica TEM, but often requires sample preparation that may alter the glass composition, such as ion beam milling. The failure mechanisms in glass make it difficult to thin samples well enough for TEM examination without creating fatal flaws in the specimen. SAXS uses short wavelength electromagnetic waves (0.1nm) and differences in electron density between co-existing phases, to provide information about the size and surface area of scattering regions in phase separated glasses.^{10,11} TEM and SAXS both provide important information in the study of phase separation in glasses, however both techniques are instrumentation intensive, expensive, and require specialized training for analysis and data interpretation.

The affect that phase separation has on physical properties has also been utilized to indirectly evaluate the microstructure of phase separated glasses. The properties of phase separated glasses can be divided into three categories, depending on the effect that the phase separation has on the property.¹ Type I properties are those that are relatively insensitive to presence of phase separation, and related to the average bulk composition only. Type I properties include density, refractive index and thermal expansion, and little can be learned about phase separation morphology from these properties. Type II properties are sensitive to the presence of phase separation, but insensitive to the details of morphology. Type II properties include light scattering and glass transition temperature, and both have limitations to detection of phase separation. Type III properties involve mass transport, such as electrical conductivity, gas diffusion, chemical durability and viscous flow, and are sensitive not only to the presence of phase separation but to the morphology (connectivity) of the phase separation in glasses. Shelby¹² showed that studies of transport properties can be used to define immiscibility boundaries and limits of connectivity of the phases in systems which contain a region of immiscibility.

Studying physical properties to indirectly infer the presence and connectivity of phase separation in glasses is labor intensive and does not provide any necessary spatial information about the phase separation morphology.

In addition to the more traditional techniques for characterizing phase separation in glasses, there is a plethora of additional techniques that have been reported to help understand the phase separation phenomenon. Infrared analysis,¹³ nuclear magnetic resonance,^{14,15} and Raman¹⁶ have been reported to provide structural information but do not necessarily provide visual microstructure data. The need for rapid, inexpensive and accurate evaluation of the microstructure of phase separation in glasses has led to the development of methods for evaluation of phase separation in glasses via Atomic Force Microscopy (AFM).

4.3 Experimental Procedures

4.3.1 Glass Melting and Sample Preparation

A binary sodium silicate composition was batched from reagent grade Na₂CO₃ and SiO₂ powders resulting in 50 grams of glass with a targeted molar composition of 12.5Na₂O*87.5SiO₂. The phase separation phenomenon in this binary sodium silicate composition has been studied in great detail,^{13,17-19} providing a well-established immiscibility boundary and historical data for comparison to the results achieved in this study. The batch was mixed with a glass mortar and pestle followed by melting in a platinum crucible at 1500°C for 3 hours in an electrically fired furnace. Occasional stirring with a silica rod was required to achieve a homogeneous melt.

A silica crucible partially filled with alumina powder was pre-heated to 1000°C and used as a setter to slow the cooling of the melt, once removed from the furnace. A cane of the sodium silicate glass, approximately 2 mm in diameter, was drawn from the melt, with the use of a 3 mm diameter silica rod, while the melt was cooling and passing through the required viscosity region. The cane was air quenched and then cut into sections approximately four inches in length. The glass remaining in the crucible was re-heated to 1500°C, and the process was repeated until a sufficient amount of cane was drawn. Faster cooling rates, that may be required for certain glass systems to avoid phase

separation on cooling from the melt, can be achieved by passing the cane through a water cooled coil directly above the melt.

The sodium silicate cane samples were isothermally heat treated at temperatures between 637°C and 800°C for various times, then air quenched to room temperature. Prior to AFM analysis the heat treated cane samples were cleaved and etched to develop surface morphology based on the differential etch properties of the silica phase versus the sodium rich phase. The canes were scored lightly with a tungsten scribe, and fractured under light tension to produce clean fracture surfaces with a distinct mirror region. The freshly cleaved cane end-faces were etched for one minute in 0.5% hydrofluoric acid, followed by a 30 second rinse in saturated boric acid, a quick rinse in ethyl alcohol and then dried with compressed air. The saturated boric acid helps to dissolve any fluoride deposits that may form on the cane end faces as a result of the HF etch, leaving debris free surfaces for AFM analysis. A very light etch is all that is required due to the outstanding z resolution of the AFM. Over-etching will result in a surface that is too rough leading to image artifacts due to the pyramidal shape of the AFM cantilevers.

A commercial alkali borosilicate glass, Corning Code 7070, was also analyzed for this paper to examine the evolution of phase separation through the nucleation and growth process. The literature contains several references on phase separation in the alkali borosilicate system.²⁰⁻²⁴ The composition of the Corning 7070 on a weight percent basis, as described by Boyd and Thompson,²⁵ is listed in Table 4.1. Commercial glass cullet of Corning 7070 was melted in a platinum crucible for four hours at 1600°C. The glass melt was removed from the furnace, partially quenched in water and then cooled in air to room temperature. The bulk Corning 7070 glass was cut into several sections which were heat treated at 700°C for times ranging from 1 to 24 hours. 700°C is in the metastable region of the immiscibility dome, resulting in phase separation through the nucleation and growth process. The viscosity of this glass at 1600°C is too high to allow for pulling cane from the melt, so alternative methods for preparing AFM specimens from bulk glasses were explored.

Table 4.1. Composition of Corning 7070 Glass

Oxide	Weight %
SiO ₂	72
B ₂ O ₃	25
Al ₂ O ₃	1
K ₂ O	1
Na ₂ O	0.5
Li ₂ O	0.5

Two successful methods for preparing bulk glasses for evaluation of phase separation via AFM analysis are: grinding/polishing and controlled fracture. The method of grinding and polishing requires that the surface finish be of exceptional quality, due to the sensitivity of the AFM to scratches and sub-surface damage, which are exaggerated if etching is required to provide surface relief. Well polished specimens can be examined directly in the AFM if the differential hardness between the phase separated regions is sufficient to create surface topography during the polishing process. Light etching, after grinding and polishing, can also be used to create surface topography that results from the difference in chemical durability of the glass phases.

To significantly decrease the sample preparation time required to achieve a polished surface sufficient for AFM analysis, and increase sample throughput, bulk glass samples can also be prepared for AFM analysis through a fracture and etch process. Samples should be cut into shapes that are easily fractured under light tension, allowing for a substantial mirror region to examine with AFM. Figure 4.3 is a schematic of a geometry that has been used successfully to provide fractured surfaces of bulk glasses. Once fractured, a light etch in the appropriate solution will provide surface topography based on the differential etch properties of the glass phases involved. A 20 second etch

in 1N nitric acid was sufficient to preferentially etch the boron rich droplets compared to the silica rich matrix of the heat treated Corning 7070 glass.

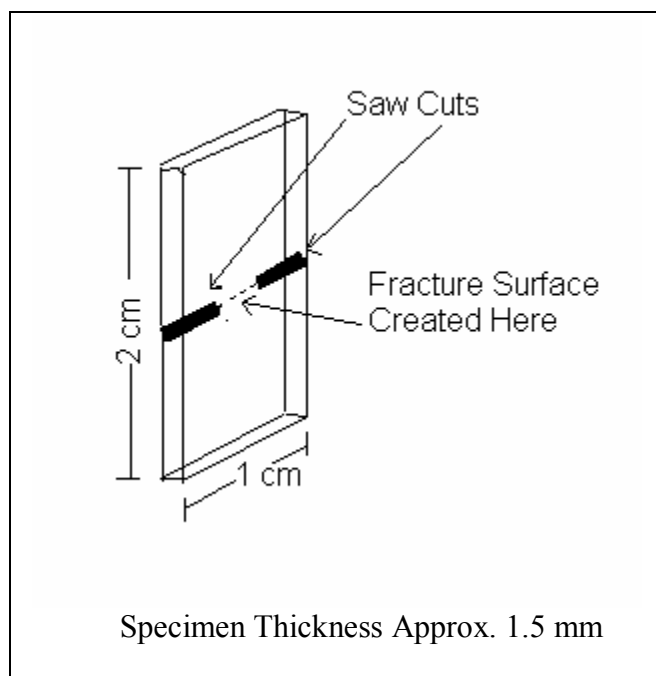


Figure 4.3. Geometry used to prepare high quality fracture surfaces of bulk glasses for AFM analysis.

4.3.2 *Atomic Force Microscopy*

A Digital Instruments Dimension 3100 Scanning Probe Microscope with a Nanoscope IIIA controller was used in TappingMode® to produce three-dimensional images of the etched surfaces. Pyramidal etched silicon probes with a half cone angle of 18° and an approximate radius of curvature of 10nm were used for all measurements. Scan sizes required to evaluate the phase separation microstructures varied from 500nm square to several microns square depending on the spatial variation of a particular sample.

TappingMode® AFM images are generated by scanning a very sharp probe tip, on the end of an integrated cantilever that is oscillated at or near its resonance frequency, in a raster pattern over the sample surface while lightly “tapping” on the surface. The motion of the tip above the sample is controlled by a piezoelectric tube scanner, and the

tip-sample interaction is monitored by reflecting a laser off the top of the cantilever into a split photodiode detector. An electronic feedback circuit, between the photo-detector and the z-piezo, maintains the tip oscillation at a constant set-point amplitude during scanning by moving the scanner vertically at every x,y data point. The three dimensional digital image is produced by mapping the motion of the z-piezo required to maintain a constant oscillation amplitude at each lateral data point. Figure 4.4 is a schematic of an AFM operating in TappingMode®.

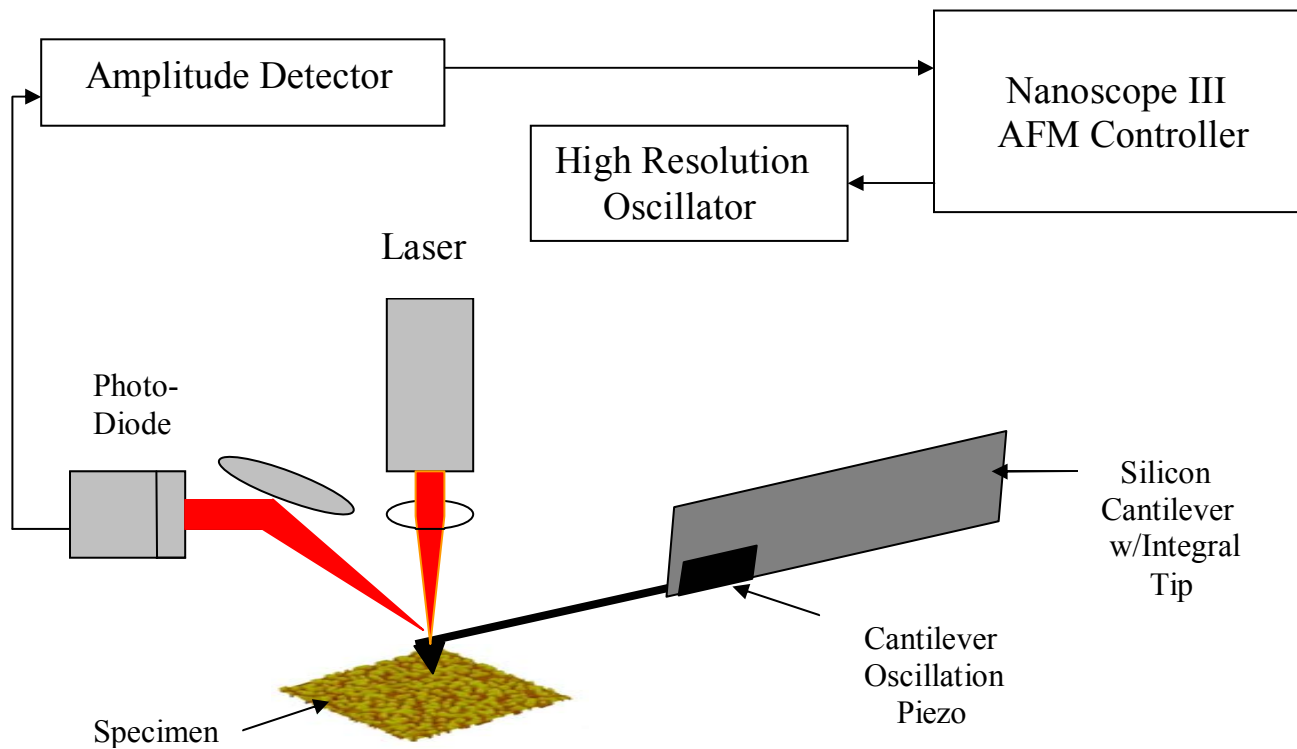


Figure 4.4. Schematic of TappingMode® AFM operation.

4.4 Results and Discussion

4.4.1 Alkali Borosilicate Results

The commercial alkali borosilicate glass, Corning Code 7070, was heat treated at 700°C for various times to evaluate the evolution of phase separation by the nucleation and growth mechanism. Due to the high viscosity of the glass at 700°C, the diffusion within the glass is slow, and the nucleation and growth process proceeds at an easily controlled rate. Figure 4.5 displays the AFM topographical images of samples of Corning 7070 heat treated at 700°C for 1, 8 and 24 hours. All samples were prepared for AFM analysis by polishing, followed by a light etch in 1N nitric acid for 20 seconds.

Growth of phase separation for nucleation-type mechanism as described schematically by Varshneya,⁹ is compared to AFM section analysis of Corning 7070 glass in Figure 4.6. The droplets have a fixed composition upon formation, and the growth of the phase separation inhomogeneity is in the physical size of the droplet. The surface topography that results in the AFM image is due to the differential etch rate between the continuous silica matrix phase and the boron rich droplet phase. The AFM data in Figure 4.6 shows that the etch depth of the droplet phase, relative to the matrix, does not change when comparing the 8 hour to the 24 hour heat treatments, although the droplet size has increased by nearly 40%. This indicates that only minimal, if any changes in composition are taking place during the growth stage of phase separation by the nucleation and growth mechanism.

Further analysis of the AFM results obtained for the alkali borosilicate glass confirm that the radius of the droplet phase is proportional to the cube root of time for an isothermal heat treatment. The driving force for growth of the droplets is a reduction of interfacial surface area through larger droplets growing at the expense of the smaller droplets. This expected result is described by nucleation and growth theory,¹⁰ as well as shown experimentally by Moriya²³ et al. for alkali borosilicate glasses characterized by replica TEM. Figure 4.7 is a plot of the radius of the droplet phase, as calculated from the AFM data, as a function of the cube root of heat treatment time at 700°C.

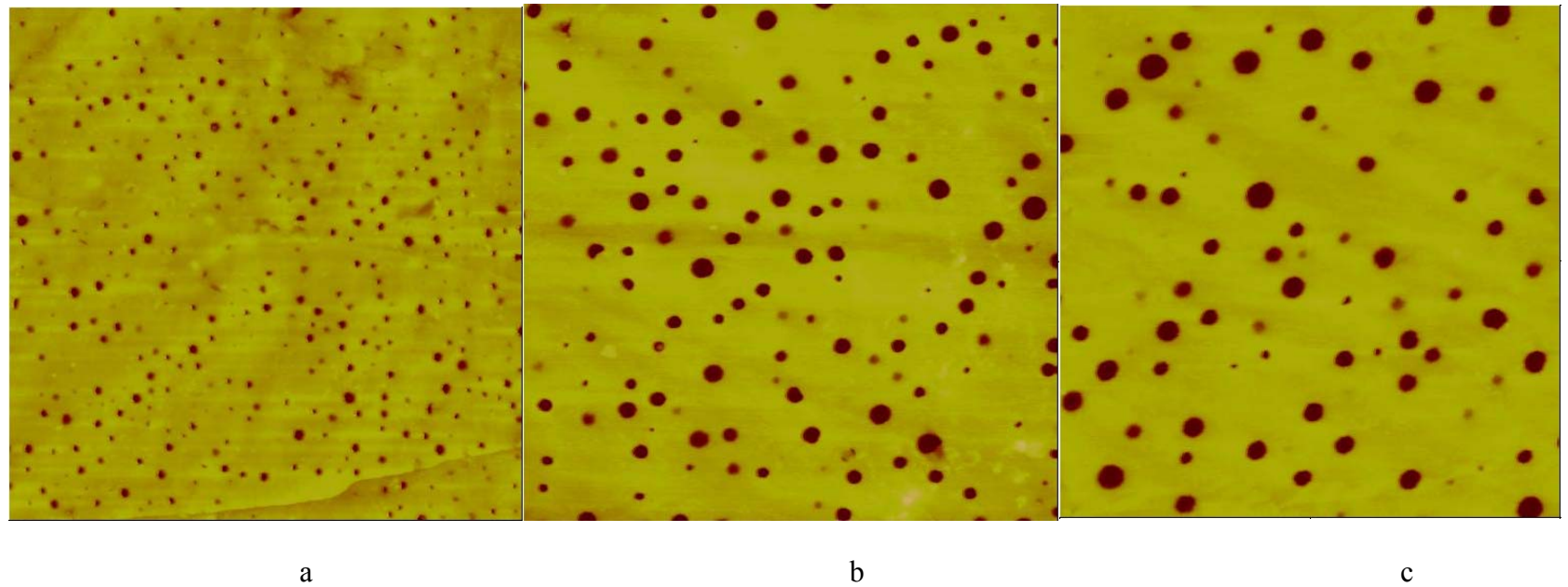


Figure 4.5. AFM images of Corning 7070 glass after heat treatment at 700°C for a) 1 hour, b) 8 hours and c) 24 hours. All scans are 2X2 microns.

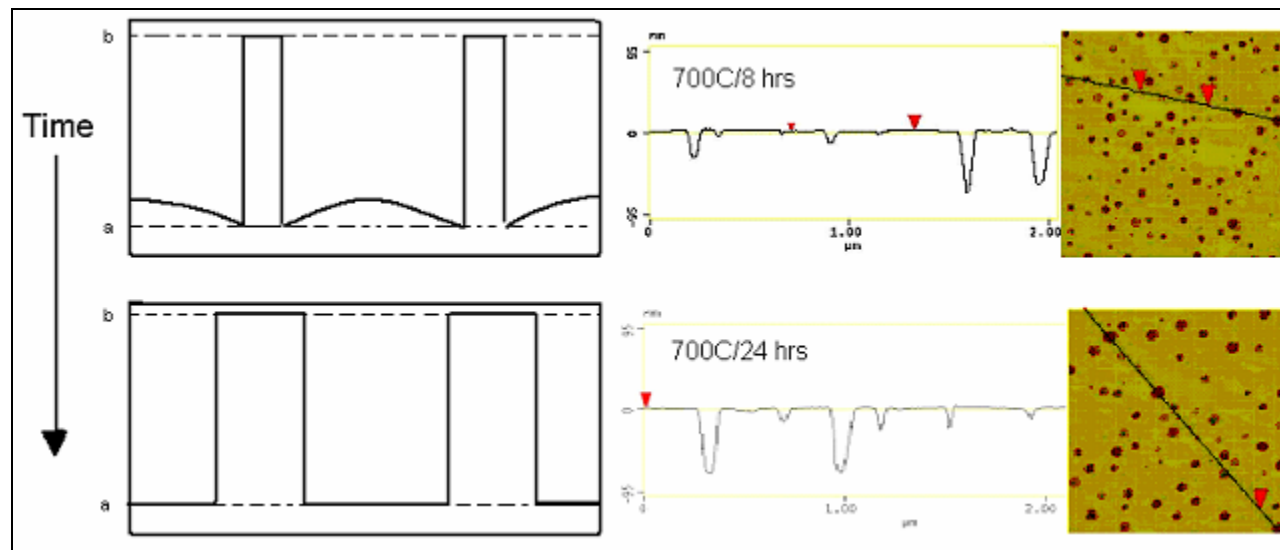


Figure 4.6. Predicted vs. observed growth of phase separation for nucleation and growth type mechanism in Corning 7070 glass.

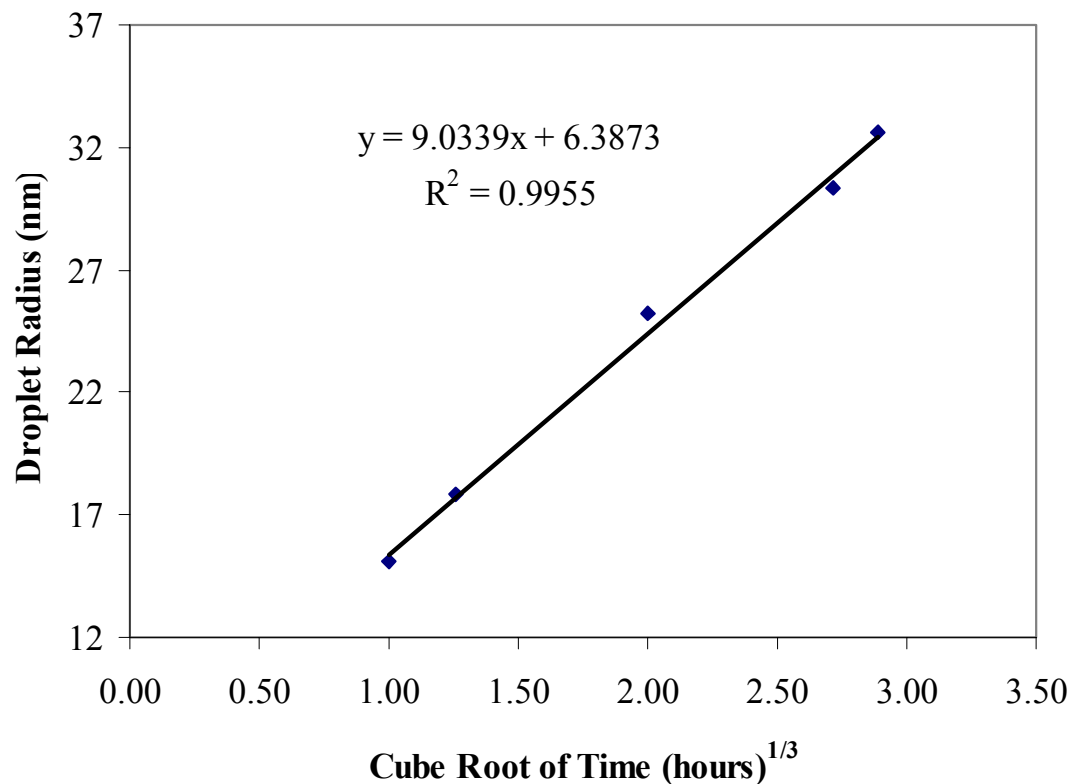


Figure 4.7. Time dependence of the droplet radius for samples of Corning 7070 heat treated at 700°C.

4.4.2 Sodium Silicate Results

Mazurin² provides TEM replica images of the phase separation microstructure that results from various heat treatments of a sodium silicate glass with a composition of 12.5 mole % Na₂O and 87.5 mole % SiO₂. Several of the heat treatment temperatures were repeated in the current study to compare AFM results to previously published TEM replica data. Figure 4.8 is an immiscibility diagram for the sodium silicate binary glass along with AFM images displaying the morphology that resulted from 15 minute heat treatments at temperatures within both the spinodal decomposition and the nucleation and growth region of the immiscibility. Additional heat treatment temperatures between 637°C and 820°C were also evaluated, in addition to the images included in Figure 4.8, with all microstructures correlating well with the previously published data of Mazurin.²

The microstructure that results from the heat treatment at 637°C, where the melt is fairly viscous, is in the early stages of spinodal decomposition after a 15 minute heat treatment. The chemical variation between the two continuous phases (high silica and sodium rich) is small resulting in a dense microstructure. The microstructure at 720°C, which is just slightly below the spinodal boundary, shows two distinct continuous phases. The high silica phase, which is more durable than the sodium rich phase when etched in nitric acid, is bright or elevated in the image while the sodium rich phase is dark or depressed. The chemical segregation is well defined compared to the heat treatment at 637°C. The evolution of spinodal decomposition will be discussed in more detail later in this paper.

Droplets of the high silica phase in a continuous matrix of a sodium rich phase results when this high alkali composition is heat treated below the immiscibility boundary, but above the spinodal boundary. The AFM images, in Figure 4.8, at 778°C and 791°C show distinct bright droplets of the more durable high silica phase. The microstructure at 778°C also indicates that secondary phase separation of the matrix has occurred on cooling from the heat treatment temperature. Figure 4.9 shows a more detailed AFM image of the glass heat treated at 778°C for 15 minutes, clearly showing that the matrix has undergone secondary phase separation, resulting in a three phase microstructure.

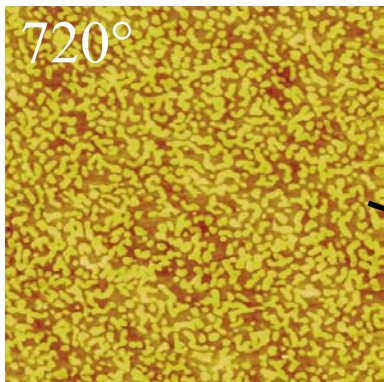
Porai-Koshits et al.¹⁹ describe the phenomena of secondary phase separation in the sodium silicate binary in detail. Secondary phase separation of a primary separated phase is described to take place as a result of over-saturation of the primary phase with silica or alkali when the temperature is lowered. Secondary phase separation is most likely to occur when heat treatment is carried out above the spinodal curve, but passes through the spinodal region during cooling, as is the case for the heat treatment at 778°C. Porai-Koshits¹⁹ explains that the alkali rich phase is more susceptible to secondary phase separation, as is seen in this study, due to the asymmetry of the immiscibility dome. The asymmetry results in different temperature dependence of the solubility of the components. The solubility of alkali in silica (left side of the immiscibility diagram) changes very little over a wide range of temperatures. In contrast, the solubility of silica in the alkali rich phase (right side of the immiscibility diagram) is highly dependent on temperature, resulting in a driving force for secondary phase separation of the alkali rich phase during cooling.

The evolution of phase separation by spinodal decomposition is displayed in Figure 4.10 for a sodium silicate glass with molar composition 12.5Na₂O*87.5SiO₂ heat treated isothermally at 650°C for times ranging from 40 to 1020 minutes. Phase separation in the spinodal region begins as small fluctuations in composition that, given time, grow in compositional differences resulting in two continuous interpenetrating phases. The system will lower its free energy by continually changing the composition of the two phases until the equilibrium compositions are reached. Once the equilibrium compositions are realized the free energy is at its lowest state, and no further chemical segregation will take place. During the chemical segregation stage of spinodal decomposition the spatial variations of the structure remain fairly constant. After reaching the equilibrium compositions the phase separated regions will then grow in size, through diffusion, to reduce the interfacial area between the two phases, and further reduce the energy of the system.

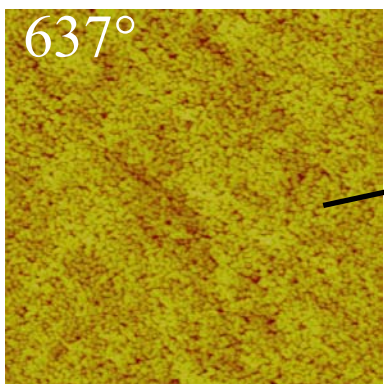
The predicted⁹ growth of phase separation for a spinodal-type mechanism is displayed in Figure 4.11 along with AFM section analysis for 12.5%Na₂O*87.5%SiO₂ glass heat treated for various times at 650°C. AFM section analysis produces a two dimensional profile of the surface across a user defined section line, and is useful to

compare the etch depths that result after various heat treatments. The variation in the section analysis is due to differential etch rate between the more durable high silica phase and the high alkali phase in a 0.5% HF etch solution. The AFM analysis follows the predicted path of spinodal decomposition, initially growing in composition (etch depth) only until the equilibrium compositions are reached sometime prior to the 240 minute heat treatment at 650°C, then growing only in size to reduce the interfacial area between the two phases. During the growth stage of spinodal decomposition no further changes in chemistry between the two phases is realized, as shown by a consistent etch depth for the longer heat treatment times. This result demonstrates that the chemical variations that result from the phase separation process can be tracked by AFM analysis, a bonus to the high quality images that the AFM provides.

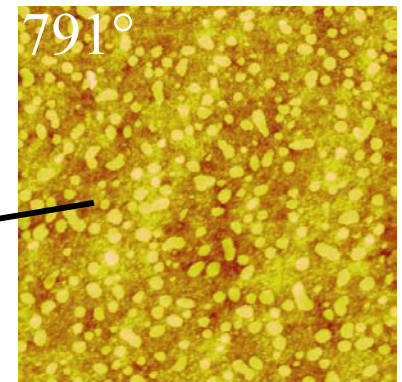
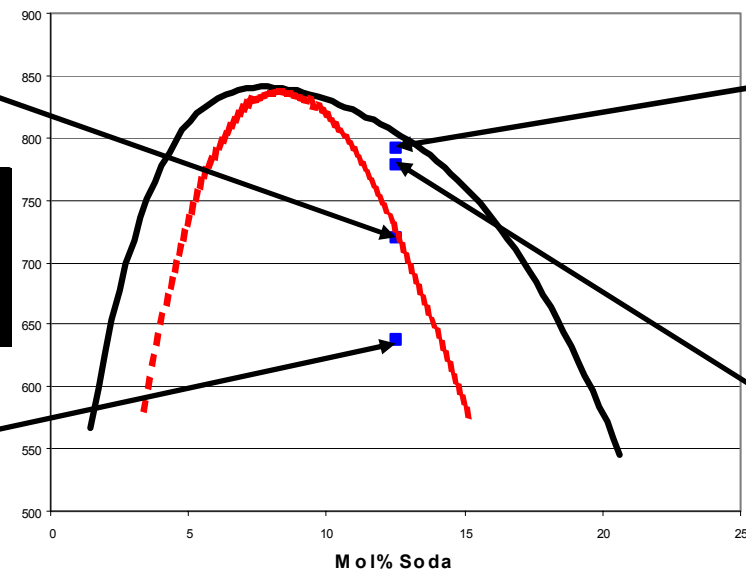
101



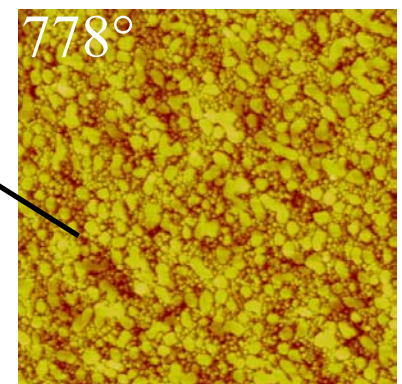
720°



637°



791°



778°

Figure 4.8. Immiscibility diagram (from Shelby)¹ for sodium silicate glass along with AFM images displaying morphology of 12.5%Na₂O*87.5%SiO₂ glass heat treated for 15 minutes at temperatures of 637, 720, 778 and 791°C. All images are 3.2x3.2 microns.

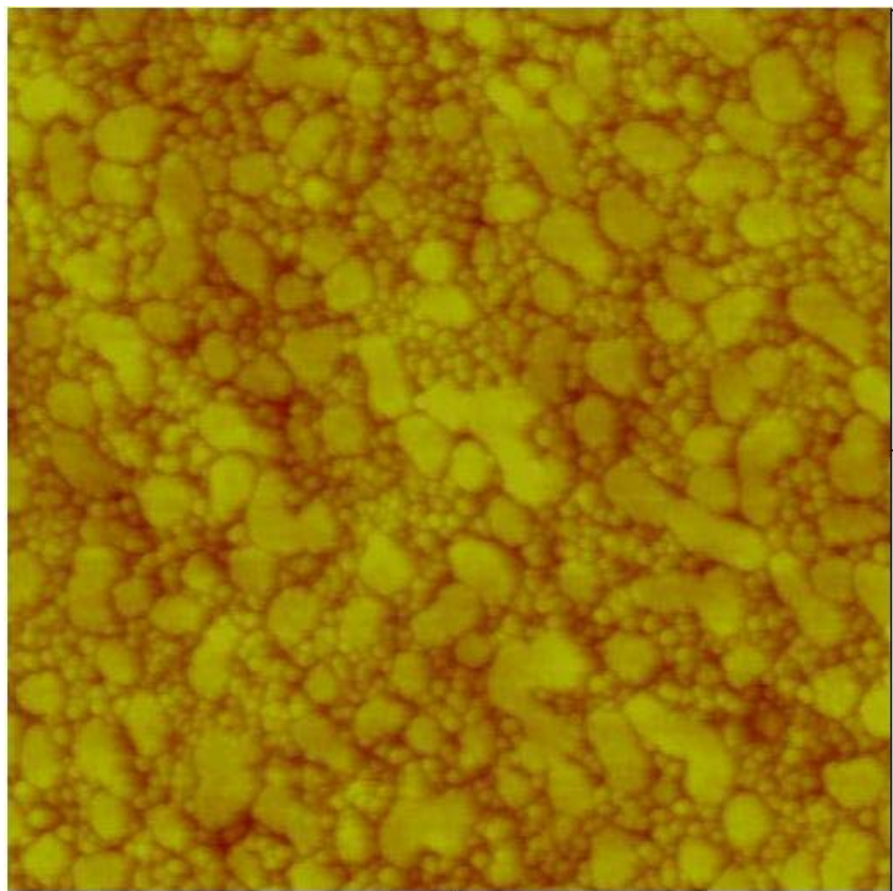


Figure 4.9. Sodium silicate glass heat treated at 778°C for 15 minutes showing secondary phase separation within the high sodium matrix phase (2umx2um).

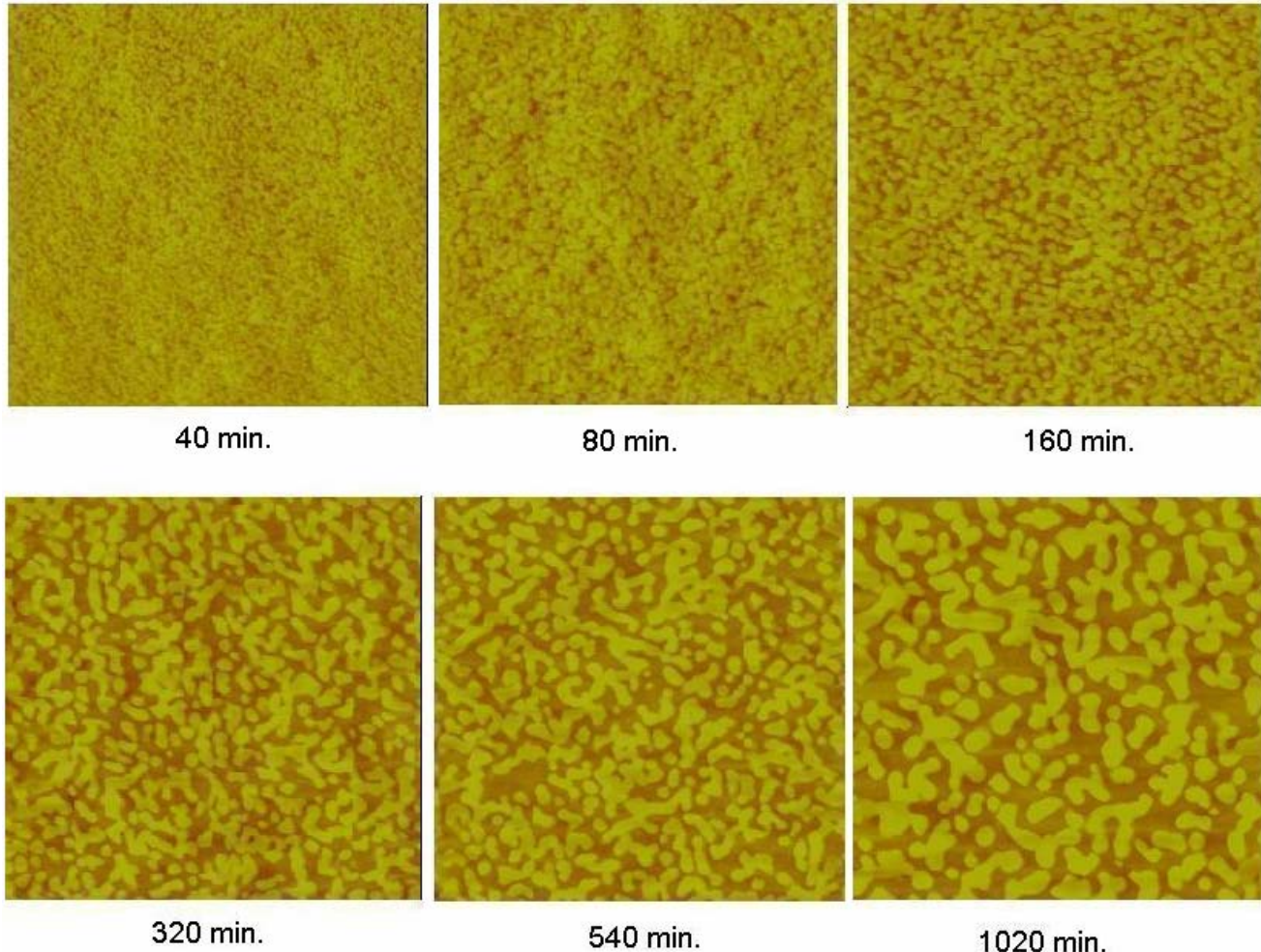


Figure 4.10. AFM topographical images displaying the evolution of phase separation in 12.5% Na_2O *87.5% SiO_2 glass heat treated for various times at 650°C.
(all scans 2 x 2 microns).

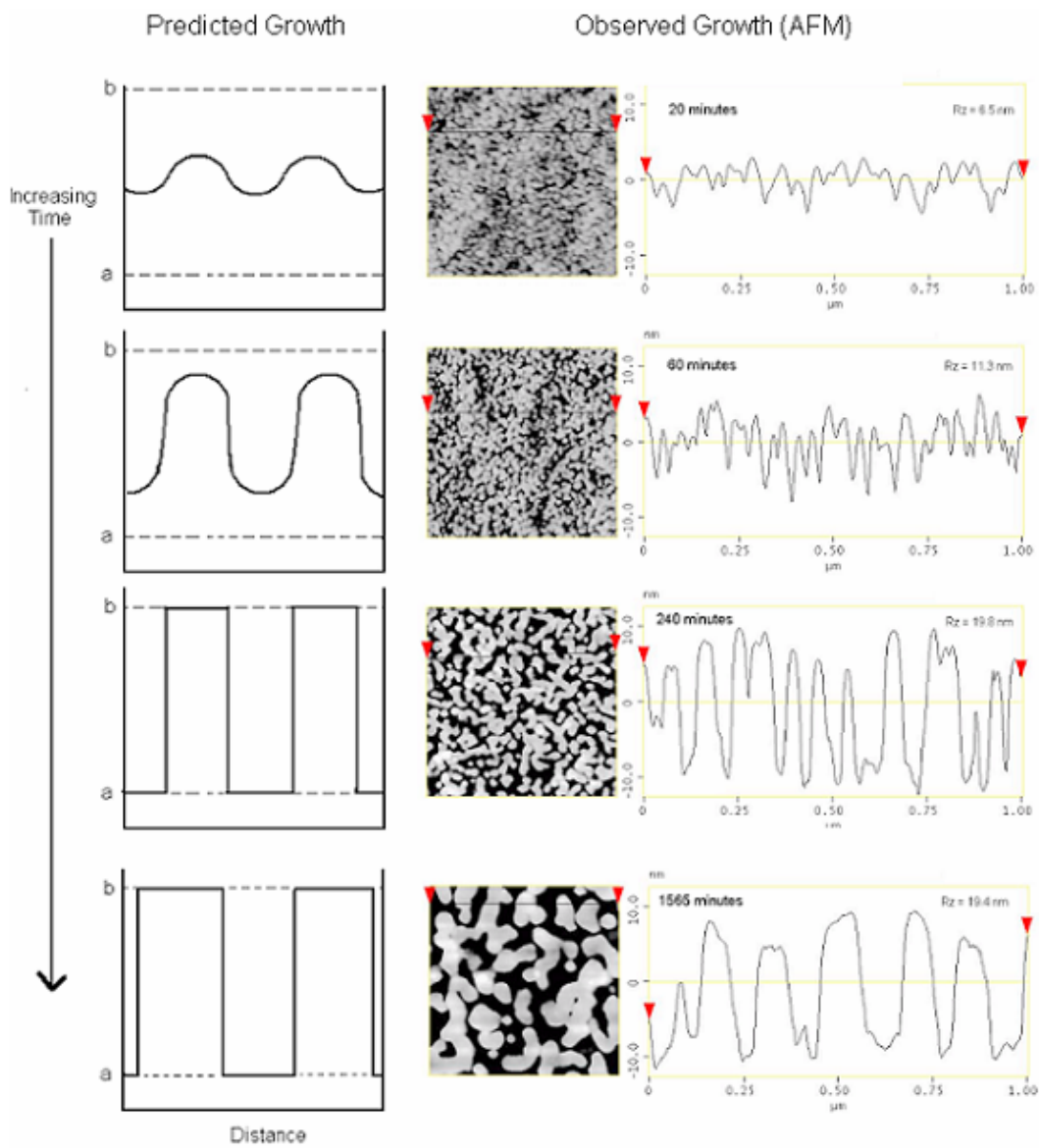


Figure 4.11. Predicted versus observed growth of phase separation for the spinodal-type mechanism. Predicted growth curves after Varshneya.⁹

To quantitatively study the variation in chemical segregation during phase separation by spinodal decomposition, the average surface roughness, Ra, was calculated for each AFM image completed on the fractured and etched sodium silicate cane samples heat treated for various times at 650°C. The average surface roughness, Ra, is the arithmetic average of the absolute values of the surface height deviations (Z) from the mean plane for all n data points in the image.

$$Ra = \frac{1}{n} \sum_{j=1}^n |Z_j| \quad (1)$$

Table 4.2 contains the Ra values for a series of heat treatment times at 650°C for a glass of molar composition 12.5Na₂O*87.5SiO₂. Figure 4.12 is a plot of the average surface roughness as a function of heat treatment time at 650°C for the sodium silicate composition studied. The plot shows two distinct trends to the changes in surface roughness. During the chemical segregation stage of spinodal decomposition the surface roughness changes rapidly with heat treatment time, indicating that the chemical compositions of the two phases are continually changing. Once the equilibrium compositions are reached, around 240 minutes, further changes in surface roughness are minimal. The longest heat treatment time at 650°C in this study was 1540 minutes (25 hours, 40 minutes).

During the chemical segregation stage of spinodal decomposition, the range which is circled in Figure 4.12, the changes in chemistry are diffusion controlled and therefore should vary with the square root of heat treatment time. Figure 4.13 displays the surface roughness data up to 240 minutes as a function of the square root of heat treatment time at 650°C. The plot in Figure 4.13 includes a best fit linear trendline with an R² value better than 0.99.

Table 4.2 Average Surface Roughness and Grain Size Results from 650°C Heat Treatment Study for Glass Composition 12.5Na₂O*87.5SiO₂.

Time at 650°C (min)	Surface Roughness Image Ra (nm)	Average Area of High Silica Phase (nm ²)
20	1.59	2060
40	2.37	2075
60	2.68	2105
120	4.09	2975
160	4.50	4206
240	5.61	5685
320	5.80	6990
400	5.83	8070
540	5.85	10354
1020	5.88	14340
1340	5.85	16350
1565	5.46	17470

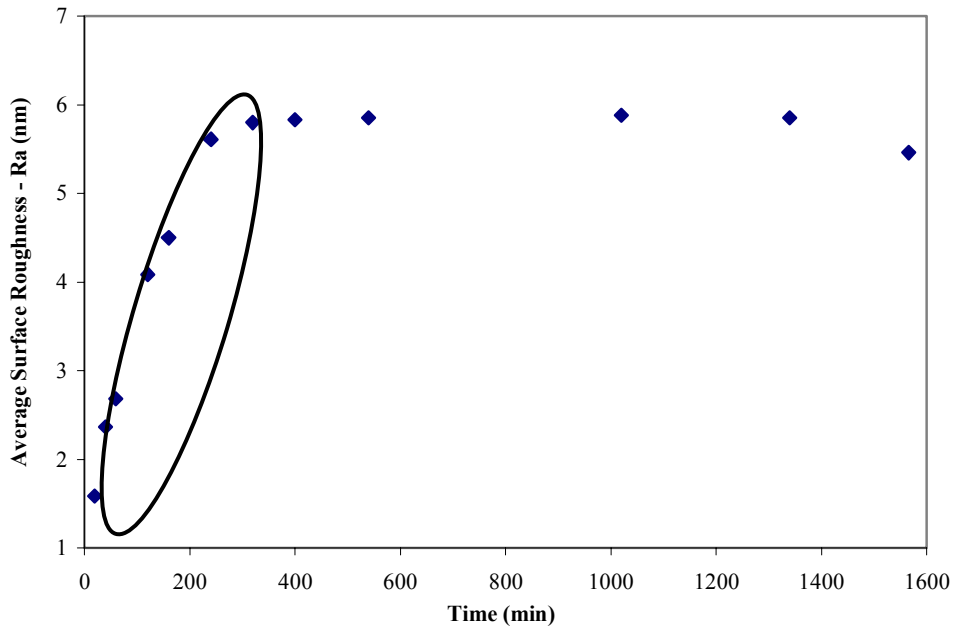


Figure 4.12. Average surface roughness (Ra) as a function of heat treatment time at 650°C for glass composition 12.5Na₂O*87.5SiO₂.

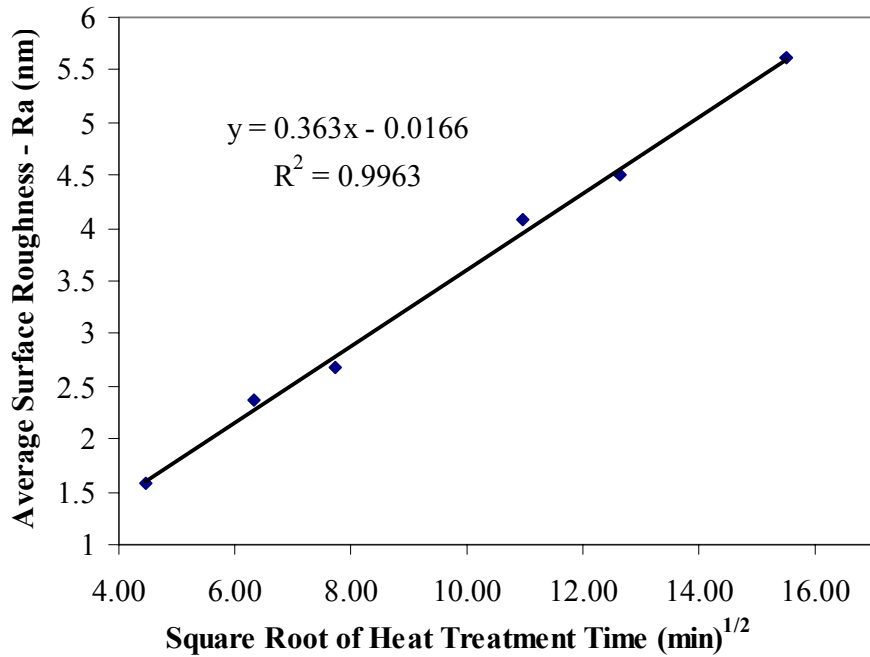


Figure 4.13. Average surface roughness (Ra), during *chemical segregation stage of spinodal decomposition*, as a function of square root of heat treatment time at 650°C for glass of composition 12.5Na₂O*87.5SiO₂.

To evaluate the spatial growth of the phases during spinodal decomposition, the Grain Size command from the Nanoscope® software was utilized. The Grain Size command defines grain boundaries based on the height of AFM pixel data. The mean area and the total number of grains are calculated and displayed. Grains are defined in terms of conjoined pixels having a height above or below a user defined threshold height. Figure 4.14 displays an example Grain Size analysis for the sodium silicate glass heat treated at 650°C for 1020 minutes. A clear bimodal distribution of pixel height is displayed, and the threshold was chosen as the minimum between the two nodes prior to execution of the Grain Size analysis. This placement of the Threshold was used consistently throughout the Grain Size analysis for the various heat treatment temperatures. The average grain size calculated for the various heat treatment times at 650°C are listed in Table 4.3. The grain size analysis was completed on the areas above the threshold, which when etched in 0.5% HF is the more durable high silica phase.

Figure 4.15 is a plot of the average area of inhomogeneity of the high silica phase, as determined by Grain Size analysis, as a function of heat treatment time at 650°C for glass of composition $12.5\text{Na}_2\text{O} \cdot 87.5\text{SiO}_2$. Very slight increases in the size of the inhomogeneities resulted for the shorter heat treatment times at 650°C. A consistent increase in the area of the high silica phase is shown for heat treatments between 160 minutes and the longest heat treatment time of 1540 minutes. Figure 4.12 indicated that chemical segregation was occurring up to a heat treatment time of 240 minutes, however Figure 4.15 indicates that the growth stage may begin prior to the completion of the chemical segregation stage and as early as 160 minutes.

The evolution of the spinodal microstructure during the growth process is controlled by the viscosities and volume fractions of the separated phases, the glass-glass interfacial energies and the diffusion coefficients.²⁶ Phase separation that results from spinodal decomposition can coarsen for long periods of time without losing connectivity. The spatial scale of the phase separated areas will increase and thereby reduce the interfacial area of the two phases. Zarzycki and Naudin¹¹ used SAXS to demonstrate that the coarsening of the spinodal microstructure increases in proportion to the cube root of heat treatment time. Figure 4.16 is a plot of the average area of the high silica phase, as

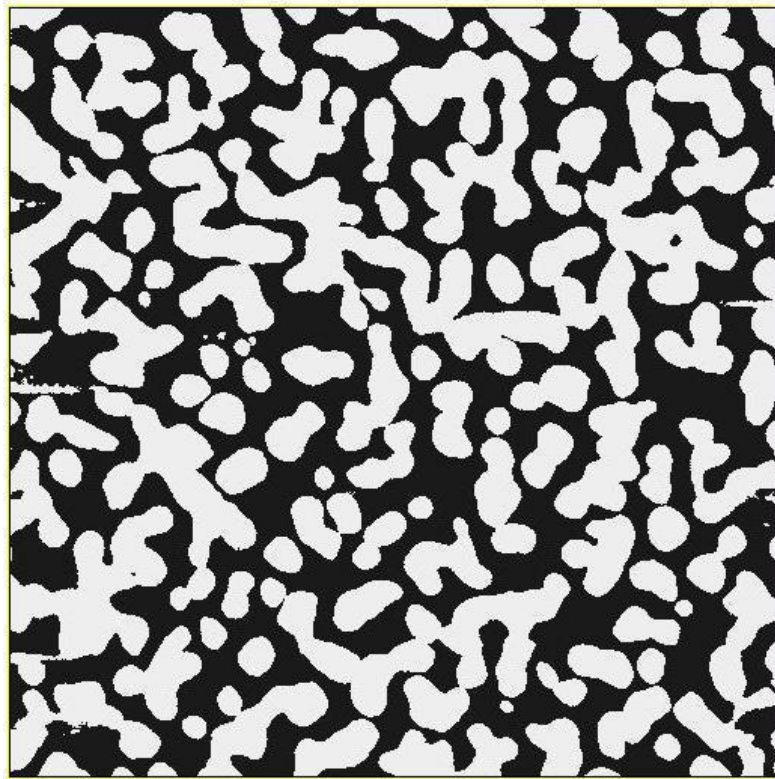
determined from the AFM Grain Size analysis software, as a function of the cube root of heat treatment time at 650°C for a glass of composition 12.5Na₂O*87.5SiO₂. As with the roughness data in Figure 4.13 the linear trendline fits the data extremely well with an R² value over 0.99.

Once the chemical composition of the phases in the glass have reached the binary composition endpoints for a given heat treatment temperature, the volume occupied by each phase should remain constant as the larger areas of inhomogeneity grow at the expense of the smaller ones. The AFM data was analyzed with the use of bearing analysis to determine the percent of each phase present during the growth stage of spinodal phase separation. Bearing provides a method of plotting and analyzing the distribution of surface height over the entire AFM image area. Through the use of bearing analysis it is possible to determine the percentage of the surface, referred to as the bearing ratio, that lies above or below a user defined height. Bearing analysis is frequently used in silicon etching processes to observe changes in etched features over an interval of time, a similar application to the current situation.

As mentioned previously, the bimodal distribution that results from the differential etch rates of the more durable high silica phase and the less durable high alkali phase results in an easy determination for the location of the bearing depth. Figure 4.17 displays the bearing analysis, with the bearing depth set at the minimum point between the two nodes, for the glass of composition 12.5Na₂O*87.5SiO₂ heat treated for 1020 minutes at 650°C. The percentage of surface occupied by the high silica phase for heat treatment times that resulted in a clear bimodal distribution are listed in Table 4.3. The percentage of high silica phase is within one percent of 55 for all six times evaluated with the bearing software. This result is as expected, and demonstrates another important tool available for evaluation of phase separation through the use of AFM.

Table 4.3 Percent Area Due to High Silica Phase for $12.5\text{Na}_2\text{O}^*\text{87.5SiO}_2$
Heat treated at 650°C

Time (min)	% High Silica Phase
320	55
400	55.1
540	55.1
1020	54.2
1340	55.2
1565	54.1



Binary AFM Image
Average Grain Size - 14,340 nm²

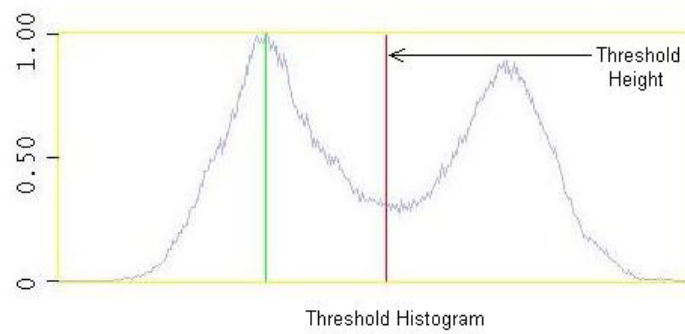


Figure 4.14. AFM Grain Size analysis for glass of composition 12.5Na₂O*87.5SiO₂ heat treated at 650°C for 1020 minutes.

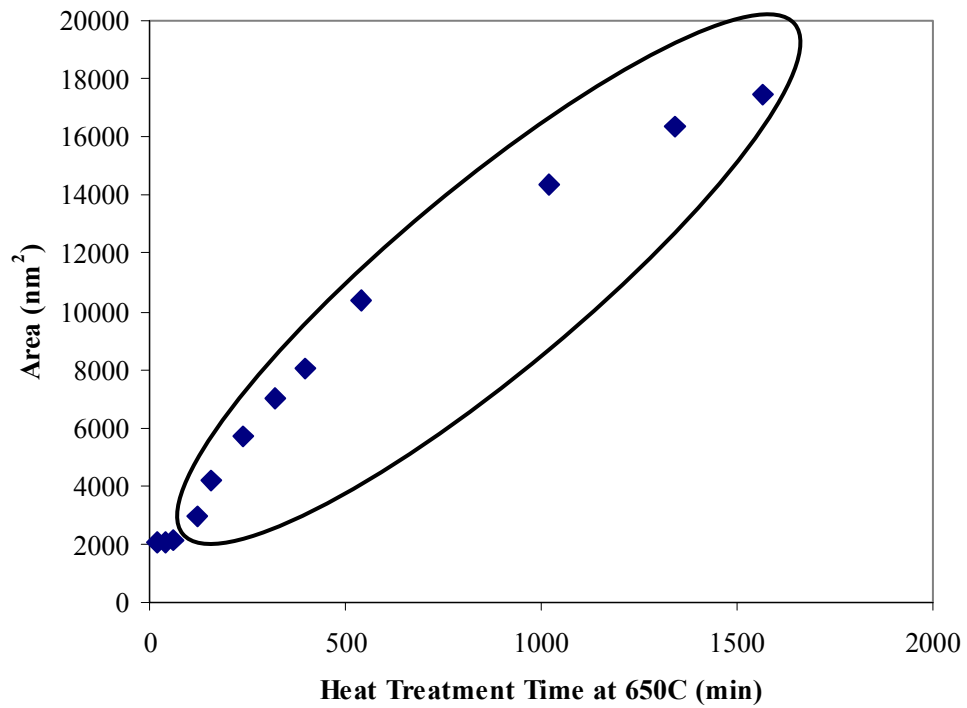


Figure 4.15. Average area of inhomogeneity as a function of heat treatment time at 650°C for glass of composition $12.5\text{Na}_2\text{O}*87.5\text{SiO}_2$.

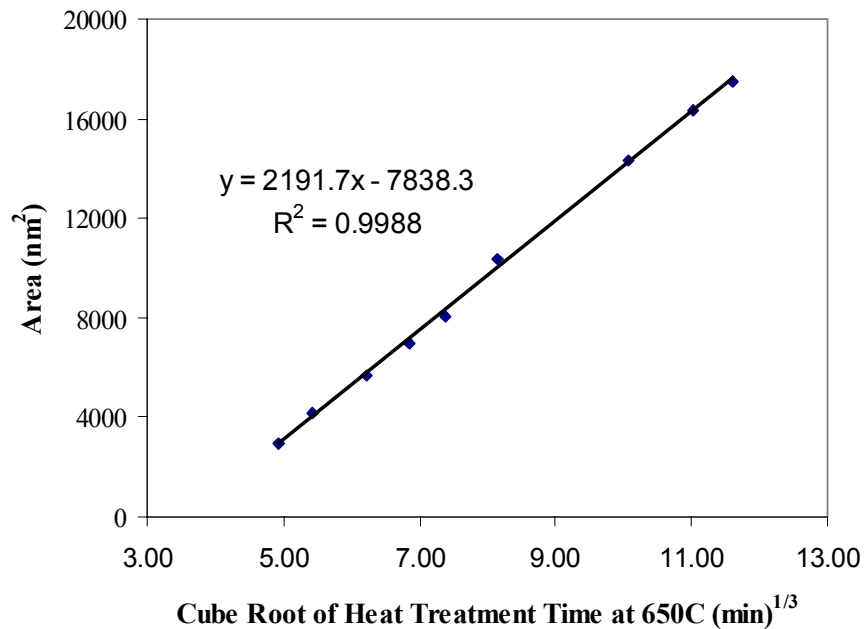


Figure 4.16. Average area of inhomogeneity, during ripening stage of spinodal decomposition, as a function of heat treatment time at 650°C for glass of composition $12.5\text{Na}_2\text{O}*87.5\text{SiO}_2$.

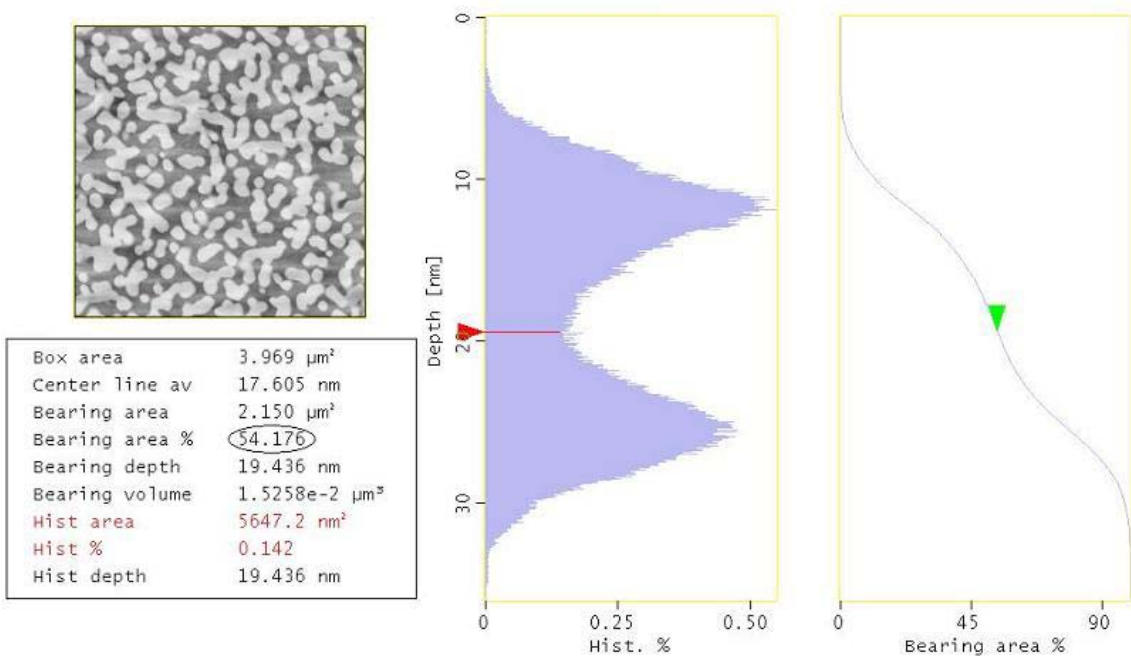


Figure 4.17. Results of bearing analysis for a 1020 minute heat treatment at 650°C for glass of composition 12.5Na₂O*87.5SiO₂.

Figure 4.16 displays the trend in the growth of the phases during spinodal decomposition for the sodium silicate glass studied. However the driving force for the ripening stage of spinodal decomposition is a reduction in interfacial area between the phases present. To calculate the interfacial area, the grayscale AFM images were converted to binary B/W images based on the local minimum in the height histogram curves generated with the use of the Nanoscope® AFM software (see Figure 4.14). The three-dimensional interfacial area was derived from the two-dimensional phase outline area through analysis of the B/W images. The analysis was performed with the use of Adobe Photoshop, The Image Processing Took Kit 5 by Reindeer Graphics, Inc., and was carried out by A. Fluegal.^{27,28} Figure 4.18 displays the outline of the interface between the silica rich and sodium rich phases for heat treatment times of 240, 540, 1020 and 1565 minutes. The percentage of area occupied by the pixels located at the interface between the two phases is listed in Table 4.4 for all images that showed clear bimodal distributions in image height.

The reduction in interfacial area is predicted to have a cube root of time dependence, due to the arguments stated above. Figure 4.19 is a plot of the interfacial area as a function of the cube root of heat treatment time at 650° (data from Table 4.4) for glass of composition 12.5Na₂O*87.5SiO₂. The trend is as predicted with a favorable R² value better than 0.98. This technique is straightforward and can routinely be used with AFM data to quickly and accurately determine the interfacial area when the distinction between the phases can clearly be determined.

Figure 4.20 is a three dimensional plot of the AFM image for a 12.5Na₂O*87.5SiO₂ glass heat treated at 650°C for 1020 minutes. The three dimensional view is another advantage of the high quality digital AFM data, that allows the scientist and the student to view phase separation in an easy to comprehend manner. Although not as quantitative as the work above, the 3-D view provides another avenue to view the evolution of phase separation in glasses.

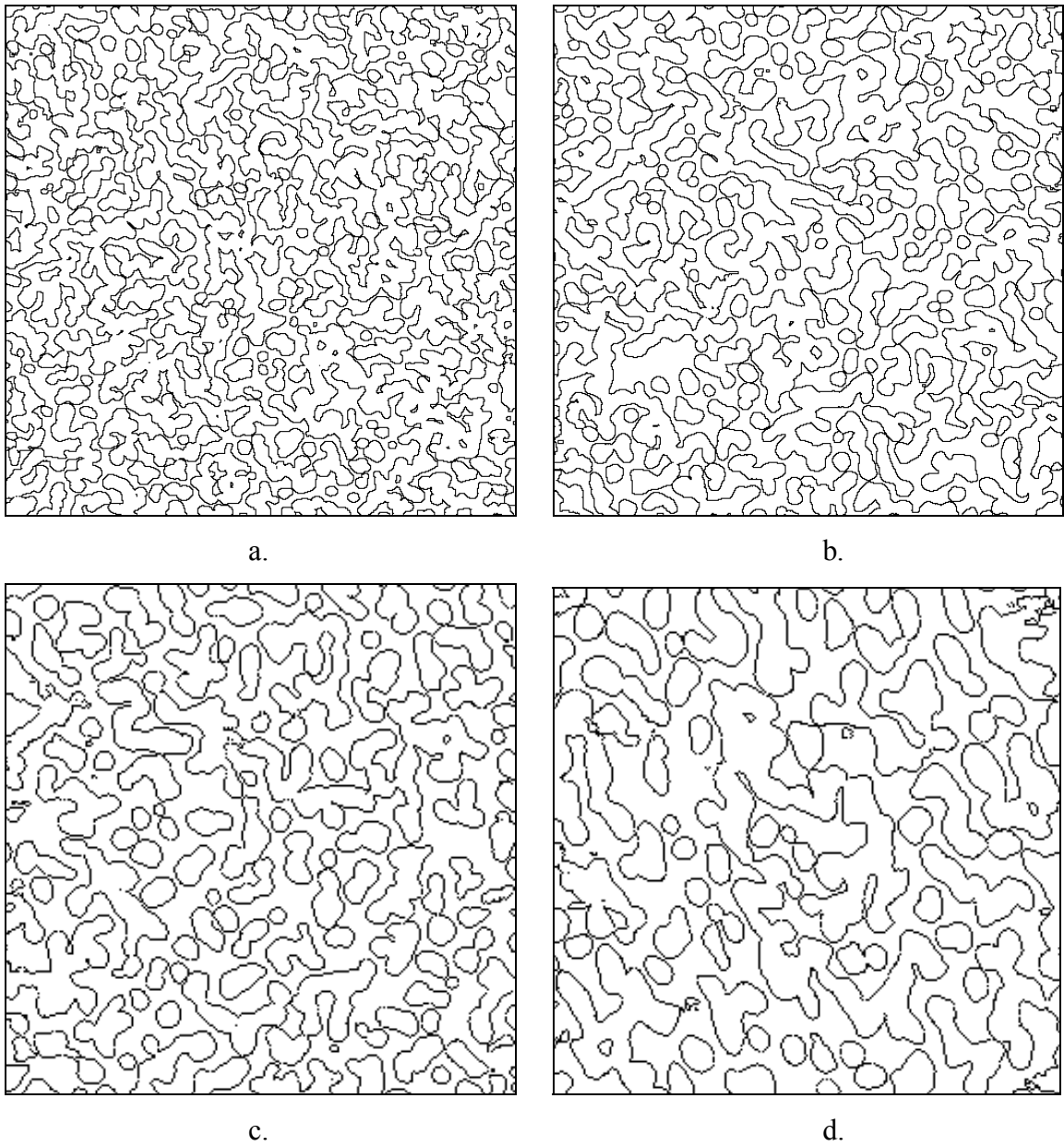


Figure 4.18. Image analysis routine of Fluegel showing the reduction of the interfacial area between silica rich and sodium rich phases for an isothermal heat treatment at 650°C. a) 650°C/ 240 min., b) 650°C/ 540 min., c) 650°C/ 1020 min., and d) 650°C/1565 min..

Table 4.4. Percent Interfacial Area for Various Heat Treatment Times at 650°C for Glass of Composition 12.5Na₂O*87.5SiO₂

Time (min)	%Interface
240	13.7
320	13.6
400	12.2
540	11.7
1020	8.8
1340	8.4
1565	7.3

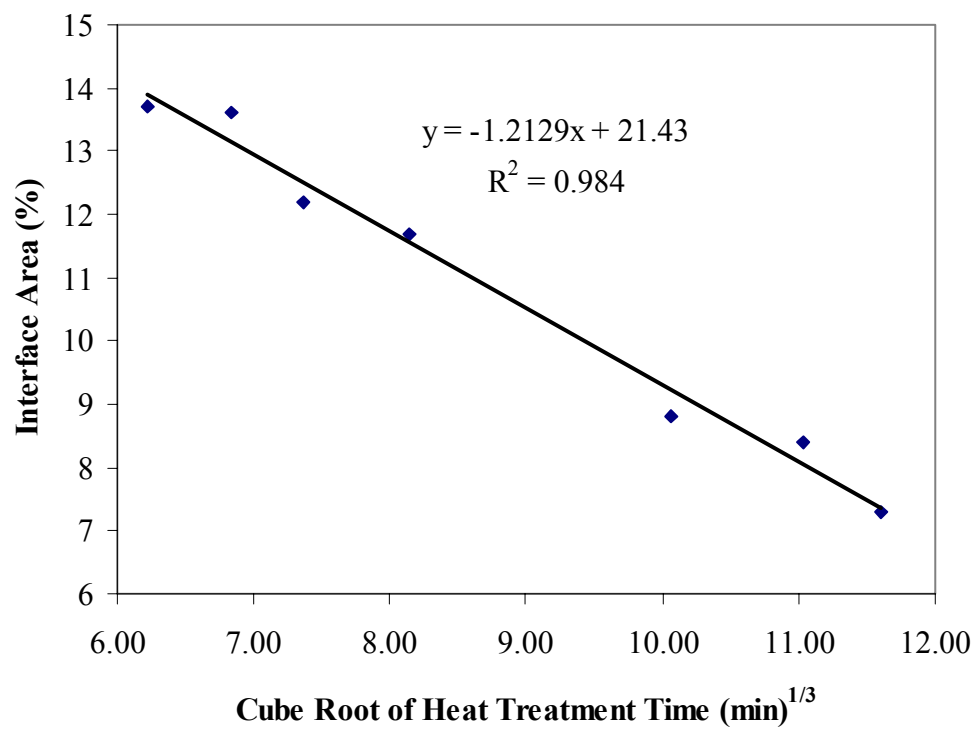


Figure 4.19. Trend in interfacial area, as determined by the routine of Fluegel, as a function of cube root of heat treatment time at 650°C for glass of composition 12.5Na₂O*87.5SiO₂.

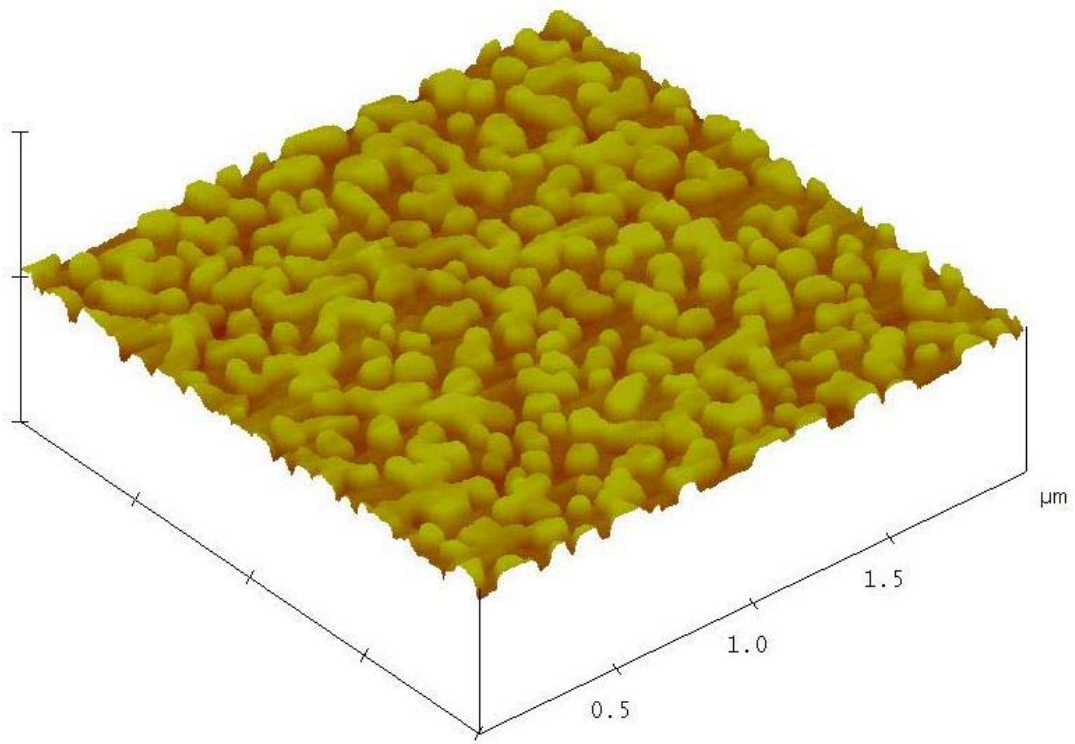


Figure 4.20. Three dimensional AFM image of $12.5\text{Na}_2\text{O} * 87.5\text{SiO}_2$ heat treated at 650°C for 1020 minutes.

4.5 Conclusions

AFM has been shown to be a powerful characterization tool for evaluation of liquid-liquid phase separation in glasses. Excellent correlation with previously published TEM data was achieved for both the sodium silicate and alkali borosilicate systems evaluated. Chemical and spatial variations during the phase separation process were easily followed with the AFM technique.

The characterization techniques traditionally used for evaluation of phase separation, such as TEM and SAXS are expensive, labor intensive and require specialized training for data interpretation. AFM on the other hand requires little sample preparation, is readily available, and analysis time can be as short as a few minutes. Although it is believed that most of the information necessary to evaluate the microstructure of phase separated glasses can be achieved through AFM analysis, the technique can also be used as a method for rapidly screening samples that require further analysis by more labor or instrument intensive characterization techniques.

4.6 References

1. J.E. Shelby, *Introduction to Glass Science and Technology*; pp. 48-68. The Royal Society of Chemistry, Cambridge, UK, 1997.
2. O.V. Mazurin and E.A. Porai-Koshits, *Phase Separation in Glasses*; p. 369. Elsevier Science, New York, 1984.
3. O.V. Mazurin, "Physical Properties of Phase Separated Glasses," *J. Non-Cryst. Solids*, **95-96** [1] 71-82 (1987).
4. M. Tomozawa, "Immiscibility of Glass Forming Systems," *J. Non-Cryst. Solids*, **84** [1-3] 142-50 (1986).
5. M. Tomozawa, V. McGahay, and J.M. Hyde, "Phase Separation of Glasses," *J. Non-Cryst. Solids*, **123** [1-3] 197-207 (1990).
6. D.R. Uhlmann, "Microstructure of Glasses: Does it Really Matter?," *J. Non-Cryst. Solids*, **49** [1-3] 439-60 (1982).
7. P.F. James, "Liquid-Phase Separation in Glass Forming Systems," *J. Mater. Sci.*, **10** [10] 1802-25 (1975).
8. J.W. Cahn, "The Initial Stages of Phase Separation in Glasses," *Phys. Chem. Glasses*, **6** [5] 181-91 (1965).
9. A.K. Varshneya, *Fundamentals of Inorganic Glasses*; pp. 61-84. Academic Press, San Diego, CA, 1994.
10. G.E. Rindone, K.T. Faber, B. Kumar, W.F. Olix, and J.F. Sproull, "Glass Microstructure Characterization by Laser Light Scattering, Small Angle X-Ray Scattering and Electron Microscopy," *J. Non-Cryst. Solids*, **49** [1-3] 253-62 (1982).
11. J. Zarzycki and F. Naudin, "Spinodal Decomposition in the B_2O_3 - PbO - Al_2O_3 System," *J. Non-Cryst. Solids*, **1** [3] 215-34 (1969).
12. J.E. Shelby and S.R. Shelby, "Phase Separation and Properties of Lithium Calcium Silicate Glasses," *Phys. Chem. Glasses*, **41** [2] 59-64 (2000).
13. S. Fujita, Y. Kato, and M. Tomozawa, "IR Peak Shift Due to Phase Separation of Na_2O - SiO_2 System Glasses," *J. Non-Cryst. Solids*, **328** [1-3] 64-70 (2003).
14. M.G. Mortuza, R. Dupree, and D. Holland, " ^{29}Si T_1 Relaxation in Alkali Silicate Glasses: A Method for Detecting Glass-in-Glass Phase Separation," *J. Non-Cryst. Solids*, **281** [1-3] 108-16 (2001).

15. L.S. Du and J.F. Stebbins, "Solid-State NMR Study of Metastable Immiscibility in Alkali Borosilicate Glasses," *J. Non-Cryst. Solids*, **315** [3] 239-55 (2003).
16. F.A. Sigoli, Y. Kawano, M.R. Davolos, and M. Jafelicci, Jr., "Phase Separation in Pyrex Glass by Hydrothermal Treatment: Evidence from Micro-Raman Spectroscopy," *J. Non-Cryst. Solids*, **284** [1-3] 49-54 (2001).
17. W. Haller, D.H. Blackburn, and J.H. Simmons, "Miscibility Gaps in Alkali-Silicate Binaries - Data and Thermodynamic Interpretation," *J. Am. Ceram. Soc.*, **57** [3] 120-6 (1974).
18. V. McGahay and M. Tomozawa, "The Origin of Phase Separation in Silicate Melts and Glasses," *J. Non-Cryst. Solids*, **109** [1] 27-34 (1989).
19. E.A. Porai-Koshits and V.I. Averjanov, "Primary and Secondary Phase Separation of Sodium Silicate Glasses," *J. Non-Cryst. Solids*, **1** [1] 29-38 (1968).
20. R.R. Shaw and D.R. Uhlmann, "Effect of Phase Separation on the Properties of Simple Glasses: I. Density and Molar Volume," *J. Non-Cryst. Solids*, **1** [6] 474-98 (1969).
21. W. Haller, D.H. Blackburn, F.E. Wagstaff, and R.J. Charles, "Metastable Immiscibility Surface in the System Na₂O-B₂O₃-SiO₂," *J. Am. Ceram. Soc.*, **53** [1] 34-9 (1970).
22. P.B. McGinnis, "The Effect of Hydroxy Content on Phase Separation in Sodium Silicate and Alkali Borosilicate Glasses"; M.S. Thesis. Alfred University, Alfred, NY, 1991.
23. Y. Moriya, D.H. Warrington, and R.W. Douglas, "A Study of Metastable Liquid-Liquid Immiscibility in Some Binary and Ternary Alkali Silicate Glasses," *Phys. Chem. Glasses*, **8** [1] 19-25 (1967).
24. M.O. Prado, A.A. Campos, Jr., P.C. Soares, A.C.M. Rodrigues, and E.D. Zanotto, "Liquid-Liquid Phase Separation in Alkali-Borosilicate Glass. An Impedance Spectroscopy Study," *J. Non-Cryst. Solids*, **332** [1-3] 166-72 (2003).
25. D.C. Boyd and D.A. Thompson, "Glass," pp. 807-80 in Kirk-Othmer Encyclopedia of Chemical Technology, 3rd ed., Vol.11. Edited by M. Grayson. John Wiley and Sons, New York, 1980.
26. T.P. Seward III, "Immiscibility and Microstructure in Amorphous Borates," pp. 427-43 in *Borate Glasses: Structure, Properties an Applications*. Edited by L.D. Pye, V. D. Frechette, and N. J. Kreidl. Plenum, New York, 1978.

27. A. Fluegel, C. Ruessel, "Kinetics of Phase Separation in a 6.5 Na₂O*33.5 B₂O₃*60 SiO₂ Glass," *Sci. Technol. (San Diego)*, **73** [3] 73-78 (2000).
28. A. Fluegel, I.M. Spinelli, W.C. LaCourse, "Study of the Kinetics of Phase Separation in 3.25 Na₂O*3.25 Li₂O/Na₂O*33.5 B₂O₃*60 SiO₂ Glasses by Skeletonization," *Ceram. Trans.*, **141**, 363-70 (2004).

Chapter 5

Thin Film Copper Oxide Layers Grown In-Situ on Alkali Borosilicate Glasses

5.1 Abstract

The formation of copper oxide films grown in-situ on the surface of copper containing alkali borosilicate glasses was studied. AFM was used to show that the thickness and uniformity of the copper oxide film increased with time and temperature, however an upper time limit was reached in which no further thickness increases were realized. Tenorite, cuprite and copper metal films were produced depending on the heat treatment environment. XPS was utilized to confirm the copper oxide film formation during heat treatments of glasses near T_g results from the oxidation of copper ions within the glass from the 1^+ to the 2^+ state. Copper ions migrate to the surface from the interior of the glass to balance the excess positive charge that results from the oxidation of Cu^+ to Cu^{2+} within the glass. The effect of alkali substitution was also studied, and the more acidic glass batches resulted in better film formation, as a result of the majority of the copper ions residing in the +1 state in the more acidid glass melts.

5.2 Introduction

5.2.1 Structure of Alkali Borosilicate Glasses

Many commercial glasses are based on alkali borosilicate systems, with the majority of glasses containing soda as the alkali oxide. Phase separation, often on a very fine scale, is prevalent in alkali borosilicate glasses, and although glasses are typically clear, the phase separation possibilities must not be ignored. There are two network formers in alkali borosilicate glasses, silicon and boron. The alkali may either enter the glass structure by association with silicon forming non-bridging oxygen (NBO) or with boron converting the boron atoms from triangular (Q_3) to tetrahedral (Q_4) coordination and creating no NBO's. NMR studies have shown that initially alkali prefers to associate with boron converting Q_3 groups to Q_4 .¹ The conversion of Q_3 groups to Q_4 groups will continue up to a Na_2O/B_2O_3 ratio of 0.5. Higher levels of alkali, depending on the ratio of Na_2O/B_2O_3 as well as SiO_2/B_2O_3 , will result in Q_3 , Q_4 as well as NBO as Soules and Varshneya demonstrated with the use of molecular dynamic simulations.² NMR was

again used to show that beyond a $\text{Na}_2\text{O}/\text{B}_2\text{O}_3$ ratio of 0.5 the fraction of NBO increases with increasing Na_2O content at fixed SiO_2 content and with increasing SiO_2 content at fixed $\text{Na}_2\text{O}.$ ¹

5.2.2 Copper in Glasses

Copper has been used as a colorant in glasses, glazes and pigments since ancient times, although the role copper plays as a former or modifier in the glass melt is not totally clear . Weyl states that under oxidizing melting conditions the Cu^{2+} ion is formed, while under reducing conditions and high melting temperatures the Cu^+ ion and/or Cu metal is formed.³ The divalent cupric ion forms color centers with different coordination producing colors from deep blue to green, and even brown. Cuprous ions, Cu^+ , on their own are colorless, however in combination with cupric ions they result in increased visible light absorption. When two oxides of an element in different valence states interact with each other they often produce a more intense color than if either valence state was present on its own. Equilibrium between different oxidation states of an element are affected in the same direction by melting temperature, and higher temperatures generally favor compounds where the element has a lower valency.³ For glasses containing copper, the majority of the copper ions will typically be in the cuprous state at typical melting temperatures, however the ratio of cuprous/cupric ions will be affected by glass chemistry and the acidity of the melt with the more acidic melts favoring the cuprous ion.⁴⁻⁶

5.2.3 Copper Oxide Films on Glass

Copper oxide has two main forms, depending on the oxidation state of the copper ions. Both forms of copper oxide are p-type semiconductors and conduct by copper vacancies. Cuprous oxide, Cu_2O , is a cubic crystal with a lattice parameter of 4.27 \AA and an energy band gap around 2.0eV. Cupric oxide, CuO , is a monoclinic crystal and has a lower energy band gap around 1.8 eV. It has been recently reported that CuO displays high-temperature superconductivity, where the specific coordination between Cu and O

atoms plays a crucial role.⁷ Copper oxides supported on suitable substrates are well known in the chemical industry as an oxidation catalyst and have been employed as catalysts for environmental processes such as NO selective reduction, CO oxidation and NO₂ decomposition.⁸⁻¹⁰ Copper oxide is also a promising semiconductor material for fabrication of photovoltaic devices such as solar cells.¹¹

Traditionally the deposition of copper oxide films on glass has been accomplished with reactive sputtering and vacuum evaporation techniques.^{12,13} Additional methods that have been reported for producing copper oxide films on glass surfaces including thermal and chemical oxidation of copper metal¹³⁻¹⁵, sol-gel chemistry,¹⁶⁻¹⁹ chemical deposition^{17,19} and plasma evaporation²⁰. In-situ production of copper oxide films on the surface of copper containing glasses have been reported for several glass systems, including aluminosilicates,²¹ lead aluminoborates,²² sodium silicates²³ and calcium aluminum borosilicates for which a patent was awarded in 1989.²⁴

5.3 Experimental Procedures

5.3.1 Sample Preparation

Alkali borosilicate glass batches with varying amounts of copper were batched with reagent grade boric acid, sodium carbonate, lithium carbonate, potassium carbonate, cupric oxide and floated silica. Table 5.1 lists the identification and composition of the glass batches that are discussed in this paper. Batch size was typically 50 grams and melting was carried out in DFC Ceramics S1 crucibles in an electrical resistance furnace. Table 5.2 provides the composition of the S1 crucible used for melting all glasses. Ceramic crucibles were necessary due to the high concentration of copper in the glasses, and the potential for the reduced copper alloying with the platinum, resulting in permanent copper contamination of the platinum crucibles. The glasses were melted in air between temperatures of 1350°C and 1450°C, and poured into a room temperature graphite mold.

Sample sections of annealed glasses were prepared by slicing with a diamond saw, followed by grinding and polishing to 1200 grit with silicon carbide embedded grinding paper. As-poured surfaces were also heat treated and analyzed when appropriate. The

glasses were heat treated in air at temperatures slightly below, at and slightly above T_g values that were determined by differential scanning calorimetry measurements. Heat treatment times varied from one hour to several days.

Heat treatments were also carried out near T_g in a hydrogen atmosphere as well as in a vacuum. Polished glass samples were placed in a silica tube on an aluminum foil setter near the end of the thermocouple. For the hydrogen treatment, a preheated furnace was placed around the tube and the tube was evacuated. Once the sample reached the heat treatment temperature, hydrogen was admitted into the tube. At the end of the heat treatment time the tube was evacuated and then vented back to ambient. For the vacuum treatment the furnace was equilibrated to 520°C and pulled over the sample and the vacuum was pulled immediately. The vacuum was better than 10 millitorr for the duration of the heat treatment which lasted 143 hours, after which the furnace was removed and the sample was cooled to room temperature before the tube was vented back to ambient.

Table 5.1 –Composition of Glass Batches Studied (Mole %)

Table 5.2 – Compostion of S1 Ceramic Crucible

Oxide	Weight %
SiO ₂	82.8
Al ₂ O ₃	14.9
Fe ₂ O ₃	0.5
TiO ₂	0.3
CaO + MgO	0.23
Na ₂ O + K ₂ O	0.8

5.3.2 Ultraviolet-Visible Spectroscopy (UV-Vis)

UV-Vis absorption and reflection spectra of polished samples and heat treated surface samples were measured on a Perkin Elmer Lambda 900 UV-Vis dual beam spectrometer. Air was used as the reference material for absorption measurements and spectra were measured over a wavelength range of 200 to 800 nanometers. The spectral reflectance stage was utilized with the long, narrow mask for spectral reflectance measurements. A baseline was established with the reflectance standard prior to the spectral reflectance measurements from 200 to 1000 nm.

5.3.3 Scanning Electron Microscopy (SEM)

Film thickness and microstructure images along with elemental information about the copper oxide films were collected using a Leo Gemini Model 1550VP variable pressure field emission SEM. The Gemini system was equipped with an in-lens multipurpose secondary detector, and a Robinson backscatter detector. Energy dispersive X-ray analysis was used to determine elemental information with the use of IXRF software.

The advantage of the field emission source is that it generates a high brightness nanometer size probe which yields high resolution images even at low accelerating potentials. Accelerating potentials as low as 5 kV were utilized to generate the most surface sensitive SEM images possible. The interaction of the beam with the sample generates a variety of signals, with the most commonly used being secondary and backscattered electrons. These signals are detected and reconstructed into a virtual image, which is displayed on a monitor. The low energy secondary electrons produce the best imaging resolution because they are generated near the surface of the specimen.

5.3.4 Differential Scanning Calorimetry (DSC)

Glass transition temperatures and crystallization onset temperatures were measured using a TA Instruments Q10 DSC. Indium, tin and zinc were used to temperature calibrate the instrument. Approximately 10 mg samples were taken from the center of the bulk glasses, and open platinum pans were utilized for the sample and reference(empty). The cell temperature was equilibrated at 100°C prior to a ramp at 10 K/min from 100 to 600°C. A constant nitrogen flow rate of 50 mL/min was used to purge the DSC cell during each heating cycle. T_g and crystallization onset temperatures were determined with the use of TA Universal Analysis Software using the slope-intercept method.

5.3.5 Thermo-gravimetric Analysis (TGA)

A TA Instruments TQ50 Thermogravimetric Analyzer was utilized to examine the weight gain associated with surface oxidation of the copper containing alkali borosilicate glasses. Approximately 100 mg of powdered glass sample was placed in a platinum pan, and an empty platinum pan was used as a reference for each heat treatment. A gas flow rate of 60 mL/min was used to purge the sample chamber while a flow rate of 40 mL/min was used to purge the balance. The kinetics of the weight gain in atmospheres of both air and nitrogen were studied for isothermal holds at 500°C.

5.3.6 X-Ray Diffraction(XRD)

Crystalline phases were determined by XRD with the use of Philips X-Ray Diffraction systems operating at a power of 40 KV and 30 ma. Jade® software was utilized to identify peak positions and crystalline compounds present with the use of chemistry filters. Samples requiring analysis of bulk crystallization were ground and back-filled into standard holders. Samples requiring analysis of surface crystallization were analyzed with the use of bulk sample holders, with the sample surface positioned at the center of the goniometer circle.

5.3.7 Atomic Force Microscopy (AFM)

A Digital Instruments Dimension 3100 Scanning Probe Microscope with a Nanoscope IIIA controller was used in TappingMode® to produce three-dimensional topographical images of as melted and heat treated surfaces. Pyramidal etched silicon probes with a half cone angle of 18° and an approximate radius of curvature of 10nm were used for all measurements. Scan sizes required to evaluate the microstructure of the copper oxide films varied from one micron square to several microns square depending on the spatial variation of a particular sample.

TappingMode® AFM images are generated by scanning a very sharp probe tip, on the end of an integrated cantilever that is oscillated at or near its resonance frequency, in a raster pattern over the sample surface while lightly “tapping” on the surface. The motion of the tip above the sample is controlled by a piezoelectric tube scanner, and the tip-sample interaction is monitored by reflecting a laser off the top of the cantilever into a split photodiode detector. An electronic feedback circuit, between the photo-detector and the z-piezo, maintains the tip oscillation at a constant set-point amplitude during scanning by moving the scanner vertically at every x,y data point. The three dimensional digital image is produced by mapping the motion of the z-piezo required to maintain a constant oscillation amplitude at each lateral data point.

Phase images were also generated simultaneously with the topographical images by monitoring the phase of the oscillating cantilever with the use of the Phase Extender

Module. Phase Imaging is a powerful extension of TappingMode® AFM that provides nanometer scale resolution about surface structure and properties that may not be revealed by simple topography.²⁵ Phase images provide image contrast based on a differential interaction between the tip and the sample surface. Phase images have limited sensitivity to surface topography but provide contrast based on adhesion, hardness, friction, viscoelasticity, and composition as well as other properties.

The AFM silicon cantilever is excited into resonance oscillation with a piezoelectric driver and the oscillation amplitude is used as the feedback signal to measure surface topography of the sample. The phase lag of the cantilever oscillation relative to the drive signal is monitored by the Phase Extender Module to provide the simultaneous phase image. The topography and phase image are viewed and collected simultaneously in real time. Phase imaging can often highlight edges and is not affected by large-scale height differences providing good grain boundary contrast even when a rough surface is being imaged.

The AFM was also used to carry out electrical force microscopy (EFM) measurements of the copper oxide films. EFM is a special AFM technique that characterizes sample surfaces based on electrical properties. A conductive AFM tip interacts with the sample through long-range Coulomb forces, which affect the oscillation amplitude and phase of the AFM cantilever. EFM images are collected in LiftMode™ which is a two-pass technique that separates topographical information from the electrical response. For each separate scan line, the topographical data is recorded in normal TappingMode® as described above. A second pass of the known topography is made with the tip lifted a given height above the sample surface, usually in the 10-100 nm range. The tip to sample separation is constant during the second pass and only the longer range electrical forces affect the oscillation of the cantilever. Figure 5.1 is a simple schematic of AFM operated in LiftMode™ where the dark regions near the surface are regions of the sample that symbolize the source of contrast in the EFM image.

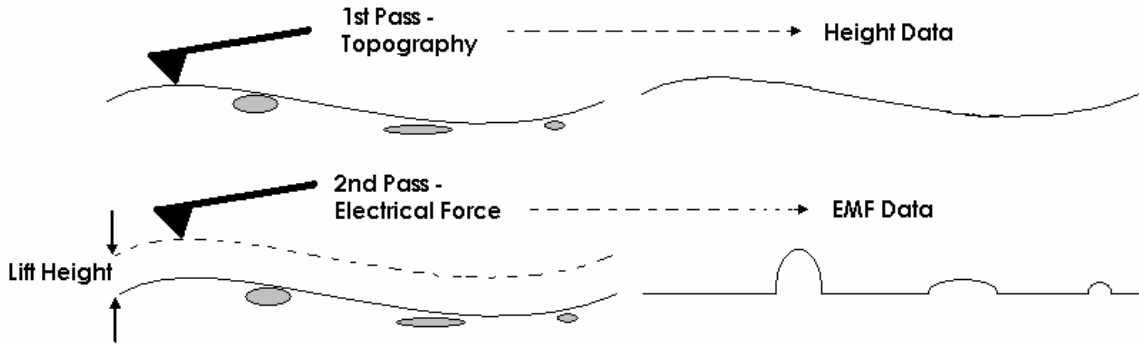


Figure 5.1. Schematic of EFM image collection in LiftModeTM.

To determine the thickness of the films by AFM, a special sample preparation technique was utilized. The low speed, precision saw was used to create a small, thin region of specimen that contained the glass/film interface. Just prior to AFM analysis the specimens were fractured under slight tension, producing a cross section that could be evaluated out to the very edge of the film. Figure 5.2 displays a schematic of the specimen preparation for AFM evaluation of film thickness. The fracture pattern provides topography to the film region, allowing for straight forward determination of the glass/film interface. The film/air interface is also easily determined from the rapid drop of the AFM image at the specimen edge.

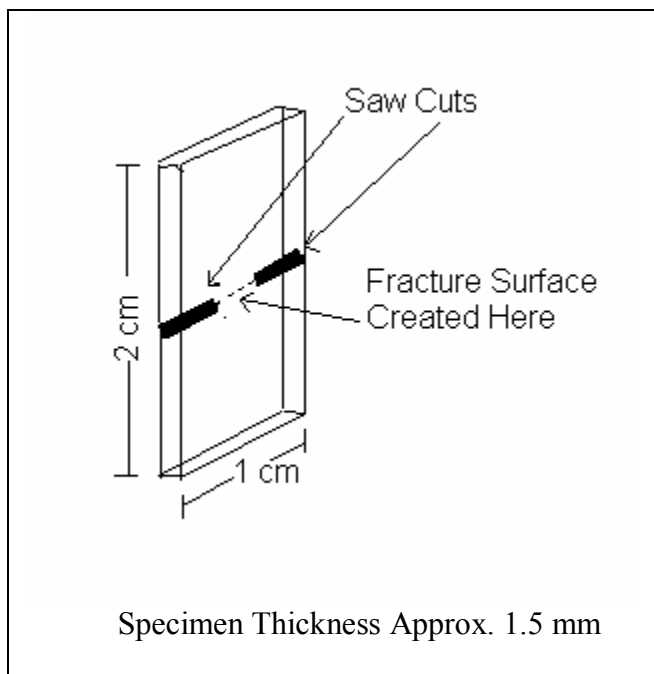


Figure 5.2. Geometry used to prepare high quality fracture cross sections of the film/glass interface for thickness determination via AFM.

5.3.8 X-Ray Photoelectron Spectroscopy (XPS)

A Physical Electronics Quantum 200 Scanning XPS Microprobe was used to acquire XPS elemental surveys and high-resolution spectra of the bulk glasses. Elemental information was also collected on the copper oxide films as a function of sputter depth from the surface. Monochromatic Al radiation was used as the excitation source and charge neutralization was employed due to the insulating properties of the glass substrate. The atomic concentrations were calculated using high-resolution data acquired for the elements detected in the elemental surveys.

To evaluate the copper oxide films, the sample specimen surfaces were first examined as received followed by a sputter depth composition profile down to the base glass composition. To evaluate the bulk compositions of the as melted glasses, the bulk glass samples were fractured, prior to introduction into the vacuum chamber, and the fractured surfaces were analyzed.

5.4 Results and Discussion

5.4.1 Initial Characterization of Glass Lab Sample

A glass melt that was batched and melted during an Alfred University Glass Lab session resulted in a shiny, silver colored and metallic looking thin film on the surface upon cooling from the melt. The batching had obviously been carried out incorrectly, as the glass was targeted to be a simple soda lime glass with a copper colorant. The well adhered film was of interest to current research as a possible thin film coating for NSOM fibers, so evaluation of the glass and film were carried out with SEM, XRD, XRF, AFM and UV-Vis.

To determine the make-up of the thin film a combination of SEM and XRD was completed. SEM analysis was carried out to determine the film thickness and to qualitatively determine the elemental make-up of the glass and film. A fracture surface was carbon coated to avoid charging and examined in the SEM at an accelerating potential of 20 kV. Figure 5.3 is an “over-the-edge” view of the glass/film interface. The average atomic number of the film is considerably higher than the bulk glass resulting in the film being brighter in the SEM image. The film thickness was estimated to be 25 nm from the SEM images.

Scrapings from the film surface of the glass were dusted onto a SEM sample stub that was covered with double sided carbon tape. Any particles that were not adhered well to the carbon tape were removed with compressed air. Glass chips that were film side up were bright and smooth in the SEM images, while chips that were glass side up were dark and their surface morphology exhibited fracture patterns. Energy Dispersive X-Ray (EDX) analysis was completed on both the glass side and film side of the chips. Due to the thin nature of the films, EDX was carried out at a lower accelerating potential of 10 kV. The lower accelerating potential results in a smaller interaction volume of the electrons with the sample, therefore resulting in a higher percentage of secondary electrons originating from the film itself. Figure 5.4 displays the results of the EDX analysis collected from the bulk glass and the film surface. The major elements in the glass were shown to be Si, O, Al, Ca, Pb, Cu and possibly K. The main difference in the EDX results of the film versus the bulk glass is the dramatic increase in the level of

copper in the film, when compared to the bulk. Even with the lower accelerating potential a considerable amount of secondary electrons will be generated from the glass beneath the film, resulting in the bulk glass composition showing up in the EDX analysis of the film surface. These EDX results therefore indicate that the film consists of a crystalline component with a high level of copper.

Initial XRD measurements were made on a powdered sample that was scraped from the surface of the specimen, and mounted onto a zero background single crystal holder. However, due to the thin nature of the film and its good adhesion to the glass body, too much glass was removed during the sampling process, and only an amorphous halo was realized in the XRD trace. The film surface of the glass was flat allowing for a surface XRD measurement. A bulk section of the specimen was sampled and mounted into a bulk sample holder, with the film surface of the specimen at the sample plane of the goniometer circle. A continuous XRD trace was completed from 5 to 70 degrees two theta with a 0.03 degree step and a one second dwell time. The results of the XRD analysis are displayed in Figure 5.5. Although the intensity of the crystalline peaks was still low, it was determined from the XRD analysis that the film was copper oxide, CuO also known as the mineral Tenorite. Copper Oxide, CuO, is a p-type semiconductor with a band gap around 1.75 eV, corresponding to an optical absorption threshold of approximately 700 nm.¹⁷ Therefore this low band gap semiconductor reflects the majority of the visible spectrum resulting in the shiny, metallic like appearance.

AFM was used to evaluate the surface of the copper oxide thin film formed on the Glass Lab specimen. Figure 5.6 is an AFM top view and section analysis of a 100 square micron area of the as-formed thin film surface. The copper oxide grain size was estimated to be between 100 and 200 nm from the AFM image. The average surface roughness (Ra) was 5.0 nm, and the Rz, which provides an indication of the maximum peak to valley distance, was determined to be 23 nm.

The composition of the bulk glass was determined quantitatively with the use of X-Ray fluorescence (XRF). Table 5.3 lists the results of the XRF analysis in weight percent as well as mole percent. The XRF results show that the glass contained sodium, which is masked by other elements in the SEM analysis, as well as a low level of magnesium and confirmed the presence of a low level of potassium.

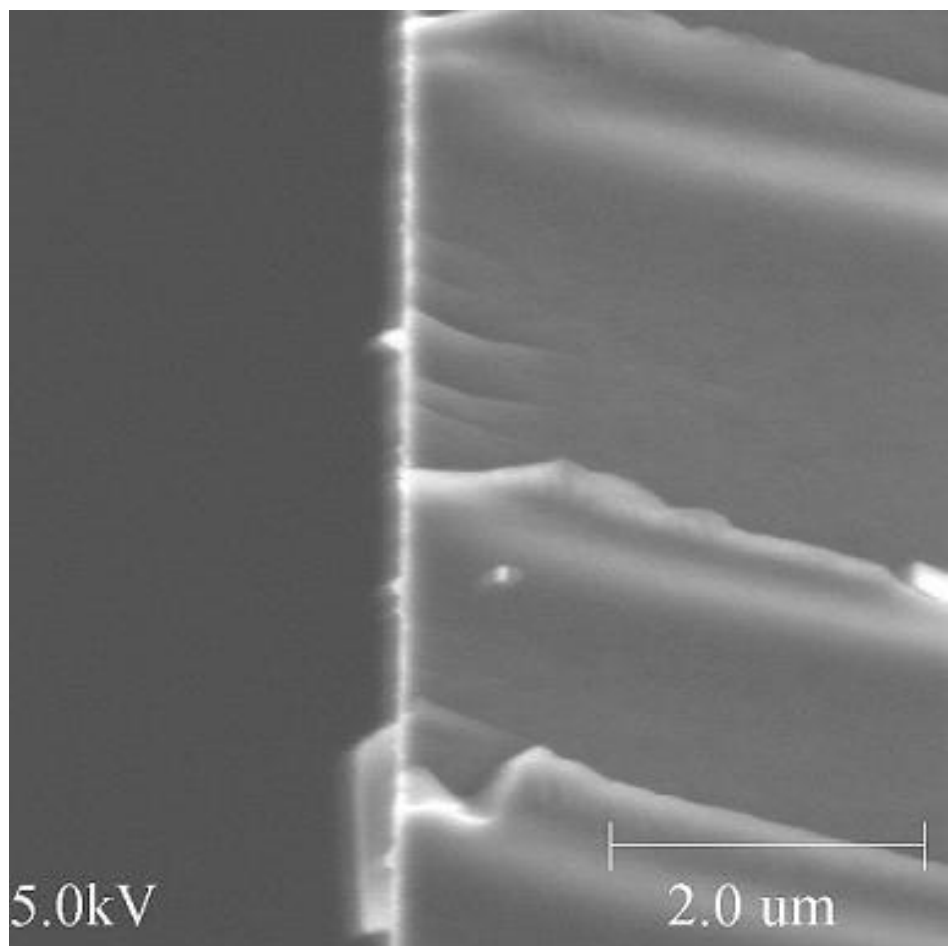


Figure 5.3. SEM image of “over-the-edge” fracture surface of Glass Lab specimen.

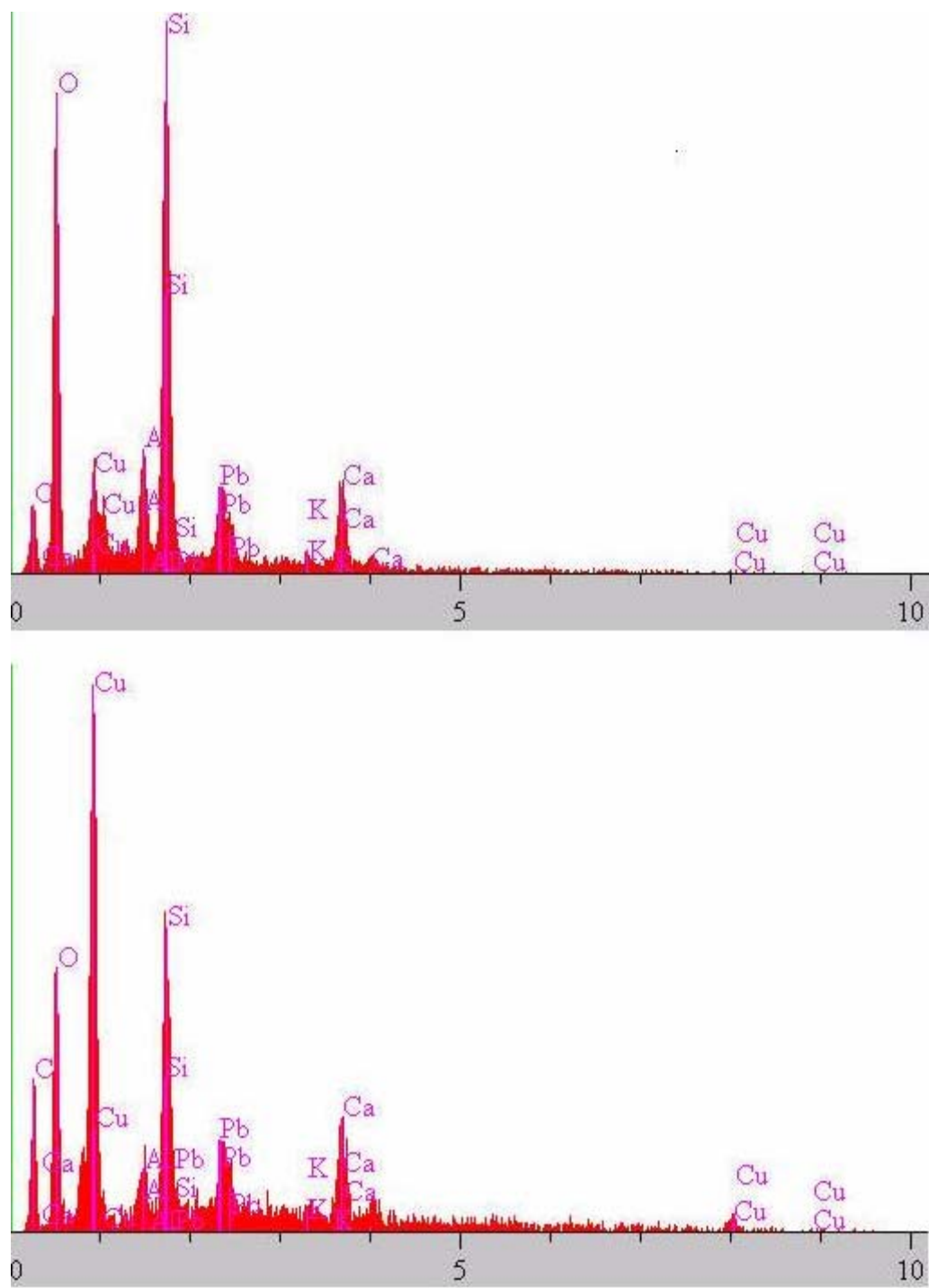


Figure 5.4. EDX analysis of bulk glass and film surface (10kV).

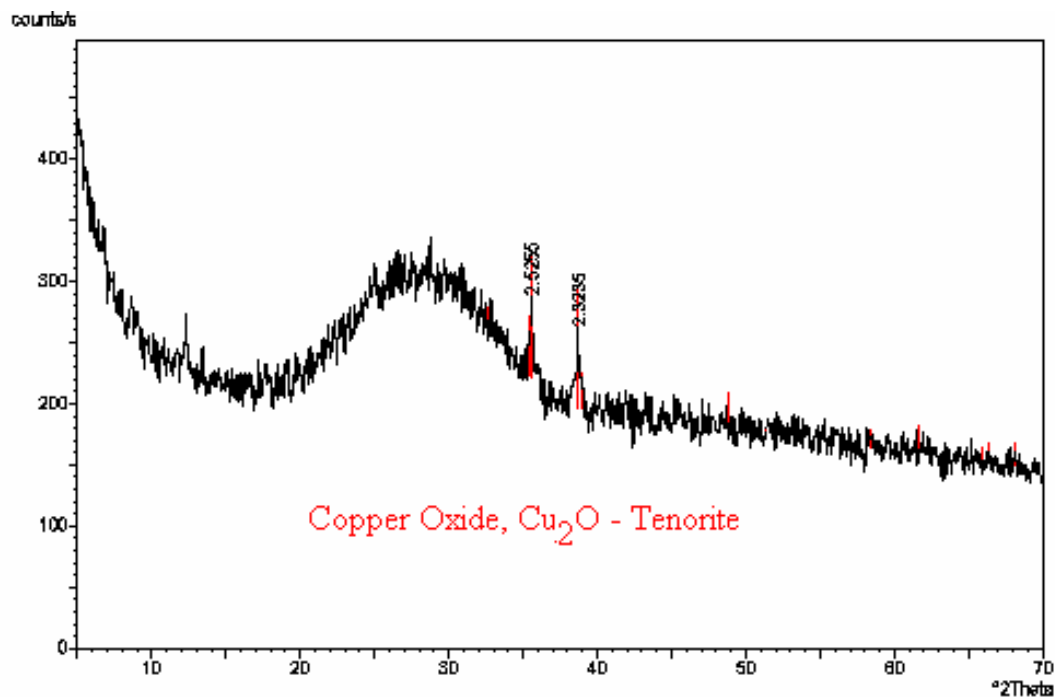


Figure 5.5. Surface XRD trace of Glass Lab specimen thin film.

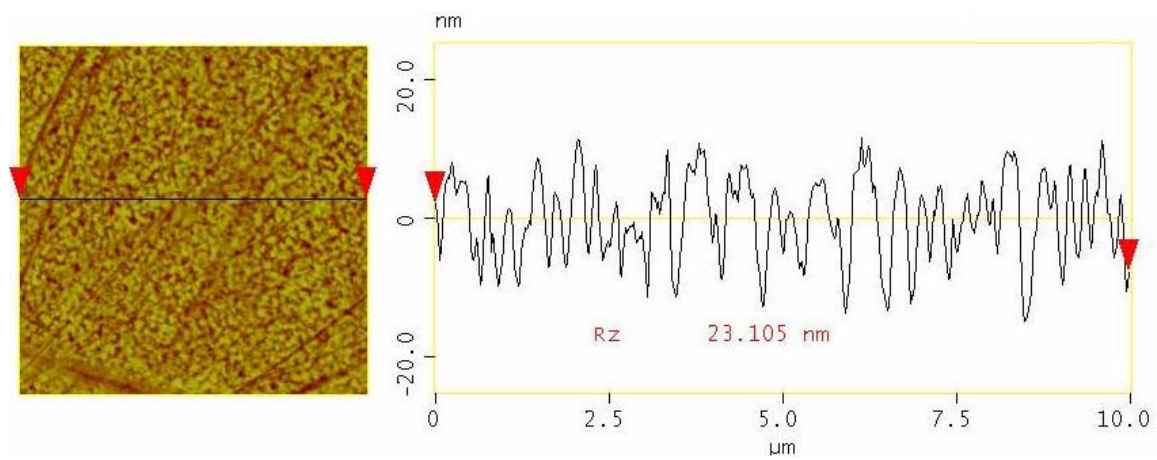
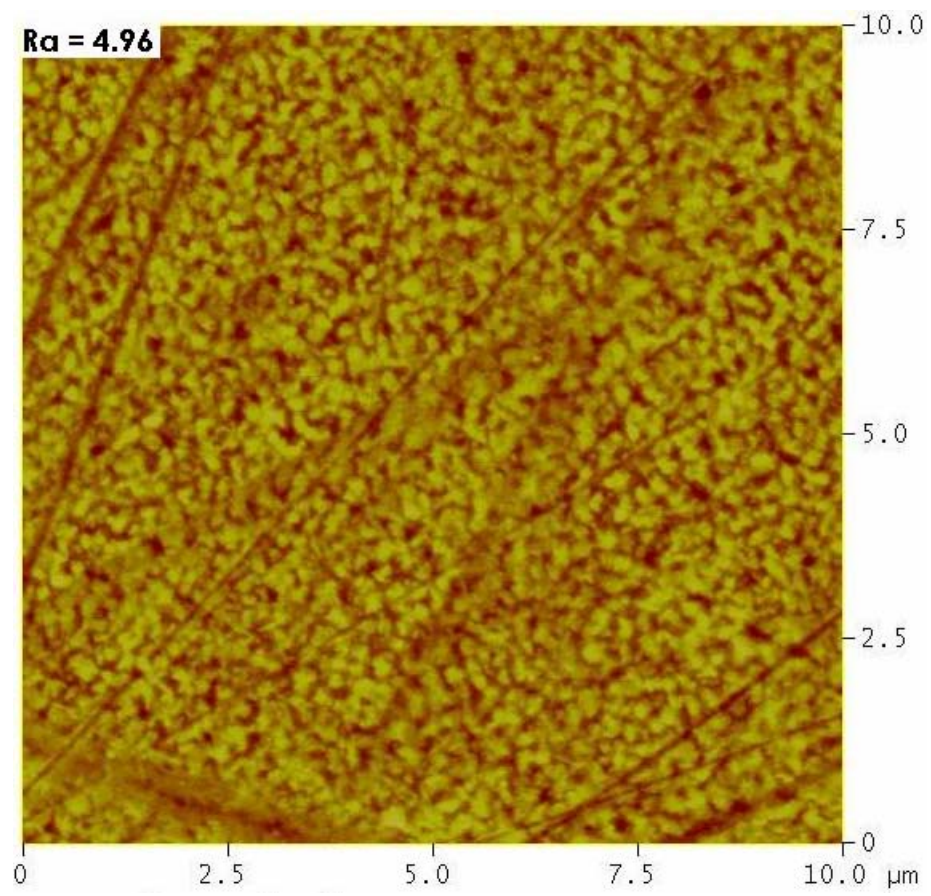


Figure 5.6. Results of AFM analysis of thin film formed on Glass Lab Specimen.

Table 5.3. Bulk Composition of Glass Lab Specimen

Compound	Weight Percent	Mole Percent
SiO ₂	43.9	51.9
CaO	21.0	26.5
PbO	16.0	5.1
Al ₂ O ₃	7.6	5.3
CuO	7.1	6.3
Na ₂ O	2.6	3
K ₂ O	1.3	1
MgO	0.5	0.9

5.4.2 Characterization of Glass Batch CU090403

The results of the XRF analysis listed in Table 5.3 were used to melt a glass of similar composition to the Glass Lab specimen. Glass composition CU090403 was melted at 1200°C for 1 hour, quenched, pulverized and re-melted at 1375°C for an additional 30 minutes before quenching onto a steel plate. Although there was no visible evidence of a copper oxide film upon quenching from the melt, annealing the glass at 600°C resulted in an excellent copper oxide film that exhibited high reflectivity. Surface XRD measurements were completed on both an as melted surface and a heat treated surface of glass CU090403. XRD did not detect any significant film formation for the as melted glass, however copper oxide (CuO) was identified on the surface of the heat treated glass surface. The result of the surface XRD measurement on glass composition CU090403 heat treated for 10 hours at 600°C is displayed in Figure 5.7.

Spectral reflectance data showed that the reflectance of the sample surface of glass CU090403 increased considerably after the formation of the copper oxide film. Figure 5.8 displays the spectral reflectance results of as melted glass of composition CU090403, compared to the same sample specimen after a 10 hour heat treatment at 600°C. With the spectral reflectance stage employed, the percent transmission is related to the reflectivity of the surface. Figure 5.8 shows that the surface reflectance increased

by nearly 2X through the majority of the visible region with the copper oxide film present. The maximum in the reflectance curve occurred at approximately 600 nm.

SEM and AFM analysis were completed on glass CU090403 to further evaluate the surface of the glass before and after heat treatment. Figure 5.9 displays SEM and AFM results of the as melted surface of glass CU090403. Although XRD did not show any significant surface crystallization, both the SEM and AFM images show small islands of surface crystals separated by a continuous glass matrix. The InLens multipurpose secondary electron detector was utilized on the Hitachi FESEM in order to provide the surface sensitivity and contrast necessary to image the small, thin surface crystals. The average roughness (R_a) of the 100 square micron AFM image was calculated to be 3.5 nm. Figure 5.10 shows additional, higher resolution AFM images used to estimate the size of the isolated crystalline areas. The size of the crystalline regions were estimated to be approximately 50-75 nm in diameter and AFM section analysis determined their average height above the surface to be 7 nm.

Figure 5.11 displays a series of SEM images of glass CU090403 after heat treatment for 10 hours at 600°C. In addition to the SEM analysis of the heat treated surface, an “over-the-edge” view of a cross-section was completed to estimate the thickness of the copper oxide film. The top left SEM image is a low magnification overview of the heat treated surface collected with the highly surface sensitive in-lens detector. This image shows discontinuous dark regions 10 to 20 microns in diameter dispersed among a continuous brighter matrix. The top right SEM image was collected with the normal secondary electron detector, which is much less surface sensitive, and results in a larger interaction volume compared to the in-lens detector. The darker regions are only slightly visible in this image, therefore providing evidence that the contrast in the first image is the result of surface variation and not variation in the composition of the bulk glass.

The bottom left SEM image in Figure 5.11 is a higher resolution image of the interface between the dark and light regions of the heat treated surface. The porosity of the copper oxide film appears to be higher in the dark regions, which would cause the average atomic number of the dark regions to be lower than the light regions, due to more of the secondary electrons originating from the base glass. No significant differences

were observed in the EDX analysis of the light and dark regions. The bottom right SEM image in Figure 5.11 is an “over-the-edge” view of the fracture surface. The horizontal distance between the white lines drawn on the SEM image estimates the copper oxide film thickness to be approximately 370 nm.

AFM was also completed on the heat treated sample surface of glass CU090403, allowing for an estimation of the grain size and to quantify the surface roughness of the glass. Figure 5.12 displays a top view image for a 100 square micron area of the heat treated glass, and a 3-D view of a 4 square micron area. The grain size was estimated from the higher magnification image to be approximately 100 nm, while the average surface roughness, Ra, was determined to be 8.3 nm. The surface roughness is more than double the surface roughness of the as melted glass surface which was determined to be 3.5 nm. The increased surface roughness can be easily visualized by comparing the 3-D images in figures 5.9 and 5.12 which have the same z range associated with them. The peak to valley distance, Rz, increased from 17.7 nm for the as melted surface to 46.4 nm for the much rougher surface of the glass heat treated at 600°C for 10 hours.

The possibility for producing highly reflective, semi-conducting glass micro-spheres from this series of copper containing glasses was briefly explored. Applications for reflective glass micro-spheres include paint pigments for road signs. The semi-conducting properties of the copper oxide films may also present applications for the glass micro-spheres that have not yet been thought of. Glass micro-spheres were prepared from glass composition CU090403. The bulk glass was ground with a mortar and pestle and the fraction of glass fragments that were greater than 44μ but less than 125μ were selected for producing the micro-spheres. The method used for producing micro-spheres from the ground glass is described in the thesis of Matt Hall²⁶, and will not be elaborated on here. Figure 5.13 displays the as-formed micro-spheres, as well as micro-spheres heat treated at 600°C for 24 hours. The surface of the as-formed spheres shows no signs of crystallization, while the heat treated spheres clearly exhibit sparse clusters of surface crystals with lathlike morphology. The high temperature of the flame used in the process for making the glass micro-spheres has a good chance of changing the glass chemistry near the surface, due to volatilization of glass constituents, which may change the dynamics of the crystallization process, when compared to the bulk glass.

Due to the hazards associated with lead containing glasses alternative composition were explored to further study and characterize the development of copper oxide semiconductor surface films formed by heat treating copper containing glasses. A much less complicated alkali borosilicate glass was used to carry out further research of the copper oxide film formation.

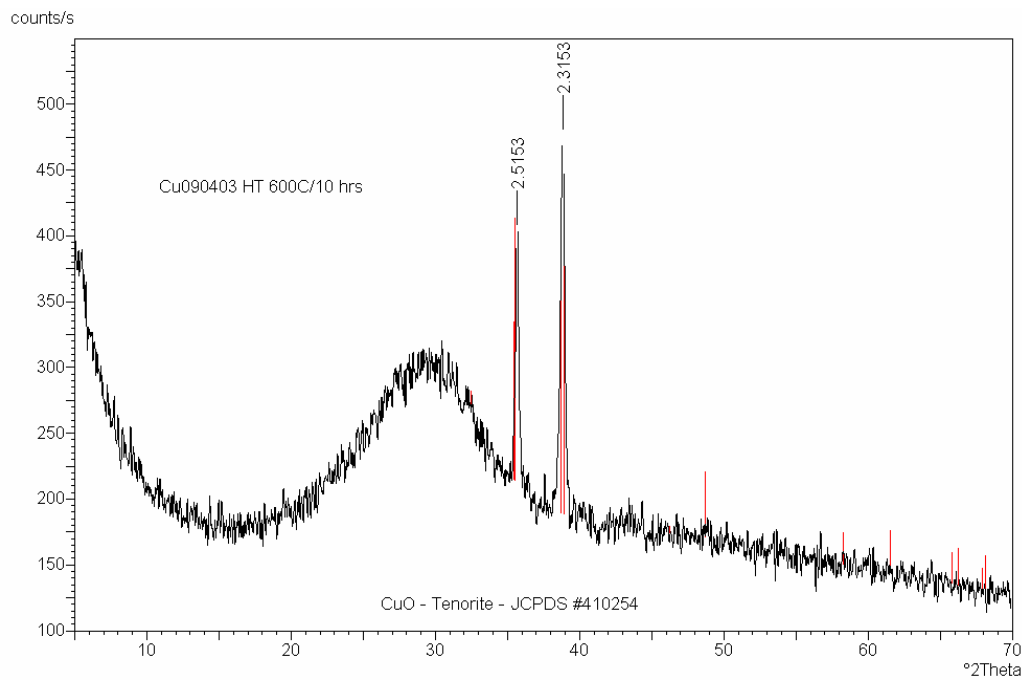


Figure 5.7. Surface XRD results of glass CU090403 after heat treatment at 600°C for 10 hours.

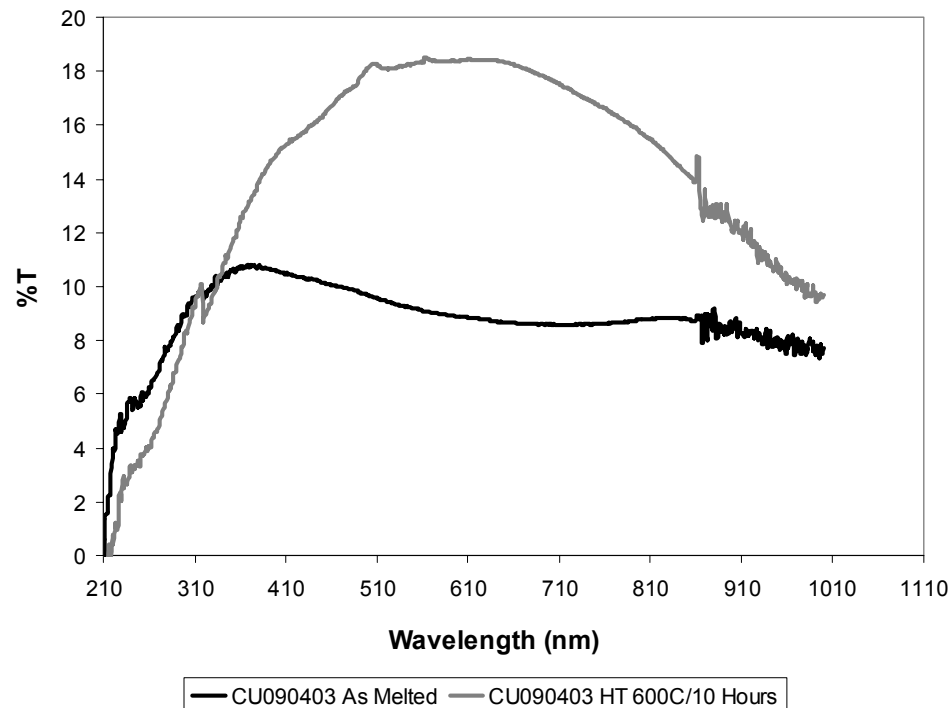


Figure 5.8. Spectral reflectance results of glass CU090403 as melted and after heat treatment at 600°C for 10 hours.

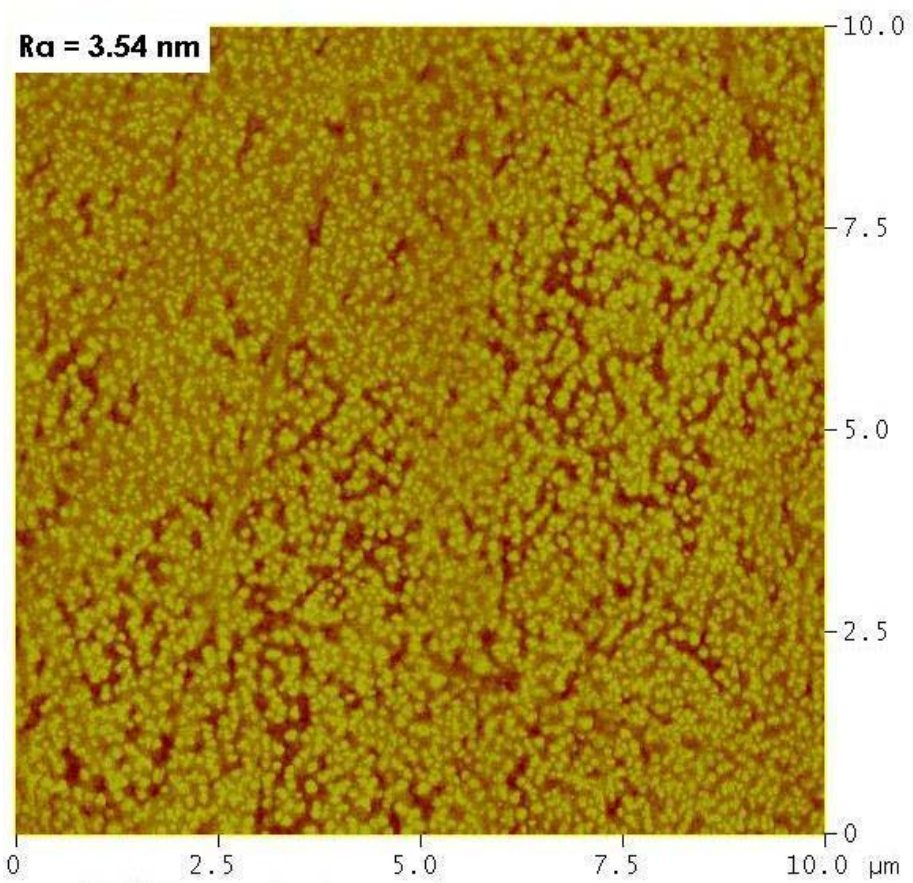
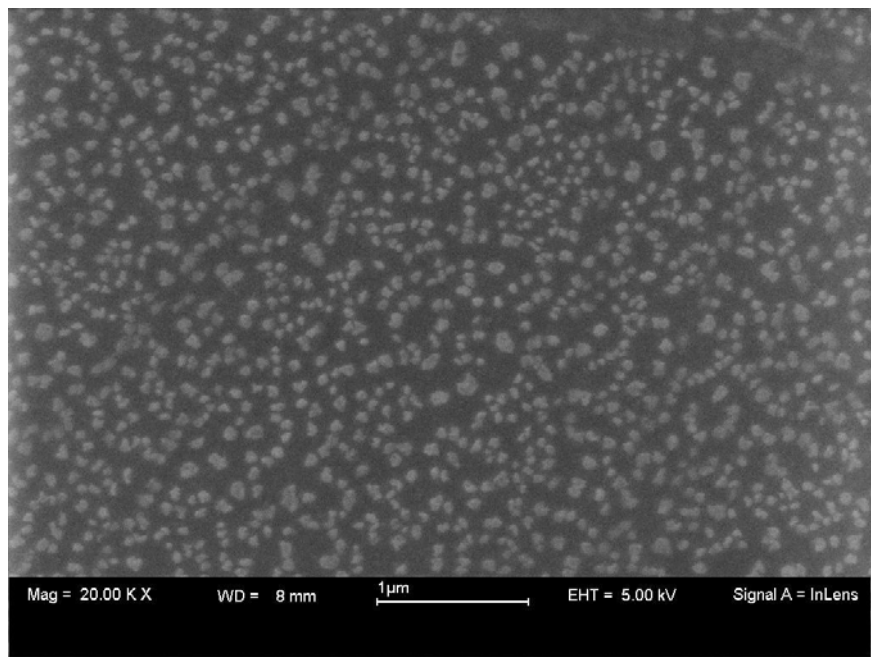


Figure 5.9. SEM and AFM results of the as melted surface of glass CU090403.

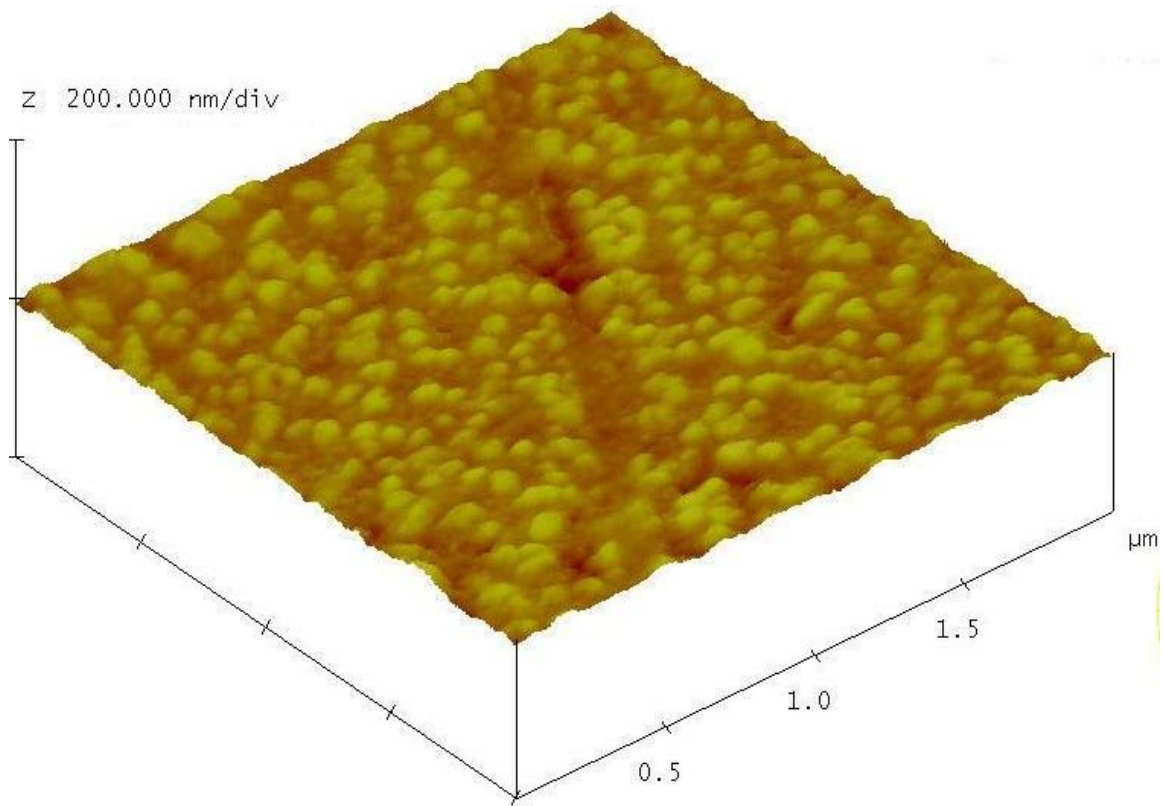
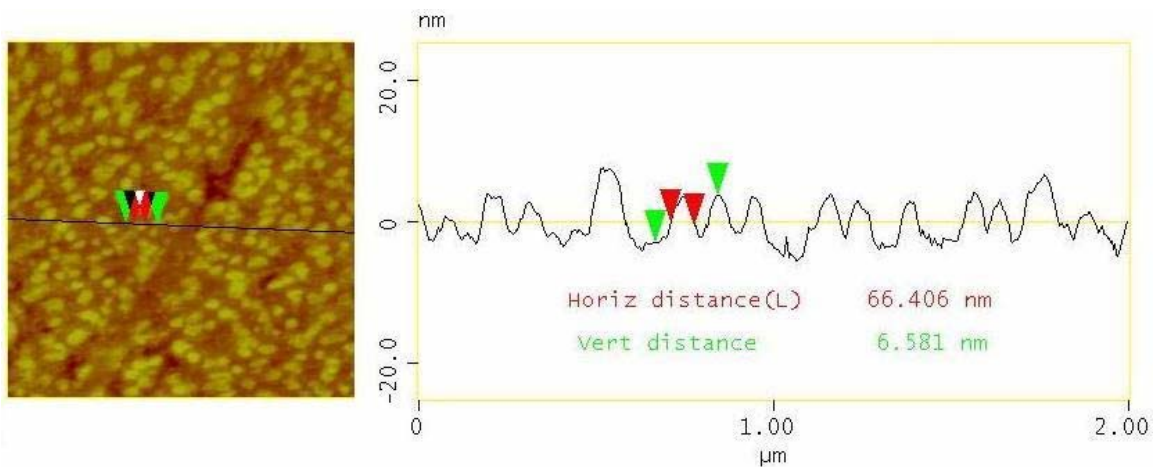


Figure 5.10. AFM section analysis and 3-D view of the as formed surface of glass CU090403.

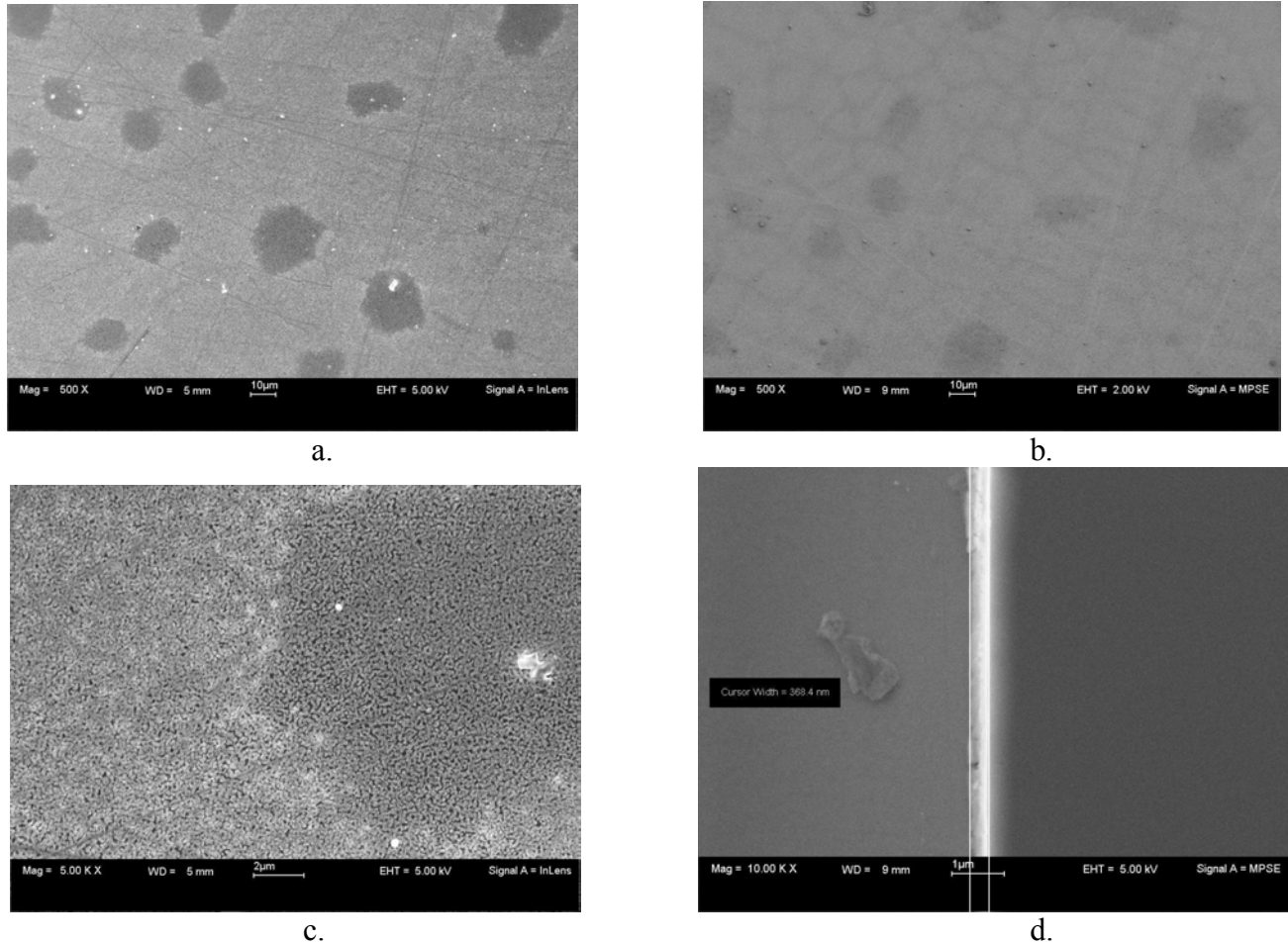


Figure 5.11. SEM results of glass CU090403 heat treated 10 hours at 600°C; a) surface image with in-lens detector, b) surface image with standard secondary electron detector, c) surface image of interface between dark and light regions, d) “over-the-edge” view of fracture surface.

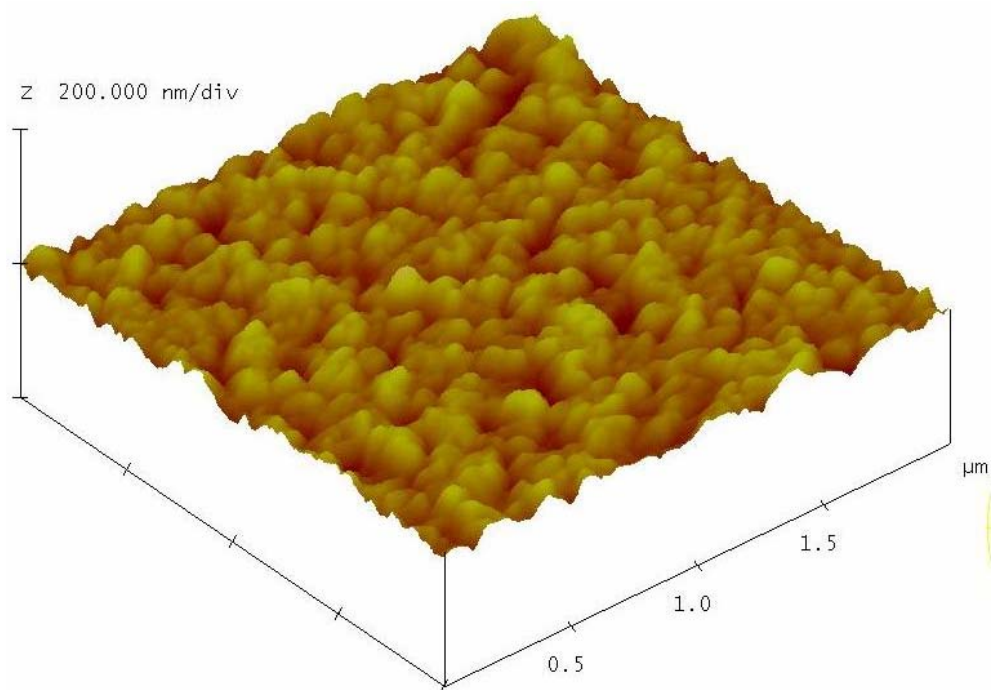
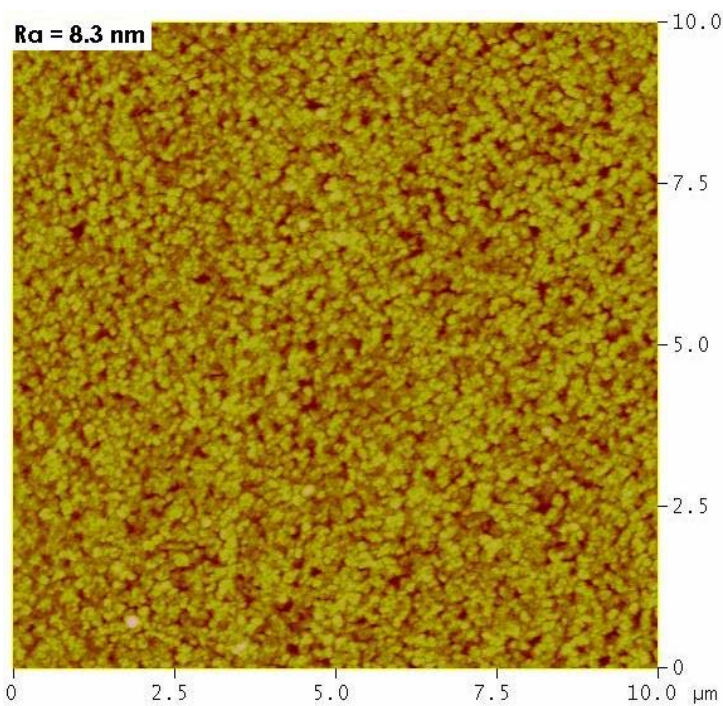


Figure 5.12. AFM results of glass CU090403 heat treated at 600°C for 10 hour.

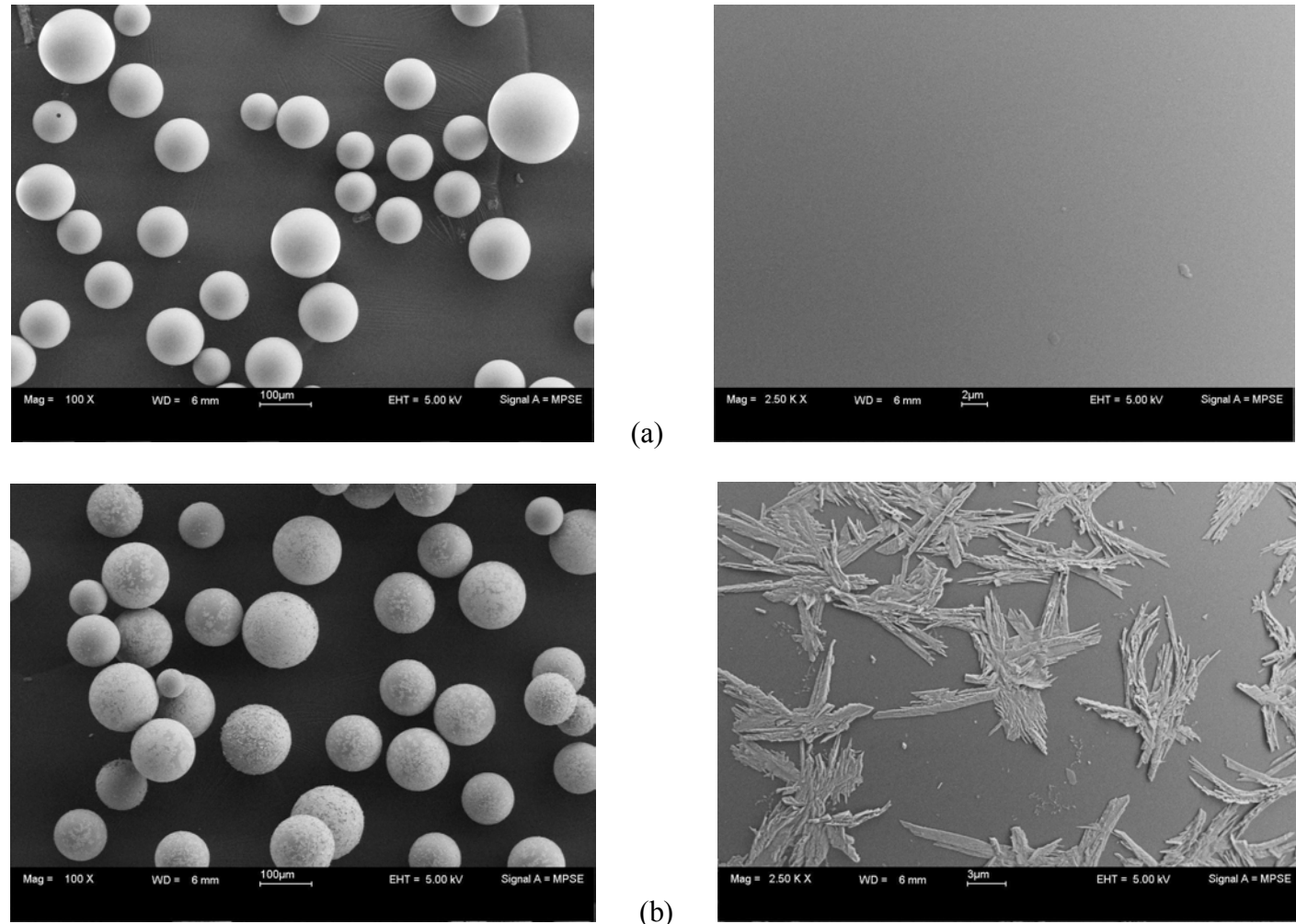


Figure 5.13. SEM images of glass micro-spheres formed from glass CU090304: a) as formed, and b) after heat treatment at 600°C for 24 hours.

5.4.3 Characterization of Copper Sodium Borosilicate Glasses

5.4.3.1 Effect of copper level on copper oxide film formation

The glass compositions studied to this point contain high levels of lead, providing safety concerns during batching, melting and disposal of the glass. To avoid melting additional lead containing glasses, the borosilicate family of glasses was explored as a possible host for the surface oxidation of copper. Rapp²⁴ discusses a series of glass compositions for making metal coated non-crystallized amorphous glass fibers. Rapp fiberized borosilicate glasses that contained high concentrations of copper oxide. Subsequent reactive reduction steps in the presence of a hydrogen atmosphere produced a semi-continuous film of metallic copper.

Glass composition CU093003 (see Table 5.1 for composition), described in US Patent 4,836,837, was batched and melted at 1565°C for 2.5 hours. This calcium aluminum borosilicate glass containing 24 weight percent CuO, formed a significant copper oxide film upon heat treatment at 500°C for 24 hours. Figure 5.14 displays the surface XRD trace of the glass CU093003 after heat treatment at 500°C for 24 hours. The increased intensity of the CuO diffraction peaks, combined with the lower intensity for the amorphous halo provides evidence that this film is thicker and more continuous than the films formed from the lead containing glasses. The main drawback to glass composition CU093003 is the high melting temperature required to form a homogenous glass, requiring clay bonded fused silica crucibles for melting. The composition was altered to provide a glass to study the copper oxidation phenomenon that resulted in a more manageable melting temperature.

A sodium borosilicate glass was chosen as a suitable host glass for the high levels of copper while providing a considerably lower melting temperature between 1300 and 1400°C. The initial sodium borosilicate composition melted was CU102903. No surface film was apparent on cooling, however heat treatment at 500°C for 24 hours resulted in the copper oxide film on the surface. To determine the role of copper in the glass structure, and the range of compositions that result in copper oxide films, a series of glasses with the same base composition, and varying levels of copper were prepared and

characterized with DSC. Copper oxide was added in excess to a base alkali borosilicate glass with a weight percent composition of 12 Na₂O * 28 B₂O₃ * 60 SiO₂. The resulting glasses had copper oxide concentrations, on a weight percent basis, of 0, 2, 5, 10 and 15 percent.

Table 5.4 summarizes the DSC results for the series of copper sodium borosilicate glasses with varying levels of copper oxide. The effect of the level of copper oxide in the glass on the glass transition temperature is shown in Figure 5.15. The decrease in the glass transition temperature as the level of copper in the glass is increased indicates that at these high levels of copper, the copper is entering the glass structure as a modifier increasing the level of non-bridging oxygen. All as-poured glasses in this series showed no level of surface crystallization, and XRD confirmed that no detectable level of bulk crystallization was present.

Figure 5.16 displays the results of the DSC analysis for the 10 and 15 percent copper oxide compositions showing that significant crystallization peaks occur above the glass transition temperature. Crystallization peaks were not present in the DSC runs up to 700°C for the compositions with lower levels of copper oxide, and no visual indication of surface crystallization was observed. Visually examining the DSC sample for the 15% copper oxide composition, after the DSC run to 600°C, showed the surface of the glass chips to be silver colored. However, when the chips were broken with a mortar and pestle, the interior of the glass chips were yellow in color, indicating possible bulk crystallization as well.

XRD was completed on the post DSC sample for the 15% copper oxide composition to determine the crystalline phase(s) present. The small sample of glass chips (18 mg) was ground to a fine powder and mounted on a zero background holder for XRD analysis. Figure 5.17 displays the result of the XRD analysis from the 15% copper oxide composition, after heating to 600°C in the DSC. The three broad peaks in the diffraction trace are the three strongest lines for Cu₂O, Cuprite, with copper in the +1 state. The broad diffraction peaks in Figure 5.17 indicate that the crystallite size was very small for the Cu₂O phase. The mean crystallite size was estimated to be 50nm with the use of the Scherrer equation²⁷, which determines the mean crystallite size from the breadth of the diffraction peaks, less any instrumental broadening, the wavelength of the

radiation and the angular position of the diffraction peak. The surface crystallization causing the silver color was probably the result of a thin layer of CuO on the surface, but this was not a large enough volume of the sample to show up in the XRD trace.

Figure 5.16 also shows that the temperature difference between T_g and the onset of crystallization is much greater for the 10% CuO composition than the 15% CuO composition. For the 10% CuO glass the temperature difference between T_g and the onset of crystallization was determined to be 90°C, compared with a much lower delta of 28°C for the 15% CuO glass. The close proximity of T_g and the onset of crystallization for the 15% CuO composition was shown to be a problem for growing the copper oxide film. Heat treatments near T_g for the 15% CuO composition, while resulting in quality copper oxide films, also resulted in bulk crystallization of Cu₂O throughout the glass body.

Twenty-four hour heat treatments near T_g for the 2 and 5 weight percent copper oxide glasses, while showing no signs of bulk crystallization, showed no signs of surface crystallization as determined by AFM. Another glass batched to result in 7.5 weight percent CuO, was also heat treated for 24 hours near T_g , and showed no sign of surface crystallization when examined by AFM. Due to the fact that bulk crystallization in the 15% CuO composition could not be avoided, and surface crystallization did not occur for the compositions evaluated with less than 10% CuO, only the 10 percent CuO composition was used for all further work in evaluation of the copper oxide thin film phenomenon.

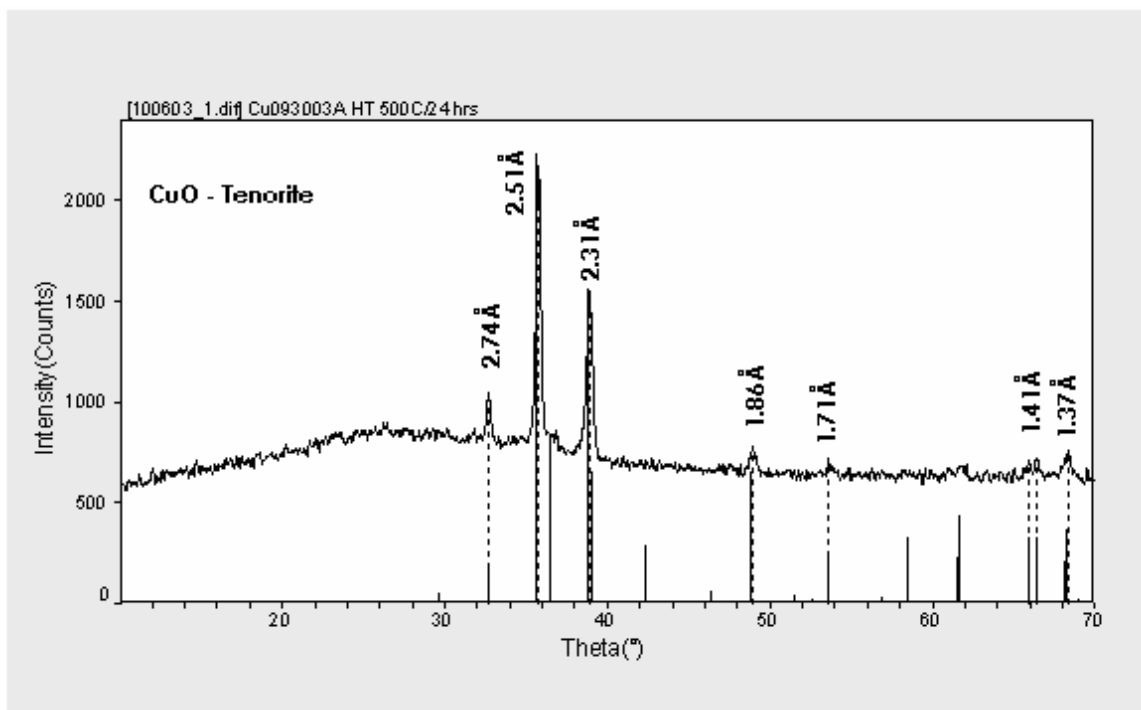


Figure 5.14. Surface XRD results of glass composition CU093003 after heat treatment at 500°C for 24 hours.

Table 5.4. DSC Results for Copper Sodium Borosilicate Glass Series

Composition ID	Weight Percent CuO	T _g (°C)	Crystallization Onset (°C)	Mole % SiO ₂
SI012904	0	587	none to 700°C	63.4
CU120203	2	562	none to 700°C	62.5
CU120303	5	540	none to 700°C	60.9
CU102903	10	509	599	58.3
CU021204	15	485	513	55.7

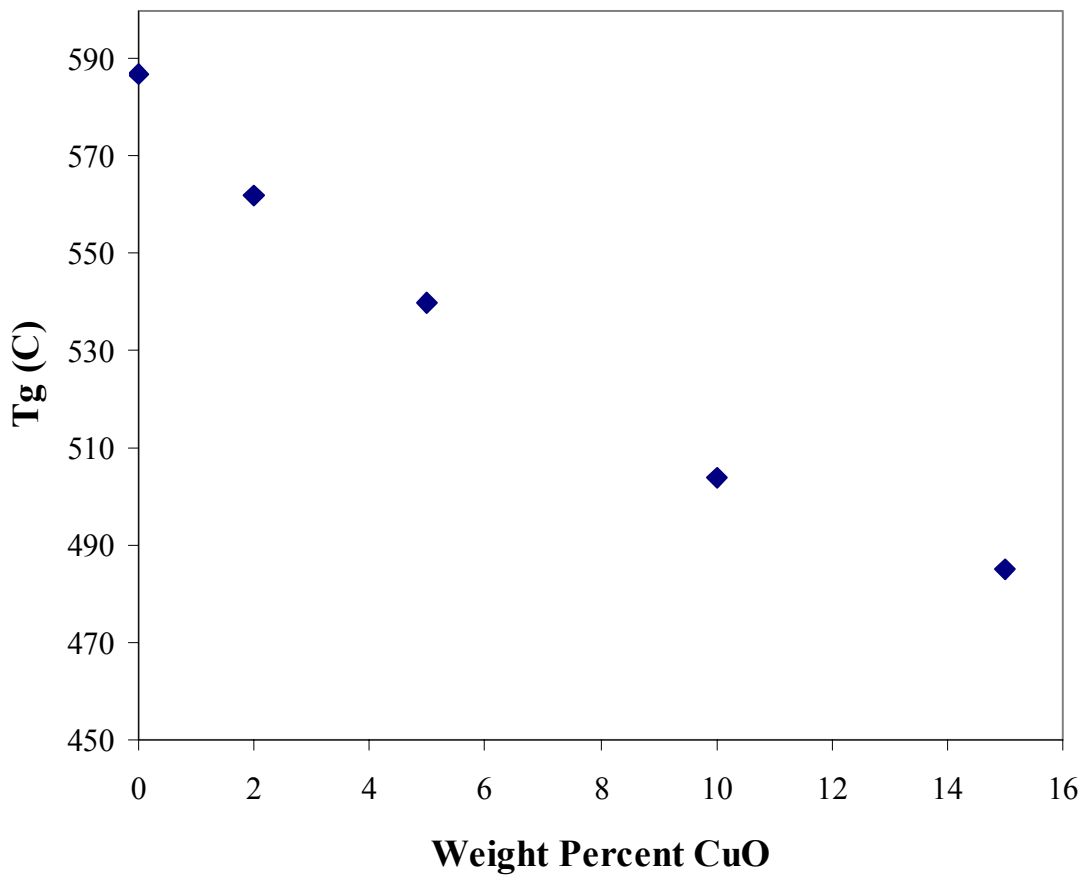


Figure 5.15. Variation in glass transition temperature as a function of copper oxide concentration in the glass.

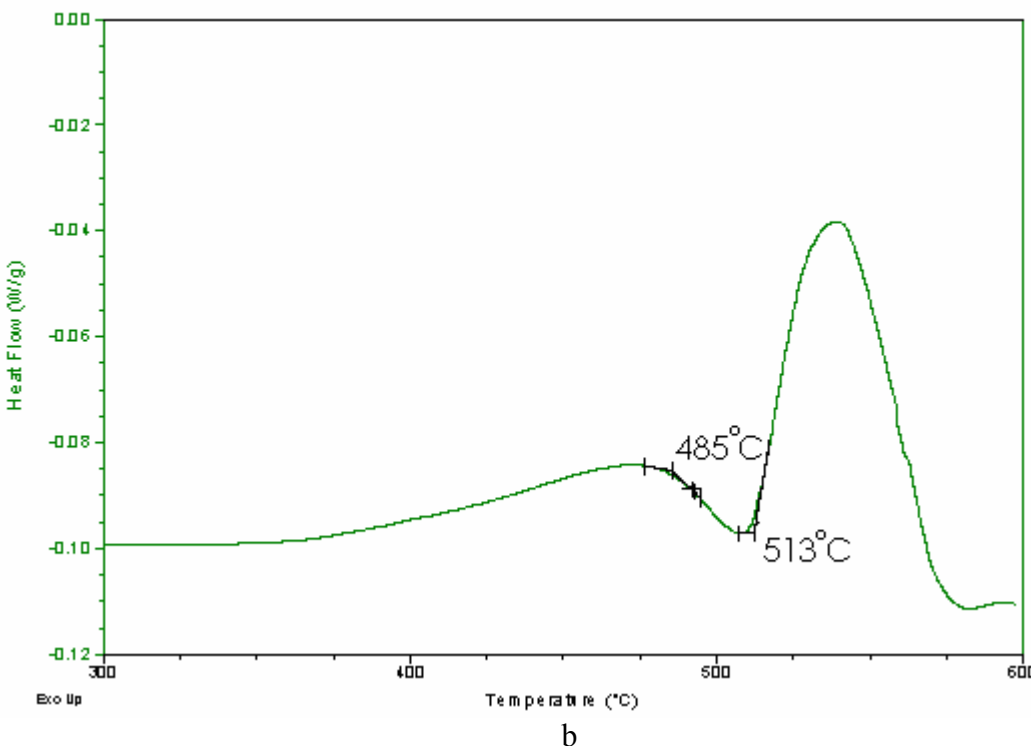
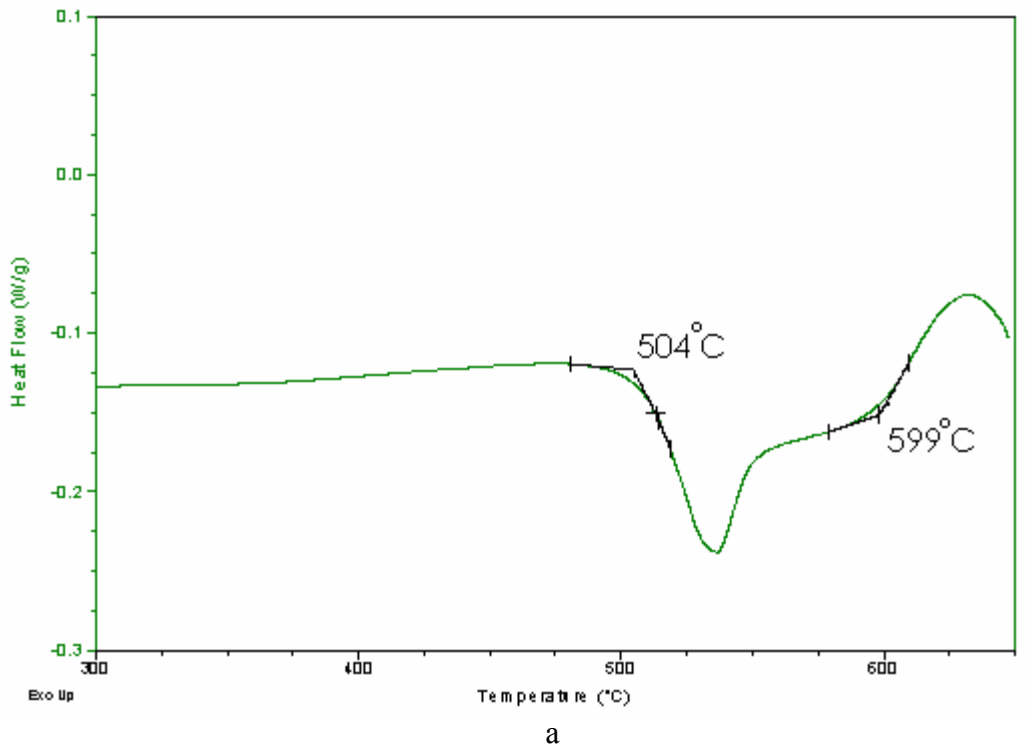


Figure 5.16. Results of DSC analysis of copper sodium borosilicate glasses with a) 10 and b) 15 weight percent CuO.

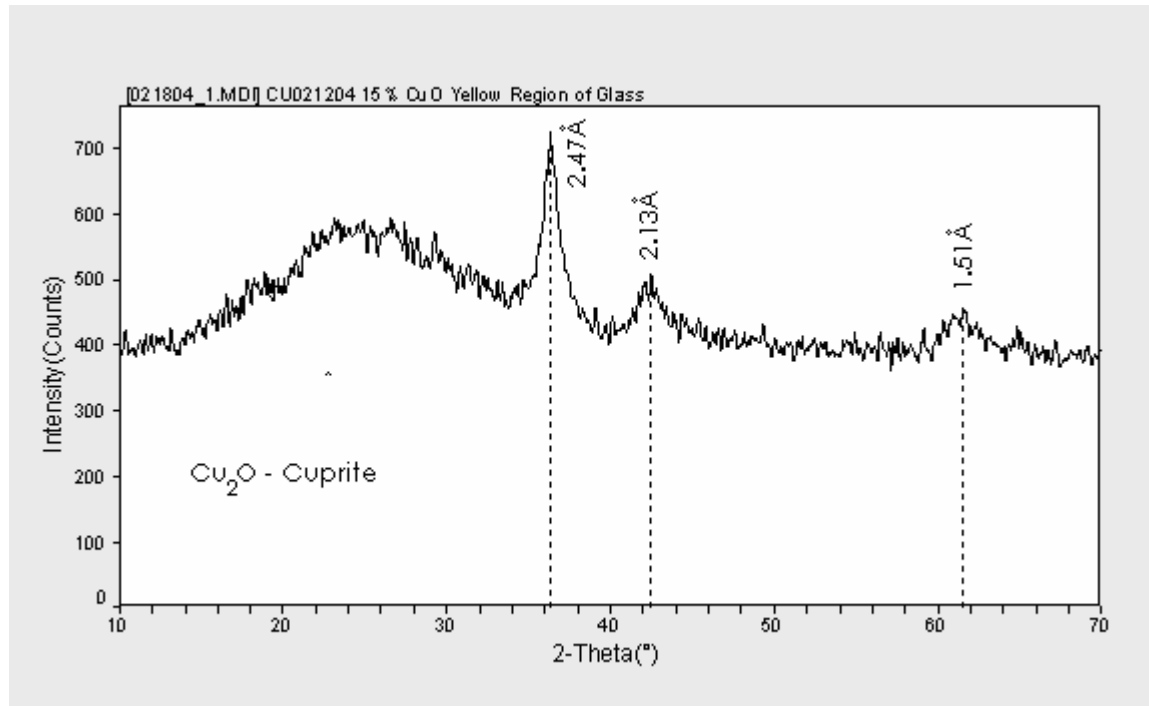


Figure 5.17. Results of XRD analysis of 15% CuO composition after DSC analysis to 600°C.

5.4.3.2 Heat Treatment Studies of Composition CU102903

Initial heat treatments of the 10 weight percent copper oxide composition were carried out on as-melted glass surfaces. The as-formed glass surfaces provides a very smooth surface for evaluation of the film formation process. Figures 5.18 displays AFM results of the as-poured glass surface, while Figures 5.19 - 5.23 provide AFM images of composition CU102903 heat treated at 400°C/24 hours, 500°C/2 hours and 500°C/24.

Figure 5.18 shows that there are no surface crystals on the as formed glass surface and the surface is very smooth with a Ra value of 1.6 Å. Clusters of CuO crystals are realized after an extended heat treatment of 24 hours at 400°C. Figure 5.20, a higher resolution image of the surface of the specimen heat treated for 400°C/ 24 hours, includes the phase image. The phase image provides contrast based on differential interaction of the AFM tip with the sample surface, and often provides information not available with topographical images²⁵. Crystal facets can often be resolved in the phase images, when the topography image does not reveal them due to problems with image height. The glass surface, which is dark in Figure 5.20, isolates the clusters of CuO crystals from each other, which would lead to very poor electrical properties of the film. AFM section analysis included in Figure 5.20 shows that the CuO crystal clusters are between 25 and 30 nm in height and approximately 75 nm in diameter. The ability of copper to migrate to the surface is very low at 400°C, which is over 100°C below the T_g for this glass composition. It is assumed that only the copper ions very near the surface are taking part in the film formation at this low temperature.

Heat treatments at 500°C, which is only slightly below T_g for this glass, provide much more continuous film coverage of the glass surface. Figure 5.21 shows that after only two hours at 500°C there are continuous pathways of CuO crystals on the glass surface. However the dark regions in Figure 5.21 indicate that the film is not fully covering the glass. The crystal height and crystal size were estimated from the AFM data for the two hour heat treatment to be approximately 20-25 nm and 60 nm respectively. The smaller crystal size, when compared to the 400°C heat treatment may be due to the shorter heat treatment time or the higher concentration of crystallites on the glass surface.

Figures 5.22 and 5.23 show that heat treatment at 500°C for 24 hours resulted in a nearly full coverage of the glass surface with the CuO film. The high resolution phase image in figure 5.23 shows a fairly random orientation of the CuO crystals. The film height, which was estimated from regions where it was believed the AFM cantilever was able to reach the glass surface between crystals, was estimated to be approximately 75 nm. Assuming a diffusion controlled process, which has to be taking place for the significant film formation, where film thickness would be related to the square root of heat treatment time, the film thickness for a 24 hour heat treatment, would therefore be approximately 3.5 times the thickness of a two hour heat treatment at the same temperature. The AFM results show that the film thickness for the 24 hour heat treatment at 500°C is in the range of three to four times that of the two hour heat treatment at 500°C. The relationship between film thickness and heat treatment time will be discussed in further detail later in this paper.

Figure 5.23 shows that the CuO film is fairly continuous after a 24 hour heat treatment at 500°C. However four point conductivity measurements to determine the conductivity of the film were not successful due to the very high resistance of the film surface. Using very high voltage, it was possible to measure a resistance of the film surface, which was considerably lower for the 24 hour heat treatment when compared to the 2 hour heat treatment at 500°C. To qualitatively evaluate the conductivity of the film on a nanoscale, electrical force microscopy (EFM), a special AFM technique, was employed. Figure 5.24 displays the results of the EFM measurement on the sample heat treated at 500°C for 24 hours. The image on the top is simple topography, while the image on the bottom is the electrical force image collected in LiftMode® with a 50 nm lift height and a 12 volt bias between a conductive tip and the film surface. The EFM results indicate that locally the grains exhibit good conductivity compared to the grain boundaries, whose dark color in the EFM image indicated poor conductivity. Comparing Figure 5.24 with the same size normal TappingMode® images in Figure 5.23 provides a good visual for the differences in the phase images where contrast in Figure 5.24 is due to the longer range electrical forces. Careful examination of the EFM phase image in Figure 5.24 shows very thin non-conducting regions within the individual grains, indicating the possible presence of trans-granular micro-cracking.

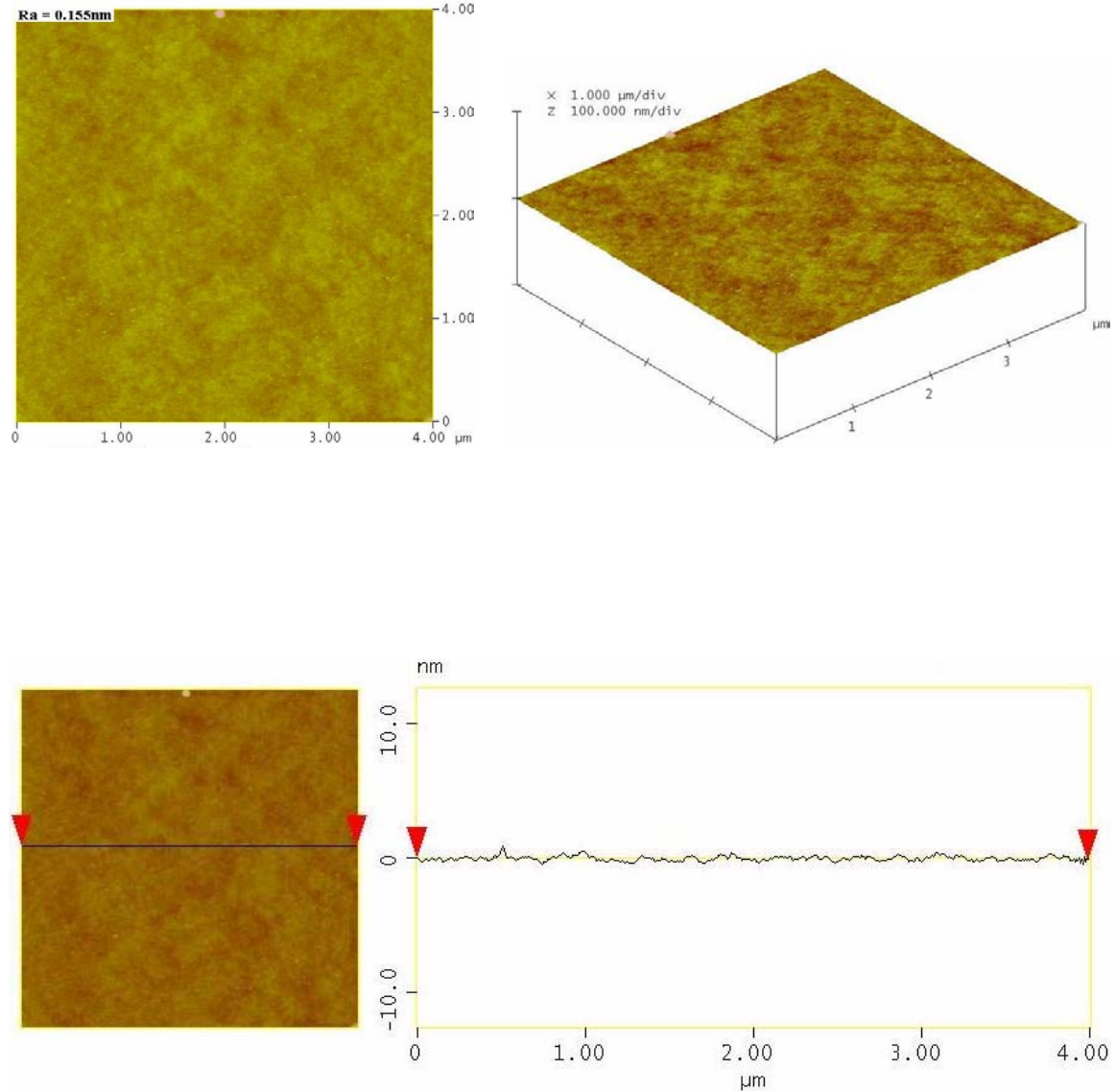


Figure 5.18. AFM top view, 3D view and section analysis of the as melted surface of glass composition CU102903.

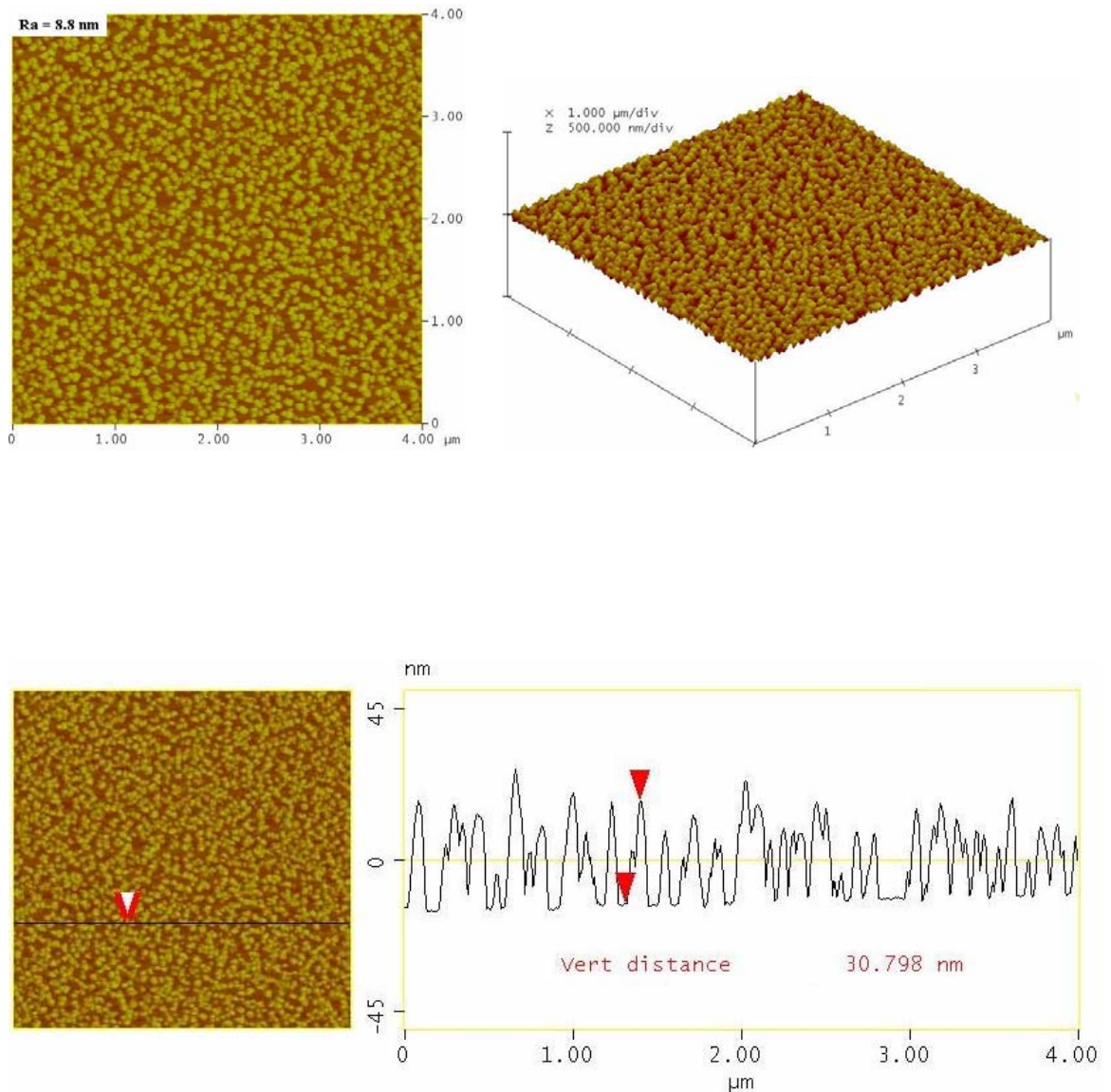


Figure 5.19. AFM top view, 3D view and section analysis of the film surface of glass composition CU102903 after heat treatment at 400°C/24 hours.

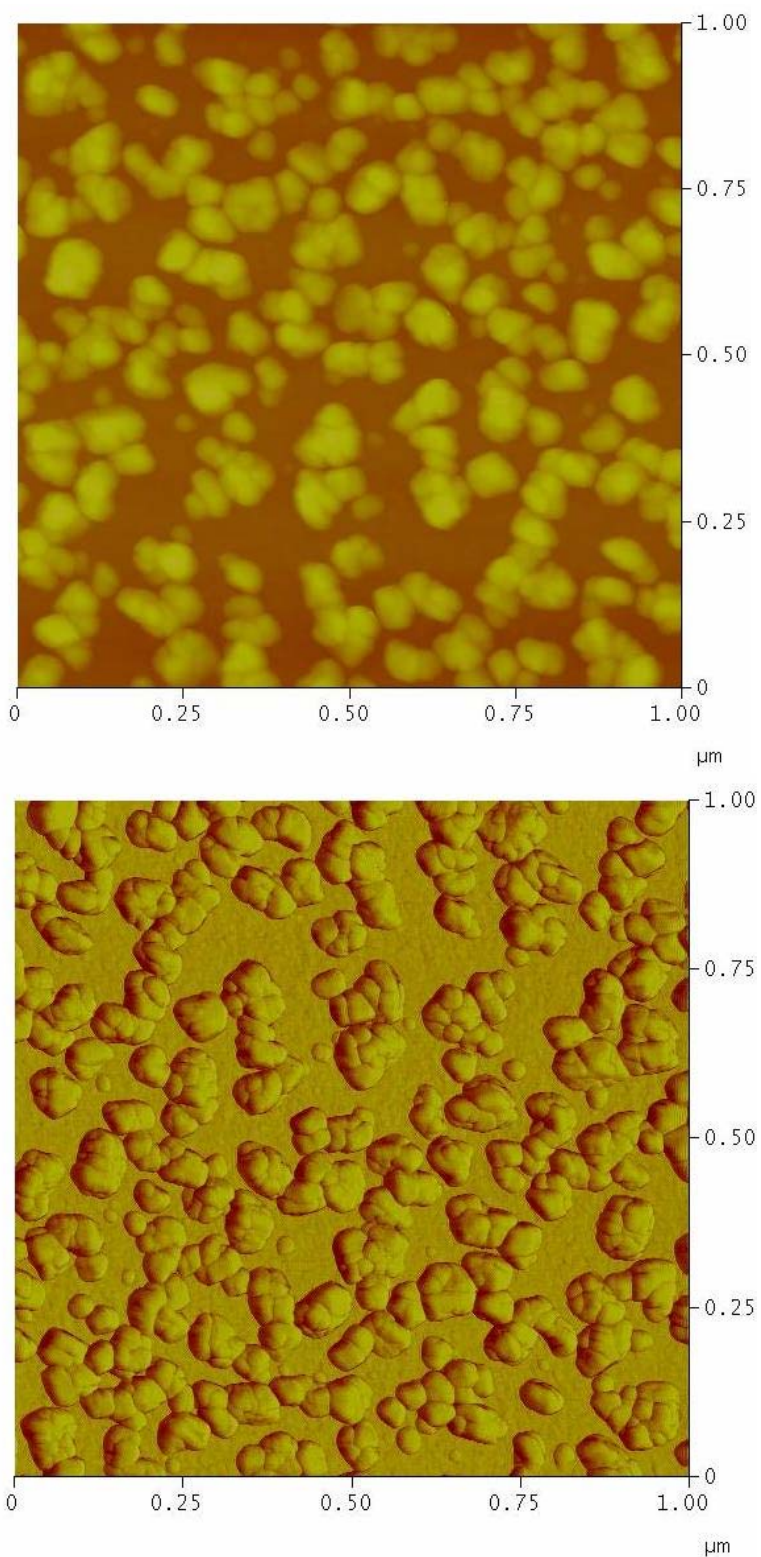


Figure 5.20. AFM top view (top) with phase (bottom) for higher resolution look at the film surface of glass composition CU102903 after heat treatment at 400°C/24 hours.

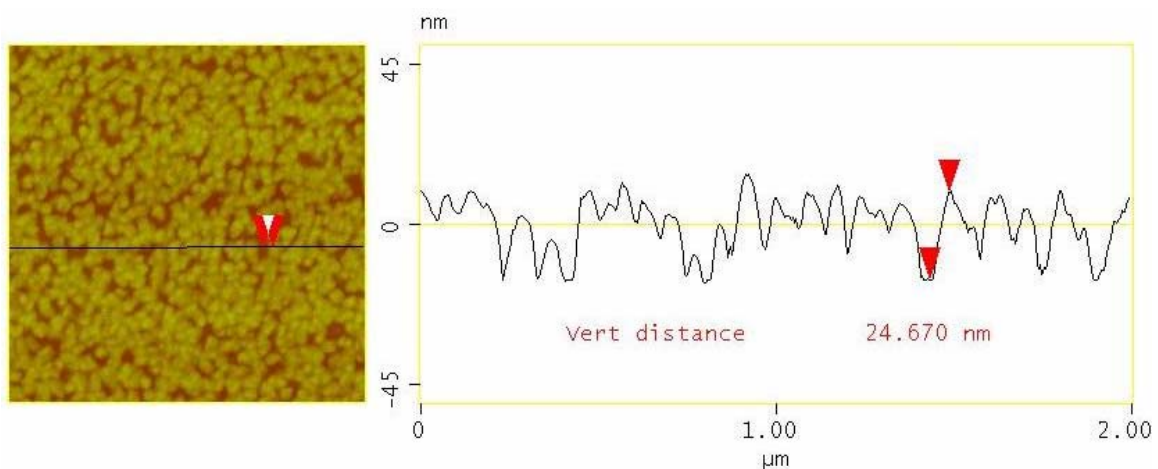
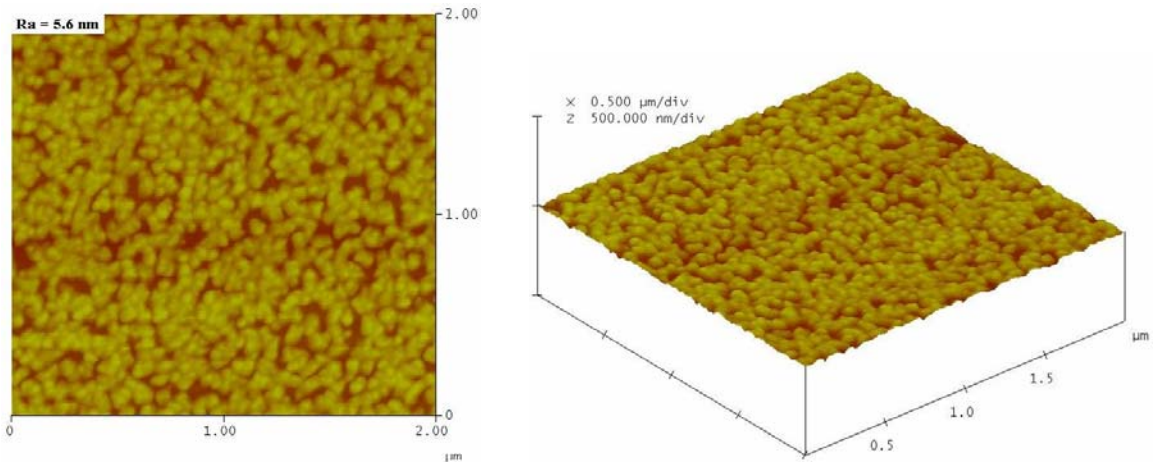


Figure 5.21. AFM top view, 3D view and section analysis of the film surface of glass composition CU102903 heat treated at 500°C/2 hours.

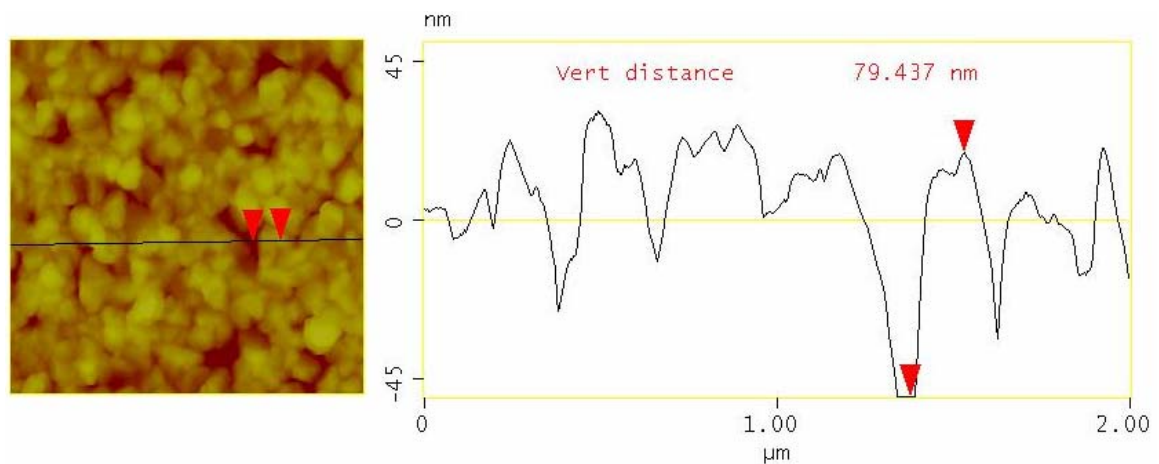
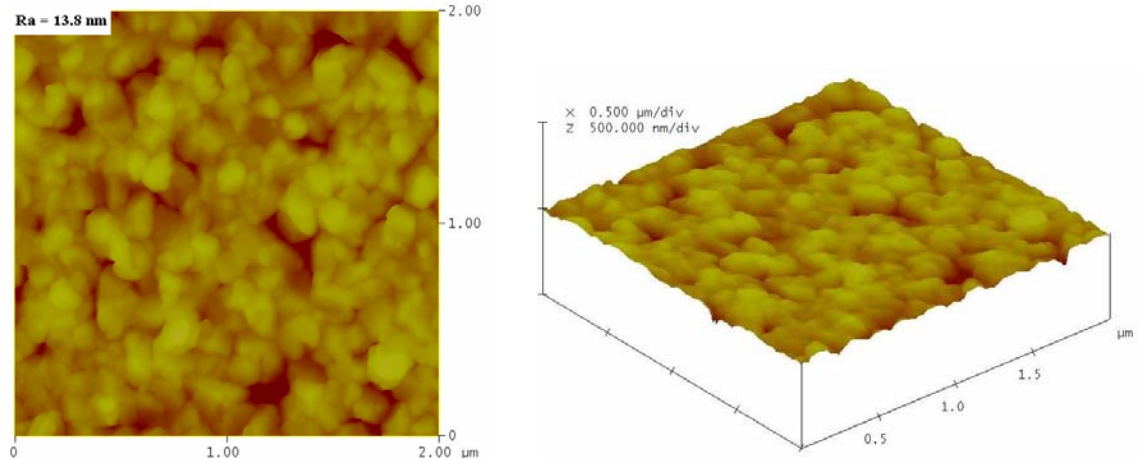


Figure 5.22. AFM top view, 3D view and section analysis of the film surface of glass composition CU102903 after heat treatment at 500°C/24 hours.

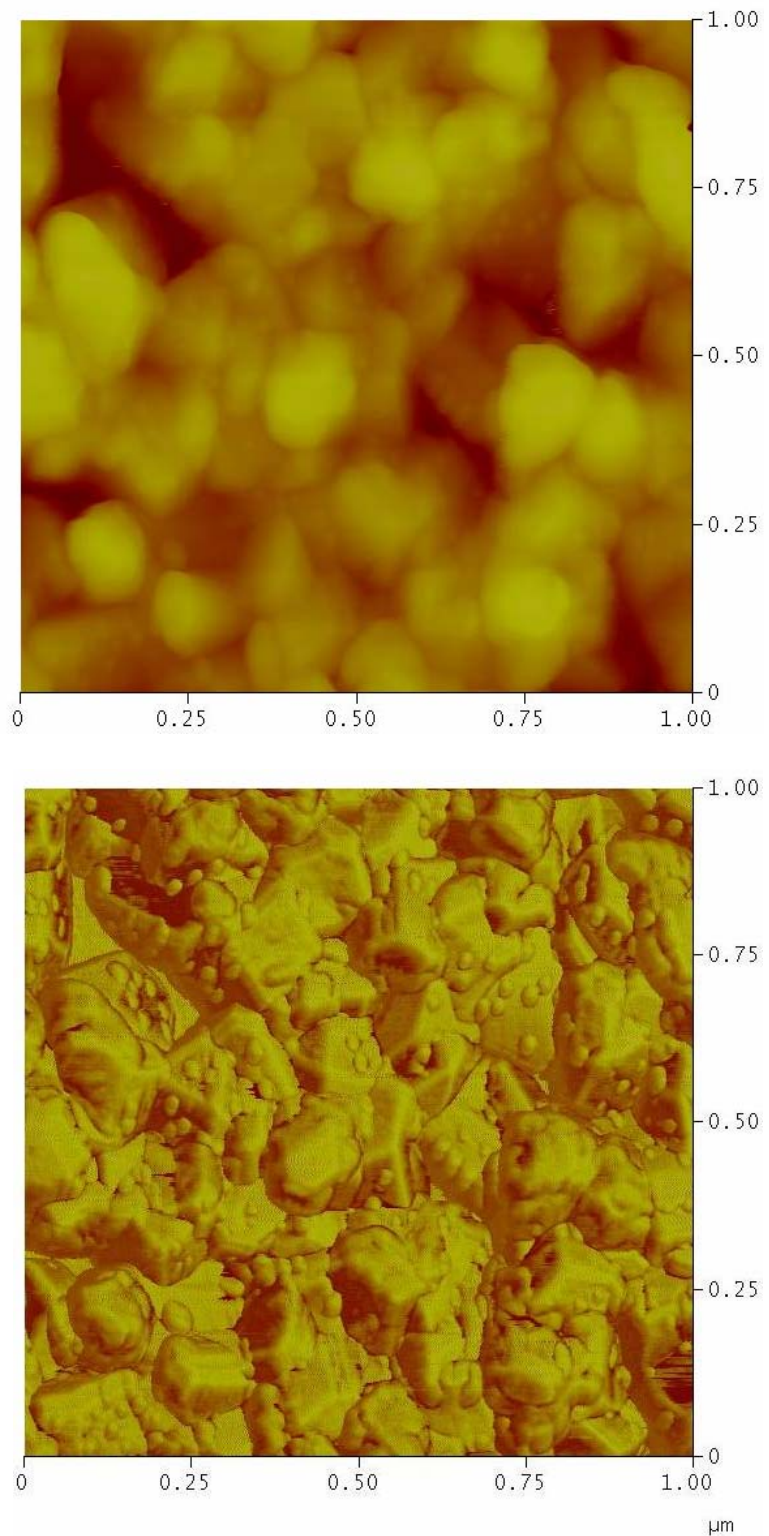


Figure 5.23. AFM top view (top) with phase (bottom) for higher resolution look at the film surface of glass composition CU102903 after heat treatment at 500°C/24 hours.

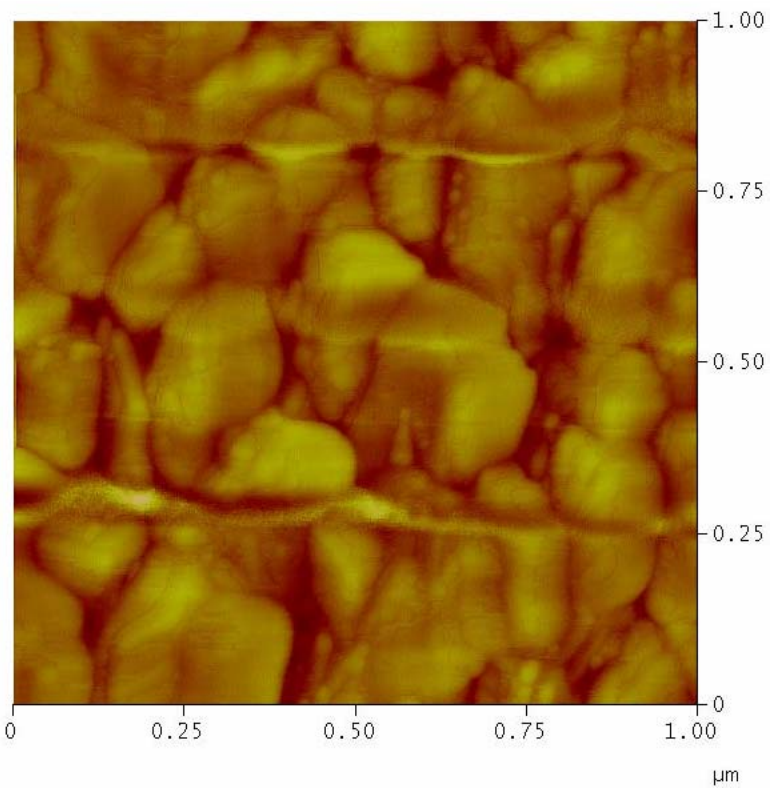
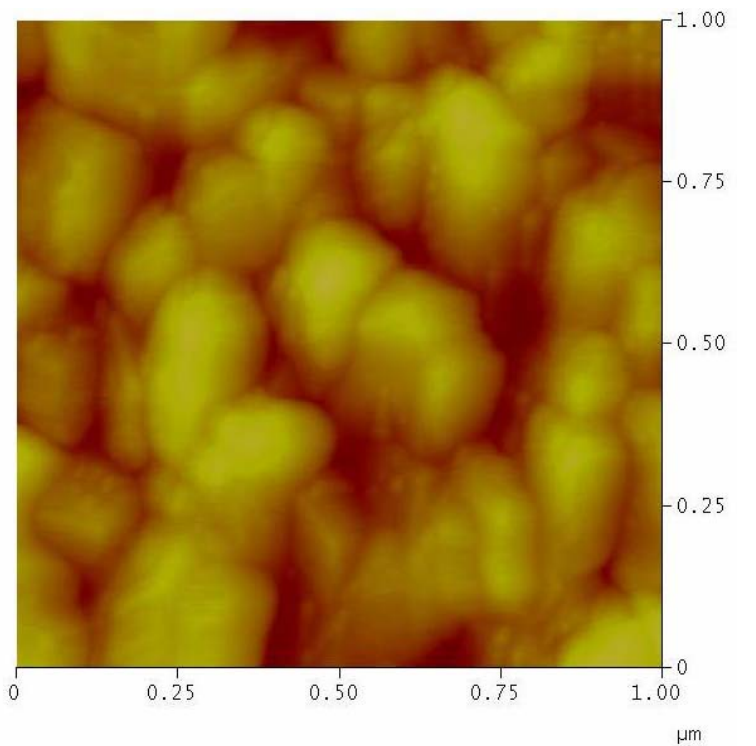


Figure 5.24. Topography (top) and EFM (bottom) results of the film surface of glass composition CU102903 after heat treatment at 500°C/24 hours.

Heat treatments of polished surfaces of the glass composition CU102903 were completed for various times at temperatures near T_g (510°C) as well as 20°C above (530°C) and 20° below (490°C) T_g . The surface roughness and thickness of the resulting films were evaluated with the use of the AFM. AFM was utilized to determine the film thickness as charging in the SEM created difficulty in determining the thickness of the thinner film.

The heat treatments at 530°C resulted in crystallization of the bulk, although good quality surface films were produced. XRD confirmed that the primary phase crystallized in the bulk glass was Cu₂O, Cuprite, with copper in the +1 state. Table 5.5 provides a summary of the AFM results for surface roughness and film thickness for the samples heat treated at 490°C and 510°C. Analysis of the 530°C heat treatment was not completed due to the observation of bulk crystallization. No bulk crystallization was detected in the samples heat treated at 490° or 510°C.

Figure 5.25 is a plot of surface roughness as a function of heat treatment time and heat treatment temperature. The plot shows that the surface roughness changes very little with increased time at 510°C, although the uniformity of the surface increases as indicated by the reduced error bars. Figure 5.26 displays the series of AFM images for the various heat treatment times at 510°C. The surface roughness changes only slightly, however the porosity of the film surface is reduced as more copper diffuses to the surface over time for oxidation to CuO. Figure 5.27 displays the AFM images for the various heat treatment times at 490°C. The increased surface roughness with longer times appears to be due to increased film thickness as the kinetics of the copper diffusion to the surface are slowed at the lower temperature. The section lines displayed in Figures 5.26 and 5.27 have different z ranges, with the 510°C heat treatments plotted at +/- 200 nm and the 490°C heat treatments plotted at +/- 50 nm, making direct visual comparison of the two temperatures difficult. For a visual comparison of the surface roughness and uniformity Figure 5.28 displays the section lines for the longest heat treatments for each temperature.

Figure 5.29 is a plot of the film thickness, as determined by AFM, for the heat treatments at 490°C and 510°C. The error bars in Figure 5.29 indicate the range of film thickness as calculated from the AFM images. The film thickness was shown to increase

with time at 490°C, while the film thickness did not increase for prolonged heat treatments beyond 27 hours for the higher temperature. This result indicates that the CuO surface layer, once uniformly thick may prevent further diffusion of copper to the surface for oxidation at the film/air interface, or prevent diffusion of oxygen through the film to participate in the oxidation of the copper at the glass/film interface. To provide further evidence that the surface film is limiting further diffusion of copper ions to the surface region for oxidation, the CuO film was removed with nitric acid, and the sample was re-heated to 510°C for an additional 24 hours. The CuO film re-formed, and the thickness was approximately 200 nm, similar to that for the initial 27 hour heat treatment.

Figure 5.30 displays AFM images of glass/film cross-sections for the heat treatments at 490°C and 510°. The thickness uniformity of the 490°C film is considerably better than the 510°C heat treatment. This uniformity difference is also indicated by the much larger error bars for the 510°C heat treatment in Figure 5.29. The lower heat treatment temperature results in a finer grain size which leads to a more uniform coverage of the surface. To provide the highest quality surface in the shortest heat treatment time, a two step heat treatment schedule should be examined, initially holding at a temperature well below T_g to provide a uniform surface, then approaching T_g for a second hold time to grow the film more quickly. This two step process would be similar to the control of crystallization through the nucleation and growth process for glass ceramics.

TGA was completed on glass powder of composition CU102903 to evaluate the kinetics of the weight gain associated with surface oxidation. The powder was used to provide added surface area for the reaction. Figure 5.31 displays the result of the TGA analysis for a three hour isothermal hold at 500°C. Oxidation of the surface was fairly rapid at first, and a slope change in the TGA data occurred after the initial 30 minutes at 500°C. The high surface area of the glass powder provides considerable copper ions for oxidation very near the surface, and results in the initial steeper increase in weight. Figure 5.32 is a plot of the weight gain as a function of the square root of time from 30 minutes (after initial increase) to 3 hours. The linear relationship between weight gain and square root of time indicates a diffusion controlled process, as expected.

Table 5.5. Summary of AFM Results for Glass Composition CU102903.

Temperature (°C)	Time (Hours)	Average Roughness (Ra)	Film Thickness (nm)
490	19.5	6.5	49
490	44.5	7.5	86
490	66.0	13.0	138
510	27.0	36.2	197
510	48.0	33.1	210
510	71.0	31.9	199

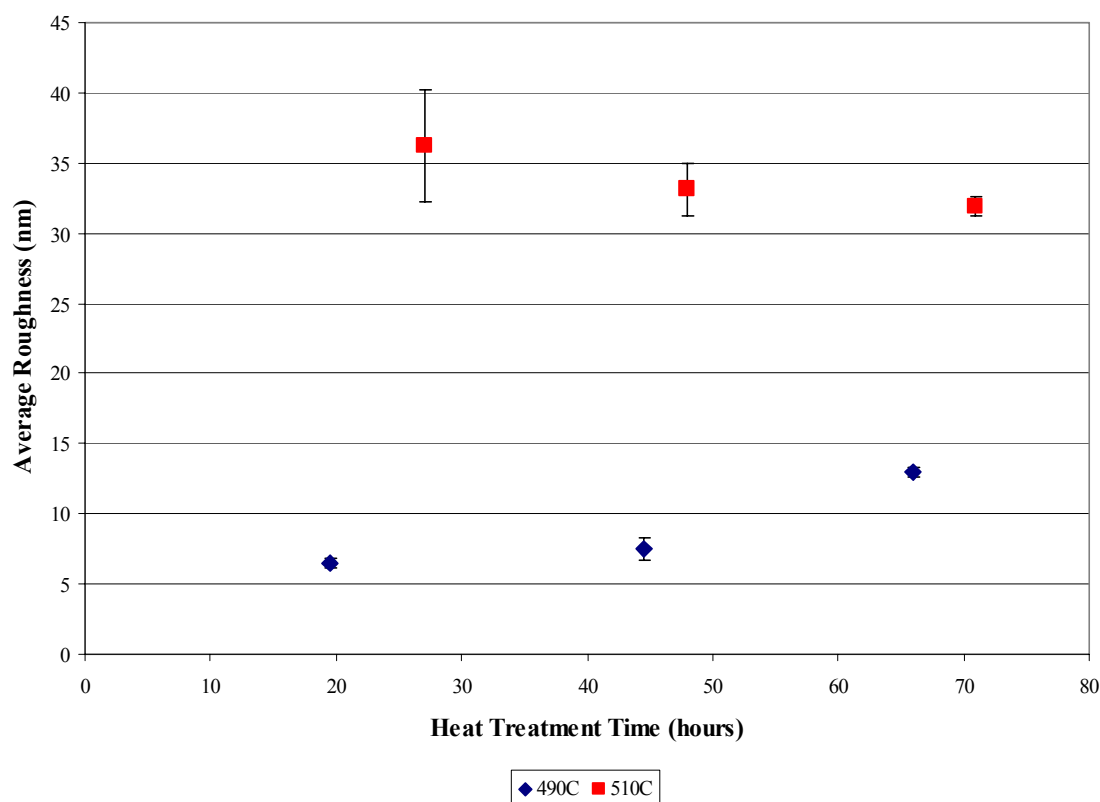


Figure 5.25. Plot of surface roughness as a function of heat treatment time, and heat treatment temperature for glass composition CU102903.

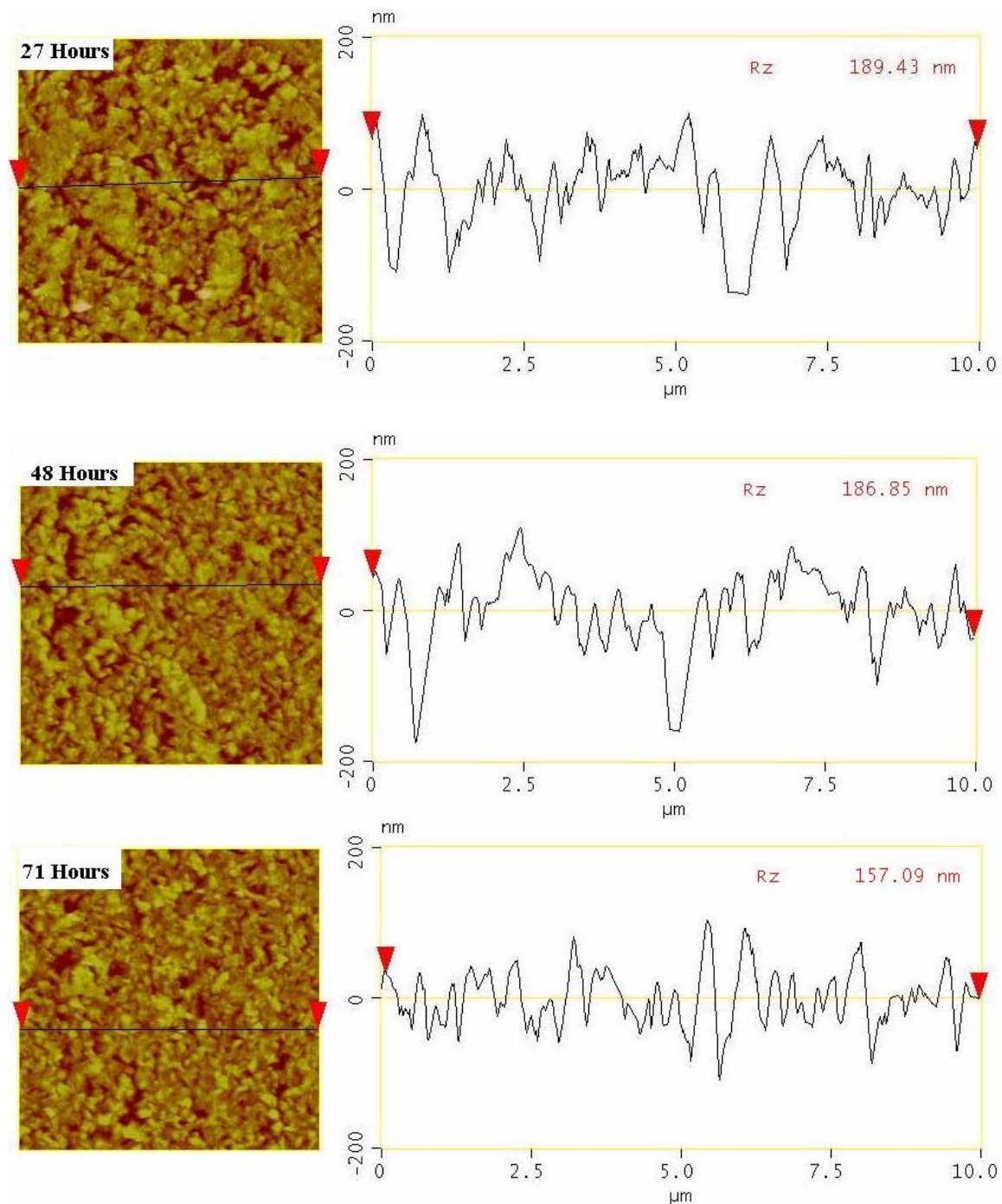


Figure 5.26. AFM section analysis for glass composition CU102903 heat treated at 510°C for various times.

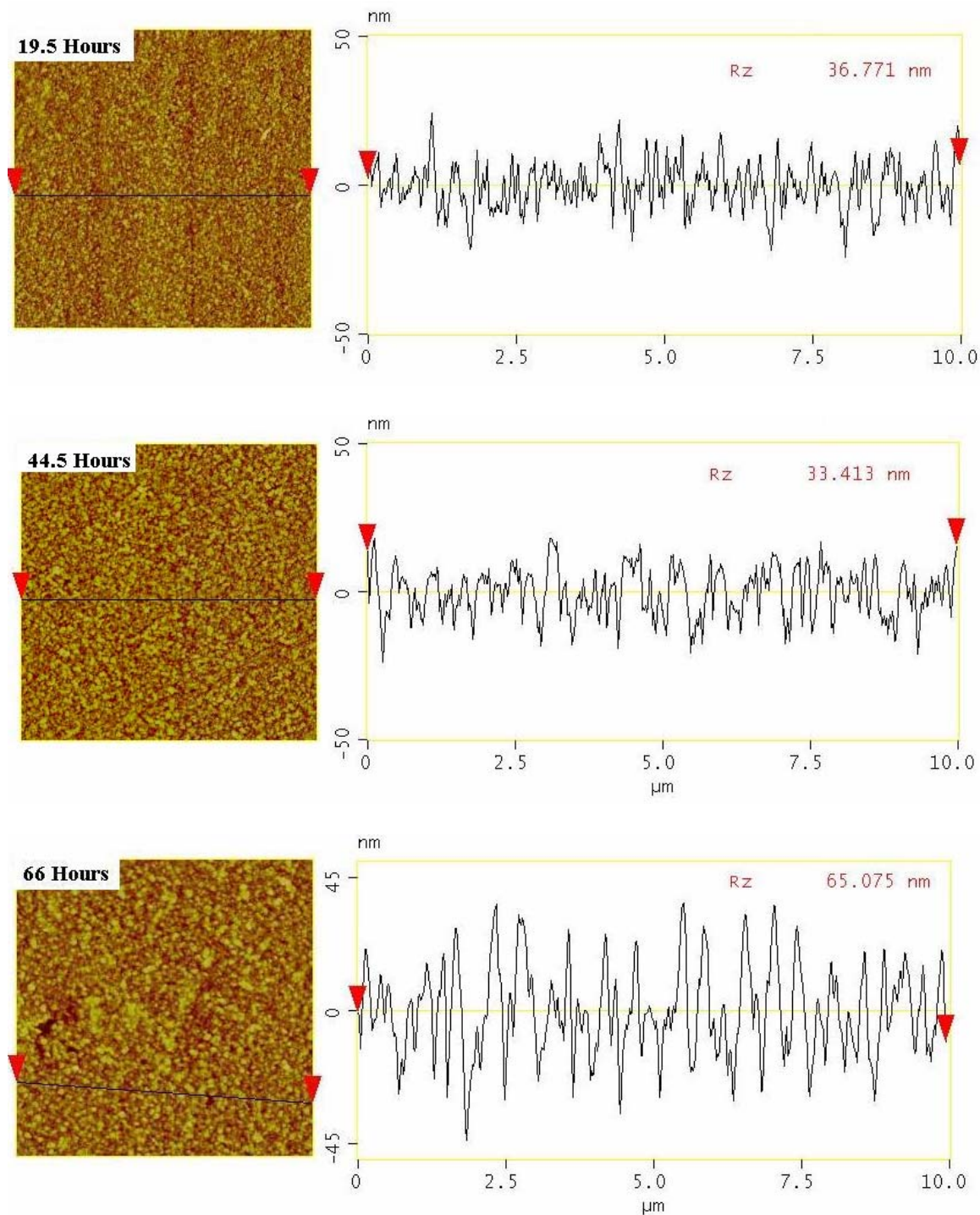


Figure 5.27. AFM section analysis for glass composition CU102903 heat treated at 490°C for various times.

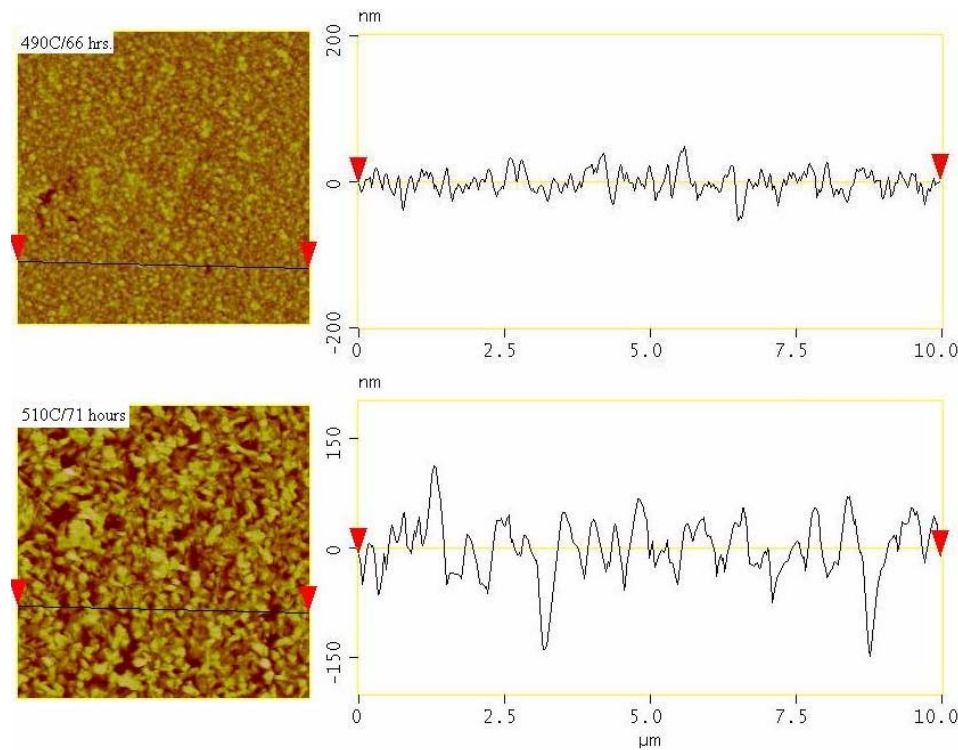


Figure 5.28. AFM section analysis, with equivalent z-scales, for the 66 hour heat treatment at 490°C and the 71 hour heat treatment at 510°C.

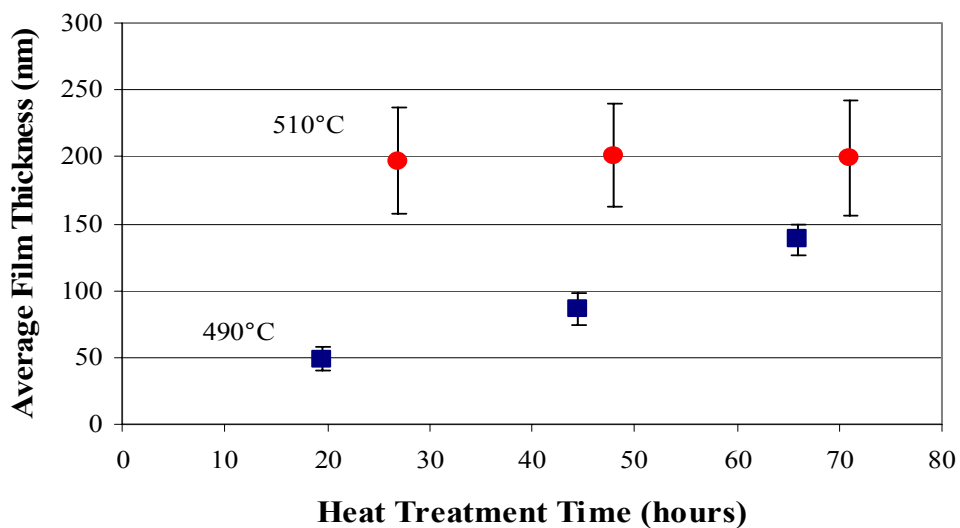


Figure 5.29. Film thickness, as determined by AFM, for glass composition CU102903 heat treated at 490°C and 510°C.

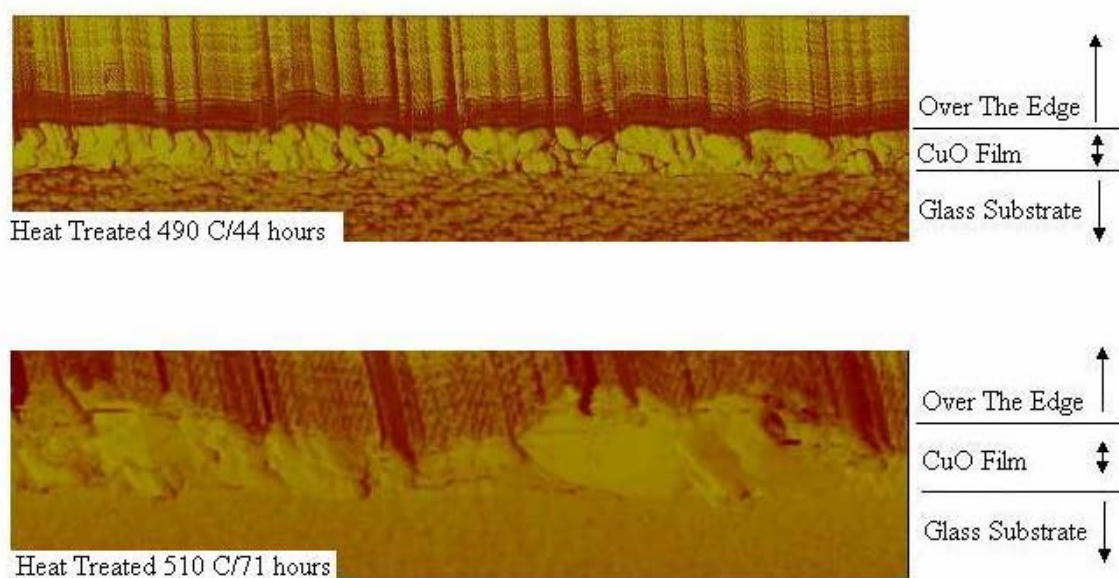


Figure 5.30. Cross section AFM images of glass/film/air interfaces for glass composition CU102903 heat treated at 490 and 510°C.

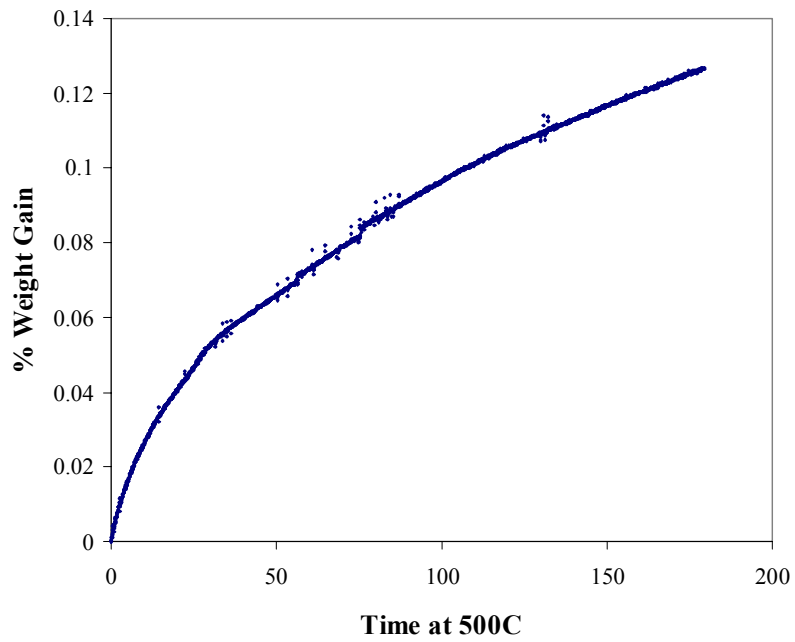


Figure 5.31. Results of TGA analysis for a 3 hour isothermal hold at 500°C of glass powder from composition CU102903.

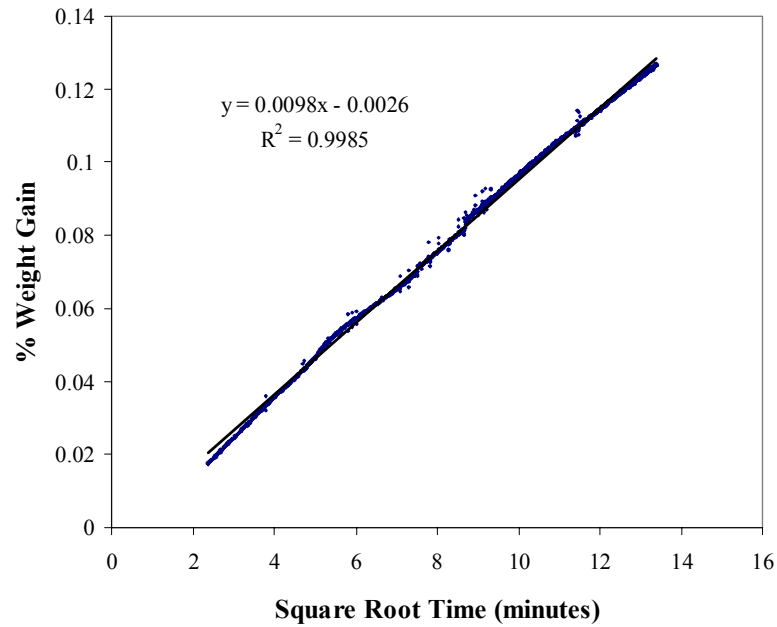


Figure 5.32. Weight gain as a function of the square root of treatment time for an isothermal hold at 500°C for glass powder from composition CU102903.

5.4.3.3 Effect of Heat Treatment Atmosphere on Film Formation

The results presented so far discuss the formation of copper oxide films formed on the surface of glasses when annealed in air. Figure 5.33 shows that the possibility exists for forming a Cu_2O , cuprite structure as well as copper metal when annealing is carried out at lower partial oxygen pressures. The ability to control the crystal structure of the film would allow for tailoring of optical and electrical properties for various applications. CuO has a band gap near 1.7 eV, and absorbs the majority of the visible region, while Cu_2O has a band gap near 2.1 eV and is only strongly absorbing below wavelengths of 600 nm. Reducing the copper to the metallic state may result in a highly conductive metal layer grown directly from the glass.

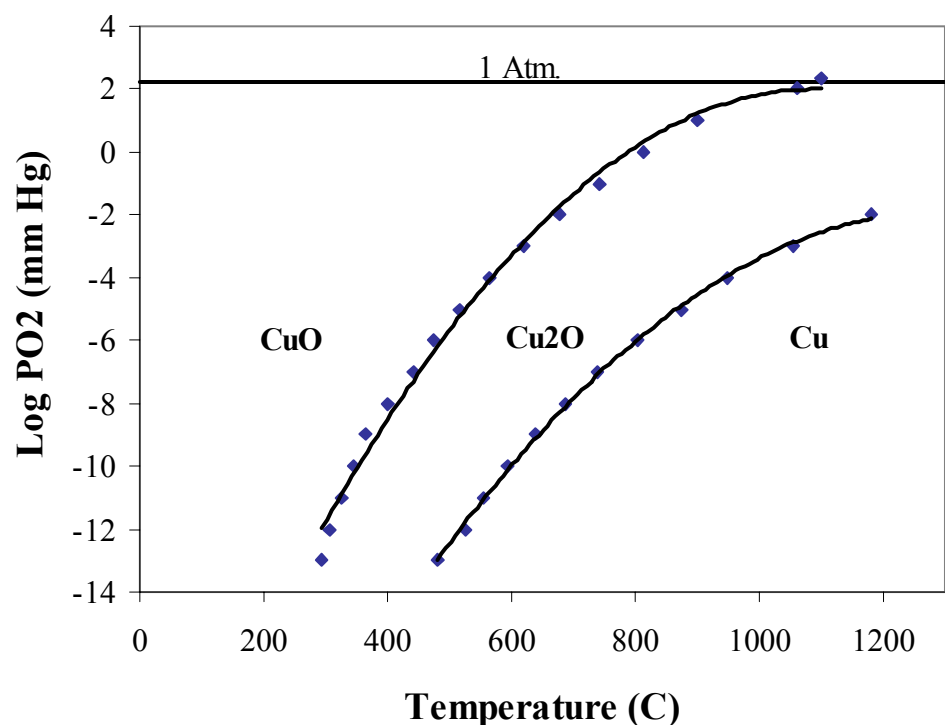


Figure 5.33. Pressure-temperature phase stability diagram for the $\text{Cu}-\text{Cu}_2\text{O}-\text{CuO}$ system. Based on data of Wright²⁸.

A polished section of glass composition CU102903 was heat treated under vacuum at 500°C for 143 hours. The vacuum in the sample tube was better than 10 millitorr for the duration of the heat treatment. The heat treatment resulted in a silver

colored film on the surface of the glass. The crystal structure was determined by X-Ray diffraction to be Cu₂O, cuprite, and the results are displayed in Figure 5.34. The X-Ray diffraction trace has much broader peaks than was observed for the CuO phase (see Figures 5.7 and 5.14), indicating that the crystallite size of the Cu₂O film is much finer than that of the CuO film. Since the diffraction was completed on a solid film, the possibility exists for the peak broadening to be the result of crystal strain, instead of crystallite size. A small amount of the film surface was scraped from the glass and ground to a fine powder, to eliminate any crystal strain, and the fine powder was analyzed by XRD. The result showed similar peak widths to the film, indicating that the peak broadening was clearly due to fine crystallite size. The mean crystallite size was estimated to be 50 nm with the use of the Scherrer equation²⁷.

An additional heat treatment was carried out on glass composition CU102903 in the presence of hydrogen, in an attempt to reduce the surface film to the metallic state. A polished glass was heat treated for 17 hours at 500°C for 710 Torr hydrogen pressure. The XRD result displayed in Figure 5.35 shows that the surface film formed is reduced to copper metal. Figure 5.36 displays the AFM results of the surface of the film produced under hydrogen atmosphere. The morphology shown in Figure 5.36 is much different from the morphology of the copper oxide surfaces. The spherical shaped grains appear to be very uniform and impinging on each other, as can be seen in the phase image included in Figure 5.36, which may result in very good electrical conductivity of the surface. One disadvantage to the metallic copper film is its durability when compared to the oxide films. The oxide films are very tightly bound to the glass surface, whereas the metallic film was rather easily wiped off the substrate. The morphology of the oxides is probably the reason for their excellent adhesion to the substrate. The crystals appear to be growing from the glass and may be protruding into the glass surface, as shown by the AFM result in Figure 5.30, providing good bonding between the glass and the film. Better adhesion of the metallic copper film may result from a two step process. Initially grow the copper oxide film in air (bond coat), then partially reduce the oxide film to metallic copper to provide the conductive surface.

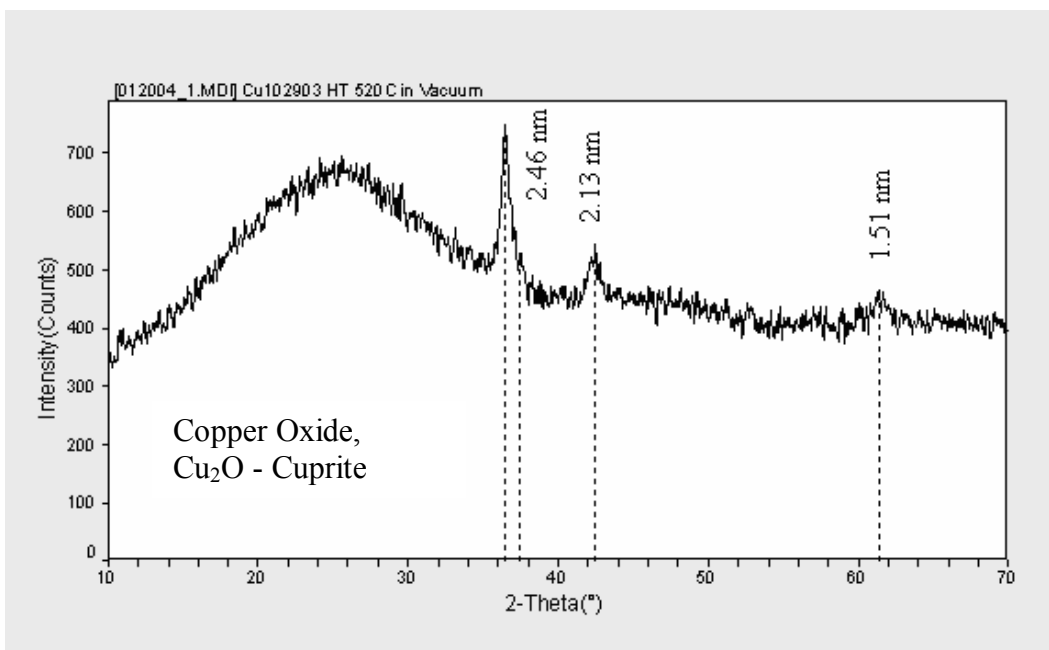


Figure 5.34. Surface XRD result of copper oxide film formed under vacuum.

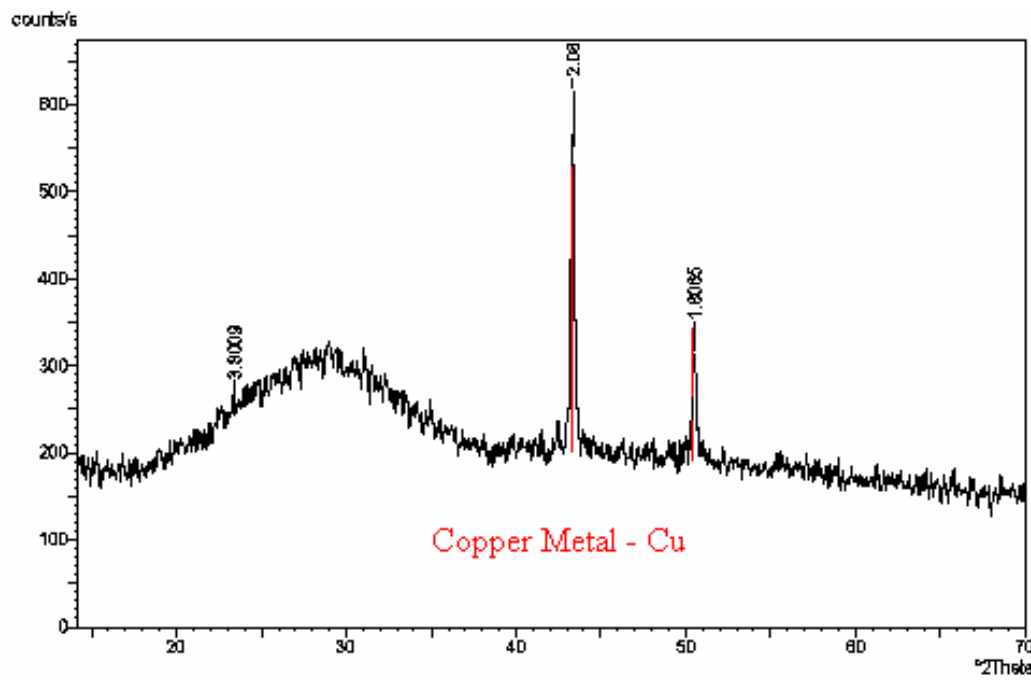


Figure 5.35. Surface XRD result of copper film formed under hydrogen atmosphere.

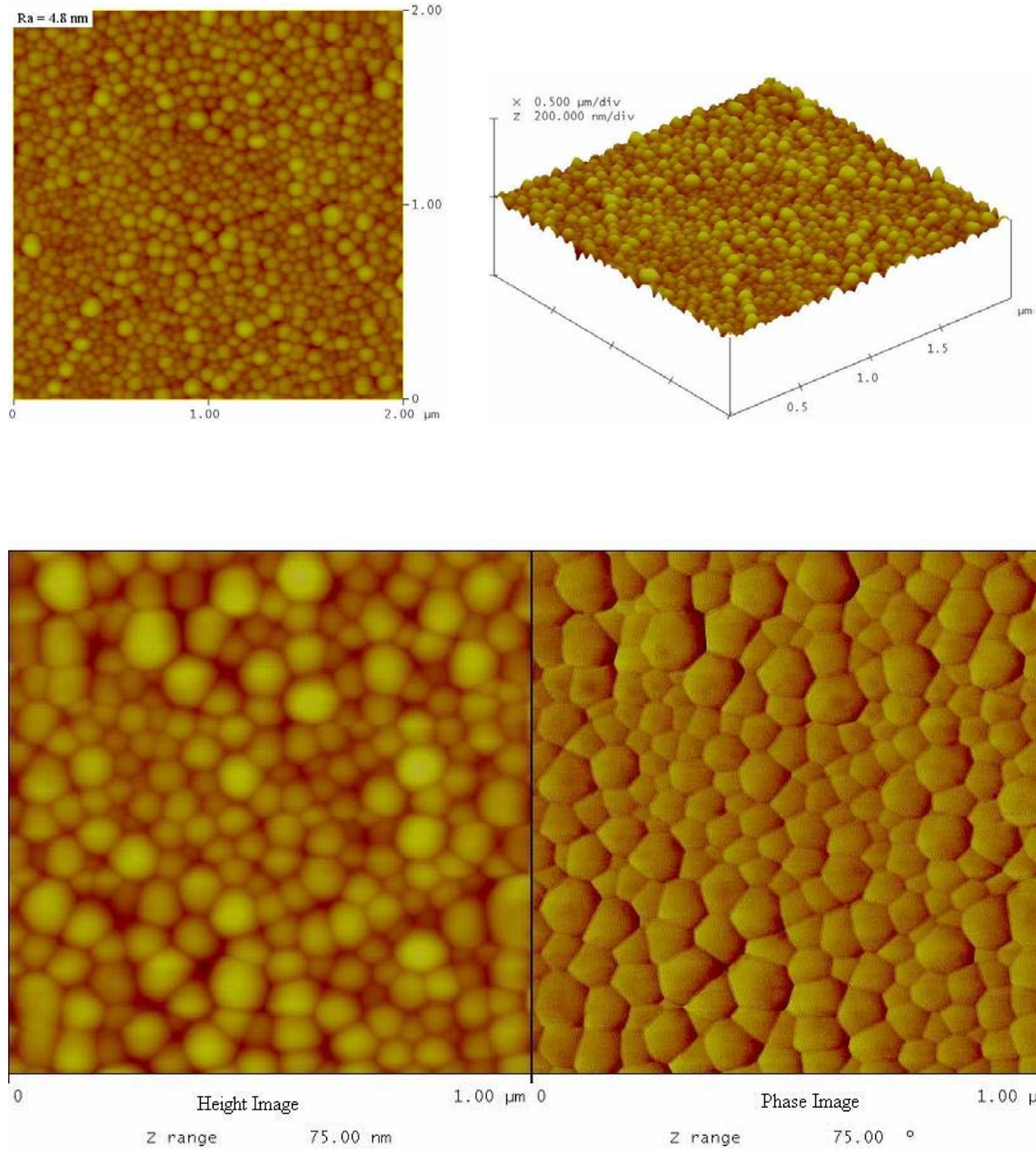
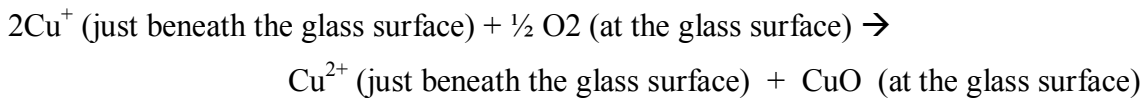


Figure 5.36. AFM images of metallic copper film grown under hydrogen atmosphere.

5.4.3.4 Mechanism for Copper Oxide Film Formation

Various oxidation mechanisms have been proposed for the evolving CuO surface layer that results when copper containing glasses are heat treated in air. Copper ions are present in glass melts as predominately Cu⁺, which at melting temperatures is more thermodynamically stable than the Cu²⁺ state.²⁹ The basicity of the glass will affect the ratio of Cu⁺/Cu²⁺ somewhat, and this will be discussed in the next section, but the predominant oxidation state of copper in the glass will remain in the Cu⁺ state upon quenching to room temperature.⁵ Heat treatments near T_g, where ions become mobile, will result in the oxidation of Cu⁺ to Cu²⁺ within the glass, as the oxidized state is more thermodynamically stable at temperatures below T_g.⁶ The formation of the CuO layer on the glass surface results from the oxidation of Cu⁺ that is removed to the surface of the glass to balance the surplus charge that results from the oxidation of Cu⁺ directly below the glass surface. X-ray Photoelectron spectroscopy (XPS) was utilized in the current study to confirm the oxidation mechanism, originally proposed in 1980, by Barton and De Billy.³⁰



XPS provides information about the chemical state of a given atom by measuring the chemical shift associated with an appropriate core level for the atoms in different bonding configurations. The chemical shift is a reflection of the change in binding energy of core electrons with changes in the chemical environment and has been proven to be useful in evaluation of the oxidation state of copper.^{31,32} The reported binding energy for the Cu 2p_{3/2} photoelectron core level for Cu₂O and CuO compounds are very close in energy at 932.6 and 933.5 eV respectively. However Cu²⁺ ions are associated with strong satellites in the XPS spectra with binding energies between 6 and 10 eV above the main core level lines that are absent for the monovalent copper ion.³³ The satellite peaks are due to shake-up transitions by ligand to metal 3d charge transfer, and only occur for copper present in the 3d⁹ configuration (Cu²⁺ state). This transition will

not take place in the Cu⁺ state (3d¹⁰ configuration) or the metallic state due to filled 3d shells. The presence of the satellite peaks makes it possible to distinguish between the two oxidation states of copper oxide by examining the Cu 2p photoemission spectrum.

A polished surface of glass composition CU102903 was evaluated by XPS, as polished, and after a heat treatment for 24 hours at 490°C. Sputter depth profiles were completed on both the as-polished and heat treated specimens. Figure 5.37 displays the XPS sputter depth profile of the as-polished sample, while Figure 5.38 displays the sputter depth profile of the heat treated sample. Region 1 of figure 5.38 corresponds to the CuO layer of the heat treated surface, Region 3 is the bulk glass while Region 2 refers to the transition between the surface layer and the bulk glass.

The XPS profiles of the as-polished surface indicate that, other than carbon contamination on the sample surface, which was removed in less than 2 minutes of sputtering, the composition of the surface is fairly unchanged due to the polishing process. Analysis of the depth profile in Figure 5.38, and the fact that the sputter rate was determined to be approximately 100 nm/15 minutes, the film thickness was estimated to be 40 nm, while the transition region was estimated to be in the range of 40 to 60 nm.

Table 5.6 compares the average composition of the bulk glass (atomic %) for the as-polished surface sputtered between 2 and 20 minutes (carbon contamination removed) and the heat treated specimen sputtered between 15.5 and 30 minutes, corresponding to Region 3 in Figure 5.38. The copper concentration in the heat treated sample below the CuO layer is twice that of the as-polished glass while the sodium concentration is lower. No changes in the concentration of Si, B or O were observed. The lower sodium concentration could be due to preferential sputtering of the sodium during the depth profile, or may indicate that sodium is leaving the glass to help balance the excess positive charge associated with oxidation of copper in the glass. The increased copper concentration below the CuO layer indicates that there may be a barrier to diffusion of copper to the surface, once the continuous CuO layer is formed. This result is consistent with the results above that indicate an upper limit to the film thickness upon prolonged heating. The surface layer results in a barrier to further diffusion of the chemical species, leading to the elevated copper levels beneath the CuO layer.

Table 5.6. Average Composition of Bulk Glasses (Atomic %)

Sample	B	O	Na	Si	Cu
As-Polished, Sputtered 2-20 min.	11	62	5.2	21	1.4
Heated 490°C, CuO removed, sputtered 15.5-30 min.	10	62	3	22	3.3

High resolution Cu 2p spectra were collected to evaluate the oxidation state changes through the interface region (Region 2), below the CuO film. Figure 5.39 shows high resolution Cu 2p spectra from the heat treated specimen comparing chemical state at the surface to that at the beginning of Region 2. The surface spectrum is consistent with CuO, as the presence of the Cu 2p_{3/2} satellite doublet near 942 eV and Cu 2p_{1/2} satellite peak near 962 eV are characteristic of the Cu²⁺ chemical state. The relative intensity of the satellite peak to the main peak near 932 eV, as well as the position of the main peak provides an indication of the concentration of Cu⁺²/Cu⁺. The relative intensity of the satellite peak to the main peak in Figure 5.39 is lower after sputtering, indicating the contribution due to Cu²⁺ has decreased as sputtering into Region 2 progresses.

Figure 5.40 displays the high resolution spectra from the as polished sample comparing the chemical state at the surface to that in the bulk glass. Note the absence of any satellite peaks at 940-945 eV. Both spectra are consistent with Cu⁺ and are comparable to the spectrum obtained in Region 3 of the heat treated specimen. The lower intensity of the Cu 2p spectra for Cycle 1 in Figures 5.39 and 5.40 is due to carbon contamination at the surface reducing the overall atomic concentration of the glass constituents.

Figure 5.41 displays high resolution Cu 2p spectra from the heat treated sample showing changes across Region 2, the CuO/glass interface. Cycle 17 (8 min. sputter) provides the oxidation state of copper at the beginning of Region 2, just below the CuO layer, while cycle 23 (11 minute sputter) provides the oxidation state of copper at the glass side of Region 2. The presence of the satellite peaks between 940 and 945 eV is again characteristic of the Cu²⁺ state. The satellite peaks clearly decrease in intensity

through the interface and are not present in the bulk glass region. The copper chemical state in the bulk glass (Cycle 23) is consistent with Cu⁺.

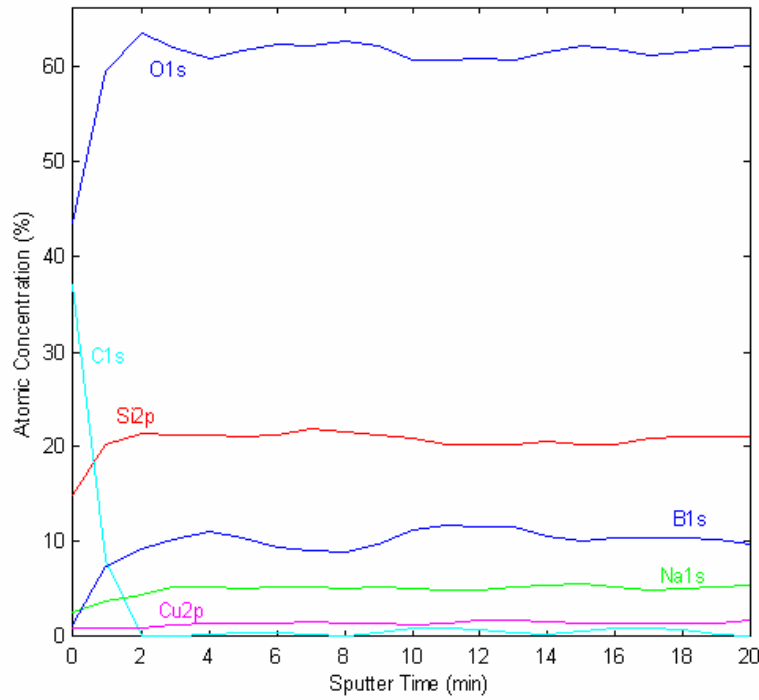


Figure 5.37. Sputter depth profile of a section of as-polished glass of composition CU102903.

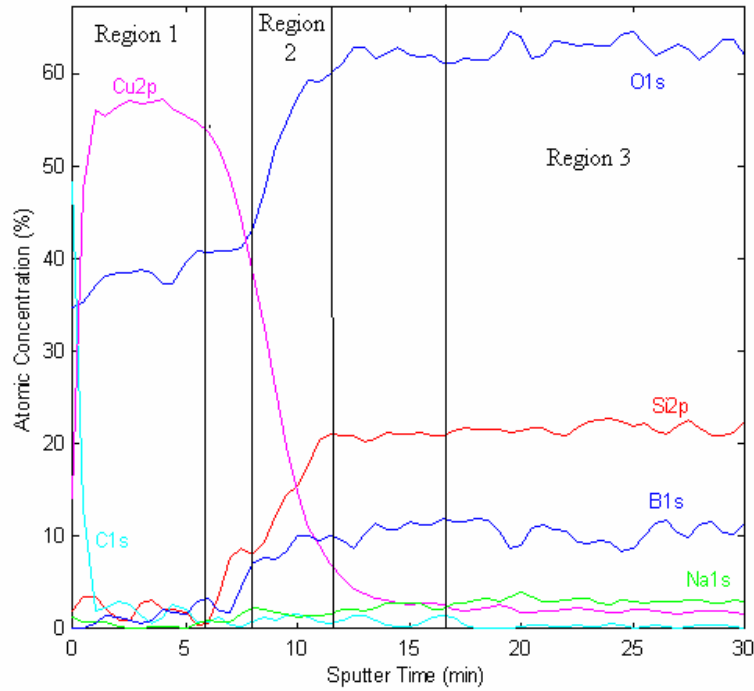


Figure 5.38. Sputter depth profile of a polished and heat treated section of glass composition CU102903.

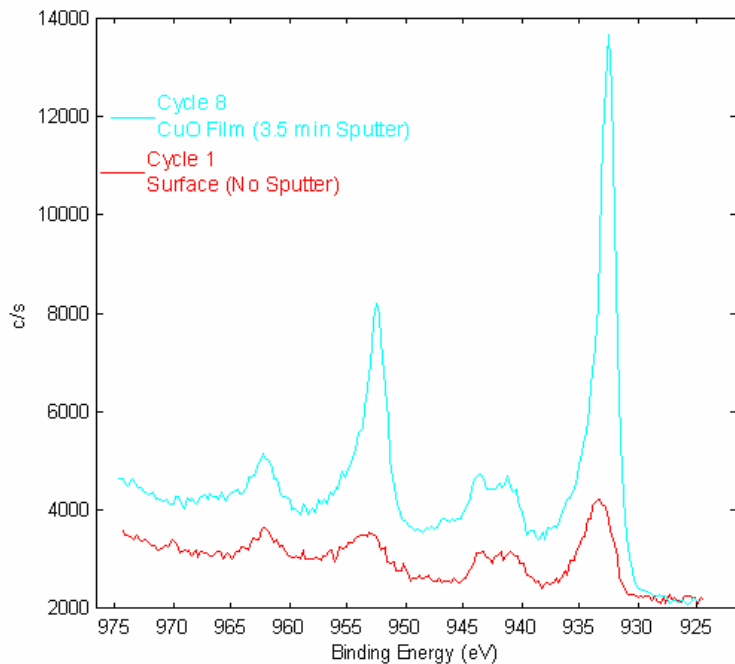


Figure 5.39. High resolution XPS Cu 2p spectra from the heat treated specimen, comparing chemical state at the film surface with that at the beginning of Region 2.

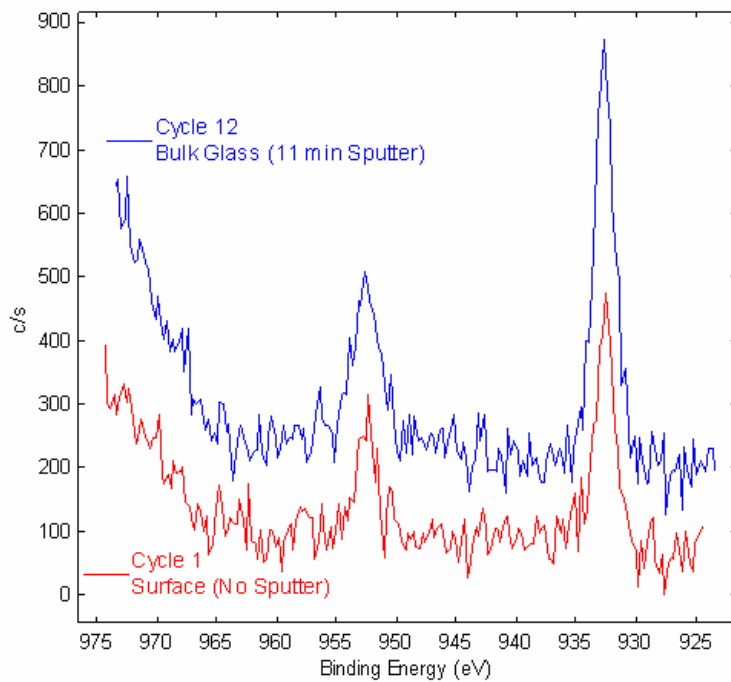


Figure 5.40. High resolution XPS Cu 2p spectra from the as-polished specimen, comparing chemical state at the surface with that of the bulk.

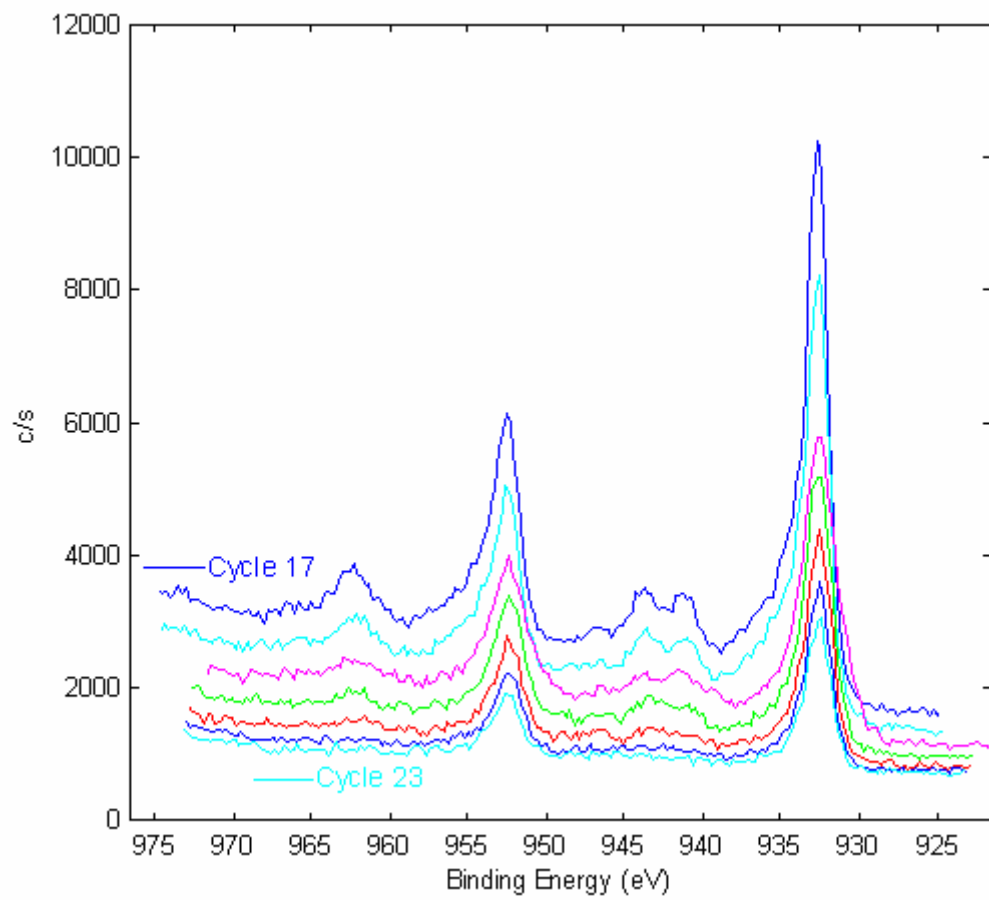


Figure 5.41. High resolution Cu 2p spectra from the heat treated sample showing changes across the CuO-glass interface (Region 2).

5.4.3.5 Affect of Alkali on Copper Oxide Film Formation

Experiments on redox equilibrium in glasses have shown that the proportion of the redox ion in the higher oxidation state increases with optical basicity of the glass. Douglas et al.⁵ studied chromium, cerium and iron in binary alkali borate and silicate glasses and demonstrated that equilibrium shifted toward the more oxidized state, for each transition metal, with increasing basicity of the glasses. Duffy³⁴ provides an optical basicity scale for oxide glasses that shows K⁺ has an optical basicity 22% higher than Na⁺, while Na⁺ is 15% higher than Li⁺. From these studies the conclusion can be drawn that the alkali present in the glass will affect the copper oxide film formation, due to the oxidation state of the copper in the glass. If more copper exists in the 2⁺ state in the glass upon melting, there is a smaller driving force for the oxidation of the copper in the glass from the 1⁺ to the 2⁺ state, and the film formation will be slowed. From these results the prediction can be made that the driving force for film formation will be greatest for Li⁺, which will have the largest ratio of Cu¹⁺/Cu²⁺ in the glass melt, followed closely by Na⁺, while K⁺ will greatly reduce the ability to form the copper oxide film, as much of the copper in the glass will already be in the 2⁺ state upon melting.

To confirm the affect of the alkali in the glass and further justify the proposed mechanism for copper oxide film formation, an alkali substitution was carried out. Lithium and potassium were fully substituted for sodium in glass composition CU102903. The glasses were melted and poured onto a steel plate for fast cooling. Upon cooling the lithium containing glass resulted in a substantial copper oxide surface film approximately 50 nm thick, which was confirmed by XRD to be CuO. Figure 5.42 displays AFM images of the surface of the as poured lithium containing glass surface.

The potassium containing melt resulted in no surface film upon cooling, as determined by AFM. Figure 5.43 displays AFM images of the potassium containing glass after a 24 hour heat treated near its T_g (515°C). The tenorite crystals are clearly isolated from each other, and a small percentage of the surface is covered with crystals.

Consistent with predictions based on optical basicity, the lithium containing glass formed the copper oxide film easily upon cooling of the melt, while the sodium containing glass required additional heat treatment to form a continuous film, and the potassium containing composition formed only sparse, isolated tenorite crystals even after extended heat treatments near T_g . Although film quality was excellent for the lithium containing glass, it was difficult to avoid phase separation with this composition. Figure 5.44 shows an as polished surface of the lithium containing glass, which clearly shows phase separation by a spinodal type mechanism. The relief in the image is due to differential hardness of the two glass phases, with the dark phase being less durable during the polishing process.

XPS elemental surveys and high-resolution spectra were acquired on fresh fracture surfaces of the as melted glass batches containing the various alkalis. Atomic concentrations were calculated from the high resolution spectra using elemental sensitivity factors provided by the instrument vendor. The compositions of the fractured surfaces determined from the high-resolution XPS data analysis are listed in Table 5.7. Cu:Si ratios indicate that the copper concentrations are comparable between the three samples. Figure 5.45 compares the Cu 2p spectra obtained from the three glasses with various alkalis present. No significant differences in the copper chemical state were realized between the three samples with various alkali. Peaks observed at 932.8 eV ($2p_{3/2}$) and 952.6 eV ($2p_{1/2}$) are consistent with the Cu^+ oxidation state. The satellite peaks at 942.2 eV and 962.3 eV observed in Figures 5.39 and 5.41, and overlaid on Figure 5.45 were not observed in the bulk of the current samples. Based on the sputter data from sample CU102903, the intensity of the lowest detectable satellite peak corresponds to approximately 20% of the Cu peak being due to Cu^{2+} . The XPS results therefore do not provide enough sensitivity to Cu^{2+} to confirm that the potassium containing glass has an elevated level of Cu^{2+} in the as melted glass, as the level of Cu^{2+} is expected to be less than 20% of the total Cu.

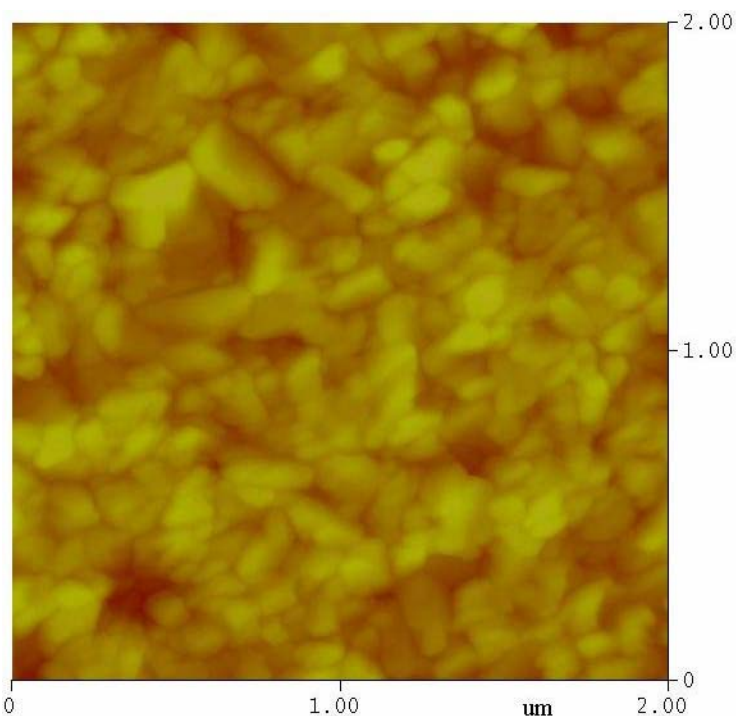
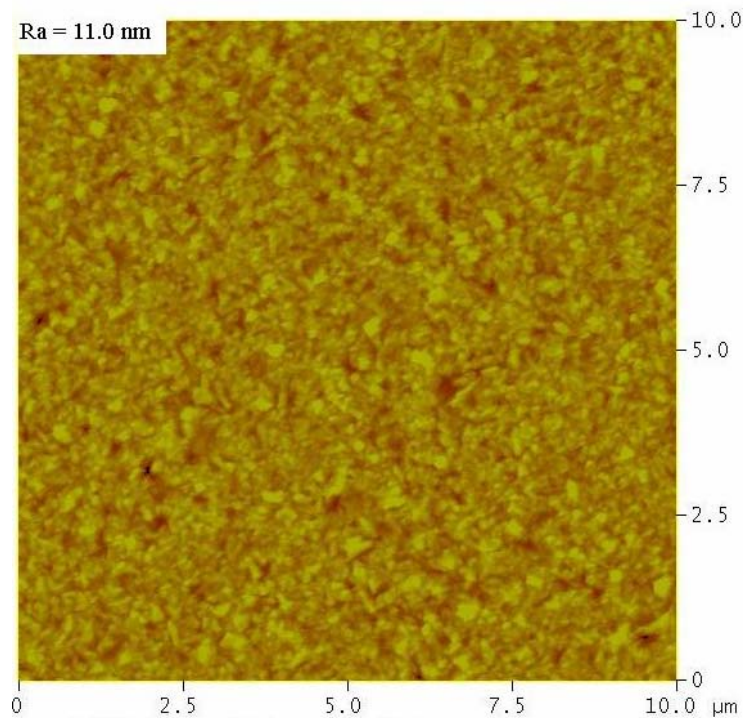


Figure 5.42. AFM images of the as poured surface of glass composition CU042104 (lithium containing glass).

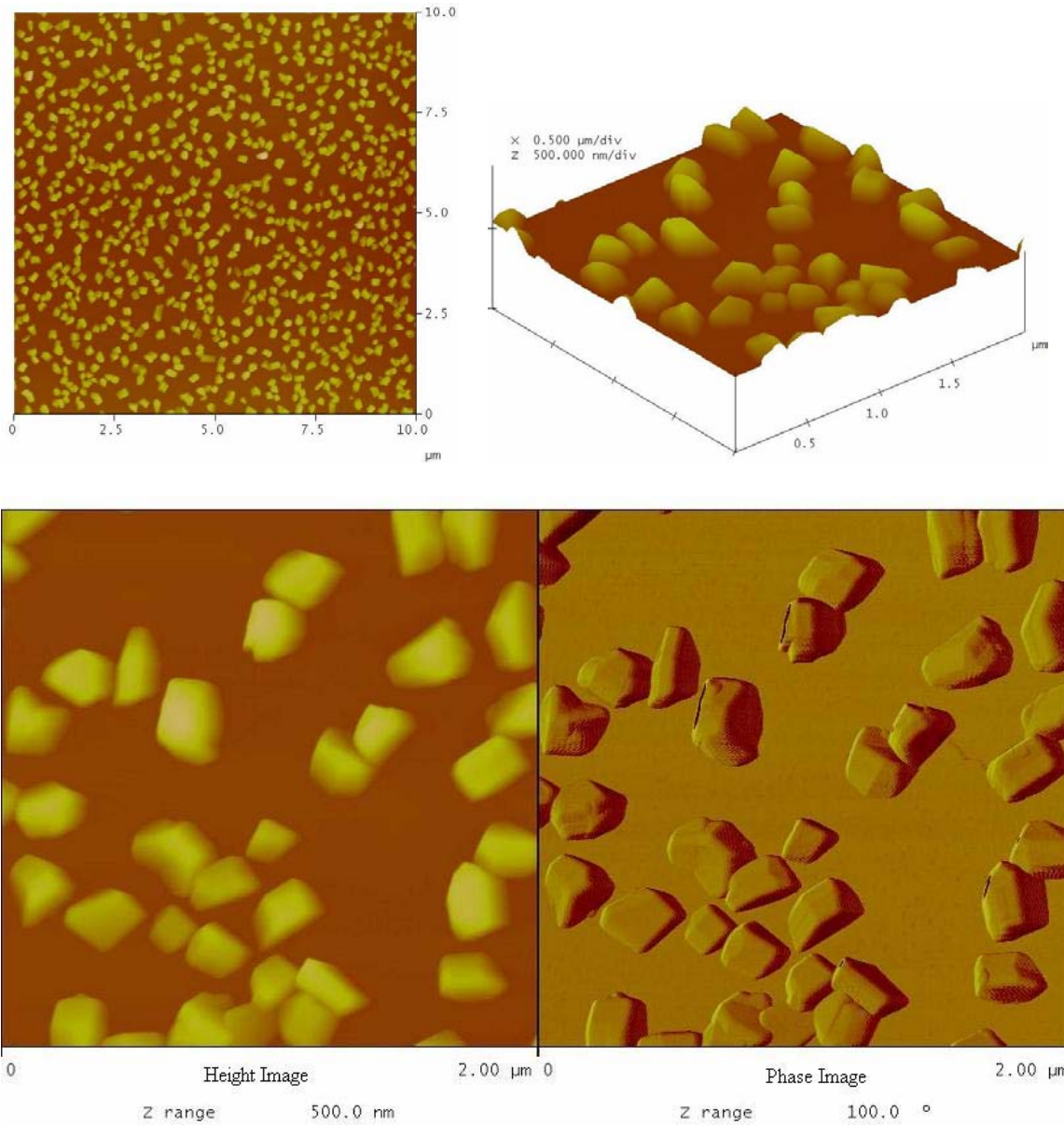


Figure 5.43. AFM images of the surface of glass composition CU042004 (potassium containing glass) after a 24 hour heat treatment at 515°C for 24 hours.

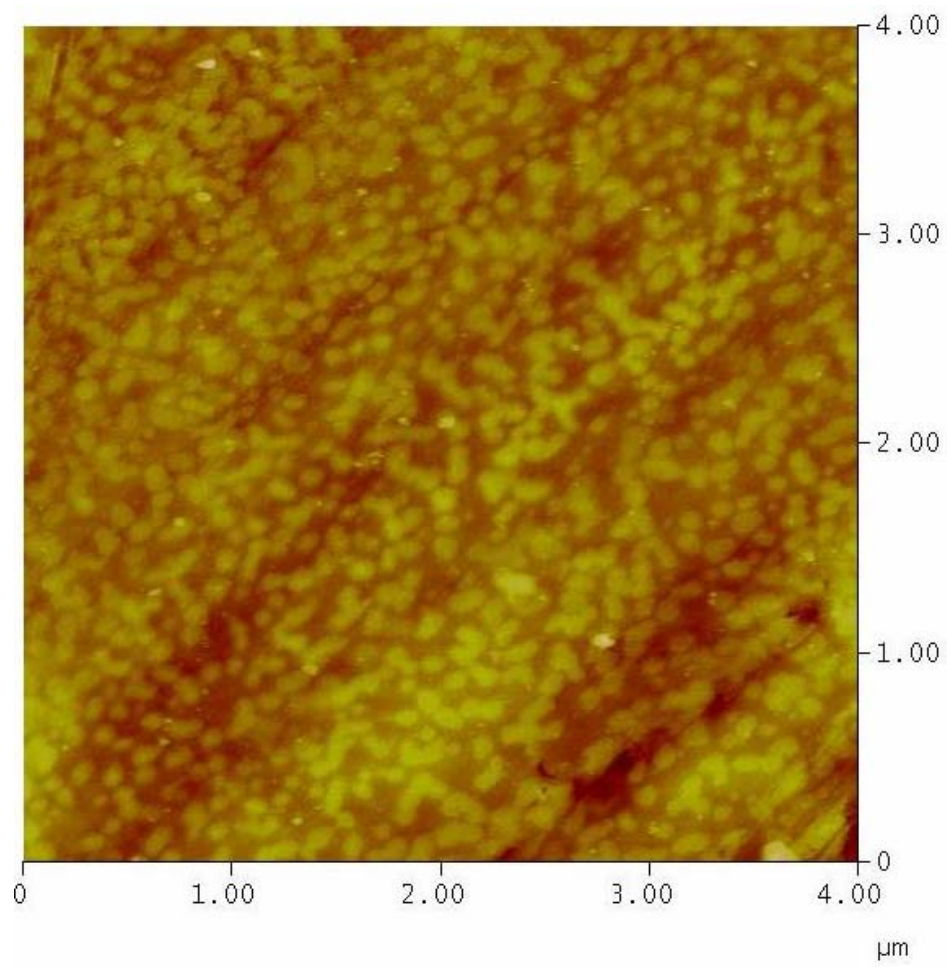


Figure 5.44. AFM of as-polished surface of glass composition CU041904 (lithium containing) showing the presence of phase separation.

Table 5.7. XPS determined glass compositions in atomic %

Sample ID	Li	B	C	O	Na	Si	K	Cu	Cu:Si
CU041904 (Li)	8.7	8.1	12.9	53.2		15.7		1.4	0.09
CU102903 (Na)			10.7	8.3	56.1	6.3	16.9		1.8 0.11
CU042004 (K)			8.3	9.4	55.9		18.3	5.8	2.0 0.11

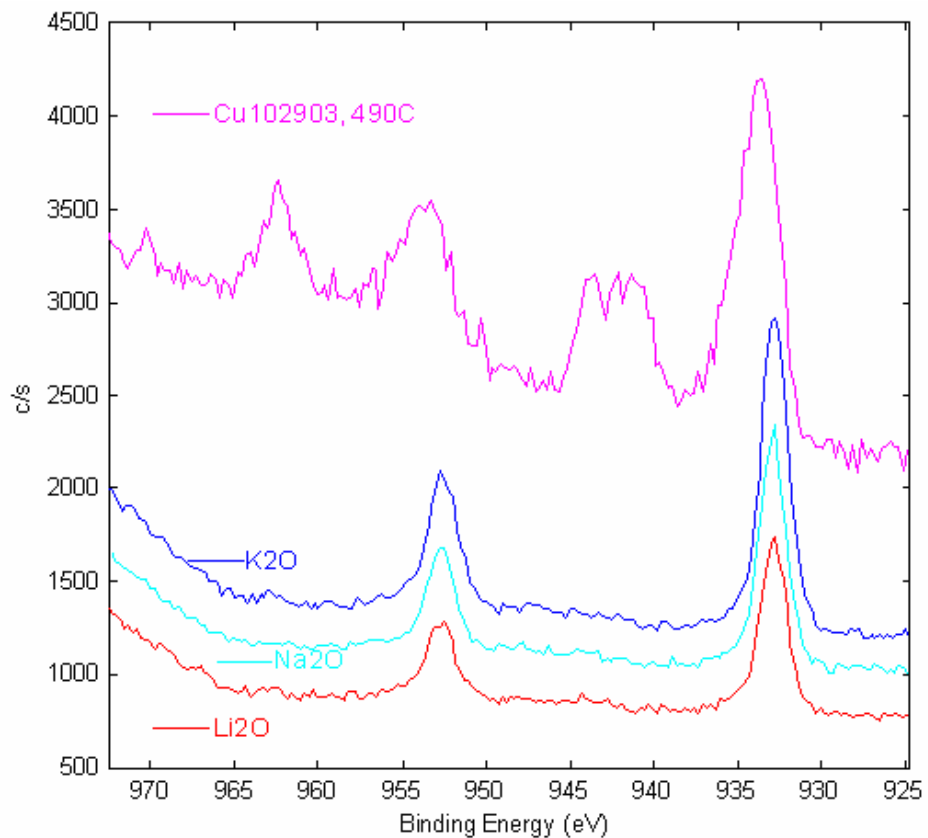


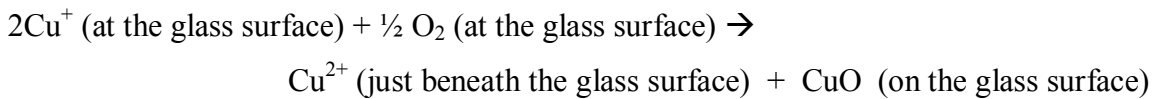
Figure 5.45. Representative high resolution Cu 2p spectra comparing copper chemical state between glasses prepared with various alkali. The CuO layer from sample CU102903 is shown for comparison. Spectra were charge referenced to C 1s at 284.8 eV.

5.5 Conclusions

Copper oxide films were grown in-situ on the surface of several glass compositions. The major effort for understanding the film formation was carried out on alkali borosilicate glasses containing 10 wt % CuO. Heat treatment in an oxidizing atmosphere resulted in CuO, tenorite, films while Cu₂O, cuprite, films were formed when heat treatment was carried out under vacuum and copper metal films resulted from heat treatment in a reducing environment.

AFM was used extensively to characterize the film surfaces as well as the film thickness and uniformity. The most uniform films resulted at temperatures below T_g while heat treatments near T_g resulted in films with an upper thickness limit, indicating that further migration of copper to the film/air surface or further diffusion of oxygen through the film to the glass/film interface is blocked at a certain thickness and uniformity of the film. Heat treatments much above T_g resulted in crystallization of the bulk glass.

XPS was utilized to determine the oxidation state of copper in the glass, and the surface film as well as in the transition region between the film and the glass. XPS clearly showed that the majority of the copper ions existed in the +1 state within the bulk glass, but were oxidized to the +2 state near the glass/film interface region. The films are believed to be the result of copper ions migrating from the glass to the surface region where oxidation from the Cu⁺ to Cu²⁺ state is charge balanced by the oxidation of copper to CuO at the glass surface. Once the Cu²⁺ ions are formed at the glass/film interface they then diffuse back into the glass creating the Cu²⁺ diffusion profile shown by XPS results.



The effect of alkali type on the film formation process was examined and the results were consistent with predictions based on optical basicity. The optical basicity

scale predicts that potassium will result in a more oxidized glass melt than sodium which will be more oxidized than lithium. If more copper exists in the 2^+ state in the glass upon melting, there is a smaller driving force for the oxidation of the copper in the glass from the 1^+ to the 2^+ state, and the film formation will be slowed. The results of alkali substitutions showed that lithium containing alkali borosilicate glass formed the copper oxide film easily upon cooling of the melt, while the sodium containing glass required additional heat treatment to form a continuous film, and the potassium containing composition formed only sparse, isolated tenorite crystals even after extended heat treatments near T_g

5.6 References

1. M.E. Milberg, J.G. O'Keefe, R.A. Verhelst, and H.O. Hooper, "Boron Coordination in Sodium Borosilicate Glasses," *Phys. Chem. Glasses*, **13** [3] 79-84 (1972).
2. T.F. Soules and A.K. Varshneya, "Molecular Dynamic Calculations of a Sodium Borosilicate Glass Structure," *J. Am. Ceram. Soc.*, **64** [3] 145-50 (1981).
3. W.A. Weyl, *Coloured Glasses*; pp. 154-67. Society of Glass Technology, Sheffield, UK, 1999.
4. W.D. Bancroft and R.L. Nugent, "Copper Oxide in the Borax Bean," *J. Phys. Chem.*, **33** [5] 729-44 (1929).
5. R.W. Douglas, P. Nath, and A. Paul, "Oxygen Ion Activity and Its Influence on Redox Equilibrium in Glasses," *Phys. Chem. Glasses*, **6** [6] 216-23 (1965).
6. T. Yoko, K. Kamiya, and S. Sakka, "Oxidation State of Copper Ions in Silicate Glasses," *J. Non-Cryst. Solids*, **71** [1-3] 245-51 (1985).
7. S.C. Ray, "Preparation of Copper Oxide Thin Film by the Sol-Gel-Like Dip Technique and Study of Their Structural and Optical Properties," *Sol. Energy Mater.*, **68** [3-4] 307-12 (2001).
8. J.R. Ortiz, T. Ogura, J. Medina-Valtierra, S.E. Acosta-Ortiz, P. Bosh, J.A. de las Reyes, and V.H. Lara, "A Catalytic Application of Cu₂O and CuO Films Deposited Over Fiberglass," *Appl. Surf. Sci.*, **174** [3-4] 177-84 (2001).
9. R. Zhou, Y. Yu, X. Jiang, X. Zheng, and F. Chen, "Temperature-Programed Reduction and Temperature-Programed Desorption Studies of CuO/ZrO₂ Catalysts," *Appl. Surf. Sci.*, **149** [3-4] 263-70 (1999).
10. K.C.C. Kharas, "Performance, Selectivity and Mechanisms in Cu-ZSM-5 Lean Burn Catalysts," *Appl. Catal., B*, **2** [2-3] 207-24 (1993).
11. R. Lange, *Photoelements and Their Applications*. Reinhold, New York, 1939.
12. G. Beensh-Marchwicka, L. Krol-Stepniewska, and M. Slaby, "Effect of Oxygen Pressure During Sputtering on the Properties of Thin CuO_x Films," *Thin Solid Films*, **88** [1] 33-9 (1982).

13. A.E. Rakhshani, "Preparation, Characteristics and Photovoltaic Properties of Cuprous Oxide - A Review," *Solid-State Electron.*, **29** [1] 7-17 (1986).
14. B.P. Rai, "Cu₂O Solar Cells: A Review," *Sol. Cells*, **25** [3] 265-72 (1988).
15. J.P. Hiernaut, A. Roch, and J. Van Cakenberghe, "Stoichiometry and Structure of Copper Oxide Films on Glass," *Thin Solid Films*, **71** [2] 249-54 (1980).
16. L. Armelao, D. Berreca, M. Bertapelle, B. Gregorio, S. Cinzia, and E. Tondello, "A Sol-Gel Approach to Nanophasic Copper Oxide Thin Films," *Thin Solid Films*, **442** [1-2] 48-52 (2003).
17. M.T.S. Nair, L. Guerrero, P.K. Arenas, and P.K. Nair, "Chemically Deposited Copper Oxide Thin Films: Structure, Optical and Electrical Characteristics.," *Appl. Surf. Sci.*, **150** [1-4] 143-51 (1999).
18. T. Lutz, C. Estournes, J.C. Merle, and J.L. Guille, "Optical Properties of Copper-Doped Silica Gels," *J. Alloys Compd.*, **262-263** [1] 438-42 (1997).
19. M. Ristov, G.J. Sinadinovski, and I. Grozdanov, "Chemical Deposition of Cu₂O Thin Films," *Thin Solid Films*, **123** [1] 63-7 (1985).
20. K. Santra, C.K. Sarkar, M.K. Mukherjee, and B. Ghosh, "Copper Oxide Thin Films Grown by Plasma Evaporation Method," *Thin Solid Films*, **213** [2] 226-9 (1992).
21. K. Kamiya, Y. Toshinobu, and S. Sakka, "Migration of Cu⁺ Ions in Cu₂O-Al₂O₃-SiO₂ Glasss on Heating in Air," *J. Non-Cryst. Solids*, **80** [1-3] 405-11 (1986).
22. A. Tawansi, E. Ahmed, D. Holland, I.A. Gohar, and N.A. Ei-Shishtawi, "Effects of Heat Treatment and Cu₂O Content of Lead Aluminoborate Glasses on their Conduction Mechanisms and Microhardness," *J. Non-Cryst. Solids*, **105** [1-2] 78-90 (1988).
23. A. Mekki, D. Holland, and C.F. McDonville, "X-Ray Photoelectron Spectroscopy Study of Copper Sodium Silicate Glass Surfaces," *J. Non-Cryst. Solids*, **215** [2-3] 271-82 (1977).
24. C.F. Rapp, Owens-Corning Fiberglass Corporation, "Metal Coated Glass Fibers," US Pat. 4,836,837, November 16, 1987.
25. K.L. Babcock and C.B. Prater, "Phase Imaging: Beyond Topography, Application Note," Veeco Instruments, Santa Barbara, CA., 1995.
26. M.M. Hall, "Protien Adsorption to Multi-Component Glasses"; Ph.D. Thesis. Alfred University, Alfred, NY, 2004.

27. R. Jenkins and R.L. Snyder, *Introduction to X-Ray Powder Diffractometry*, p. 90, John Wiley & Sons, New York, 1996.
28. M.R. Wright, "The Hall Effect and Electrical Conductivity of Single Crystal Cuprous Oxide"; Ph.D. Thesis. Wayne State University, Detroit, Michigan, 1962.
29. K.T. Jacob and C.B. Alcock, "Thermodynamics of CuAlO₂ and CuAl₂O₄ and Phase Equilibria in the System Cu₂O-CuO-Al₂O₃," *J. Am. Ceram. Soc.*, **58** [5-6] 192-5 (1975).
30. J.L. Barton and M. De Billy, "Diffusion and Oxidation of Cu⁺ in Glass," *J. Non-Cryst. Solids*, **38/39** [Part 2] 523-6 (1980).
31. U. Linder and H. Papp, "XPS and ISS Characterization of Potassium or Copper Containing Fe/Mn Oxide Catalysts for Fischer-Tropsch Synthesis," *Appl. Surf. Sci.*, **32** [1-2] 75-92 (1990).
32. G. Moretti, S. De Rossi, and G. Ferraris, "Characterization of Well Dispersed Copper Species on the Surface of ZnO by X-ray Photoelectron Spectroscopy," *Appl. Surf. Sci.*, **45** [4] 341-9 (1990).
33. K. Wandelt, "Photoemission Studies of Adsorbed Oxygen and Oxide Layers," *Surf. Sci. Rep.*, **2** [1] 1-121 (1982).
34. J.A. Duffy, "A Common Optical Basicity Scale for Oxide and Fluoride Glasses," *J. Non-Cryst. Solids*, **109** [1] 35-9 (1989).

Chapter 6

Thesis Conclusions

6.1 Understanding the Near-Field Scanning Optical Microscopy Fiber Optic Tip Formation Process

The cone angle is an important variable in producing NSOM tips and the ability to vary the cone angle is a major advantage of the fiber etching method over producing NSOM tips by fiber pulling. This study demonstrates the feasibility of predicting the cone angle after short etch times, without taking the etching process to completion, which may take several hours. It has been demonstrated that AFM is a powerful characterization tool for visualizing the evolution of the tip that results from etching single mode optical fibers. The data gathered for short etch times showed that the cone angle changed initially, but then leveled off with further etching.

The relationship between cone angle and the ratio of core etch rate to differential etch rate was demonstrated through a simple model and shown to correlate extremely well with experimental data. The larger the differential etch rate between the core and the cladding, and therefore the smaller the ratio of core etch rate to differential etch rate, the smaller the cone angle that evolves. Cone angles reported in this study ranged from 157 degrees for an SMF28 fiber in a 1:1:1.8 solution to 58 degrees for a HI fiber in a 1:1:6 solution. Additionally it was shown that the cone angle possible for the SMF28 fiber varied from 157 to 113 degrees providing excellent opportunity to modify the NSOM tip for specific applications. Larger cone angles result in shorter tips and improve the transmission coefficient as the propagation mode runs into cut-off and begins an exponential decay closer to the aperture. However if sharper tips are needed, and intensity can be sacrificed the smaller cone angles result in longer, sharper tips and may provide better resolution for some applications.

6.2 Evaluation of Phase Separation with Atomic Force Microscopy

AFM has been shown to be a powerful characterization tool for evaluation of liquid-liquid phase separation in glasses. Excellent correlation with previously published TEM data was achieved for both the sodium silicate and alkali borosilicate systems evaluated. Chemical and spatial variations during the phase separation process were easily followed with the AFM technique.

The characterization techniques traditionally used for evaluation of phase separation, such as TEM and SAXS are expensive, labor intensive and require specialized training for data interpretation. AFM on the other hand requires little sample preparation, is readily available, and analysis time can be as short as a few minutes. Although it is believed that most of the information necessary to evaluate the microstructure of phase separated glasses can be achieved through AFM analysis, the technique can also be used as a method for rapidly screening samples that require further analysis by more labor or instrument intensive characterization techniques.

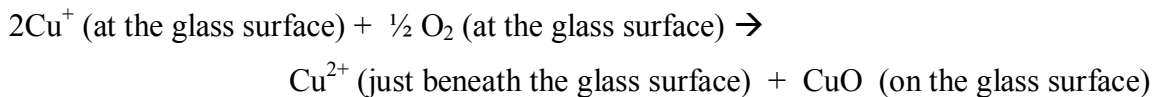
6.3 Thin Film Copper Oxide Layers Grown In-Situ on Alkali Borosilicate Glasses

Copper oxide films were grown in-situ on the surface of several glass compositions. The major effort for understanding the film formation was carried out on alkali borosilicate glasses containing 10 wt % CuO. Heat treatment in an oxidizing atmosphere resulted in CuO, tenorite, films while Cu₂O, cuprite, films were formed when heat treatment was carried out under vacuum and copper metal films resulted from heat treatment in a reducing environment.

AFM was used extensively to characterize the film surfaces as well as the film thickness and uniformity. The most uniform films resulted at temperatures below T_g while heat treatments near T_g resulted in films with an upper thickness limit, indicating that further migration of copper to the film/air surface or further diffusion of oxygen through the film to the glass/film interface is blocked at a certain thickness and

uniformity of the film. Heat treatments much above T_g resulted in crystallization of the bulk glass.

XPS was utilized to determine the oxidation state of copper in the glass, and the surface film as well as in the transition region between the film and the glass. XPS clearly showed that the majority of the copper ions existed in the +1 state within the bulk glass, but were oxidized to the +2 state near the glass/film interface region. The films are believed to be the result of copper ions migrating from the glass to the interface region where oxidation from the Cu^+ to Cu^{2+} state is charge balanced by the formation of CuO at the glass surface. Once the Cu^{2+} ions are formed at the glass/film interface they then diffuse back into the glass creating the Cu^{2+} diffusion profile shown by XPS results.



The effect of alkali type on the film formation process was examined and the results were consistent with predictions based on optical basicity. The optical basicity scale predicts that potassium will result in a more oxidized glass melt than sodium which will be higher than lithium. If more copper exists in the 2^+ state in the glass upon melting, there is a smaller driving force for the oxidation of the copper in the glass from the 1^+ to the 2^+ state, and the film formation will be slowed. The results of alkali substitutions showed that lithium containing alkali borosilicate glass formed the copper oxide film easily upon cooling of the melt, while the sodium containing glass required additional heat treatment to form a continuous film, and the potassium containing composition formed only sparse, isolated tenorite crystals even after extended heat treatments near T_g .

Appendix A

Monolithic Lens Formed Through Etching at End of Optical Fiber

Figure 3.16 showed that the tip structure formed at the end of an optical waveguide fiber would be positive (protruding from the cladding) if the cladding etch rate exceeded the core etch rate, and negative (core depressed into the cladding) if the core etch rate exceeded the cladding etch rate. Some encouraging results to develop monolithic lenses on the end of glass optical fibers to help focus the light exiting the fiber end were achieved through a combination of etching steps.

Small diameter (3-4 microns), high index fibers with cleaved ends were being utilized to integrate optical fibers with photonic crystals as described by Suzuki, Chen and Kohnke.¹ The authors developed a novel silicon platform where light from optical fiber was coupled directly into and out of silicon-based photonic crystal structures. Problems with insertion losses, due to poor coupling and significant divergence of the light from the cleave fiber end, led to this work on improving the coupling between the fiber and the photonic crystal with a monolithic lens.

Figure A1.1 displays 3-D AFM images of cleaved optical fiber end faces used for this application after a 1 and 5 minute etch in 1:1:1.9 (1 part water:1 part 50% HF:1.9 parts 40% NH₄F) etch solution. The height of the lens structure and the angle the tangent (drawn to the sidewall at the middle of the tip height) makes with the horizontal is listed on the section traces. The 1 minute etch results in a low profile tip (2.5°) while the 5 minute etch results in a much steeper tip structure (11.7°). By adjusting the etch concentration and etch time a series of tip shapes can be formed that will result in various focal lengths, and spot sizes for the light emerging from the fiber end.

References

1. L. Chen, Y. Suzuki, and G.E. Kohnke, "Integrated Platform for Photonic Crystal Devices at Near Infrared Wavelengths," *Appl. Phys. Lett.* **80** [9] 1514-16 (2002).

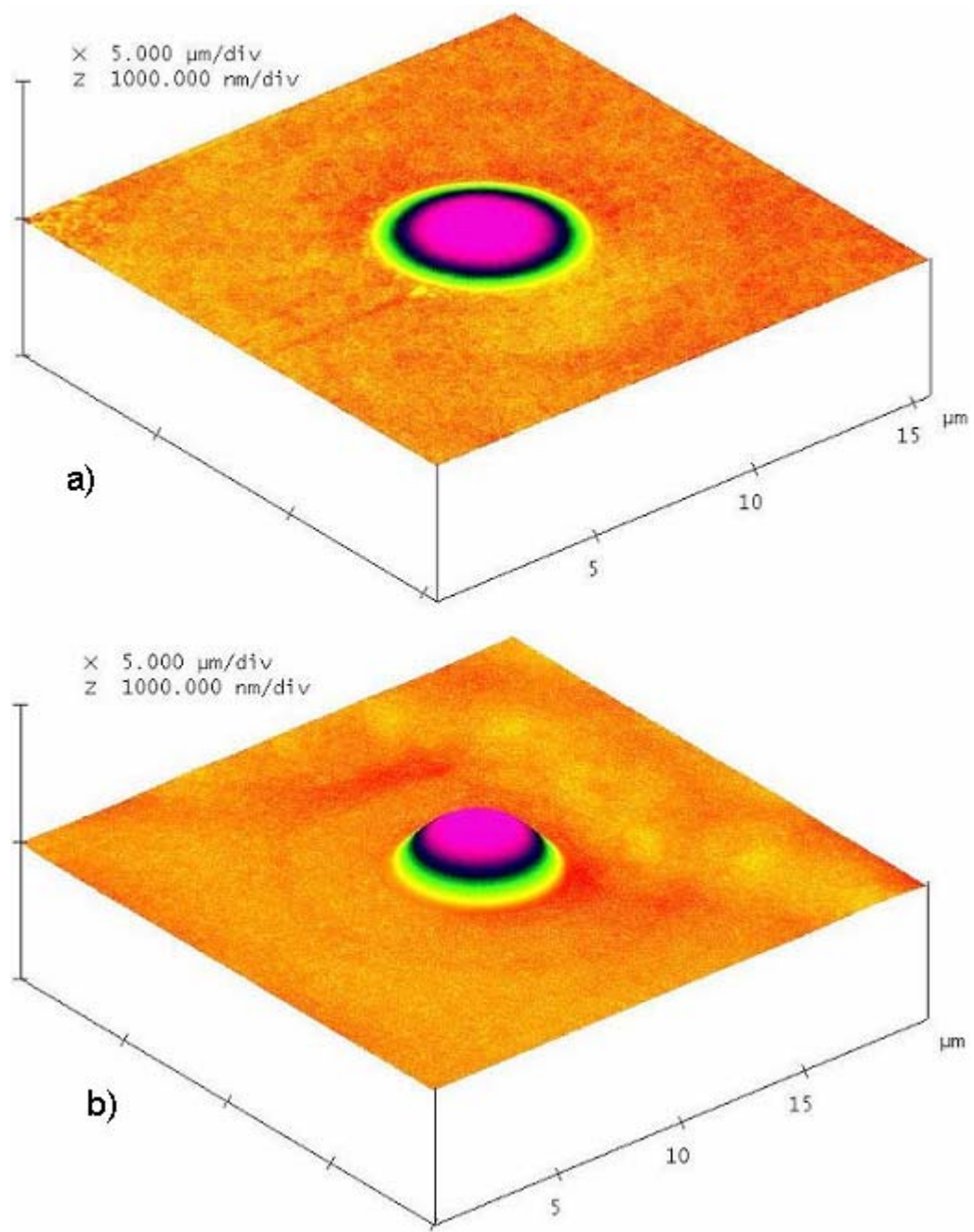


Figure A1. 3D AFM images of optical fiber etched in 1:1:1.9 etch solution for a) 1 minute and b) 5 minutes.

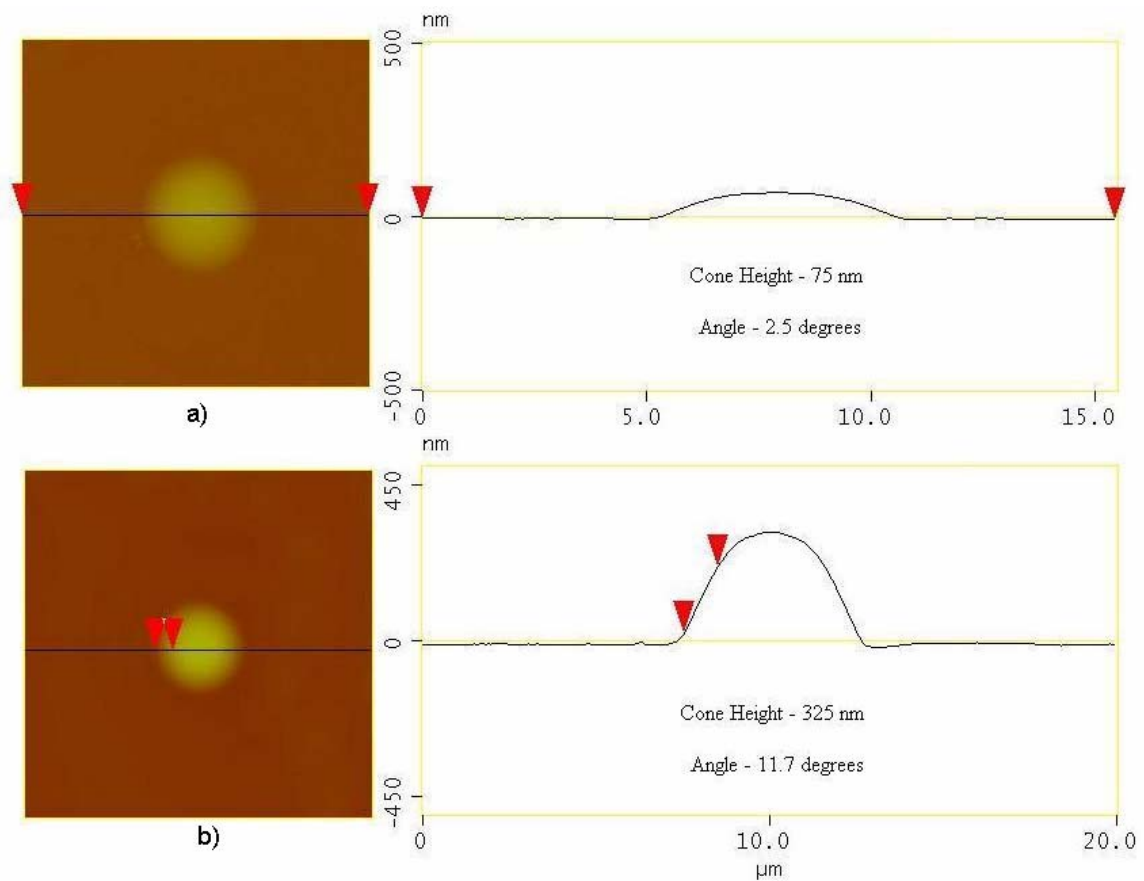
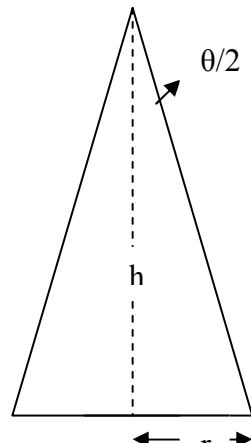


Figure A2. Section AFM images of optical fiber etched in 1:1:1.9 etch solution for
a) 1 min and b) 5 minutes.

Appendix B

Trigonometric Analysis of Optical Fiber Radial Etch Rate



Right Cone

$$\text{Surface Area of Cone} = \pi r \sqrt{r^2 + h^2}$$

$$\frac{r}{h} = \tan\left(\frac{\theta}{2}\right)$$

$$h = \frac{r}{\tan\left(\frac{\theta}{2}\right)} = r \cdot \cotan\left(\frac{\theta}{2}\right)$$

$$\text{Surface Area of Cone} = \pi r \sqrt{r^2 + r^2 \cdot \cotan^2\left(\frac{\theta}{2}\right)} =$$

$$\pi r^2 \sqrt{1 + \cotan^2\left(\frac{\theta}{2}\right)}$$

$$\text{therefore, Surface Area of Cone} = \pi r^2 \cdot \csc\left(\frac{\theta}{2}\right)$$

Equating the rate of fiber volume exposure to the rate of loss by etching:

$$\text{Exposure} = \Pi r^2 d_{cl}$$

$$\text{Etching} = \Pi r^2 \cdot \cosec\left(\frac{\theta}{2}\right) d_{co}$$

$$\Pi r^2 d_{cl} = \Pi r^2 \cdot \cosec\left(\frac{\theta}{2}\right) d_{co}$$

therefore:

$$\frac{d_{cl}}{d_{co}} = \cosec\left(\frac{\theta}{2}\right)$$

and,

$$\theta = 2 \cdot \cosec^{-1}\left(\frac{d_{cl}}{d_{co}}\right)$$